Dynamic modelling of traction loads and renewable energy systems on shared power lines for power quality assessment

by

Hein Naudé

Thesis presented in fulfilment of the requirements for the degree
Master of Engineering (Research) in the Faculty of Engineering
at Stellenbosch University

Supervisor: Dr. Johan Beukes

Co-Supervisor: Dr. Ulrich Minnaar

Department of Electrical & Electronic Engineering

April 2019

Declaration

By submitting this thesis electronically I declare that the entirety of the work contained therein is my own, original work, that I am the sole author thereof (save to the extent explicitly otherwise stated), that reproduction and publication thereof by Stellenbosch University will not infringe any third party rights and that I have not previously in its entirety or in part submitted it for obtaining any qualification.

April 2019

H. Naudé

Acknowledgements

I would like to thank my study leaders and mentors Dr. Johan Beukes and Dr. Ulrich Minnaar for allowing me to learn from their vast experience as engineers. Thank you for the continual support, advice and guidance during this project.

I would like to acknowledge the EPPEI Specialisation Centre in Renewable Energy and Power System Simulation for their financial support and contribution to this work.

I would like to thank my family in particular my parents, Hennie and Annerine Naudé, for their continual support during my student years and all the sacrifices that they have made for me to be able to do this work. I would not be in this position if not for them.

I would like to thank my close friends who made this road so much easier, including but not restricted to: Hennie Louw, Armin Wagner, Jacques Wattel and Janke Jacobs.

Abstract

Eskom has recently started investigating the effect of traction on renewable energy sources due to the power quality problems associated with traction networks. Poor power quality generated by means of traction networks have always been of concern. The impact of the traction load power quality issues has greatly increased due to the increasing number of renewable power producers (RPPs) being connected to the national grid. Studies has shown an increase in voltage unbalance and harmonic distribution at various points of concern in the network which leads to the loss of power production from the RPPs. Recent power quality assessment reports from Eskom has indicated that power quality problems, particular harmonic emissions, exist at RPPs. Harmonic sources such as non-linear (traction loads) are contributors to voltage harmonic distortion on the network in addition to harmonic emissions of RPPs.

To gain insight into the problem the need exist to model and simulate traction drive systems and renewable power plants. DIgSILENT PowerFactory, was chosen as the software simulation package to design and build generic models of renewable system inverters and traction load rectifiers to conduct dynamic time domain simulations. To validate the accuracy of the models, the simulation results were compared to measured results. Due to good correlation, the models can be used for future network planning and power quality assessment.

The aim of this thesis is further to investigate the power quality issues related to traction loads and to perform a power quality assessment at the POC of a local wind farm. The assessment of voltage unbalance indicated that traction loads is generally the largest contributor to voltage unbalance on a traction network and can cause inverter trips at RPPs at certain conditions. It is observed that various conditions such as the traction load type, operating conditions and control of the traction load, power demand of the traction loads and three-phase fault level will impact the voltage unbalance caused by traction loads.

The impact of traction loads on the network voltage distortion is investigated and it is determined that small current harmonics emissions of traction loads can generate large voltage distortion at the presence of a parallel resonance. The impact of impedance and background harmonics is investigated and the results show that the methods often described in standards for calculating impedances to establish harmonic contribution will not always be valid, especially when having inverters as harmonic sources.

A two-point measurement approach is followed for investigating the impact of traction load current emissions on the assessment of RPP current emissions based on international guidelines. A method is presented to approximate current emissions of the RPP without the impact of the traction load current emissions on the assessment. The results show that traction

loads do impact the harmonic assessment of RPPs and therefore the current assessment method will not always be accurate.

Abstrak

Eskom het onlangs begin ondersoek wat die effek is van elektriese treinlaste op hernubare energiebronne, weens die kragkwaliteitsprobleme wat verband hou met treinnetwerke. Swak kragkwaliteit wat deur middel van treinnetwerke gegenereer word, was nog altyd ‘n probleem. Die impak van die probleem het aansienlik toegeneem met die toename in die aantal hernubare kragaanlegte wat gekoppel word aan die nasionale netwerk. Studies toon ‘n toename in spanningswanbalans en harmoniek verspreiding op verskeie punte in die netwerk wat lei tot die verlies van kragproduksie in hernubare kragaanlegte. ‘n Onlangse kragkwaliteit assesseringsverslag in Eskom het aangedui dat kragkwaliteitsprobleme, veral harmoniese emissies, by hernubare energiebronne bestaan. Nie-lineêre bronne soos treinlaste dra by tot die harmoniese versteuring van spanning op die netwerk, asook harmoniese emissie van hernubare kragaanlegte.

Om insig te verkry rakende die probleem, bestaan daar ‘n behoefte om treinstelsels en hernubare kragaanlegte te modelleer. DIgSILENT PowerFactory, is gekies as die sagteware simulasiepakket om generiese modelle van spanning wisselrigters in hernubare kragaanlegte en spanning gelykrigters in treine te ontwerp en te bou om dinamiese tyddomein-simulasies te doen. Die simulasie resultate is vergelyk met gemete resultate om die akkuraatheid van die modelle te bevestig. Danksy goeie korrelasie tussen die simulasie resultate en gemete resultate kan die modelle gebruik word vir toekomstige netwerkbeplanning en kragkwaliteit assessering.

In hierdie studie word die kragkwaliteits probleme rakende elektriese treinlaste verder ondersoek, asook die assessering van die kragkwaliteit by die punt van konneksie van 'n plaaslike windplaas. Die assessering van die spanningswanbalans het aangedui dat elektriese treinlaste hoofsaaklik die grootste bydrae lewer tot spanningswanbalans op treinnetwerke en kan onder sekere omstandighede wisselrigter onderbrekings by hernubare kragaanlegte veroorsaak. Daar word opgemerk dat verskillende toestande soos die tipe trein, bedryfsomstandighede, beheer en drywingsaanvraag van die treinlas asook die driefase-foutvlak die spanningswanbalans wat deur treinlaste veroorsaak word, sal beïnvloed.

Die impak van elektriese treine op die netwerkspanningvervorming is ondersoek en daar is vasgestel dat die generasie van klein stroomharmonieke deur elektriese treinlaste groot spanningsvervorming kan veroorsaak in die teenwoordigheid van parallelle resonansies. Die impak van impedansie en agtergrond harmonieke is ondersoek en die resultate toon dat die metodes wat in standaarde beskryf word om die impedansies te bereken vir die vasstelling van die harmoniese bydrae, nie altyd geldig sal wees veral as wisselrigters as harmoniese bronne voorkom nie.

‘n Tweepunt metingsbenadering word gevolg om die impak van stroom harmonieke in elektriese treinlaste op die assessering van stroom harmonieke in hernubare kragaanlegte te ondersoek. ‘n Metode word aangebied om die stroom harmonieke van hernubare kragaanlegte te benader sonder die impak van elektriese treinlaste op die assessering. Die resultate toon dat die harmoniese stroom van elektriese treinlaste wel die assessering van stroom harmonieke in hernubare kragaanlegte beïnvloed en dat die huidige asseseringsmetode dus nie altyd akkuraat sal wees nie.

Contents

List of tables

List of figures

List of acronyms and abbreviations

AC	Alternating Current
APQC	Active Power Quality Compensator
CSI	Current Source Inverter
CT	Current Transformer
DC	Direct Current
DCUOSA	Distribution Connection and Use-of-System Agreement with Generators
DSL	Dynamic Simulation Language
EHV	Extra High Voltage
EMT	Electro-Magnetic Transient
HV	High Voltage
HVDC	High Voltage Direct Current
IGBT	Insulated-Gate Bipolar Transistor
LV	Low Voltage
MV	Medium Voltage
PI	Proportional Integral
PLL	Phase-Locked Loop
POC	Point of Connection
PQ	Power Quality
PV	Photovoltaic
PWM	Pulse Width Modulated
RMS	Root Means Square
RPC	Railway Power Static Conditioner
RPP	Renewable Power Plant
SAGCRPP	South Africa Grid Code for Renewable Power Plants
STATCOM	Static Synchronous Compensator
SVC	Static VAr Compensator
SVM	Space Vector Modulation
VRTC	Voltage Ride Through Conditions

VSC	Voltage Source Converter
VSI	Voltage Source Inverter
VT	Voltage Transformer

CHAPTER 1
INTRODUCTION

1.1. PROJECT BACKGROUND

The introduction of renewable power plants (RPPs) on traction/railway networks has introduced power quality (PQ) problems in South Africa. Therefore, it has recently become importance to investigate the effect of traction loads on renewable energy sources, particularly solar photovoltaic (PV) and wind. Traction loads are typically locomotives with multiple power units that are used to move a large load such as freight or passenger vehicles. Poor PQ generated by means of traction networks has always been of concern. The impact of this concern has greatly increased due to the increasing number of RPPs being connected to the national grid, as it presents a new dimension to traction/railway network PQ concerns. Recent reports from Eskom has shown an increase in voltage unbalance and harmonic distribution at various points of concern in the network which leads to the loss of power production from the RPPs [1]. A particular Eskom report claimed for unfavourable network conditions which in turn prevented maximum power production and exportation to the grid [2]. This may be due to an unbalanced supply caused by large single-phase loads within a traction network or a disconnection of inverters caused by harmonics generated in traction loads.

Traction loads are dynamic and depend on a number of parameters that need to be considered such as the mass, traction effort and speed of the train [3], [4]. Current network simulations being done in Eskom assumes a constant traction load and consequently require an updated traction load simulation model to provide a more accurate simulation analysis in time domain. The existing measurement framework as required by local standards e.g. NRS048-2 [5] does not make provision for the short-term dynamic PQ changes and needs to be investigated as short-term dynamic behaviour of traction loads will influence RPPs. It is important to ensure high quality of power at all times as this problem will only increase due to legislation and supply constraints to add as much renewable generation capacity as possible.

The aim of the project is to investigate the impact of traction networks on RPPs with the focus on wind power generation. Therefore, a detailed research study will be done on the PQ problems introduced by 25 kV alternating current (AC) traction networks. Various PQ problems such as voltage unbalance, harmonics, parallel resonance effect and low-frequency voltage fluctuations have drawn more attention in recent years due to their adverse effect on traction network devices and utility grids thus leading to a detailed study of these issues [6]. To investigate PQ in a power system it becomes important to understand the different non-linear loads and sources within a network.

Therefore, the time domain modelling of AC traction load simulation models will be studied utilizing DIgSILENT PowerFactory software and an embedded application of either Python or DIgSILENT programming language. Different wind farm inverter topologies will be studied using measurement data and the simulation of time domain DIgSILENT PowerFactory models. The network load and generation change dynamically due to the dynamic nature of traction loads and inverters. Therefore, inverters will trip on instantaneous ratings. An average frequency analysis approach is not sufficient in describing the PQ issues in a dynamic network. Consequently, a time domain approach is required to accurately describe PQ issues on a dynamic network. Two local wind farms will be used as case studies for the investigation. The South African grid code for renewable power plants (SAGCRPP) to which every RPP must adhere to obtain compliance as well as the IEC 61000-4-30 which determines how PQ is measured will be investigated to develop guidelines to minimize the impact of traction loads on renewable energy generation.

1.2. OVERVIEW OF THE TRACTION NETWORK IN SOUTH AFRICA

The network on which this research study is based is located in the Northern Cape Province and Eastern Cape Province of South Africa between Cradock and De Aar. Refer to Figure 1 for the network overhead geographical diagram as obtained from DIgSILENT PowerFactory.

The 132 kV line is mainly used as a traction line that contain RPPs in the form of a wind farm (Wind farm A) and a solar PV plant (Solar PV). The encircled dots show the traction substations along the 132 kV line. This makes this particular network a useful case study as the PQ impact of traction can be studied on both wind and solar PV generation. A recent quality of supply report at Wind farm A has indicated that PQ problems, particular harmonic emissions, exist at the RPP, therefore making this study relative to the present problem at the RPP. The quality of supply report also indicated a change in power flow direction when the RPP reached a certain power generation which could contribute to the PQ problems present. Therefore, it is clear that a number of issues are at play in this network. Refer to Figure 171 in Appendix for the detailed traction layout diagram of the above network.

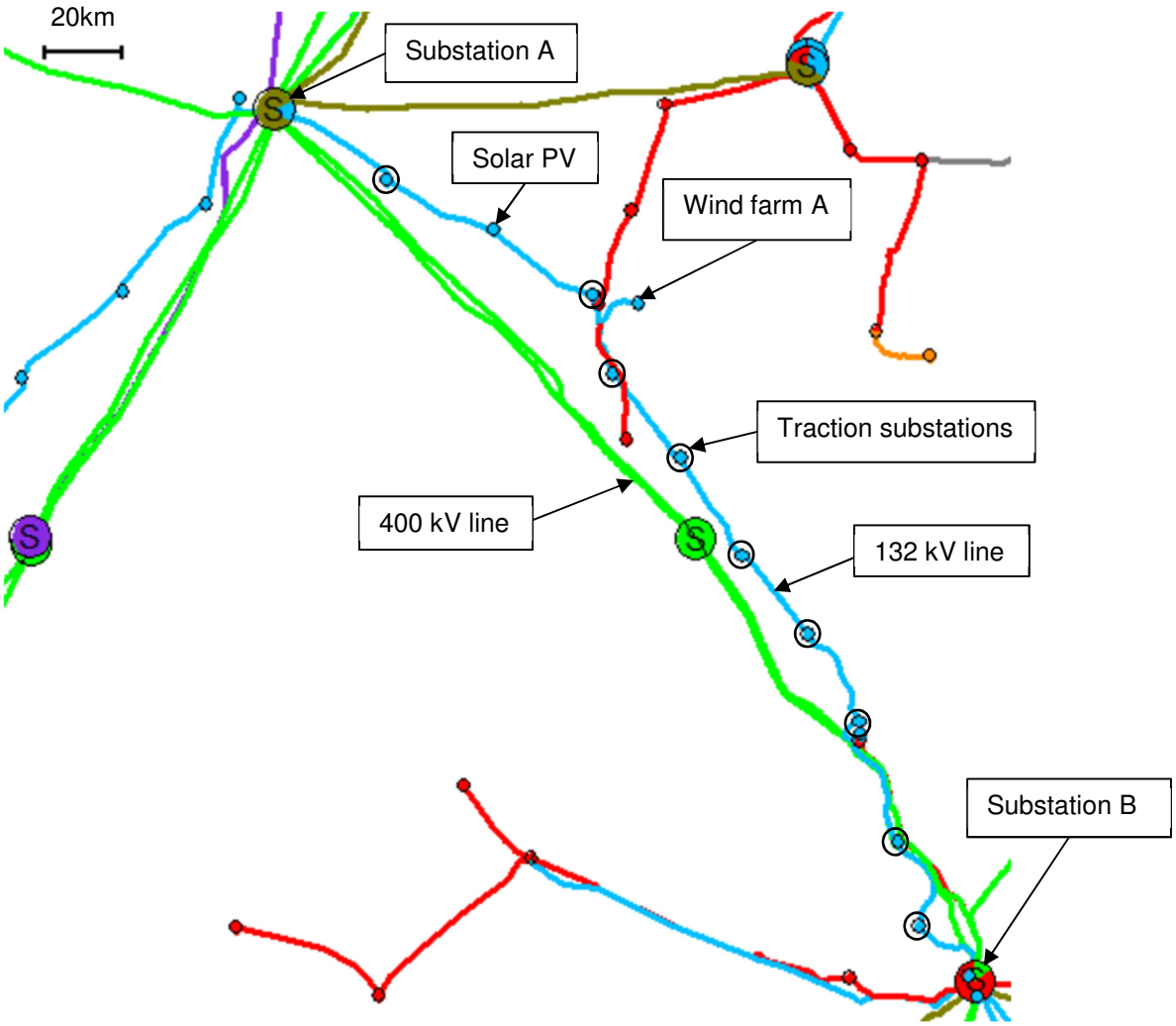

Figure 1: Network geographical diagram

1.3. OVERVIEW OF TRACTION SUBSTATIONS IN SOUTH AFRICA

The typical traction system in South Africa is supplied by a single-phase 25 kV (50 Hz) 15 MVA single-phase traction transformer that is connected to two phases of the 132 kV network. Individual traction transformers are connected across various phases to balance the power drawn on different phases of the three-phase 132 kV supply. The traction transformers are set up in such a way that adjacent transformers are connected to different phases. The adjacent substations are placed 25 km to 35 km apart along the 132 kV line. The pantograph of the locomotive ensures the connection between the locomotive and the 25 kV catenary. The return current path is through the body of the locomotive and the wheels to the rails, which are electrically grounded. Figure 2 shows the equivalent diagram of the conventional 25 kV AC traction substation.

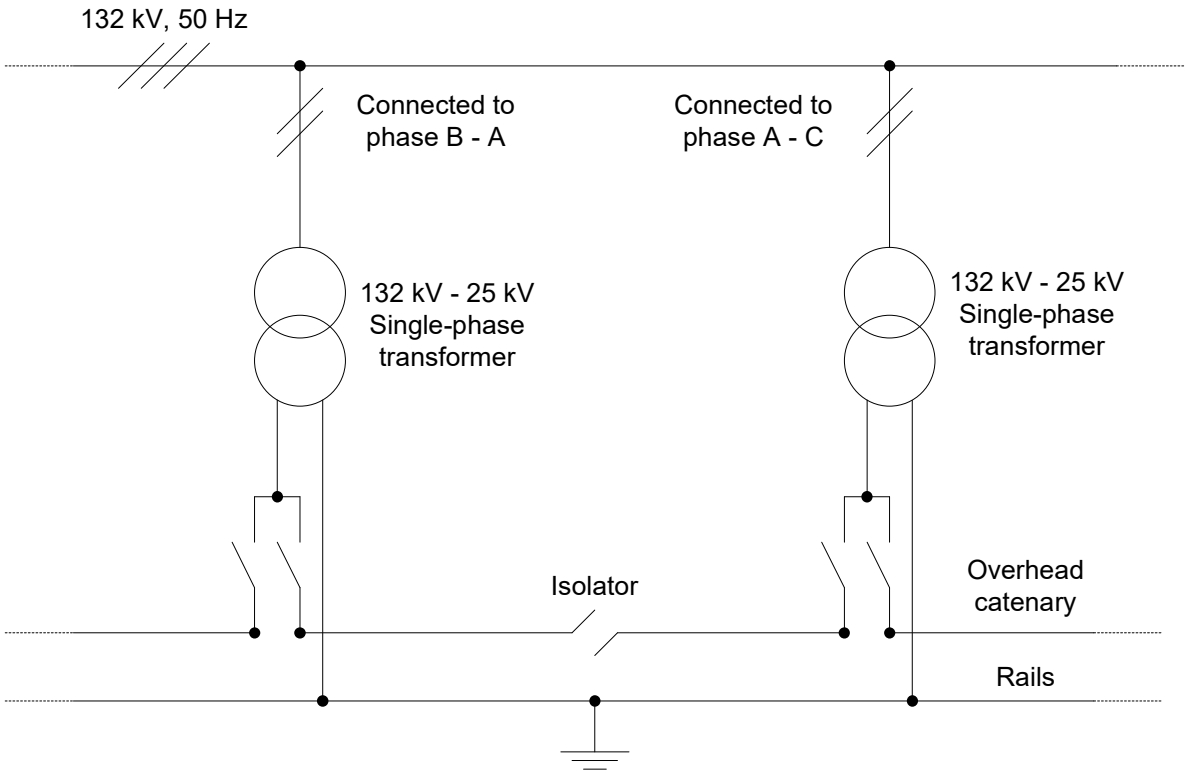

Figure 2: Conventional 25 kV AC traction substation diagram

Due to the change in phase pair between neighbouring substations the voltage of the overhead line is phase shifted by ±120º. Therefore, the overhead catenary has to be installed with neutral sections using isolators. Neutral sections are usually located halfway between adjacent traction substations and at traction substations. A neutral section consists of an isolator which ensures that an overhead line is only supplied from one end as shown in Figure 2. The locomotive is required to pass through the neutral section with the power off to prevent flashing arcs and damage to the overhead catenary. Figure 6 to Figure 8 shows the connection of two typical traction substations to the overhead catenary.

Figure 3: Traction substation with one transformer

Figure 3 shows a 132/25 kV AC traction substation that consists of one traction transformer. This is an example of a conventional traction substation. The single-phase output of the transformer is connected to the overhead catenary through the line conductors in Figure 3. Figure 4 shows that the line conductors are fed to both sides of the network, with the ground conductor being connected to the frame of the structure which is connected to the rails.

Figure 4: Connection between catenary and traction substation with one transformer

Figure 5 shows the equivalent diagram of a 25 kV AC traction substation that contains two traction transformers.

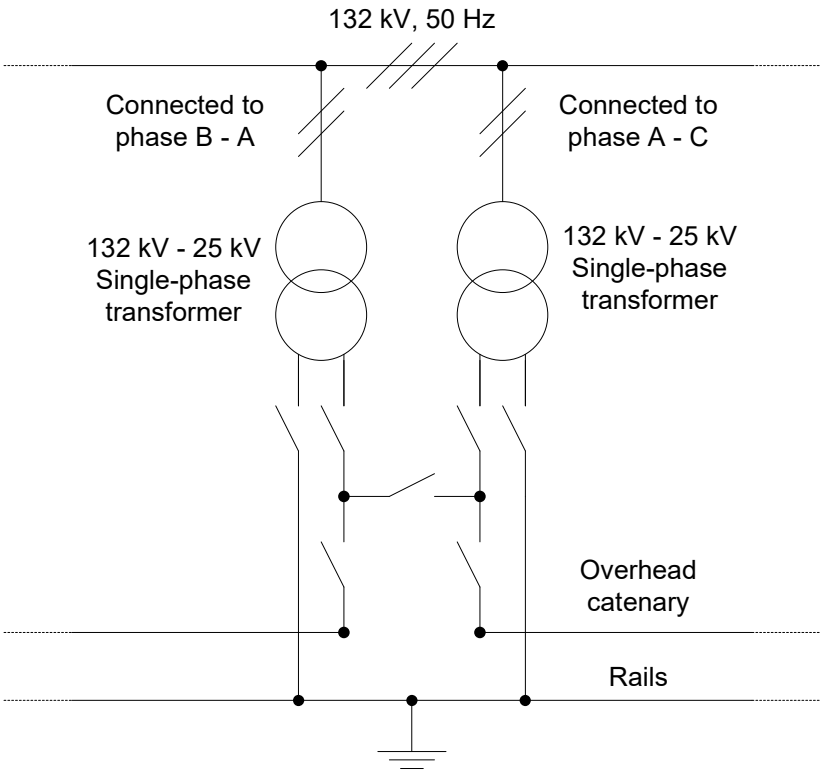

Figure 5: 25 kV AC traction substation diagram with two transformers

Figure 6: Traction substation with two transformers

Figure 6 shows a 25 kV AC traction substation that contains two traction transformers. In general one transformer is fed to both sides of the overhead catenary with the other being used as a backup transformer. The customer can also choose to use one transformer to feed the one side of the overhead catenary and the other transformer to feed the other side of the overhead catenary. In this example it shows that the switches for transformer 2 is open, therefore, only transformer 1 is in use and is fed to both sides of the overhead catenary. These traction transformers are connected to two different phases of the 132 kV network. The single-phase outputs of the transformers are connected to the overhead catenary through the line

conductors in Figure 6. Figure 7 shows that the line conductors are connected to the overhead catenary and the ground conductors of both transformers connected to the frame of the structure which is connected to the rails.

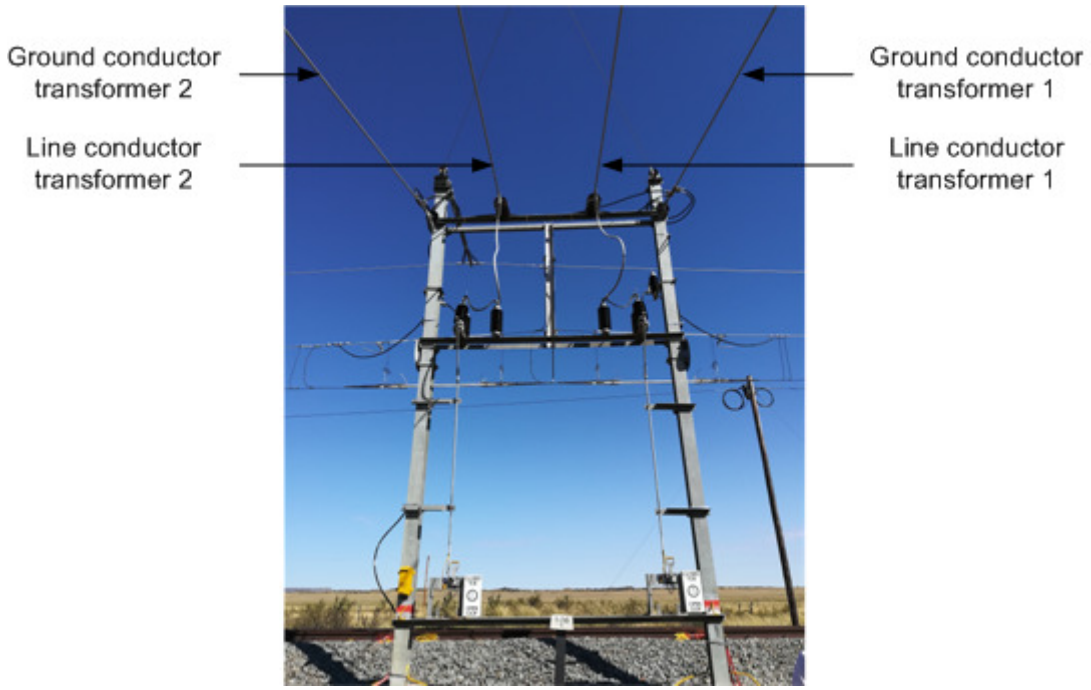

Figure 7: Connection between catenary and traction substation with two transformers

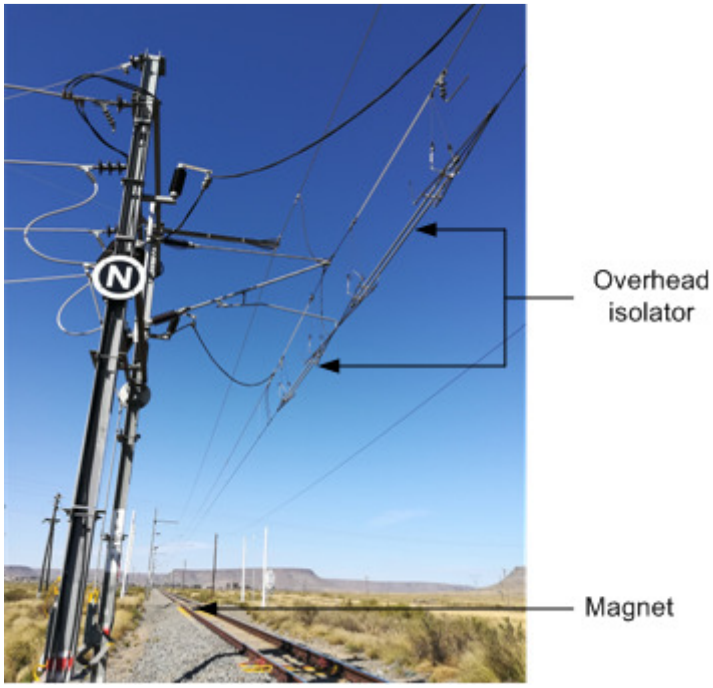

Figure 8: Neutral section

Figure 8 shows the overhead isolator that is used for the neutral section as well as the magnet that is used by the locomotive to cut the power supply to the traction drive.

1.4. OBJECTIVE

The main objective is to gain insight and describe the PQ impact of traction loads on RPPs which are connected to a traction network. This study further aims to develop time domain simulation models for various RPPs and different traction load types which can be used for network planning and future PQ studies.

1.5. RESEARCH QUESTIONS

The thesis can be divided into a main research question and a series of sub-questions. The main research question is: What impact does typical traction loads have on renewable energy sources due to PQ phenomenon?

The sub-questions are as follows:

- What PQ problems are introduced into the Eskom network because of traction loads?
- What PQ problems do RPPs contribute to the Eskom network?
- What effect does harmonics and voltage unbalance have on inverters?
- What mitigation methods exist that can be installed to reduce the PQ impact of traction loads?
- What are the current RPP standards, rules and regulations in South Africa to which every RPP must abide by to obtain compliance?
- What current international rules and regulations exist that determines how PQ is measured?
- How can a locomotive be modelled in the time domain?
- Can a significant voltage unbalance caused by traction loads lead to inverter trips?
- Does traction loads impact the harmonic assessment of RPPs?

1.6. THESIS STRUCTURE

The remainder of this thesis is structured according to the following outline:

- Chapter 2 start with an overview of the types and working principles of traction loads in South Africa. The dynamic behaviour of traction loads are mathematically described to gain insight into the characteristics of traction loads. The working principle of inverters in RPPs are illustrated and discussed in this chapter. The standards used for power quality management and assessment in South Africa are presented. Finally, the PQ issues related to traction loads and some possible mitigation methods to improve the PQ issues caused by traction loads are discussed.
- Chapter 3 gives an overview on the functions and limitations of DIgSILENT PowerFactory. Various built-in DIgSILENT PowerFactory models and elements are discussed. It further describes the design and implementation of generic rectifier and

inverter models in DIgSILENT Powerfactory for time domain simulations. A method is presented to first overcome the limitation of DIgSILENT PowerFactory in modelling single-phase rectifiers by controlling each phase separately. In addition, a method is investigated to overcome the limitation of DIgSILENT PowerFactory in modelling a half-controlled thyristor rectifier that requires the direct connection of a DC system to an AC system.

- In Chapter 4 the DIgSILENT PowerFactory models are first adjusted and updated to reflect the measured results as closely as possible. Then the reliability of each DIgSILENT PowerFactory model is investigated by comparing the simulation results to measurement results. The models in Chapter 4 can be used for future network planning and power quality studies.
- A voltage unbalance assessment at the point of connection is done in Chapter 5 to investigate the impact of traction loads on network voltage unbalance. Measured and simulated results are presented and compared to voltage trip limits of inverters to investigate the impact of voltage unbalance on RPPs.
- In Chapter 6 the impact of traction loads on the network voltage distortion is investigated. Furthermore, the impact of impedance and network background harmonics on harmonic emissions is investigated. Lastly, a two-point measurement approach is followed for investigating the impact of traction load current emissions on the assessment of RPP current emissions based on international guidelines. A method is presented to approximate current emissions of RPPs without the impact of the traction load current emissions on the assessment.
- Lastly, some conclusions and future work are provided in Chapter 7.

CHAPTER 2
LITERATURE REVIEW

2.1. INTRODUCTION

This chapter first presents background on the typical traction loads in South Africa and the different rectifier technologies utilised. Then the dynamic nature of traction loads will be described using mathematical equations to contextualise the need for time domain analysis. The working principles of inverters in grid-connected energy sources will be explored to gain a better understanding on the modelling of inverters in RPPs. Thereafter a review on the main PQ issues related to traction loads are described, followed by a discussion on the relevant mitigation methods to reduce the PQ impact of traction loads on the network. The chapter concludes with a review on the present PQ standards and management techniques in South Africa.

2.2. OVERVIEW OF TRACTION LOADS IN SOUTH AFRICA

Most electrical traction systems contain a range of different locomotive technologies with a wide variety of control methods. The grid side rectifier type used within the traction drive system determines the PQ effect of the locomotives on the network and vice versa. A traction system can consist of the following traction drive technologies [7]:

- A single-phase diode rectifier that feeds DC motors.
- A single-phase fully controlled thyristor rectifier that feeds DC motors.
- A single-phase half controlled rectifier that feeds DC motors.
- A single-phase diode rectifier that feeds a pulse width modulation (PWM) converter connected to an AC motor.
- A single-phase active rectifier that feeds a four-quadrant PWM converter connected to an AC motor via a DC link capacitor bank.

A train may also contain a combination of the above locomotive traction drive technologies.

Various locomotive types are in service in South Africa, consequently, care was taken to determine which locomotives are in service in the traction network that will be studied in this thesis. Two locomotives in particular which at the time of writing are in service on the traction network and make use of different traction drive technologies. These are the Transnet Freight Rail Class 7E and 20E electrical locomotives. The 20E electrical locomotive first entered serviced in March 2014, and operates on the line from Hotazel in the Northern Cape to Port Elizabeth in the Eastern Cape via Kimberley, De Aar and Noupoort [8]. It is manufactured and designed in China by Zhuzhou Electric Locomotive Company. The locomotive has a maximum

speed of 100 km/h, continuous speed of 40 km/h, continuous power rating of 3000 kW, starting effort of 320 kN, continuous effort of 270 kN and a brakeforce of 250 kN [8], [9].

The 7E electrical locomotive first entered serviced in 1978 and was the first AC locomotive used in South Africa [10]. The 7E is in service at various locations in South Africa including the line from Hotazel in the Northern Cape to Port Elizabeth in the Eastern Cape via Kimberley, De Aar and Noupoort. It is manufactured and designed by the so called 50 c/s group which include companies and groups of companies such as ACEC (Ateliers de Constructions Electriques de Charleroi), Siemens Mobility, Alstom and Brown Boveri [10]. The locomotive has a maximum speed of 100 km/h, continuous power rating of 3000 kW, starting effort of 450 kN, continuous effort of 300 kN and a brakeforce of 210 kN [10].

2.2.1. Single-phase active rectifier locomotives

The more recent locomotive models, such as the 20E locomotive, consist of single-phase active rectifiers. The electrical drive of a single-phase active rectifier locomotive consist of a traction transformer, single-phase active rectifier, DC link capacitor, three-phase PWM inverter and three-phase induction motors as shown in Figure 9. A PWM rectifier allow for bidirectional power flow which allows for regenerative braking.

The locomotive has dual voltage capability which allows the train to operate in either AC or DC mode, depending on the overhead catenary supply feeding the pantograph of the locomotive. The electrical drive system is designed to operate with a nominal voltage of 25 kV 50 Hz in AC mode and between 2 kV (minimum) and 4 kV (maximum) with a nominal voltage of 3 kV in DC mode. Furthermore, the locomotive is equipped with rheostatic and regenerative braking capabilities. The electricity generated by regenerative braking can be fed back into the supply system. Note that regenerative braking is only permitted when the catenary voltage is within specified limits.

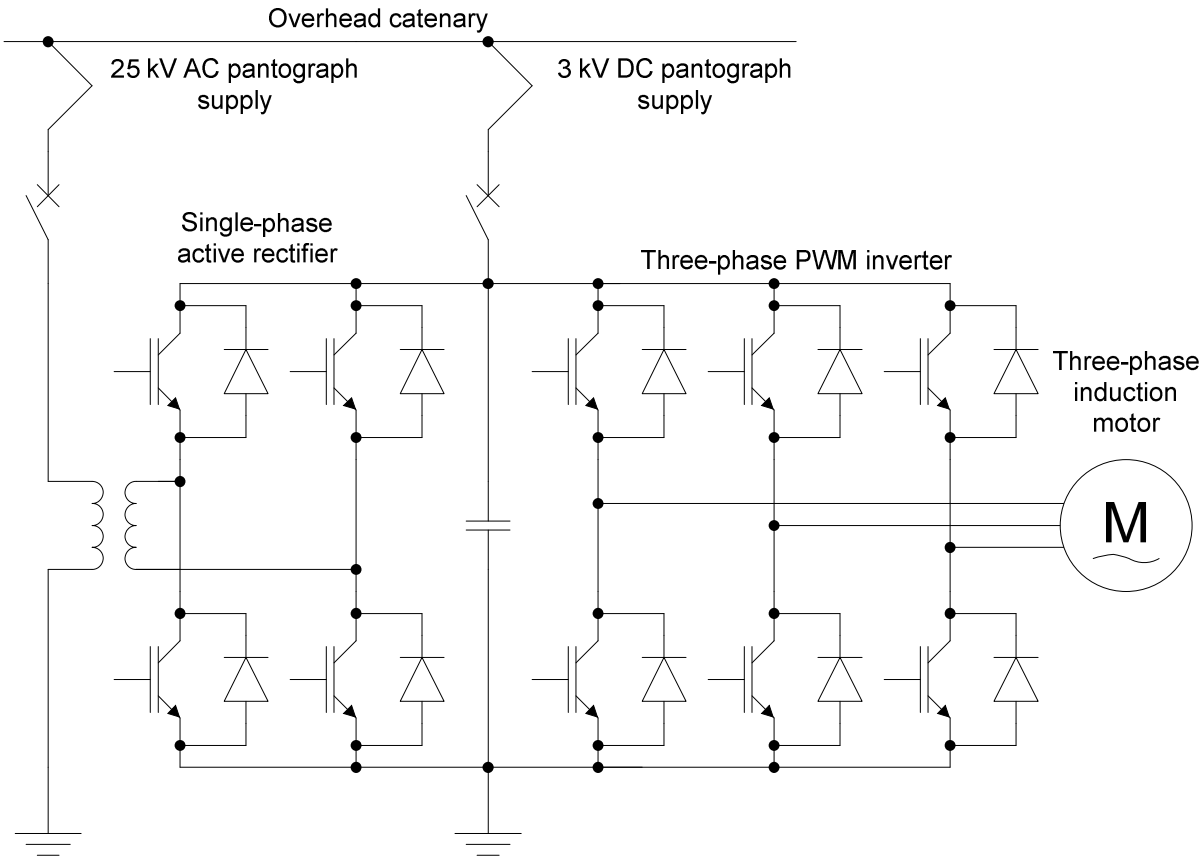

Figure 9: Traction drive system

The traction drive equipment ratings and specifications for this particular locomotive was not available at the time of writing and was therefore chosen from the equipment ratings of known manufacturers such as Siemans, ABB and Toshiba. The on-board traction transformer is used to step down the 25 kV AC catenary supply to the 1000 V range for the single-phase converter. The general rated power of a 25 kV traction transformer was found to be in the 2 MVA to 6 MVA range. A single-phase four quadrant converter is supplied from the output of the traction transformer. Each leg of the converter consists of silicon based insulated gate bipolar transistors (IGBTs) and power diodes. During normal operating conditions the controller will operate as a rectifier that converts the traction transformer secondary AC voltage to a controlled 3 kV DC voltage that will form the DC link of the drive system. To control the harmonics or voltage ripple contained in the traction drive, a capacitor is placed in the DC link. During regenerative braking the DC link voltage is inverted to single-phase AC voltage and fed back into the grid. The DC link voltage is converted to three-phase AC voltage through a three-phase four quadrant traction converter. The output voltage of the three-phase converter can be varied in magnitude as well as frequency. During normal operating conditions the three-phase converter operates as a variable voltage variable frequency controlled PWM inverter. The switching frequency of the system will be chosen from the analysis of the measured current waveform's harmonic spectrum at a traction substation which will be shown in a latter section of this thesis. The output of the PWM inverter is applied to a squirrel cage three-phase

induction motor. The class 20E locomotive consists of four induction motors each with a 750 kW power rating. During regenerative braking the three-phase induction motors operate as three-phase asynchronous induction generators converting kinetic energy to electrical energy, which can be fed back into the grid through the converters. The control of a single-phase active rectifier locomotive will be discussed in Section 3.4 along with its implementation in DIgSILENT PowerFactory in Section 3.5.1. The simulated voltage and current waveforms and respective harmonic spectrums will be discussed and compared to measured voltage and current waveforms and respective harmonic spectrums in CHAPTER 6.

2.2.2. Single-phase half-controlled rectifier locomotives

The older locomotive models, such as the 7E locomotive, consist of single-phase diode or thyristor rectifiers. A conventional thyristor traction system is shown in Figure 10.

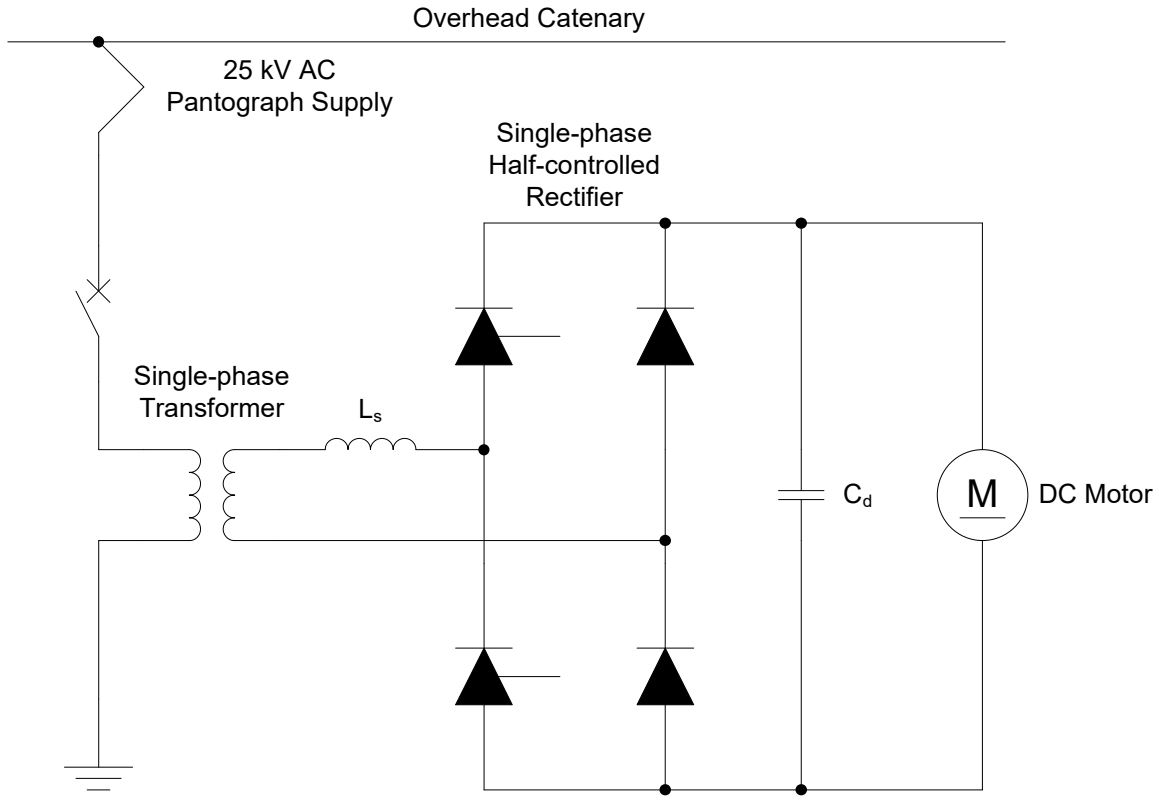

Figure 10: Conventional half-controlled thyristor traction system

A conventional thyristor traction system consists of an on-board tap-changing transformer, smoothing filter, single-phase half-controlled rectifier and DC motors. The single-phase half controlled rectifier is an adaptation of a single-phase fully-controlled rectifier. A single-phase fully controlled rectifier is a two-quadrant converter that consists of four thyristors with rectifier and inverter mode of operation and thus unidirectional current operation. Some applications, however, such as old locomotives do not utilise regenerative braking, therefore, do not require two-quadrant operation. In such applications the control and gate circuit of four thyristors are

unnecessary. Two of the thyristors can be replaced by diodes for one-quadrant operation. The input voltage of a conventional traction thyristor rectifier is 850 V. The DC motor's nominal voltage is 750 V. The control and implementation of a single-phase half-controlled rectifier locomotive in DIgSILENT PowerFactory will be discussed in Section 3.5.2. The simulated voltage and current waveforms and respective harmonic spectrums will be discussed and compared to measured voltage and current waveforms and respective harmonic spectrums in CHAPTER 6.

2.3. DYNAMIC NATURE OF TRACTION LOADS

The electrical characteristics related to traction loads are different to other loads connected to power systems. Traction loads introduce dynamic effects to the power system. Locomotives are continuously moving along a catenary line under different operating conditions. These dynamic effects become more complex due to the fact that the location infrastructure (moving resistance, slope etc.) change as the locomotive moves from station to station creating the following problems:

- The dynamic effects produce a time varying power consumption that is determined by a number of variables such as the locomotive tractive efforts, position, mass etc.
- The harmonic emissions are time varying and depend on the operating conditions of the locomotive. A traction load can therefore not be represented by a single set of harmonic current emissions.
- The system topology changes as the locomotive moves past a neutral section.
- Aggregated PQ issues from a number of running locomotives where each locomotive produce harmonic current emissions into the system that propagate through the network.

Various papers have already investigated the power demand of locomotives as well as the harmonics generated by electric locomotives using simulation software such as MATLAB/Simulink, PSCAD/EMTDC, DIgSILENT PowerFactory, etc. [4], [11]–[15]. These articles accurately simulate the power consumption of locomotives but fall short in accurate harmonic evaluation due to the dynamic effects and behaviour of locomotive harmonics. A harmonic current source model has been proposed in [12], to accurately model the harmonics produced by locomotives as described in [16]–[18]. The problem with a constant/static current source model is that it lacks the ability to accurately evaluate the harmonic impact of locomotives that are dynamic due to constant changes in operating conditions, position and various other external effects. The continuous movement of locomotives on the network results in dynamic changes in the network impedance and can lead to possible resonance issues. A the need exists to provide a method for analysing the PQ impact of traction systems while considering rail infrastructure, train movement and train operating conditions. This thesis will

present a method to analyse the dynamic network unbalance and harmonic behaviour of a traction system in DIgSILENT PowerFactory while considering all operating condition of a locomotive that moves past a RPP. Wind farm A and surrounding utility network has been used as a case study to evaluate the dynamic PQ impact of traction on RPPs.

2.3.1. Mathematical model

One possible method that was investigated was to use measured field data of the power consumption and electrical current of the locomotive. This method would provide the most accurate traction model for power consumption and harmonic studies. The field data was, however, unavailable at the time of investigation and thus this method was not pursued further. Another method had to be investigated that would provide an accurate traction model even without any field data. A more idealised and mathematical model was investigated, by using general equations of motion. Similar mathematical models using equations of motion have been presented in various papers [4], [14], [15], [19]–[22]. The train movement from station to station can be divided into five operating conditions: constant starting acceleration, stable velocity, constant velocity, coasting and constant stop deceleration. Figure 11 shows the typical velocity curve throughout the five operating conditions of a locomotive [14].

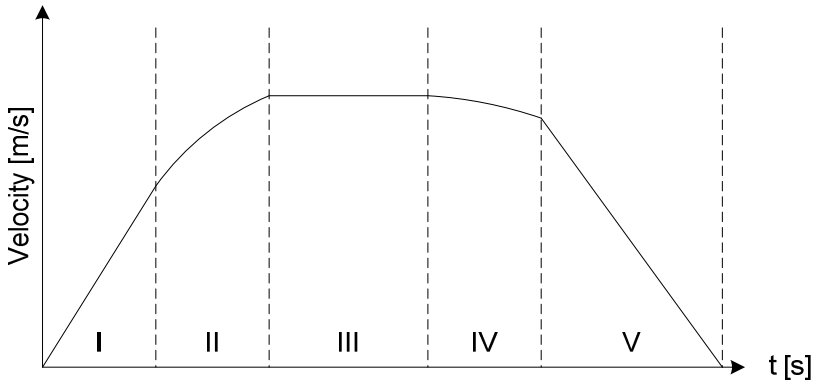

Figure 11: Velocity curve of a locomotive

The locomotive's velocity increases with a constant acceleration in the first operating stage. When reaching a moderate velocity the acceleration starts to decrease while still increasing the velocity as illustrated in the second stage. In stage three the locomotive's velocity increases until reaching the maximum velocity where the velocity is then kept constant and the acceleration is decreased to zero. When a locomotives passes through a neutral section, the locomotive's power is cut off and the velocity decreases due to the movement resistance, as illustrated in stage four. When the locomotive has passed through the neutral section the power is immediately recovered and the locomotive continues in the third stage. The locomotive continues to move with constant velocity until it is required to decelerate with a constant value until reaching a complete stop, this is the fifth operating condition. It is important to note that the curve in Figure 11 is drawn under ideal conditions. Practical conditions such as the slope,

moving resistance, wind resistance and position of the train will influence the velocity and in turn the power consumption and current graphs of the locomotive.

The traction effort and power consumption curves throughout all operating conditions are shown in Figure 12 and Figure 13 respectively.

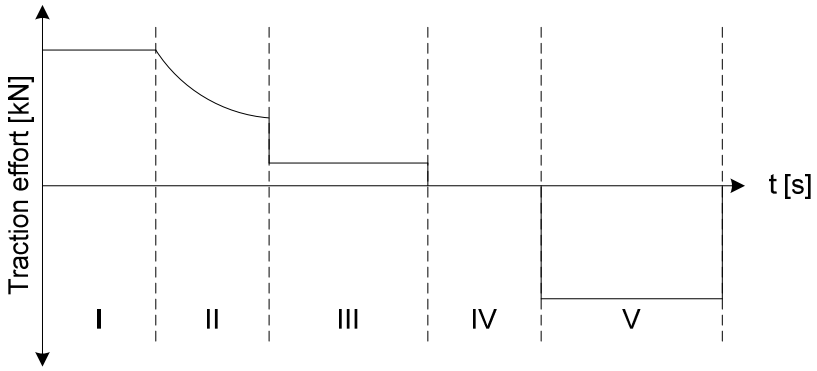

Figure 12: Traction effort curve of a locomotive

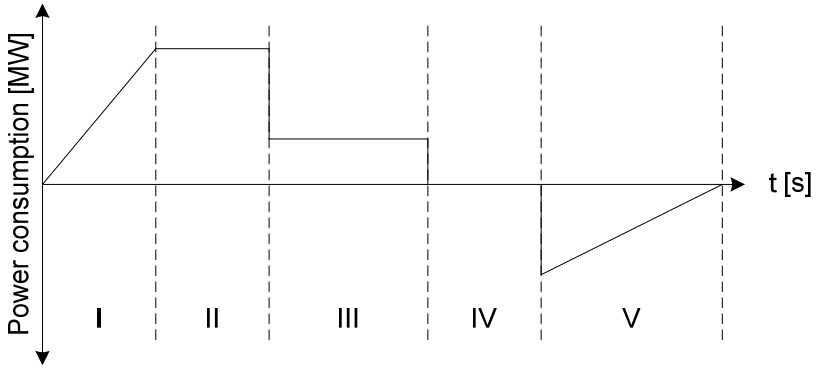

Figure 13: Power consumption curve of a locomotive

In region I the power will increase constantly up to the maximum power. In region II the motor will run at maximum power until the maximum velocity is reached. It is highly unlikely that the traction equipment is capable of running continuously at maximum power for a long period of time. For this thesis the worst case scenario is assumed, therefore, the maximum power is maintained until the maximum velocity is reached.

From Newton's first law the force (F) needed to move a locomotive with a certain mass (M) is given by:

$$F = Ma = M\frac{dv}{dt} \tag{2.1}$$

with a the acceleration and v the velocity of the locomotive.

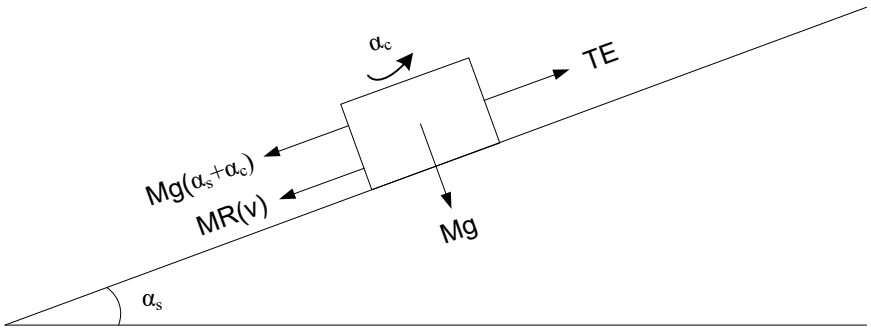

Figure 14: Forces on a locomotive

Expanding (2.1) to include the traction effort of the locomotive and take external factors such as the moving resistance and railroad slope into account gives [14], [22]:

$$F = (1+r)M\frac{dv}{dt} = TE - M\left(A + Bv + Cv^2\right) - Mg\left(\alpha_s + \alpha_c\right) \tag{2.2}$$

with A, B and C the movement resistance coefficients, TE the traction effort, g the acceleration of gravity, α_s the railroad slope and α_c the curvature converted an equivalent railroad slope value. Even though this mathematical model provide an accurate approach it requires detailed information regarding the aerodynamic properties of the locomotives which were unavailable at the time of writing and is thus considered unnecessary for this case study. The curvature of the slope, α_c, can be assumed to be very small since the railroad is mostly straight and can thus be removed from (2.2). Therefore, (2.2) can be further simplified to [4], [45], [46]:

$$F = TE(v) - MR(v) - Mg\left(\alpha_s\right) - BE(v) \tag{2.3}$$

with $TE(v)$ the traction effort of the locomotive that produces the required force to overcome inertia and move the locomotive, $MR(v)$ the movement resistance that work in the opposite direction of the traction effort and $BE(v)$ the braking effort of the locomotive that produces the required force to decelerate the locomotive until reaching a complete stop. Note that the railway track slope could be obtained from Google maps and thus was not removed from (2.3). The movement resistance calculation can now be expressed as follows:

$$MR(v) = \left(2.5 + \left(k\left(v + \Delta v_{wind}\right)^2 \times 10^{-3}\right)\right) \times M \times g \times 10^{-3} \tag{2.4}$$

with k a constant, generally assumed as 0.33 for passenger vehicles, and Δv_{wind} the variation in the wind velocity. The power demand of the induction motors is obtained from (2.5).

$$P_{motor}(t) = \left(F(t) + MR(v) + Mg\left(\alpha_s\right)\right) \times v \tag{2.5}$$

Finally, (2.5) can be simplified to (2.6) for the first three operating conditions, considering that $BE(v)$ is equal to zero. Likewise, (2.5) can be simplified to (2.7) for the braking condition, considering that $TE(v)$ is equal to zero.

$$P_{motor}(t) = TE(t) \times v \tag{2.6}$$

$$P_{motor}(t) = BE(t) \times v \tag{2.7}$$

The active power at the input of the traction system can thus be calculated using (2.8) for the first three operating conditions and (2.9) for the braking condition.

$$P_{input}(t) = \frac{P_{motor}(t)}{\eta_{gear} \times \eta_{motor} \times \eta_{vvvf} \times \eta_{rectifier} \times \eta_{transformer}} \tag{2.8}$$

$$P_{input}(t) = P_{motor}(t) \times \eta_{gear} \times \eta_{motor} \times \eta_{vvvf} \times \eta_{rectifier} \times \eta_{transformer} \times \eta_{braking} \tag{2.9}$$

where $\eta_{gear}, \eta_{motor}, \eta_{vvvf}, \eta_{rectifier}, \eta_{transformer}$ and $\eta_{braking}$ are the operating efficiencies of the gears, motors, inverter, active rectifier, transformer and regenerative braking efficiency respectively [20]. This mathematical model can be further defined by adding the auxiliary power demand of the locomotive but was considered unnecessary for this study due to the auxiliary power demand being a lot smaller than that of the induction motors.

The movement of a locomotive can be described with a displacement function. To obtain the displacement function the idealised velocity curve and operating conditions of the locomotive in Figure 11 is further simplified as shown in Figure 15.

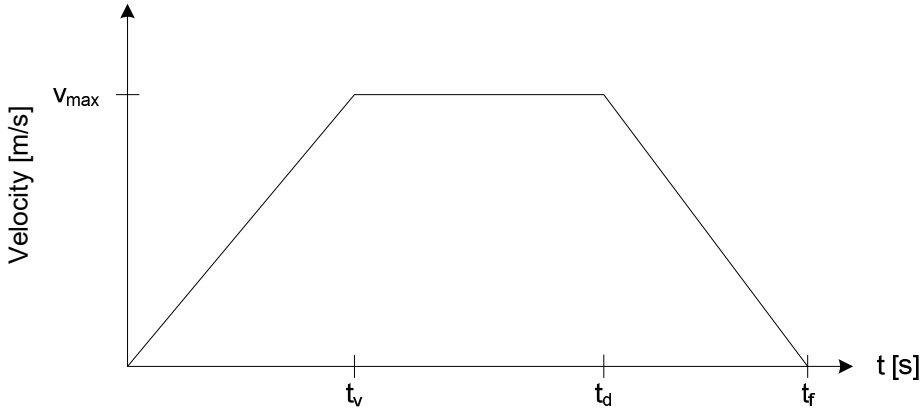

Figure 15: Simplified velocity curve of a locomotive

From Figure 15 the constant acceleration and deceleration curve can be drawn as shown in Figure 16.

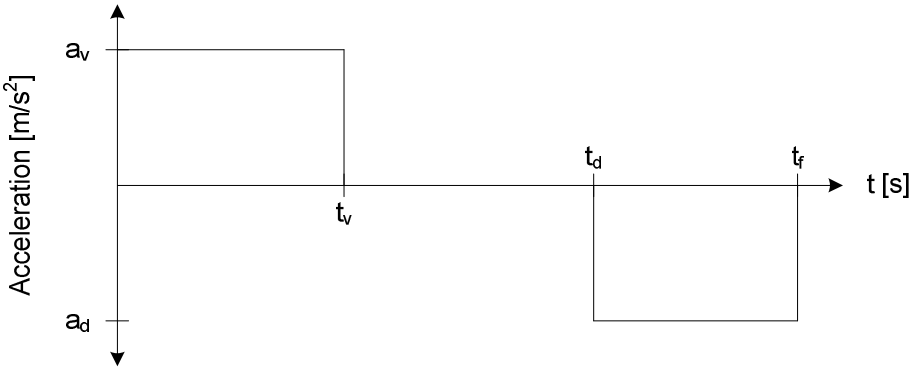

Figure 16: Acceleration and deceleration curve of a locomotive

By substituting the variables in Figure 15 and Figure 16 into the standards equation of motion

$$x(t) = x_0 + v_0 t + \frac{1}{2} a t^2 \tag{2.10}$$

the displacement function x(t) can be defined as

$$x(t) = \begin{cases} \frac{1}{2} a_v t^2 & \forall 0 \le t \le t_v \\ \frac{1}{2} a_v t_v^{\,2} + v_{max}(t - t_v) & \forall t_v \le t \le t_d \\ \frac{1}{2} a_v t_v^{\,2} + v_{max}(t - t_v) + \frac{1}{2} a_d (t - t_d)^2 & \forall t_d \le t \le t_f \end{cases} \tag{2.11}$$

where

$$t_v = \frac{v_{\max}}{a_v},\ t_d = t_f - t_s \text{ and } t_s = -\frac{v_{\max}}{a_d} \tag{2.12}$$

If a_v is at all times assumed to be positive and a_d negative. The train position can be graphically represented against time by plotting (2.11) as shown in Figure 17.

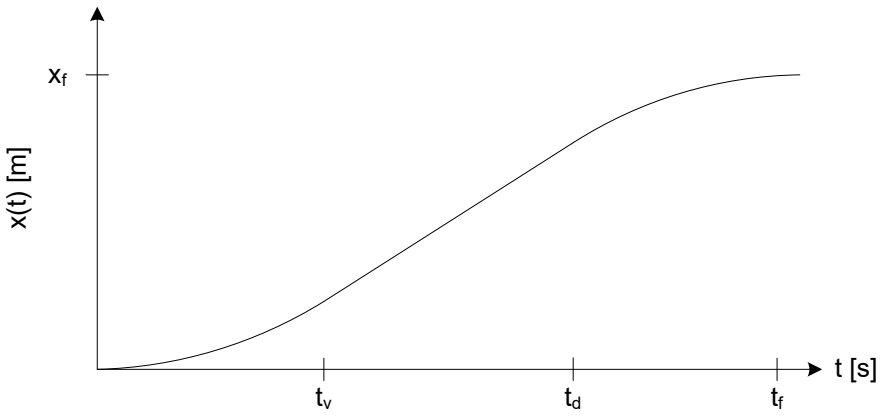

Figure 17: Locomotive displacement curve

2.4. INVERTERS IN RENEWABLE ENERGY SYSTEMS

It is important that the modelling of power electronic converters in grid-connected wind and solar PV generation systems be studied due to the limited knowledge on customer models. In this section an overview literature study of power electronic converters is shown.

2.4.1. Overview on inverter topologies

In this thesis the DC-AC converter will be analysed as this type of converter is known as an inverter which produces a sinusoidal AC output where the magnitude and frequency can be controlled from a DC voltage input to connect solar PV and wind generation systems to the AC grid and to supply AC loads.

There are two different inverter topologies that can be used to provide DC-AC conversion: current source inverters (CSI) which are line/grid-commutated or voltage source inverters (VSI) which are self-commutated. The commutation is based on the switch type. The former consists of diodes and thyristors (SCR), while the latter consists of transistors or self-commutated thyristors which include the IGBT, gate turn-off thyristors and integrated gate-commutated thyristors. A VSI contains a constant DC voltage source on the input while a CSI contains a constant DC current source on the input as seen in Figure 18. The latter will not be discussed in the thesis due to their limited applications in high power AC motor drives. In addition, VSIs provide better steady-state and transient responses as well as lower generation of input power harmonics compared to CSIs as shown in [23] and is used in all grid-connected inverters and is thus implemented in this thesis. Grid-connected inverters operate in parallel with the grid. Therefore, a VSI controls the current on the AC terminals and act as a current source on the terminals. Consequently, a VSI must be connected to the grid through a series inductor to avoid the direct connection of two voltage sources as seen in Figure 18(a). The voltage is thus predominately governed by the grid.

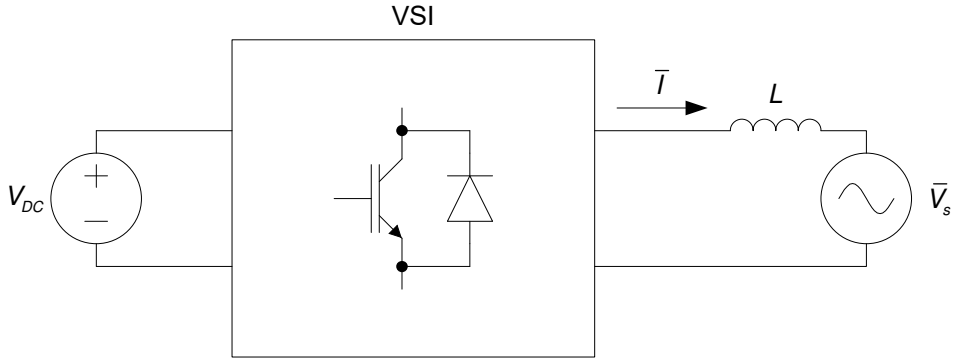

(a)

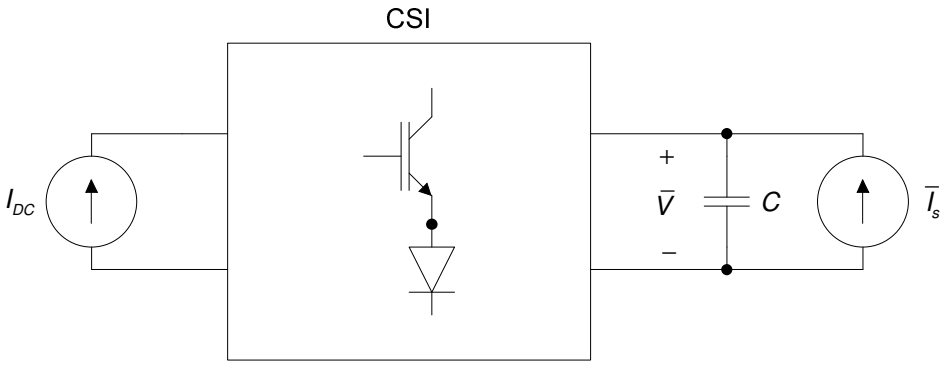

(b)

Figure 18: Type of inverters: (a) VSI (b) CSI

A VSIs can be further divided into square wave inverters and PWM inverters. Square wave inverters are fed with a controlled DC input voltage so as to control the AC output voltage magnitude. Therefore, only the frequency of AC output voltage needs to be controlled by the inverter.

PWM inverters are fed with a constant DC input voltage through a diode rectifier. The PWM inverter control is responsible for obtaining a controlled AC output voltage with regards to magnitude and frequency. This is achieved by controlling the on and off inverter switch periods. Various PWM inverter modulation schemes exist which can be implemented to obtain the desired sinusoidal AC output voltages such as sinusoidal based PWM and space vector based PWM.

The equivalent circuit of a three-phase VSI is shown in Figure 19. A large DC link capacitor is necessary on the input side of the inverter to maintain a steady DC voltage during switching operation of the inverter. Most practical voltage supplies consist of significant series impedance which can cause large voltage spikes at the input DC bus resulting in a decrease in the quality of the output voltage. Furthermore, most inverter applications consist of a high frequency DC current ripple due to the high frequency switching in the inverter. To bypass this DC current ripple, a DC link capacitor is used [24].

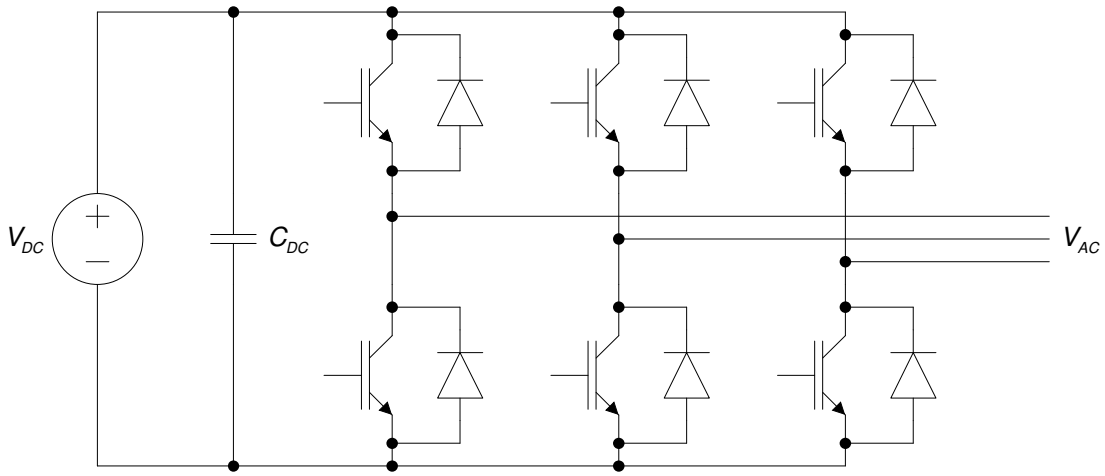

Figure 19: Three-phase VSI equivalent circuit

2.4.2. Overview on sinusoidal based PWM scheme

The basic principle of the PWM inverter to obtain a sinusoidal AC output voltage waveform at a desired frequency (50 Hz in South Africa) is to compare a low frequency sinusoidal control signal $f(t)$ to a high frequency triangular or sawtooth carrier signal $c(t)$, as shown in Figure 20 for a single-phase leg of an inverter.

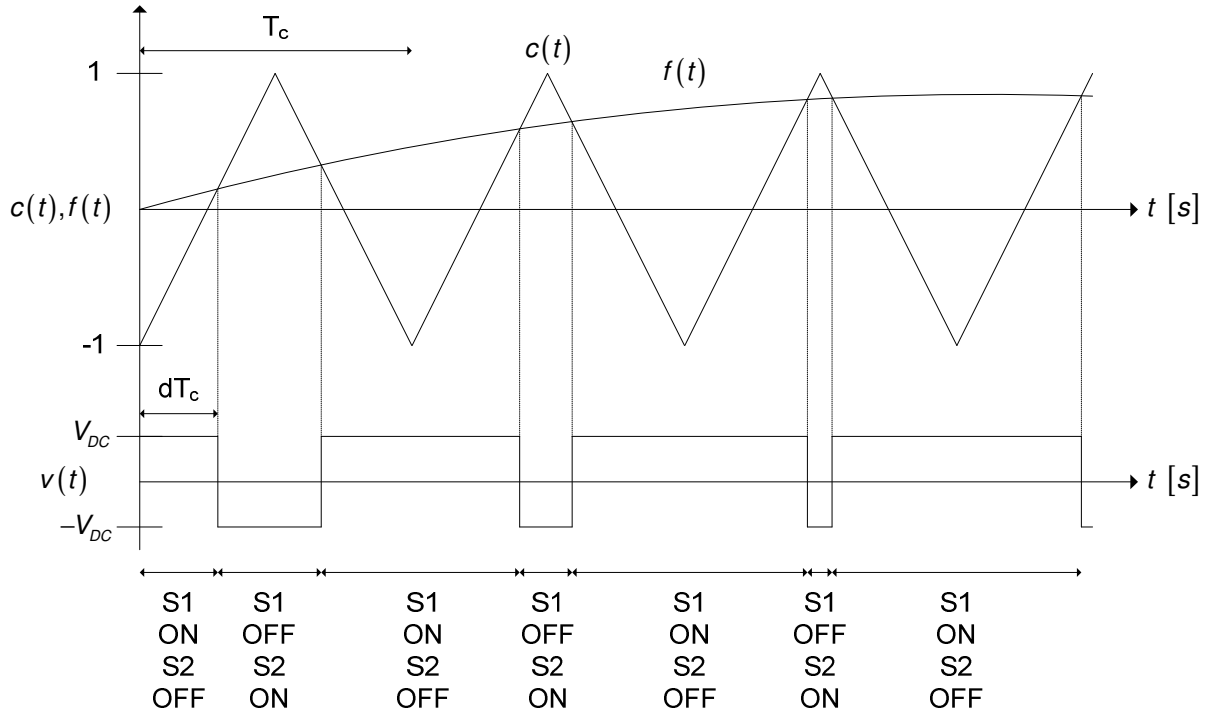

Figure 20: Pulse width modulation

The phase leg of the inverter is switched to the positive DC value when the reference signal is greater than the carrier signal and to the negative DC value when the carrier signal is greater than the reference signal. The modulation frequency also called the switching frequency is chosen from the frequency of the triangular waveform. This frequency determines the rate in

which the inverter switches. The cycle of the switches is determined by the frequency of the control signal which is equal to the high voltage AC frequency of the network. The amplitude of the modulation index, P_m, is defined as:

$$P_m = \frac{\hat{f}(t)}{\hat{c}(t)} \tag{2.13}$$

where $\hat{f}(t)$ is the peak value of the sinusoidal control signal and $\hat{c}(t)$ the peak value of the triangular carrier signal. The amplitude of the fundamental frequency output voltage component varies linearly with P_m when P_m is in the linear region ($0 \leq P_m \leq 1$). An advantage of working in the linear region is that the harmonics of the inverter are shifted to sidebands of the switching frequency. The only drawback of working in the linear region is that the amplitude of the fundamental frequency output voltage component is limited. The maximum RMS inverter line to line output voltage V_{AC} that can be obtained with a constant DC voltage V_{DC}, is $\frac{\sqrt{3}}{2\sqrt{2}} V_{DC}$ within the linear operating region. By increasing P_m above 1, into the overmodulation region, the amplitude of the fundamental frequency output voltage component can be increased but also with an increase in low-order harmonics which is undesirable. Only low levels of overmodulation are normally allowed. Furthermore, in overmodulation the amplitude of the fundamental frequency output voltage component no longer varies linearly with m_a [18]. The frequency modulation, m_f, is defined as:

$$m_f = \frac{f_s}{f_1} \tag{2.14}$$

where f_s is the switching frequency and f_1 the desired output frequency. The selection of m_f depends largely on two factors, the switching losses and filtering of harmonics. The switching losses increases proportionally with an increase in switching frequency. In turn, at higher switching frequencies it is easier to filter out harmonics. Higher switching frequencies are therefore desirable to achieve a desirable level of PQ. The switching frequency is generally selected to be either below 6 kHz or above 20 kHz to avoid the audible range [18].

2.4.3. Output filters for grid-connected inverters

Most grid-connected inverters are connected to an output filter to reduce its output harmonics. The most commonly used filters in grid-connected systems are L, LC or LCL filters which are constructed from a combination of inductors (L) or capacitors (C).

2.4.4. Sampling

A PWM inverter can be controlled by using a variety of different sampling techniques which are briefly discussed below.

2.4.4.1. Naturally sampled PWM

The naturally sampled PWM implementation is also known as the analog PWM implementation. For naturally sampled PWM an analog comparator is required where a sinusoidal reference signal is compared to a high frequency triangular or sawtooth carrier signal [25] as explained in Section 2.4.2. A mathematical or analytical approach to the brief discussion above can be found in [18], [26], [27]. The approach shows that harmonics for PWM inverters operating in the linear region only exist at sidebands centred around the switching frequency and integer multiples of the switching frequency. In addition, the approach shows that using a triangular carrier signal has an advantage over a sawtooth carrier signal. With the triangular carrier signal, the odd harmonics around odd multiples of the switching frequency as well as even harmonics around even multiples of the switching frequency are removed. A major disadvantage of naturally sampled PWM is the difficulty with digital implementation, therefore, regularly sampled PWM is commonly used in digital modulation.

2.4.4.2. Regularly sampled PWM

In the implementation of regularly sampled PWM a low frequency current reference signal is sampled and held constant during a carrier period [25]. In regularly sampled PWM a sampled reference signal, instead of a sinusoidal reference signal, is compared to the high frequency triangular or sawtooth carrier signal. For a triangular reference signal, regularly sampled PWM can further be divided into symmetrical or asymmetrical regularly sampled PWM. With symmetrical regularly sampled PWM the reference signal is sampled at either the positive peak or negative peak of the triangular carrier signal and held constant during the carrier period. With asymmetrical regularly sampled PWM the reference signal is sampled and held constant every half period, or in other words at the positive and negative peak of the triangular carrier signal and held constant during the half carrier period. Note that for a sawtooth carrier signal the reference signal is only sampled at the end of the ramping period and held constant for the entire carrier period. A mathematical or analytical approach to the brief discussion above can be found in [26], [27]. The approach shows the presence of low-order harmonics as multiples of the fundamental harmonic which is a consequence of the regularly sampled PWM implementation. In addition, it is shown that the low-order harmonics are reduced with the implementation of regularly sampled PWM using a triangular carrier signal compared to a sawtooth carrier signal. Lastly, it is shown that asymmetrical sampled PWM provides a better low-order harmonic performance than that of symmetrical sampled PWM as the even low-order harmonics are completely eliminated.

2.4.4.3. Direct modulation

Direct modulation is proposed as an alternative method to regularly sampled PWM but will not be discussed in this thesis as it is not a practical sampling method for implementation on grid-connected inverters [27].

2.4.5. Third harmonic injection

Third harmonic injection is widely used in VSIs to overcome the maximum output voltage limitation in three-phase inverter modulation [28]–[30]. By implementing third harmonic injection one can increase P_m to 1.155 without overmodulation and so increase the output voltage and rating of the inverter. The method will inject triplen harmonics into the output phase voltages of the inverter. The line-to-line inverter voltages remain undistorted with naturally sampled PWM since the triplen harmonics are cancelled between the phase voltages.

Third harmonic injection can also be implemented in naturally sampled and regularly sampled PWM inverters. A mathematical and analytical approach to third harmonic injection for different sampling schemes has been done in [27] to determine the magnitude of the harmonic components and to compare the harmonic spectrum of the different PWM sampling implementations. The approach shows that P_m can successfully be increased to 1.155 by injecting a one-six third-harmonic component into the phase voltages. In addition, the approach shows that third harmonic injection increases the low-order harmonics produced by regularly sampled PWM. Non-triplen voltage harmonics do not cancel and thus increase in the inverter line to line output voltage. With asymmetrical regularly sampled PWM the 5th, 7th, 11th and 13th harmonic components look to be the dominant harmonics that are amplified in the inverter line-to-line output voltages. With symmetrical regularly sampled PWM the 4th, 5th, 7th, 8th, 10th, 11th and 13th harmonic components look to be the dominant harmonics that are amplified in the inverter's line-to-line output voltages.

2.4.6. Overview on space vector based PWM scheme

Space vector modulation (SVM) is widely implemented in grid-connected inverter systems and provide improved performance over naturally and regularly sampled PWM inverters [27]. The concept of SVM in PWM inverters are widely discussed in literature [25], [27], [31]–[33] and will therefore only briefly be discussed in this thesis as SVM is still relevant to the modelling of grid-connected inverters but not the main concern of this thesis.

The required instantaneous inverter output voltages are transformed into the $\alpha\beta$ reference frame through the Clarke transformation to provide the inverter output reference voltage $\bar{V}_{ref}$. $\bar{V}_{ref}$ will rotate at the angular velocity of the grid fundamental frequency in the 2-dimensional

$\alpha\beta$ reference frame. The inverter output phase voltages are controlled in such a manner that each switch within a three-phase inverter will either be equal to the DC voltage or zero, therefore obtaining 8 possible switch configurations. The concept of SVM, as illustrated in Figure 21 is, therefore, to obtain $\bar{V}_{ref}$ by using superposition of the inverter's phase voltage vectors. Within every sampling period the sector in which $\bar{V}_{ref}$ is located, is determined and then the required time period for each phase voltage vector is calculated to obtain the desired output voltage.

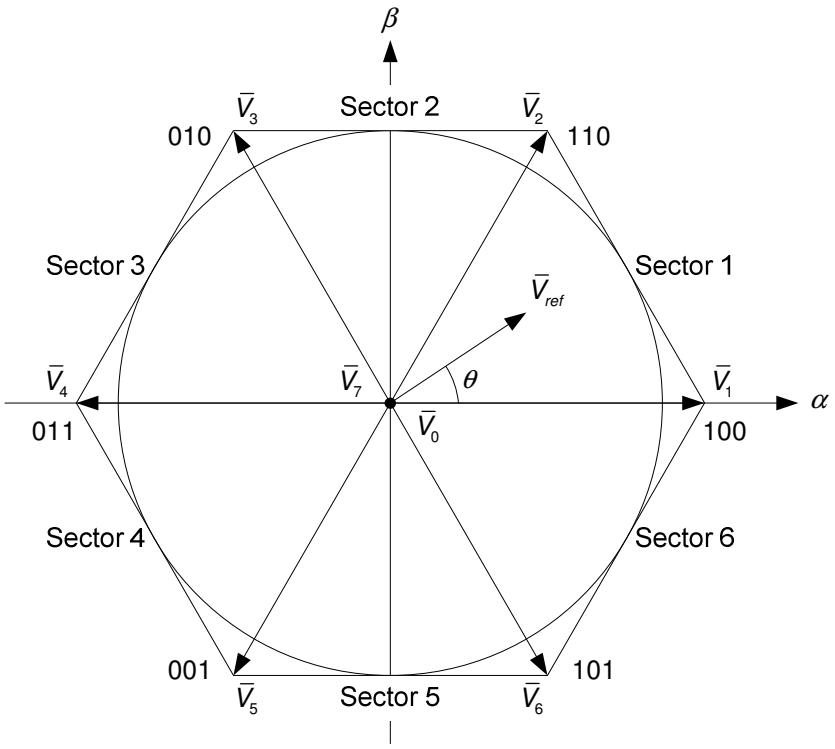

Figure 21: Illustration of SVM

For a detailed analysis and mathematical approach to SVM refer to [27], [34]. It is important to mention that through calculations as shown in [25], that SVM inherently has a similar advantage with regards to the modulation index as that of third harmonic injection. One can increase P_m to 1.155 without entering inverter saturation. SVM is, however, a more advanced and superior method to third harmonic injection as one can increase P_m to 1.155 without the negative impact of low-order harmonics found with third harmonic injection in naturally and regularly sampled PWM inverters [27]. It has the effect of a PWM inverter with a higher inverter voltage rating and lower output harmonics.

2.4.7. Inverter control techniques

There are a variety of control techniques used for different applications. The most popular and appropriate voltage-source three-phase inverter control techniques for grid-connected

systems have been briefly discussed in [35], [36]. The control techniques used for the simulation models in this thesis will be discussed in Section 3.6 with the implementation in DIgSILENT PowerFactory.

2.5. PQ STANDARD IN SOUTH AFRICA

2.5.1. Overview

The PQ standards used to manage the PQ levels between utilities and customers in South Africa as specified in the SAGCRPP for power plants connected to the transmissions and distributions systems [37] include the following:

- NRS 048-2 [5], a standard that defines the compatibility levels and limits for utilities.
- NRS 048-4 [38], guidelines for apportionment and assessment of PQ parameters of customers.
- NRS 048-7 [39], guidelines to manage PQ application practices within customers.
- SANS 1816 [40], which provide technical requirements for PQ instruments.

The NRS 048-2 and SANS 1816 standards are adopted from international standards such as IEC 61000-4-30 [41].

In this chapter a brief discussion surrounding the requirements of every RPP that connects to the utility network will be given. In addition, the present South African standards that are applicable to this thesis will be discussed. PQ measurement standards, PQ management and PQ assessment methods will also be presented.

2.5.2. PQ standards in renewable energy

2.5.2.1. Design and operation requirements of RPPs

In accordance with the Electricity Regulation Act (Act 4, 2006), it is mandatory that all RPPs adhere to the minimum grid connection design and operation requirements stated in the SAGCRPP to ensure the stability and reliability of the grid operation before obtaining compliance to connect to any Eskom Transmission System or Distribution System [37], [42]. The SAGCRPP was first published in 2010 and is currently on version 2.9 of the code at the time of writing.

The SAGCRPP applies to all renewable power plants, namely: solar PV, concentrated solar power, wind, small hydro, landfill gas, biomass and biogas. The most important for this thesis is wind and solar PV generation. Compliance with the minimum design and operation requirements of the SAGCRPP are determined in accordance to the RPPs rated power or if otherwise stated the nominal voltage at the point of connection (POC). Therefore, the RPPs are categorized into five groups as seen in Table 1.

Table 1: RPP categories [37]

Category	Minimum Power	Maximum Power	Type
A1	0 kVA	13.8 kVA	Low voltage (LV) connected
A2	13.8 kVA	100 kVA	LV connected
A3	100 kVA	1 MVA	LV connected
B	1 MVA	20 MVA	Medium voltage (MV) connected
C	≥ 20 MVA		MV/high voltage (HV) connected

The design and operation requirements will not be discussed further as it is out of the scope of this thesis.

2.5.2.2. PQ parameters of RPPs

It is the responsibility of any RPP that connects to the utility network to minimise and limit their PQ impact according to the SAGCRPP.

All RPPs must prove compliance according to the PQ guidelines and parameters described in NRS 048 series of specifications for RPPs to be allowed to connect to the network. The PQ parameters that must be measured, monitored and reported on by RPPs include:

- voltage unbalance
- harmonics
- flicker

RPPs can prove compliance to connect to the network before or at the time of connection by using a combination of simulation studies and measurements. Note that simulations only allow for initial compliance until on site measurements can be done. At the time of writing the national service provider allows RPPs to exceed the specified current emission limits by 50% or less. To prove full compliance category B and C RPPs must follow the assessment process described in [37]. If RPPs exceed the specified limits as agreed upon with the national service provider it requires the RPP to implement mitigation methods to reduce the PQ impact on the national network. One such method includes the design and installation of filters. The PQ management and assessment for RPPs will be discussed in Section 2.6.

2.5.3. PQ measurement standards

PQ measurement standards on instruments are required to ensure that different measurement instruments provide comparable measurement results on the same signal. The accurate

comparison and investigation of PQ results are challenging due to the large number of PQ instrument manufacturers. Thus, a standard on methods and interpretation of PQ results was required. These standards can be found in SANS 61000-4-30 [43] which was adopted from IEC 61000-4-30 [41] for South Africa. The main purpose of the standard is to define the PQ parameters that must be recorded as well as the recording precision of each parameter. It provides performance specifications regarding measurement equipment rather than design specifications.

The following PQ parameters are described in SANS 61000-4-30: frequency, supply voltage magnitude, flicker, harmonics, inter-harmonics, voltage dips, voltage swells, interruptions and rapid voltage changes.

In addition, SANS 61000-4-7 [44] is used as the reference standard for measuring current and voltage harmonics. IEC 61000-4-15 [45] focuses on the measurement of flicker. Some of the main requirements of these standards will be described and summarized below.

2.5.3.1. Measurement instrument classes

SANS 61000-4-30 defines three instrument classes (Class A, Class B and Class S) for measurement methods.

The Class A measurement method will ensure repeatable and comparable results for all Class A instruments regardless of the instrument manufacturer. Class A instruments are therefore used to verify customer compliance [43].

Class B and Class C instruments provide comparable results for statistical analysis such as surveys. Consequently, Class B and Class C performance methods do not provide the required precision as found in Class A measurement instruments.

All instruments used for compliance and emission level assessment must adhere to Class A measurement methods and performance. Therefore, all measurements in this work will be done using class A instruments.

2.5.3.2. Data aggregation

The following is a summary of data aggregation in 50 Hz systems and in Class A instruments. The basic measurement aggregation interval standard used for PQ analysis for PQ parameters is 10-cycle (200 ms) intervals. The 10-cycle values are aggregated over three time intervals as seen below:

- 150-cycle (3-second) intervals. Aggregated from 15 10-cycle (200 ms) average values.
- 10-minute intervals. Aggregated from 3000 10-cycle (200 ms) average values.
- Two hour intervals. Aggregated from 12 10-minute average values.

The aggregated values are calculated as follows [41]:

$$U_{rms} = \sqrt{\frac{U_1^2 + U_2^2 + ... + U_n^2}{n}} \quad (2.15)$$

where U_i is a 10-cycle or 10-minute measurement value and n the number of aggregated 10-cycle or 10-minute values. For Class A instruments all aggregated values must be gapless and not overlapping. Moreover, the 10-minute interval values must be synchronised to the clock.

2.5.3.3. Flagging due to dips, swells or interruptions

Flagging is important to avoid counting a single PQ event more than once in different measurement parameters. Flagging only occurs for voltage dips, swells and interruptions during the measurement of power frequency, flicker, voltage unbalance, voltage harmonics and voltage interharmonics. If during a certain time interval a value is flagged, then the aggregated value which includes the flagged value must also be flagged. The customer or utility can decide on how to evaluate the flagged data by either including or excluding the flagged data into the calculation of voltage magnitude, flicker, supply voltage unbalance, voltage harmonics and voltage interharmonics [46].

2.6. PQ MANAGEMENT AND ASSESSMENT IN SOUTH AFRICA

2.6.1. Overview

The methods described in this section are used to manage the PQ of the network. The key PQ levels for the purpose of this paper are the compatibility levels, planning levels and emission limits of RPPs connected to the utility network. The compatibility levels are defined in the NRS 048-2 [5]. The planning levels are defined in the NRS 048-4 [38]. The emission levels of each RPP must be calculated according to the procedure described in the NRS 048-4 [38] which are adopted from the IEC 61000-3-6 [47] and IEC 61000-3-7. The emission levels represent the allowable PQ impact of the RPP at the POC for voltage unbalance, harmonics and flicker. These parameters must be monitored by using SANS 61000-4-30 [43] Class A compliant PQ meters.

2.6.2. Assessment requirements

Assessment refers to the method of interpretation of the aggregated measured values with the purpose to compare these values to the compatibility levels and planning levels specified in the NRS 048. The assessment value used for all PQ parameters, with an exception for short term harmonics, is the 95% percentile of the 10-minute interval values. For short term harmonics the assessment value is the highest value of the 99% percentile daily values obtained by using the measured 150 cycle (3 seconds) interval values. The assessment period

is minimum one week. Flagged data as described in SANS 61000-4-30 and Section 2.5.3.3 must be removed from the measured data for the purpose of assessment. Note that the exclusion of flagged data is only applicable provided that less than 10% of the data have been flagged.

The instantaneous PQ effects per cycle are lost in the aggregates. The reason for this is that the conventional PQ methods (NRS048 and other) make use of 3000 successive aggregated 200 ms window averages of harmonic content, forming 10-minute windows, spread over one week, of which the 95th percentile is prepared to produce a quantification of the levels of harmonics present.

The assessment standard monitor long term trends. Consequently, short term PQ issues which will impact the operation of RPPs are not covered by the assessment. Effectively, the standards are aimed at the long term health of the network and not the dynamic type of events associated with traction loads. The PQ parameters that will be investigated in this paper are voltage unbalance and harmonics. This thesis will focus on the PQ levels in HV networks as most AC traction substations are connected to an HV network.

2.6.3. Voltage Unbalance

2.6.3.1. Compatibility levels

The compatibility level for voltage unbalance in HV networks is 2% as defined in the NRS 048-2. The compatibility level of HV networks may be increased to 3% on networks that consist of a predominance of single-phase loads such as traction loads. This exception is only applicable when the 2% compatibility level is not exceeded for more than 80% of the assessment period.

2.6.3.2. Planning levels

The recommended planning levels for voltage unbalance in HV networks is 1.4% as per the NRS 048-4 [38].

2.6.3.3. Calculation of unbalance emissions

Voltage unbalanced is defined in the IEC 61000-4-30 in terms of the negative sequence contribution. The voltage unbalance (V_{UB}) can be calculated as follows:

$$V_{UB}(\%) = \frac{|V_2|}{|V_1|} \times 100 \tag{2.16}$$

Where V_1 and V_2 is the magnitude of the positive sequence and negative sequence voltage components respectively. Note that (2.16) requires the measurement of the magnitude and phase angle of the phase to neutral voltages to calculate the positive and negative sequence components.

The voltage unbalance can also be calculated as follows when considering phase-to-phase voltages:

$$V_{UB}(\%) = \sqrt{\frac{1-\sqrt{3-6\beta}}{1+\sqrt{3-6\beta}}} \times 100 \tag{2.17}$$

where

$$\beta = \frac{|V_{ab}|^4 + |V_{bc}|^4 + |V_{ca}|^4}{(|V_{ab}|^2 + |V_{bc}|^2 + |V_{ca}|^2)^2}. \tag{2.18}$$

By using (2.17) and (2.18) one can use the phase to phase (line) voltages rather than using the magnitude and phase angle of the phase to neutral voltages as required in (2.16).

2.6.3.4. Calculation of unbalance emissions of RPP for compliance assessment

The voltage unbalance at the POC should be measured before and after the connection of an RPP to the network. If the total voltage unbalanced increased after the connection of the RPP then the resultant unbalance contribution of the RPP should be used for assessment. It is therefore assumed that the negative sequence contribution from the background unbalance is negligible compared to the contribution from the RPP then the unbalance contribution from the RPP can be calculated as follows:

$$|\bar{V}_{UB,i}| = |\bar{V}_{UB,post} - \bar{V}_{UB,pre}| \tag{2.19}$$

where $\bar{V}_{UB,i}$ is the voltage harmonic emission responsible by the RPP and $\bar{V}_{UB,pre}$ and $\bar{V}_{UB,post}$ the voltage unbalance before and after connecting the RPP respectively. If the phase angles are not available then IEC 61000-3-13 describes the use of (2.20) with α equal to 1.4.

$$|\bar{V}_{UB,i}| = \left(|\bar{V}_{UB,post}|^{\alpha} - |\bar{V}_{UB,pre}|^{\alpha}\right)^{1/\alpha} \tag{2.20}$$

The unbalance contribution of the RPP is compared to the apportioned limit set for the specific RPP.

2.6.4. Harmonics

2.6.4.1. Voltage harmonic compatibility levels

The steady state voltage harmonic compatibility levels for HV networks are defined in NRS 048-2 [5] for both short-term effects and long-term effects. Short-term effects relate to the effects of harmonics on electronic devices that are sustained to voltage harmonics for 3 seconds or less. Long-term effects relate to the thermal effects of harmonics on power system equipment such as transformers, motors, etc. that are sustained to voltage harmonics for 10 minutes or more. Individual voltage harmonics are measured up to the 50th order.

The total harmonic distortion (THD) limit for harmonics up to the 40th individual harmonic is 4% on HV and extra high voltage (EHV) networks as defined in NRS 048-2. The individual voltage harmonic compatibility levels, expressed as a percentage of the reference voltage, on HV and EHV networks are shown in Table 2.

Table 2: Compatibility levels for voltage harmonics on HV networks [5]

Harmonic order	**Harmonic voltage (%)**
3	2.5
5	3
7	2.5
11	1.7
13	1.7
17	1.2
19	1.2
23	0.8
25	0.8

The compatibility levels of even harmonics and higher-order odd harmonics are not defined. Therefore, the planning levels as defined in the NRS 048-4 [38] must be used as reference for these harmonics.

2.6.4.2. Voltage harmonic planning levels

The recommended planning levels for individual voltage harmonics, expressed as a percentage of the reference voltage, is shown in Table 3.

HV and EHV customers have written contracts with apportioned voltage and current harmonic levels determined by the network service provider. These levels are normally less than those specified in Table 3 and based on the size of the connected customer. If any individual voltage harmonic level is not specified in the apportioned voltage harmonic levels then the value of that specific individual harmonic voltage level may not exceed 30% of the compatibility levels in Table 2 or otherwise the planning levels in Table 3.

Table 3: Planning levels for voltage harmonics on HV networks [38]

Odd harmonics for non-multiple of 3		**Odd harmonics for multiple of 3**		**Even harmonics**	
Order	**Harmonic voltage (%)**	**Order**	**Harmonic voltage (%)**	**Order**	**Harmonic voltage (%)**

h	HV/EHV	h	HV/EHV	h	HV/EHV
5	2	3	2	2	1.5
7	2	9	2	4	1
11	1.5	15	0.3	6	0.5
13	1.5	21	0.2	8	0.4
17	1	>21	0.2	10	0.4
19	1			12	0.2
23	0.7			>12	0.2
25	0.7				
>25	$0.2+\left[0.5\times(25/h)\right]$				

2.6.4.3. Calculation of harmonic emissions of RPP for compliance assessment

The continual integration of RPPs into the distribution network requires that RPPs comply with the requirements specified in the SAGCRPP to ensure minimal impact of RPPs on the operation of the distribution network. Therefore, the harmonic emissions of RPPs need to be evaluated. The methodology used to calculate the harmonic emissions of a RPP for compliance assessment as well as to determine the apportioned harmonic emission limits is based on the guidelines described in the following documents: IEC 61000-3-6 [47], RPP Power Quality Guidelines [48], Review of Disturbance Emission Assessment Techniques [49] and The Assessment of Harmonic Emission described by CIGRE/CIRED C4.109 working group [50]. These guidelines can also be applied to electrical energy consumers such as non-linear load. These guidelines are theoretically clear but the challenge lies in determining by practical measurements if RPPs and loads are meeting the levels specified by the utilities [51]. A need exists to obtain a practical measurement approach to evaluate the harmonic emissions of a RPP once commissioned. The challenge for electrical engineers is to obtain a fair assessment approach in calculating the RPP harmonic emissions at the POC if background harmonics are present on the distribution network. Harmonic sources such as non-linear loads (traction loads) exist all over a traction network and will impact the voltage THD at the POC in addition to the harmonic emissions of a RPP. Compliance assessment for RPPs are currently being done using a single-point harmonic measurement at the POC. From [52] it was established that a single-point harmonic measurement approach for harmonic assessment does not provide conclusive assessment results for networks with more than one harmonic source. It has been shown in [51] that a multi-point measurement approach provide an improved harmonic assessment when based on the IEC 61000-3-6 guidelines. A two-point measurement approach will therefore be followed when investigating the impact of traction loads on the

harmonic emissions of a RPP based on the IEC 61000-3-6 guidelines. The IEC 61000-3-6 approach is illustrated in Figure 22.

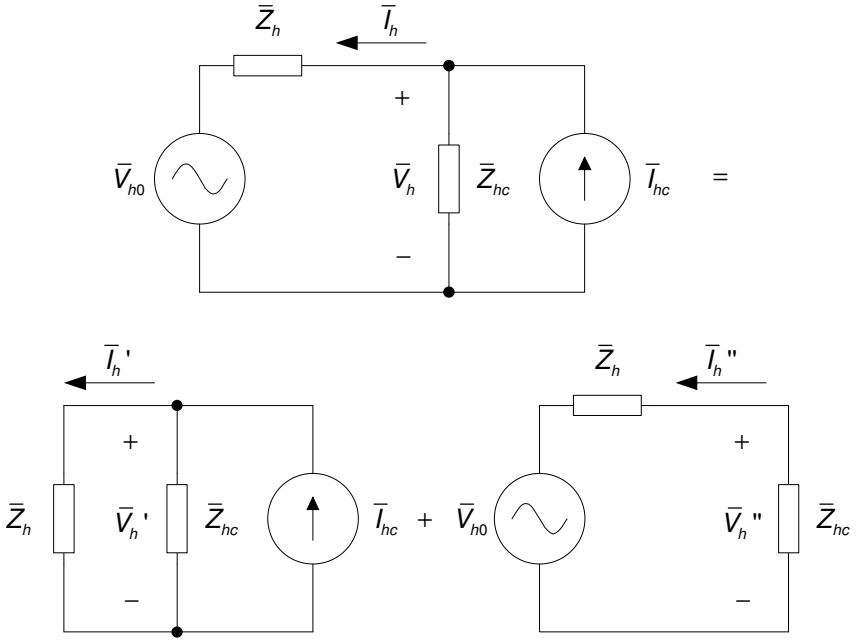

Figure 22: Superposition of harmonic sources

The approach is described using a consumer load as a harmonic source. The harmonic current flowing from the harmonic producing consumer load into the system is a function of the harmonic current generated by the load ($\bar{I}_{hc}$) and the load impedance ($\bar{Z}_{hc}$) which provides a sink for harmonic currents caused by the background distortion ($\bar{V}_{h0}$). Harmonic current flowing through the line impedance ($\bar{Z}_h$) causes harmonic voltage distortion ($\bar{V}_h$) at the POC. By using superposition in the circuit of Figure 22, the contributions from $\bar{I}_{hc}$ and $\bar{V}_{h0}$ on $\bar{I}_h$ can be calculated as follows:

$$\bar{I}_h = \bar{I}_h' + \bar{I}_h'' \tag{2.21}$$

where

$$\begin{aligned} \bar{I}_h' &= \bar{I}_{hc} \frac{\bar{Z}_{hc}}{\bar{Z}_{hc} + \bar{Z}_h} \\ &\approx \bar{I}_{hc} \quad \text{if } \bar{Z}_{hc} \gg \bar{Z}_h \end{aligned} \tag{2.22}$$

and

$$\begin{aligned} \bar{I}_h'' &= -\frac{\bar{V}_{h0}}{\bar{Z}_{hc} + \bar{Z}_h} \\ &\approx -\frac{\bar{V}_{h0}}{\bar{Z}_{hc}} \quad \text{if } \bar{Z}_{hc} \gg \bar{Z}_h \end{aligned} \tag{2.23}$$

The harmonic voltage distortion at the POC becomes:

$$\bar{V}_h = \bar{V}_h' + \bar{V}_h'' \tag{2.24}$$

where

$$\begin{aligned} \bar{V}_h' &= \bar{I}_h' \bar{Z}_h \\ &= \bar{I}_{hc} \frac{\bar{Z}_{hc}}{\bar{Z}_{hc} + \bar{Z}_h} \bar{Z}_h \\ &\approx \bar{I}_{hc} \bar{Z}_h \quad \text{if } \bar{Z}_{hc} \gg \bar{Z}_h \end{aligned} \tag{2.25}$$

and

$$\begin{aligned} \bar{V}_h'' &= \bar{I}_h'' \bar{Z}_h \\ &= -\frac{\bar{V}_{h0}}{\bar{Z}_{hc} + \bar{Z}_h} \bar{Z}_h \\ &\approx -\frac{\bar{V}_{h0}}{\bar{Z}_{hc}} \bar{Z}_h \quad \text{if } \bar{Z}_{hc} \gg \bar{Z}_h \end{aligned} \tag{2.26}$$

To provide a customer load with an adequate voltage and for proper protection coordination, the line impedance is typically much smaller than the load impedance. The equations above can therefore in many cases be simplified. The harmonic current caused by background harmonics is predominantly a function of the load impedance, while the harmonic voltage distortion caused by the harmonic currents generated by the load is predominantly a function of line impedance. In other words an increase in individual harmonic emissions would result in an increase in the corresponding voltage harmonic along the network impedance. On the other hand, the absorption of individual harmonic currents by the consumer would result in an increase in the corresponding voltage harmonics along the consumer impedance line. A representation of the harmonic impedance lines are shown in Figure 23.

It can be said that a load can either be seen as a source of harmonics or a load that absorbs harmonics. IEC 61000-3-6 defines that harmonic emission are only considered if there is an increase in voltage distortion after an RPP is connected to the network compared to the voltage distortion prior to connection. The effective harmonic load impedance at the consumer installation can be calculated by using harmonic voltage and current measurements as follows:

$$\left|\bar{Z}_{he}\right| = \frac{\left|\bar{V}_h\right|}{\left|\bar{I}_h\right|} \tag{2.27}$$

If $\bar{Z}_{he} \approx \bar{Z}_{hc}$ the background harmonic voltage source predominantly causes current to flow towards the consumer load and the grid can be seen as the dominant harmonic current source, but if $\bar{Z}_{he} \approx \bar{Z}_h$, harmonic current generated by the consumer predominantly flows towards the source and the consumer can be seen as the dominant harmonic current source. All data

points in between these two borders reflect the combination of both harmonic current contributors. Cigre [49] suggests this concept as a method to determine harmonic contribution at a customer installation.

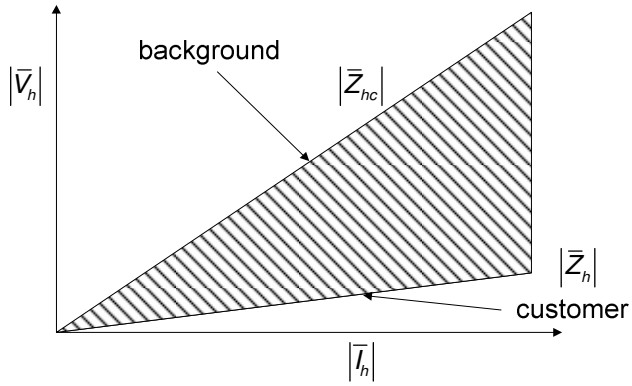

Figure 23: Harmonic impedance representation

Equipment at consumer installations is considered as harmonic current sources by standards such as IEC 61000-3-6. The effect of these current sources on voltage is evaluated to determine compliance. Therefore, only part b) of Figure 22 is considered and current emission is calculated using (2.25). In this equation it is important to understand the nature of the harmonic impedance ($\bar{Z}_h$). At a low voltage the impedance of the transformer can be seen dominant. It becomes more complex when there are other equipment on the network that contains capacitors in parallel with the installation as this causes parallel resonance.

Since parallel impedances influence the network impedance at different frequencies it is difficult to predict scenarios accurately. Due to the uncertainty of network the impedance, utilities typically adopt a rule that they assume the network impedance has a value of three times the impedance at a specific harmonic. If the network impedance is $\bar{Z}_1$ at the fundamental frequency of supply, the impedance used for harmonic analysis is:

$$\bar{Z}_h = 3 \times h \times \bar{Z}_1 \tag{2.28}$$

By using (2.28) in (2.25) the voltage distortion levels can be determined and compared to the apportioned emission values given by the national service provider.

2.6.4.4. Current harmonic emission levels

The PQ current emission limits are apportioned values which are fair, transparent and conservative so to include the upwards RPP contributions on the network as well as future customer contributions. At the time of writing the RPP is allowed to exceed the individual harmonic emission limits by 50% provided that the measured group harmonic distortion does not exceed the group harmonic distortion limits. The measured group harmonic distortion and

group harmonic distortion limits for the 4 harmonic groups (2≤h≤13, 14≤h≤25, 26≤h≤39 and 40≤h≤50) are calculated as follows:

$$HD_{\text{limit}} = \sqrt{\sum_{i=h}^{j} I_{\text{limit}}(h)^2}$$
$$HD_{measured} = \sqrt{\sum_{i=h}^{j} I_{measured}(h)^2} \quad (2.29)$$

where it required that $HD_{measured}$ be smaller than HD_{limit} for grid code compliance.

2.7. PQ IMPACT OF AC TRACTION ON NETWORK

2.7.1. Introduction

Traction loads are nonlinear and generally cause the following PQ characteristics on the power network [53]:

- harmonic currents
- negative sequence currents/voltage unbalance
- voltage fluctuations

These PQ characteristics will impact the upstream power supply network [54]–[56], power supply equipment such as three-phase induction motors [57] and the railway signalling and telecommunication systems [58]. According to [53], [59] the primary PQ concern on the power network due to traction loads are the voltage unbalance and harmonics. The above PQ issues will be discussed in more detail below with the focus on AC traction sytems.

2.7.2. Voltage Unbalance

AC traction systems are one of the most common contributors of network voltage unbalance as AC traction loads are fed through a single-phase traction transformer [55], [60]. The primary of the transformer is connected to two phases of the three-phase system which gives rise to voltage unbalance [61]. For a conventional single-end feeding traction system the voltage drop increases as the locomotive moves further away from the supply point at the traction substation. Thus, the maximum voltage drop will occur halfway between two adjacent traction substations or just before and after the neutral section when assuming a constant power demand [62]. The voltage unbalance caused by traction loads typically peak as the train moves past the POC where PQ measurements are done. Multiple traction loads connected to the system at the same time and can collectively worsen the voltage drop and PQ impact.

The unbalance is typically for a short duration, approximately two or three 10-minute values. The unbalance will cause considerable negative sequence currents. These negative sequence currents can impact electrical devices on the network [6], such as induction machines. Due to the single-phase connection, power is drawn from two of the three-phase network which

consequently cause voltage unbalance in the three-phase network. The voltage unbalance caused by traction loads can be accurately estimated by using the following equation [55], [63]:

$$V_{UB} = \frac{S_{traction}}{S_{grid,fl}} \times 100\% \tag{2.30}$$

with $S_{traction}$ the power demand of the traction load and $S_{grid,fl}$ the grid three-phase fault level at the supply point. With the growing demand in traction systems it is important that the three-phase fault level of the three-phase grid is large enough to support large traction power demands.

Voltage unbalance may cause the malfunction of grid-connected power electronics devices such as three-phase inverters in RPPs. The level at which inverters malfunction or trip is determined by PQ standards as described in Section 2.6. This will be further investigated in CHAPTER 5.

2.7.3. Harmonics

Another PQ problem associated with traction loads is the injection of current harmonics into the network. These harmonics are caused by power electronic rectifiers/converters on locomotives. The two most common technologies as discussed in section 2.2 are thyristor rectifiers and PWM converters. The conventional thyristor locomotives are rich in low-order odd current harmonics [64]. The single-phase active rectifier traction drive system consists of a single-phase active rectifier, a DC link capacitor and a three-phase PWM inverter as seen in Figure 9. The front end rectifier produces a range of characteristic harmonics. Various papers have investigated the harmonic characteristics of active rectifiers in locomotives [16], [17].

An active rectifier operating at a high switching frequency will essentially draw a sinusoidal current with a small ripple at high frequency. The harmonics components for converters operating in the linear region exist at sidebands centred around the switching frequency and multiples of the switching frequency of the converter [18].

Some applications require that the amplitude of the fundamental-frequency AC voltage be increased beyond that which can be achieved in the linear region of the converter. This results in overmodulation which causes an increase in voltage harmonics compared to those generated in the linear operating region. There are several studies that investigated the PQ issues associated with traction systems regarding harmonic disturbances [65], harmonic resonance [66] and short circuit behaviour [67]. These studies show that inverters only generate lower-order harmonics due to non-ideal behaviour, such as a low DC voltage, dead time and controller instability.

The contribution of injected individual current harmonics caused by traction loads on the voltage harmonics and voltage THD on the power supply network has been investigated in

[61]. From [61] it is evident that individual voltage and current harmonics as well as the voltage THD exceeded the standard limits set for that country.

Various papers have investigated different control strategies to decrease the harmonic contribution of PWM converters for railway application [25], [26]. Therefore, the production of low-order harmonics are generally low in PWM converters. However, the problem of high-order harmonics that overlap with natural frequencies cause overvoltages due to harmonic resonance [70], [71]. The harmonic resonance and propagation of harmonic current in the power supply network due to traction loads are investigated in [72], which shows that harmonic resonance at higher frequency harmonics can lead to a substantial increase in the amplitude of harmonic current components compared to the original injected harmonic current components.

The present harmonic standards only consider harmonic components up to the 50th harmonic. Various papers report an increase in the severity of higher-order harmonics in the switching frequency range due to the increase in PWM converters within energy sources (RPPs) and traction loads in the distribution network [38]. These significant high-order harmonics will impact power system equipment and can result in temperature increases in equipment and thus lead to additional losses in the network [53], [17].

From [73] it was established that the magnitude of the low-order harmonics produced by the PWM converter in traction loads are almost always different and dependent on the mode of operation and loading level of the locomotive. The magnitude of the high-order harmonics produced by the PWM converter is independent of the operating mode and loading level of the locomotive [73].

Low-order harmonics associated with diode and thyristor locomotives produce significant low-order harmonic distortion in the voltage and current waveforms. Poor quality due to harmonics is generally a bigger concern with diode and thyristor locomotives than with active rectifier locomotives.

2.7.4. System resonance

2.7.4.1. Overview

Harmonic distortion problems in power systems usually arise due to the effect of resonance. Low levels of harmonic emissions at the presence of a harmonic resonance can lead to a significant increase in harmonic distortion [74]. The effect of resonance is common in power systems with harmonic filters, large cable networks and power factor correction capacitor banks [75]. A RPP is a typical example of a system that has the potential for resonance problems [76].

Generally, harmonic resonance can be classified as, parallel and series resonance. Both are discussed below.

2.7.4.2. Parallel resonance

Most turbine inverters are connected to the grid through a filter capacitor, a MV collector cable network and transformer. The MV collector cable network usually has a large capacitive impedance. The interaction between the filter capacitive impedance, cable capacitive impedance, transformer impedance and network impedance produce a parallel resonance circuit. The parallel resonance circuit for a grid-connected RPP is shown in Figure 24.

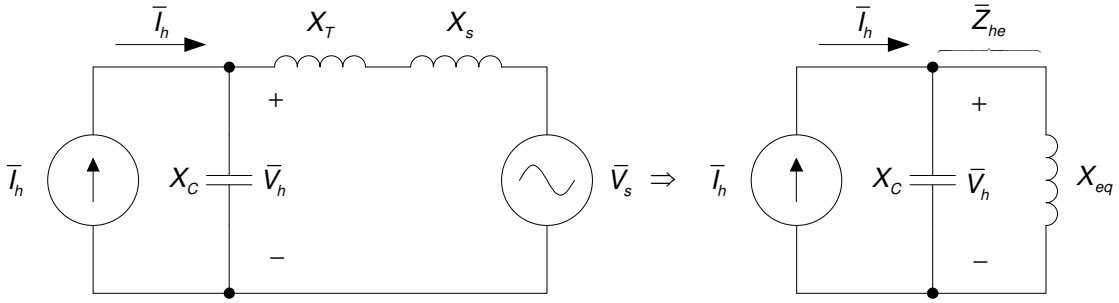

Figure 24: Parallel resonance between line impedance and customer load impedance

Where:

$\bar{I}_h$ is the harmonic current phasor generated by the inverter,

X_C is the filter capacitance,

X_T is the transformer reactance,

X_s is the source reactance,

X_{eq} is the equivalent network reactance,

$\bar{V}_h$ is the network voltage phasor,

$\bar{V}_s$ is the grid voltage phasor.

From the harmonic source or turbine's perspective the filter capacitor C is then connected in parallel with the equivalent network inductance L. The Thevenin equivalent source impedance then becomes:

$$\begin{aligned}\bar{Z}_{he} &= \frac{1}{\frac{1}{X_{eq}} + \frac{1}{X_C}} \\ &= \frac{1}{\frac{1}{j\omega L} + j\omega C} \\ &= \frac{j\omega L}{1-\omega^2 LC}\end{aligned} \tag{2.31}$$

The line impedance for the parallel combination of the equivalent inductance and capacitor becomes very high as ω approaches $\frac{1}{\sqrt{LC}}$. The resonance frequency f_r, therefore, becomes $\frac{1}{2\pi\sqrt{LC}}$. Note that in practical systems the impedance will not become infinitely large at f_r due to the frequency independent resistive component in the network impedance. A typical frequency sweep of harmonic impedance in a parallel resonance circuit is shown in Figure 25.

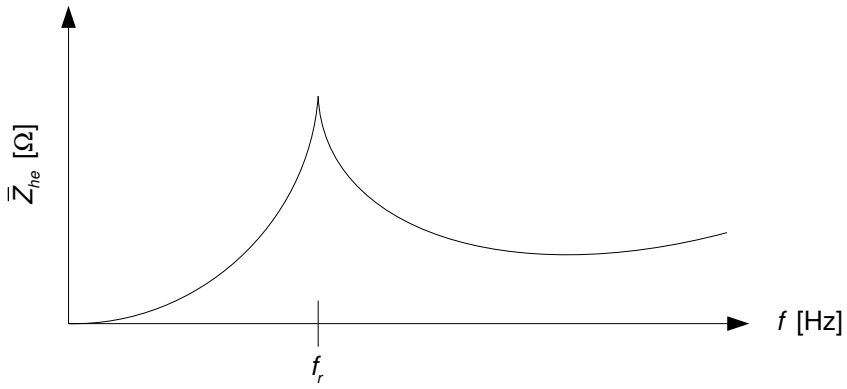

Figure 25: Frequency sweep of parallel resonance network

At the resonance frequency small harmonic currents can result in the voltage $\bar{V}_h$ being magnified and severely distorted. Lower resonance points below the 50th harmonic are normally of a greater concern due to the proximity of the resonance frequency to the frequency of the harmonic currents. Resonance points are also generated by traction loads and the interaction between the inductive and capacitive components on the locomotive with that of the grid. Resonance will amplify the injected current harmonics that are generated by traction loads. The impact of different equipment in a power system on the number of parallel resonance points and location of resonance points have been investigated in [77]–[80]. It is important to mention that the catenary line impedance, number of catenary lines and number of locomotives on a network will all influence the number of resonance points as well as the location of the resonance points as described in [77]. From [78], [79] it was found that the lower parallel resonance points depend on the interaction between the traction system impedance and network impedance and not by the position of the locomotive on the network. The higher

parallel resonance points are highly dependent on the length of catenary lines as shown in [80]. Traction power systems should be connected to grids with high three-phase short-circuit power as [78] has shown that higher three-phase short-circuit power will results in the resonance points shifting to higher frequency positions. The problem of parallel resonance is of a great concern and becomes complex with the addition of different traction load types on the network.

2.7.4.3. Series resonance

The line impedance for the series combination of the equivalent inductance and capacitor becomes very low as ω approaches $\frac{1}{\sqrt{LC}}$. The resonance frequency f_r, is therefore located at $\frac{1}{2\pi\sqrt{LC}}$. A series resonance provides a low impedance path for the currents generated by the network background harmonic distortion, $\bar{V}_h$. These currents will be amplified at the point of series resonance and cause large currents to flow to the inverter of a RPP [75]. Consequently, it will appear as if the inverter is generating a large harmonic current $\bar{I}_h$. Note that in practical systems the impedance will not be equal to zero at f_r due to the frequency independent resistive component in the network impedance. A series resonance circuit is shown in Figure 26.

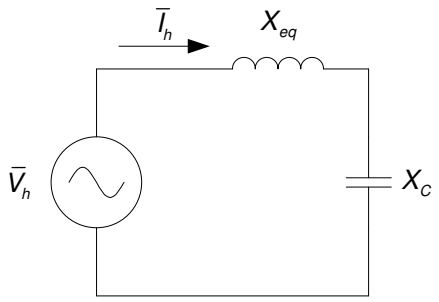

Figure 26: Series resonance circuit

A typical frequency sweep of harmonic impedance in a series resonance circuit is shown in Figure 27.

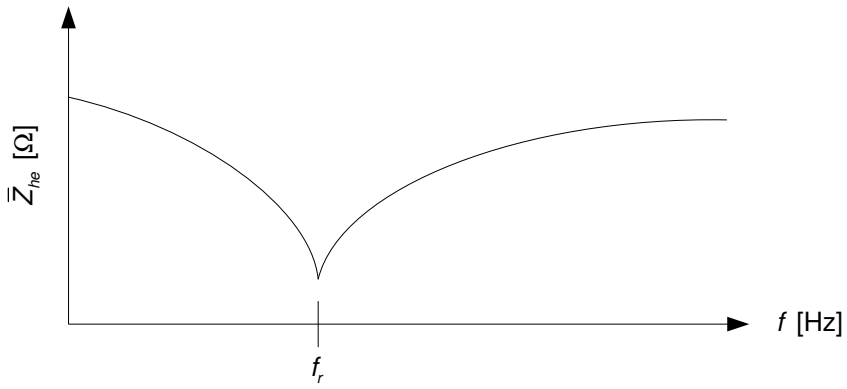

Figure 27: Frequency sweep of series resonance network

The grid can be seen as the dominant harmonic source as described in Section 2.6.4.3 and should a series resonance exist on the network then non-linear loads such as traction loads will cause large currents to flow to the inverters of the RPP.

2.7.5. Voltage fluctuations

The voltage magnitude can have long term (greater than 1 minute) variations which are called under or over voltages as well as short term (smaller than 3 second) variations which are called voltage dips or swells as defined in the NRS 048-2 [81]. Voltage fluctuations are experienced by power system consumers at the Point of Common Coupling (PCC). Several causes of voltage dips are described in [82]. Two that are of relevance to this study and can be linked to traction drives namely: load switching or starting of induction motors and the energizing of transformers. Load switching occurs as a train moves past phase-breaks or neutral zones. During neutral zones the traction power or induction motors are disconnected completely. As the train re-enters the new zone, the full power is switched back on and connected to a new traction substation through a transformer that needs to be energized [62], [83]. This can result in large inrush currents that lead to voltage dips and in turn flicker. The new traction transformer is connected to a different phase sequence which causes the voltage dip to occur in the two new phases. Large inrush currents can also be drawn by a large filter capacitance located in the DC link of the drive, as seen in Figure 9, to charge the capacitor when the train re-connects an energized circuit [84]. The severity of the voltage dip depends on the three-phase fault level rating and voltage level of the three-phase network.

Flicker on traction networks is as result of frequent changes in operating conditions between starting, constant acceleration, constant power, constant speed, coasting and regenerative braking as described in [60], [85] and in Section 2.3. The rapid and dynamic changes in the power demand of traction loads give rise to voltage fluctuations and flicker [61].

In most standards a dip is detected once the voltage value falls under a threshold value. Figure 28 illustrates the voltage dip characteristic for a single-phase voltage dip. The dip threshold

value, as defined in NRS 048-2 [81], is 90% of the nominal voltage for MV, HV and EHV systems and 85 % for LV systems. The dip duration is defined as the time between the instant when the half-cycle RMS voltage decreases below the threshold voltage to the instant when the voltage increases above the threshold voltage.

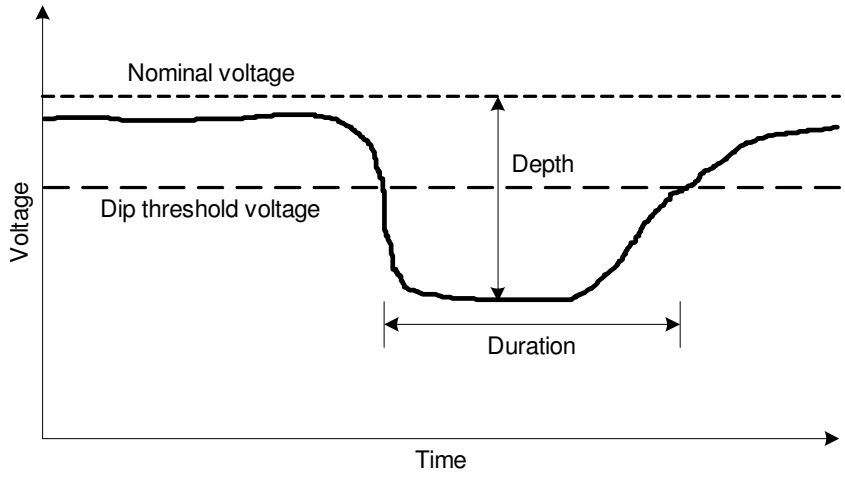

Figure 28: Single-phase voltage dip characteristics

It can generally be assumed that a number of faults will occur on a network and thus RPPs have to take counter actions to ensure that the stability and reliability of the grid is maintained at any given moment. Hence, voltage ride through conditions (VRTC) have been put in place by the SAREGC [37] to prevent the loss of generation and to ensure continuous operation when network voltage disturbances are experienced. All the turbines for category C RPPs will be programmed to withstand voltage variations as shown in Figure 29.

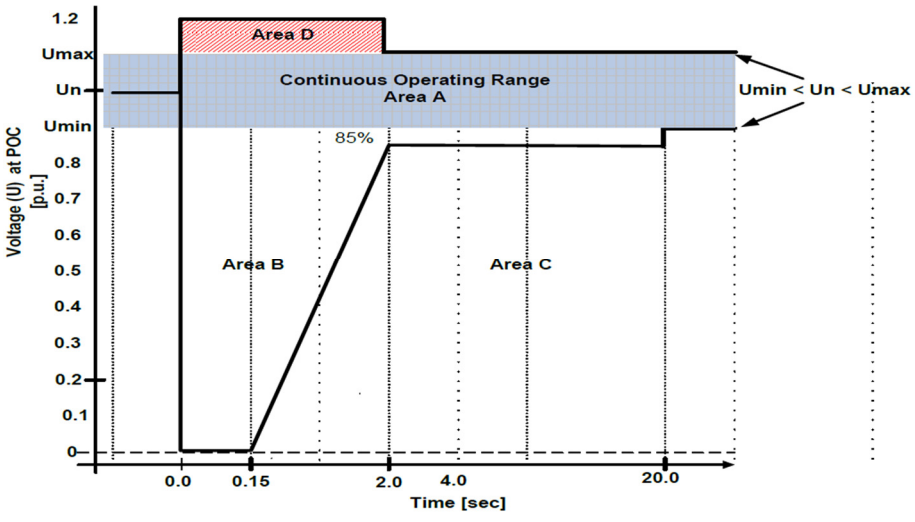

Figure 29: VRTC for category C RPPs [37]

A voltage dip will be countered by exporting a controlled amount of reactive power into the grid to assist in stabilising the network voltage. The reactive power support requirements are shown in Figure 30.

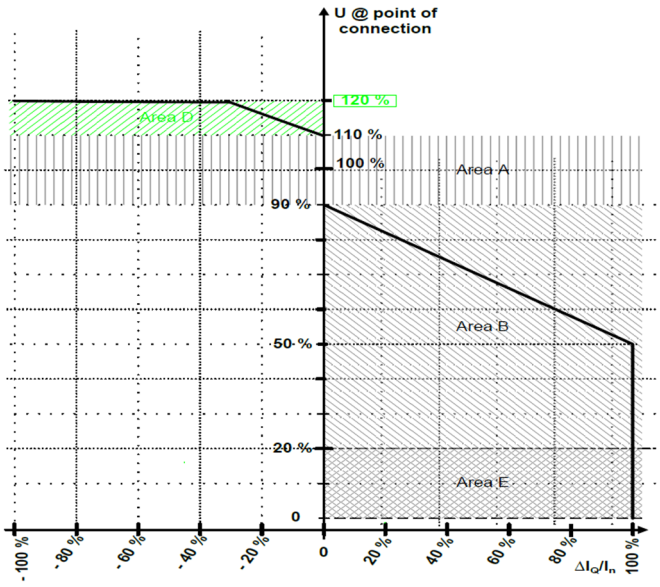

Figure 30: Reactive power support requirements for RPPs [37]

The windfarm has two control modes, voltage control and reactive power control mode. If the plant exports more than 5% of maximum active power then the plant is automatically controlled in voltage controlled mode with a voltage set point of 135 kV. If the plant export less than 5% of maximum power then the plant is controlled in reactive power control mode, and the reactive power is taken down to 0 MVar at a certain slope. In other words the power factor is 1 in reactive control mode. The reason is that Eskom bills RPPs according to their apparent power usage and not just their active power usage. RPPs can assist in network stability through reactive power support but due to the billing procedure in South Africa most RPPs limit reactive power support.

Inverters as used in RPPs can be highly sensitive to voltage dips. Voltage dips can result in various PQ problems such as the loss of control within an inverter [86] and tripping of inverters. The tripping of inverters depends on its protection control settings and the type of dip. Dips produced by capacitors energizing, motor starting and transformer energizing fall within the design voltage tolerance requirements of the RPP and should not lead to operational problems or equipment failure [86] due to the counter measures taken as described. This is shown in Section 5.4.1.2.

2.8. MITIGATION METHODS TO REDUCE POOR PQ IN TRACTION NETWORKS

There is a wide range of mitigation methods in literature that can be used to improve the PQ problems associated with traction loads discussed in Section 2.7. In this section some of the mitigation methods mentioned in literature will be discussed briefly due to the large amount of research already done on this topic.

2.8.1. Phase-shift method

One way in which voltage unbalance can be reduced is by connecting adjacent traction substations to different phase pairs. This method is investigated in [53] and is found to effectively reduce voltage unbalance if the railway sections are equally loaded [59]. This is not the case in systems with dynamic power demand, in short railway sections and in railway sections that contain a railway station. The phase-shift method is also an ineffective voltage unbalance mitigation method in long rural lines with very little traffic, since a single locomotive will be in service for the majority of the time. Hence the railway sections will not be equally loaded. In most traction networks the phase-shift method is not an adequate mitigation method on its own since the loads on a traction network cannot be distributed evenly [87]. This method is already implemented in South Africa but will only be effective in certain network conditions. It is certainly not the case in the traction network being investigated as it contains short railway sections, with high traffic and dynamic power demand. The network of concern also contains a railway station near the POC of the RPP.

2.8.2. Self-balancing traction transformers

One form of voltage unbalance mitigation is the implementation of special self-balancing traction transformers to mitigate the unbalance of single-phase loads. Such transformers include the V/v, Scott and Le Blanc transformers. The V/v traction transformer is connected to the three-phase 132 kV, 50 Hz network using two single-phase transformers as shown in Figure 31. The V/v traction transformer draws three-phase current, $\overline{I}_a$, $\overline{I}_b$ and $\overline{I}_c$ which supplies two single-phase currents $\overline{I}_\alpha$ and $\overline{I}_\beta$ to traction loads on the railway system. The single-phase transformers have a turn ratio of $\frac{N_1}{N_2}$.

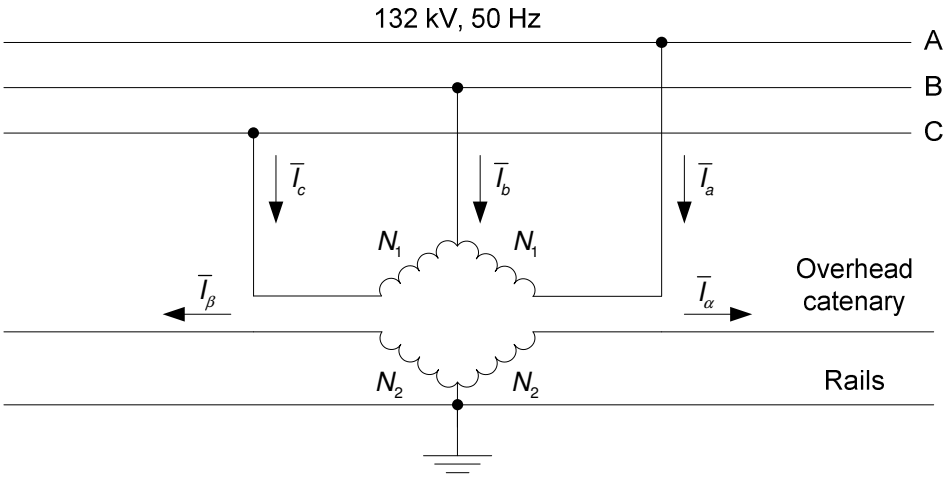

Figure 31: Traction power supply system with V/v traction transformer

The Scott traction transformer is connected to the three-phase 132 kV, 50 Hz network through a single-phase centre-tapped main transformer and a single-phase teaser transformer as shown in Figure 32. The main single-phase centre tapped transformer has a turn ratio of $\frac{N_1}{N_2}$. The teaser transformer is connected to the centre tapped point of the main transformer and has a turns ratio of $\frac{\sqrt{3}N_1}{2N_2}$.

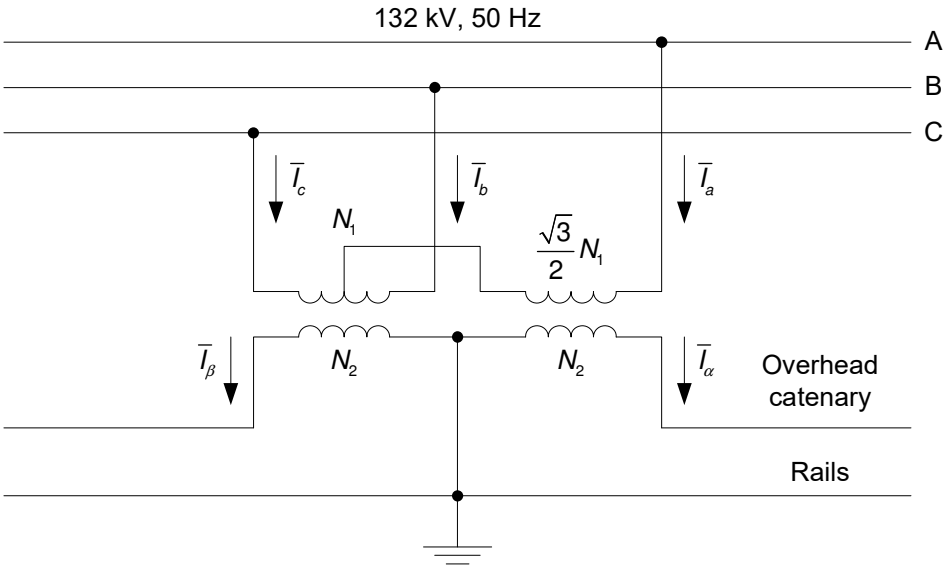

Figure 32: Traction power supply system with Scott traction transformer

These special traction transformers have been investigated in [63], [88]–[90]. A comparison between these transformers have been made in [53], [63]. A detailed comparison between the Scott and Le Blanc transformers have been made in [91]. From the above comparisons it can be concluded that all of the above traction transformers will reduce the voltage unbalance compared to the conventional delta-wye transformer. The Scott and Le Blanc type provide the best voltage unbalance mitigation but are more expensive compared to the V/v type due to their complex structure. Therefore, it was concluded that the V/v transformer provides the best performance and cost option for traction substations.

The use of self-balancing traction transformers do not remove voltage unbalance completely due to the dynamic power demand of traction loads that lead to railway sections that are unequally loaded [14], [21]. Self-balancing traction transformer will be most effective in heavy traffic railway lines that do not contain a railway station. Furthermore, the self-balancing transformers are incapable of compensating for reactive power and harmonics. Methods to compensate for voltage unbalance, harmonics and reactive power are hence required.

It should be noted that there is a trade-off between cost and performance when utilizing the above mentioned self-balancing transformers. These transformers provide better performance

compared to the conventional delta-wye transformers but are more expensive thus leading to most substations utilizing conventional delta-wye transformers. It is important to mention that conventional delta-wye transformers are currently being used in South Africa traction substations. A recommendation that can be made is to implement self-balancing transformers at points in the network where voltage unbalance is a big problem.

2.8.3. Passive filter and reactive power compensation

Passive compensation methods such as reactive power compensation capacitors and passive filters can be used for reactive power and harmonic compensation. In [70] a passive filter control scheme was proposed for co-simulation of single tuned filters to reduce low-order harmonics and reactive power compensation and a high-order filter to reduce high-order harmonics and harmonic resonance in the power system. Passive filters are limited to a number of harmonic orders and are normally designed for specific applications. Moreover, passive filters are designed for fixed reactive power compensation, therefore, a thyristor controlled reactor combined with a passive filter is proposed in [92] to control the amount of reactive power compensation. Passive filters, however, are not ideal for traction loads due to their inability to compensate for dynamic load changes [93] and thus the need for more advanced compensation methods are required. Passive filters are unable to compensate for voltage unbalance which is the major concern of traction loads. Active filters provide the best harmonic compensation but are more expensive.

2.8.4. Dynamic compensation methods

The inability to completely mitigate voltage unbalance by using the phase-shift method or by installing a self-balancing traction transformer, has led designers to utilize dynamic compensation devices such as static VAR compensators (SVCs) or static synchronous compensators (STATCOMs). Dynamic compensation provides a more effective solution for loads that have dynamic characteristics such as traction loads.

Different SVCs have been widely used for voltage unbalance and reactive power compensation [94]–[97]. SVCs can rapidly compensate by supplying or absorbing reactive power. This is done by controlling the firing angle of the fixed-capacitor/thyristor reactor based on the voltage and current of the network. In an unbalanced system, a SVC may not provide adequate compensation as it most likely requires asymmetrical control of the thyristor fire angles. In addition, SVCs do not provide the required tracing capabilities to compensate for dynamic voltage unbalance changes [98]. Other disadvantages of SVCs are harmonic current injections caused by an unbalance system, and resonance between the shunt capacitor and the network inductance [99], [100]. In an unbalanced system, the current magnitude of the three SVC branches will be different which will cause large current harmonic distortion

(particularly, the third harmonic) in the system [100]. Various different SVC types have been investigated in [101] with the purpose of obtaining the SVC type with the best performance with regards to the harmonic and resonance impact to the network. STATCOMs provide better voltage unbalance compensation compared to SVCs but are generally not widely used as they require more complex control and are more costly. In addition, SVCs are unable to compensate for harmonics. Figure 33 shows a traction power supply system with a SVC.

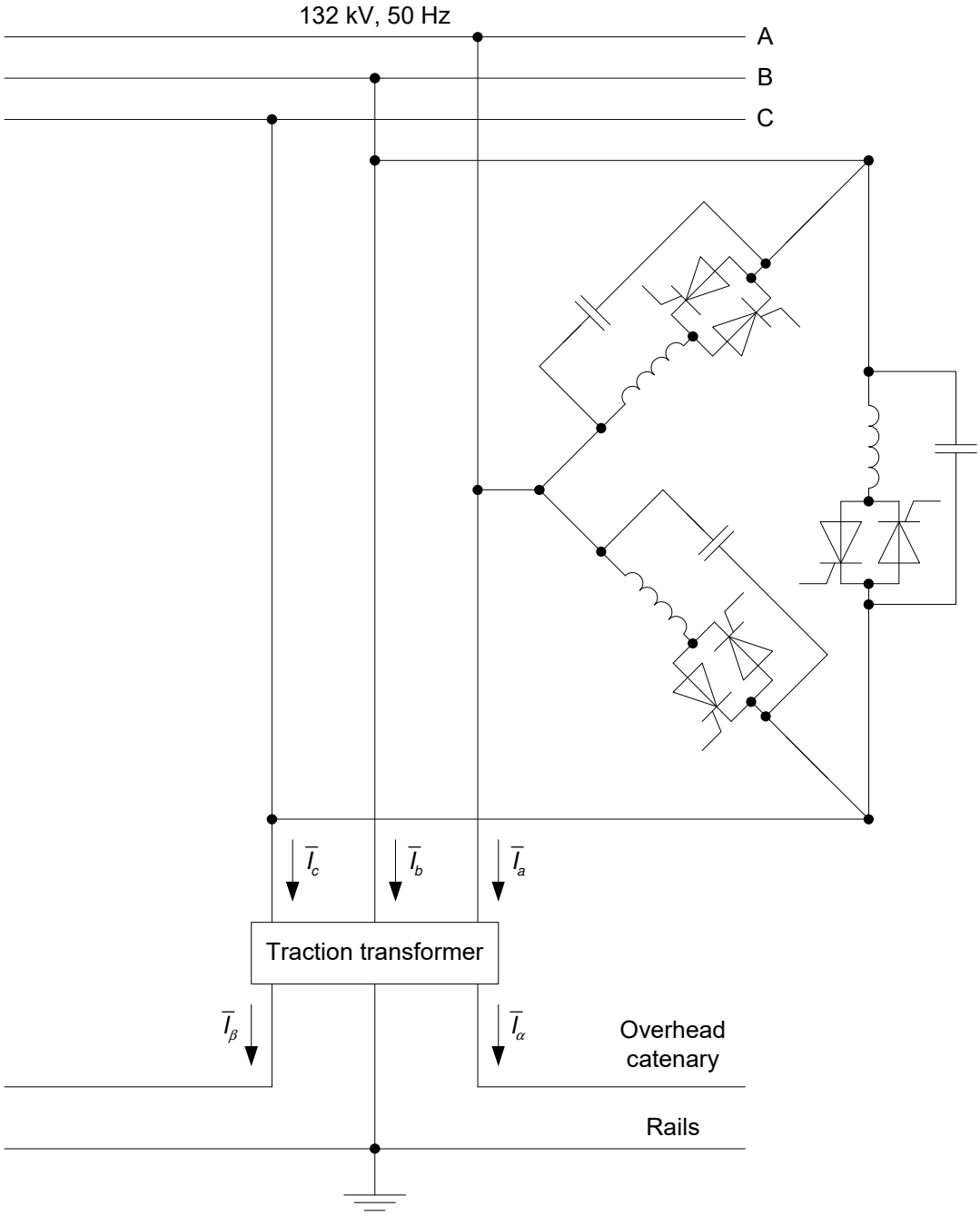

Figure 33: Traction power supply system with conventional SVC

A more improved compensation method for railway applications utilising back-to-back single-phase PWM converters and a coupled DC link capacitor have been proposed in [102]. It is

more commonly known as a railway power static conditioner (RPC) and the connection of a RPC in a traction power supply system is shown in Figure 34.

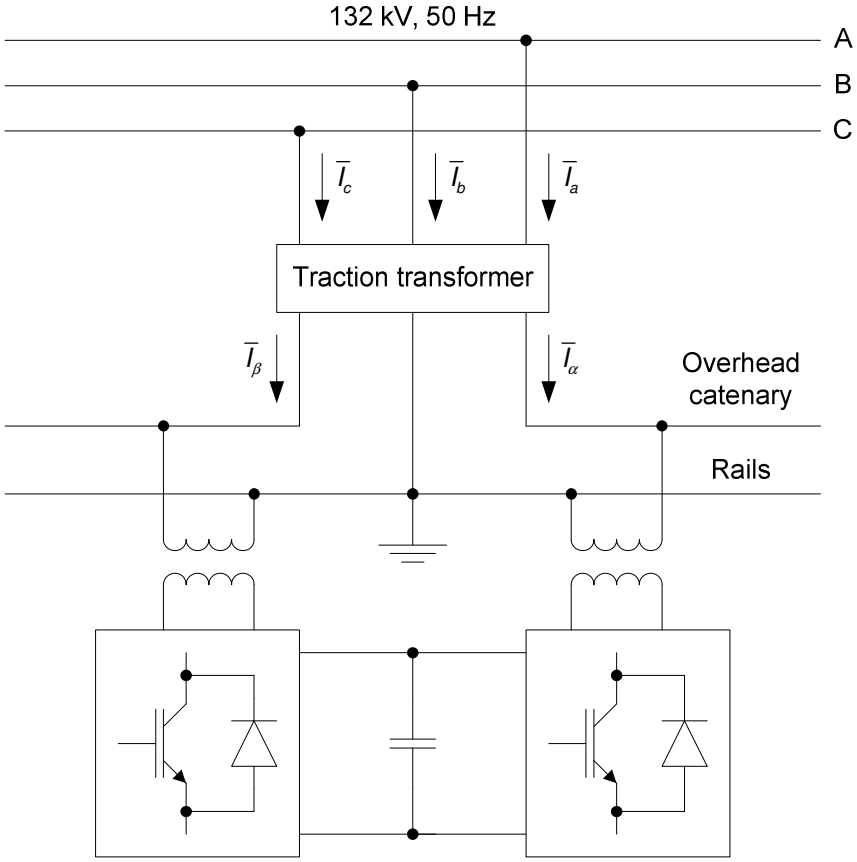

Figure 34: Traction power supply system with RPC

The RPC is connected to two phases of a traction transformer's secondary winding. RPCs can compensate for voltage unbalance, harmonic current and reactive power of traction loads by injecting a controlled current into the traction feeder. The DC link capacitor allows the flow of active and reactive power between the converters and thus in both phases of the traction network. RPCs provide significant voltage unbalance compensation [53]. RPCs can has the ability to completely compensate for voltage unbalance. Another advantage of the RPC is its ability to operate regardless of the traction transformers connection type. The high capacity needed for complete compensation of dynamic traction loads and the high cost of the RPCs compared to other compensation methods will limit the utilization of this method in traction applications. A number of modified compensators based on the RPC have been proposed for further research and development to decrease the overall cost of the system while maintaining the same level of performance of a RPC. A simplified half-bridge RPC has been proposed in [98], which utilizes two half bridge converters coupled by two DC link capacitors. Another modified RPC type of compensator that consist of a three wire, 6 switch converter and a Scott traction transformer, more commonly known as active power quality compensator (APQC) has been proposed in [93]. The proposed APQC connects to the traction system that is supplied

by the Scott transformer. This method of compensation transforms two single-phase orthogonal voltages to three-phase symmetrical voltages. Due to the wide use of V/v transformers in railway applications a similar method that can transform two single-phase non-orthogonal voltages to three-phase symmetrical voltages was required. An improved APQC compensator that operates with a V/v transformer has been proposed in [89].

Co-phase systems are proposed in [103], [104] which utilises a self-balancing transformer in combination with a RPC and can be seen as a modified APQC. A co-phase system reduces the amount of neutral sections in the railway network by half which has various advantages. The remaining neutral sections can be replaced by insulators for safety purposes. The insulation requirements and length of insulators can thus be reduced [104]. Consequently, locomotives do not need to be switched off that often and can be switched off for a smaller duration. Also locomotives do not need to change operation conditions that often and PQ impact will decrease. However, to achieve complete compensation a power converter with a large rating is required leading to a high cost system. Various hybrid co-phase systems have been proposed to achieve the same level of compensation through a power converter with a smaller rating [105]–[107]. Consequently, leading to a system with a decreased overall cost.

An advanced co-phase system are proposed in [108] which is another configuration type of the conventional co-phase system. In the advanced co-phase method the traction system is supplied through a three-phase and single-phase converter rather than a self-balancing transformer. This method of compensation provides the capability of removing all neutral sections in the railway network. The traction loads therefore becomes less dynamic and the need for frequent changes in the operating conditions of locomotives are reduced. The complete railway system is powered through the converters which will lead to high cost and low reliability.

SVCs is a low cost dynamic compensator compared to STATCOMs, active power filters and APQCs.

2.9. CONCLUSION

This chapter presented the reader with background on the working principles of traction loads in South Africa. The dynamic behaviour of traction loads are mathematically described to gain insight into the characteristics of traction loads. The PQ issues associated with traction loads and the possible PQ impact these issues can have on RPPs are investigated. To investigate the impact that poor PQ in traction networks will have on the PQ assessment of RPPs the standards used for PQ management and assessment in South Africa are presented. Finally, a brief overview is given on possible mitigation methods that can be used to reduce poor PQ in traction networks.

CHAPTER 3
SIMULATION MODELS

3.1. INTRODUCTION

Modern AC railway networks are complex in nature as they contain various characteristics, such as dynamic moving loads, single-phase supply and railway earthing, which can have a big impact on the national power supply in terms of PQ. These railway networks are connected to a larger electrical power supply system, in this case Eskom national grid that contains RPPs which further add to the complexity. It is important that the combination of these systems be designed and analysed as accurate as possible to minimise the possibility of future problems. This has come apparent with the introduction of renewables to the national grid and their increased rate of connection. The design, maintenance, management and planning of a power system is a difficult task that requires high accuracy and efficiency. Software tools enable the electrical engineer to analyse and simulate these systems for the optimal solution. In addition, software tools offer the advantage of investigating the network and finding various solutions prior to any physical change to the network infrastructure and is thus essential in network planning.

Various software tools are available for modelling of power systems such as DIgSILENT PowerFactory, Matlab/Simulink and PSCAD. It was deemed necessary that the software tool of choice provide high functionality, capable of simulating large power systems in the time domain. Eskom utilise both PSCAD and DIgSILENT PowerFactory as simulations tools. Most of the original equipment manufacturer time domain models of RPPs have been done in PSCAD as it provides the best functionality for time domain modelling. PSCAD, however, lacks the capability in modelling large power systems. Therefore, the need exist in utilising DIgSILENT PowerFactory for time domain modelling of RPPs as it provides high functionality in large power system modelling. Eskom mostly use DIgSILENT PowerFactory for power system stability simulations and network planning which further highlights the need for accurate RPP and traction load models for future network studies in DIgSILENT PowerFactory. Eskom is continually working on updating and improving there DIgSILENT PowerFactory distribution models. Therefore, DIgSILENT PowerFactory will be used as the PQ analysis software for this thesis.

It is important to understand the functions, limitations and assumptions inherent in software implementation. Therefore, an overview of the functions and limitations of DIgSILENT PowerFactory will be presented. Methods will be investigated to overcome these limitations.

It is known that the accuracy and quality of output of any simulation is directly proportional to the accuracy and quality of the input variables. Typical input variables required for accurate RPP (inverter) and traction (rectifier) system modelling include:

- Power system information such as system configuration and three-phase fault levels.
- Cables, overhead lines and catenary system information and impedance ratings.
- Transformer information such as rating, phase connection impedance and tap settings.
- Train traffic timetable with start, stop, dwell and passing times.
- Locomotive drive ratings such as motor rating, weight, acceleration and maximum speed.
- Turbine passive filter information such as configuration and rating.
- Locomotive passive filter information such as configuration and rating.

At the time of writing limited information was available with regards to locomotive drives and filter equipment ratings. Therefore, various assumptions and simplifications had to be made. To understand the PQ impact of traction loads on the network and on RPPs it is necessary to model locomotive rectifiers in detail, so to investigate various effects that a rectifier can have on the network. In this chapter the theory, control, modelling and implementation of the two main locomotives technologies types identified in Section 2.2 will be presented. Therefore, an active rectifier and half-controlled thyristor rectifier will be designed and implemented in DIgSILENT PowerFactory. It is important that the simulation models reflect the physical system as closely as possible. These traction load models will provide insight on the working principles of traction loads and describe the PQ issues related to traction loads.

RPP manufacturers protect their designs by not disclosing all parameter values and other design detail. Therefore, to completely understand the PQ impact on RPPs it is necessary to model inverters in detail, so to investigate various effects that an inverter can have on the network and vice versa, rather than using the available customer models. In this chapter the modelling of a generic conventional PWM inverter, interleaved PWM inverter and a hysteresis controlled inverter along with their respective implementation in DIgSILENT PowerFactory will be discussed.

The purpose of all these models are to perform time domain simulations to model the dynamic PQ behaviour of traction loads in detail and with a high degree of accuracy. In time domain simulations the voltages and currents are expressed as instantaneous values. Therefore, the individual harmonic content of voltage and current waveforms can be accurately expressed and compared to PQ measurements conducted on the network. The assumptions and simplifications that were required in the design and implementation of generic RPP (inverter) and traction (rectifier) models in DIgSILENT PowerFactory will be discussed.

3.2. OVERVIEW ON DIGSILENT POWERFACTORY

DIgSILENT GmbH, is a German software and consulting company that provides a wide variety of electrical engineering services in the field of power systems. They develop DIgSILENT PowerFactory, a Windows-based integrated analysis software package for power system simulation in industrial plants, generation, transmission, distribution and smart grids. Eskom Distribution has obtained a corporate licence for DIgSILENT PowerFactory in 2003 after a comprehensive evaluation of all the technical operations offered [109]. DIgSILENT PowerFactory caters for the full range of standard power system analysis needs to vastly refined applications in modern technologies such as wind power, performance monitoring for system testing and real-time system simulation [110], [111]. PowerFactory is easy to use with advanced solution algorithms combined with comprehensive and flexible modelling capabilities that include a large suite of libraries and electrical power equipment models. Users are able to design and create dynamic models for time domain simulations. Therefore, providing the user with the required tools to undertake a grid impact analysis on wind farms and solar PV plants to determine their PQ impact on the grid and vice versa. Consequently, DIgSILENT PowerFactory has become the industry standard in utility and RPP simulations in South Africa as most RPPs are connected to the Eskom distribution network.

DIgSILENT PowerFactory is capable of performing balanced and unbalanced power flow studies, protection coordination of relays, short circuit analysis, long-term quasi dynamic load flow simulations, etc. Some of the functions more relevant to PQ studies include [111]:

- Harmonic analysis which includes harmonic load flow, frequency sweep, flicker calculation and harmonic distortion analysis.
- Balanced and unbalanced stability analysis in RMS or EMT dynamic simulations.
- Dynamic simulation language (DSL) modelling of dynamic models.
- The ability to model any combination of single-phase AC, three-phase AC and DC network topologies, which will be important to model single-phase traction loads.

DIgSILENT PowerFactory also support scripting features that include the complete integration of the built-in C++ style DIgSILENT programming language and open source Python programming languages. Scripting is generally used to access objects and to automate tasks which require the execution of time-consuming simulations e.g. short circuit sweep [112], [113]. However, the application can be used for far more than that such as inserting external parameter characteristics from a comma-separated values format file, processing results, exporting results and plots to excel, changing parameter values within the code, etc.

3.2.1. DIgSILENT PowerFactory limitations

DIgSILENT PowerFactory is not designed for simulating and analysing railway networks but rather for analysing general power systems. The traction network of a railway system is simulated and analysed as an electrical power system rather than a detailed locomotive rolling stock model. Therefore, DIgSILENT PowerFactory lacks the capability to model and simulate moving AC traction loads along a railway network. Consequently, challenges exist in simulating dynamic models of traction loads in the time domain. Moving DC traction loads in DIgSILENT PowerFactory has been simulated in [114] and a similar approach could be implemented for AC traction systems. The modelling and implementation of moving dynamic models, however, is out of the scope of this thesis.

DIgSILENT PowerFactory does not contain a built-in model for a half-controlled thyristor rectifier and thus a method had to be explored to obtain the required functionality of a half-controlled thyristor rectifier. This challenge is further increased by a lack in DIgSILENT PowerFactory to simulate the combination of an AC and DC system. A method to overcome these limitations is presented in Section 3.5.2.

3.2.2. RMS and EMT simulations

It was already stated that the models need to be analysed in time domain and that DIgSILENT PowerFactory provide the user with two dynamic simulation functions: RMS, which are used for three-phase networks under steady state conditions for mid- to long-term transient analysis and EMT, which are used for three-phase dynamic networks for short-term electromechanical and electromagnetic transient analysis [115].

In RMS simulations the voltages and currents are expressed as phasors in frequency-domain. Therefore, the voltage and current equations are represented as follows [116]:

$$\bar{V} = jwL\bar{I} \text{ and } \bar{I} = jwC\bar{V} \tag{2.32}$$

In EMT simulations the voltages and currents are expressed by their instantaneous values in time-domain. Therefore, the voltage and current equations are represented by differential equations as follows [116]:

$$v = L\frac{di}{dt} \text{ and } i = C\frac{dv}{dt} \tag{2.33}$$

EMT simulation present a closer representation of the physical world due to the simulation domain. Furthermore, in EMT simulations the network dynamics and events can be simulated with a greater degree of accuracy in both short-term transient analysis as well as with longer-term transient analysis. Trains move past substations and renewable plants at a high speed, therefore, making the measured data at the site inaccurate due to aggregated 10-minute

values based on frequency-domain rms values. Therefore, it is important to analyse the short-term effect of traction loads on RPPs as the impact of traction loads will be instantaneous thus making EMT simulations preferable. However, it must be stated that due to the increase in dynamic simulation of all passive network elements that the simulation time will be increased significantly [115].

3.3. DIGSILENT POWERFACTORY BUILT-IN MODELS

It was already stated that DIgSILENT PowerFactory provides a global library with a wide range of components that includes predefined built-in equipment models. In addition, DIgSILENT PowerFactory provide the user with the possibility to design and construct mathematical and graphical composite models through DSL by using the available predefined equipment models as well as user defined common models. These user defined composite and common models can be connected to network elements. In this section the relevant predefined built-in equipment models that were implemented in the models and do not need to be designed using DSL will be discussed in more detail.

3.3.1. PWM converter model

The built-in PWM converter model (ElmVsc) is used to model rectifiers and inverters within DIgSILENT PowerFactory. In EMT simulation the built-in PWM converter can be modelled and controlled in two different ways: as a controlled voltage source or a detailed model. For the controlled voltage source model the PWM converter is represented by a self-commutated three-phase voltage source converter (VSC) as shown in Figure 35. Note, however, that for the controlled voltage source model the three-phase VSC in Figure 35 does not contain actual switches. A DC link capacitor is not included within the PWM converter model and has to be added externally.

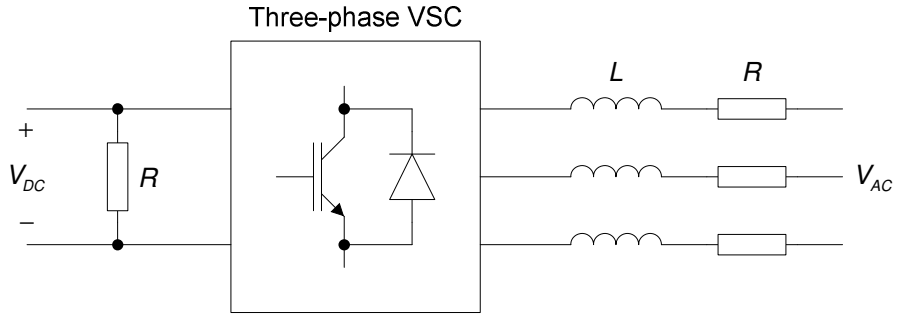

Figure 35: PWM converter model with series reactance, no-load losses and load losses

For the detailed model the three-phase VSC in Figure 35 is represented by a three-phase detailed VSC composed out of IGBT switches and is similar to the three-phase VSI equivalent diagram as seen in Figure 19. Note that the external DC link capacitor and DC voltage source in Figure 19 is not included in the detailed PWM converter model and must be added externally.

3.3.1.1. Modelling of PWM inverter losses

A grid-connected PWM inverter is connected to the grid through a reactance, therefore, the AC series reactance is included within the built-in PWM converter model to simplify modelling. Both no-load and load losses models are included in the PWM converter model. No-load or switching losses are represented and modelled by a shunt resistance between the DC terminals. Furthermore, load losses are represented and modelled as a series resistance on the AC side. Refer to Figure 35 for the equivalent circuit of the built-in DIgSILENT Powerfactory PWM converter model with series reactance and losses represented.

3.3.1.2. Load flow control conditions of PWM converter

The load flow analyses results of the PWM converter depend on the chosen control condition. DIgSILENT PowerFactory provide various control conditions that are supported by the PWM converter. The description and general application of each condition are defined below [47]:

- V_{AC} - *phi* : The AC terminal magnitude and phase are specified. This is generally used with motor-side converters in variable speed drives.
- V_{DC} - *phi* : The magnitude of DC voltage and phase of AC terminals are specified. There is no typical application for this condition.
- *PWM* - *phi* : This condition provide no control as the magnitude and phase of the amplitude modulation factor are directly set.
- V_{DC} - *Q* : The magnitude of the DC voltage and reactive power output are set. This control condition result in various common application such as STATCOM and a VSC for high voltage direct current (HVDC) applications.
- *P* - V_{AC} : The magnitude of the AC voltage terminals and active power output are set. This control condition result in common applications such as grid-side converter of converter driven synchronous machines and VSC-HVDC.
- *P* - *Q* : The active power and reactive power output is set at the AC output. Similar typical applications as described in the *P* - V_{AC} control condition.
- V_{DC} - V_{AC} : The magnitude of DC voltage and AC voltage. Similar typical applications as described in the V_{DC} - *Q* control condition.
- *P* - cos(*phi*) : The active power at AC output and power factor are specified. Typical application with PWM grid-connected converters for renewables.
- V_{DC} - cos(*phi*) : The magnitude of DV voltage and power factor are specified. Typical applications include VSC-HVDC and renewable implementations.

3.3.1.3. RMS and EMT control of PWM converter – controlled voltage source model

For the controlled voltage source model, at fundamental frequency, the ideal PWM converter is modelled as a DC controlled AC voltage source and the following voltage equations are applicable to the PWM converter when operating within the linear region ($P_m \leq 1$) [118]:

$$\begin{aligned} V_{AC,r} &= K_0 \bullet P_{mr} \bullet V_{DC} \\ V_{AC,i} &= K_0 \bullet P_{mi} \bullet V_{DC} \end{aligned} \tag{2.34}$$

where, $V_{AC,r}$ and $V_{AC,i}$ represent the real and imaginary RMS values of the AC voltage, V_{DC} the DC voltage, P_{mr} and P_{mi} the real and imaginary values of the amplitude modulation index and K_0 a constant gain depending on the ratio between the DC and AC voltage as well as the type of modulation used. The PWM converter model supports both sinusoidal modulation for a sinusoidal PWM inverter as well as rectangular modulation for a square wave inverter [118]. For a sinusoidal PWM inverter, K_0 is:

$$K_0 = \frac{\sqrt{3}}{2\sqrt{2}} \tag{2.35}$$

For the controlled voltage source model, the PWM amplitude modulation index $\bar{P}_m$ (magnitude and phase), in RMS and EMT simulations, can be controlled through different input signals, depending on the type of application [118]:

- P_{mr} and P_{mi}: In this method, the real and imaginary values of the PWM amplitude modulation index are used as inputs. The reference frame for this method is the global reference frame. Therefore, the PWM controller inputs must be used in combination with reference frame transformations in addition to phase measurement devices such as phase-locked loop (PLL) to measure *cosref* and *sinref* for accurate transformations.
- P_{md}, P_{mq}, *cosref* and *sinref*: $\bar{P}_m$ is defined in a reference frame specified by *cosref* and *sinref*. This method can typically be used for grid-connected applications where the system is implemented in the dq reference frame in combination with a PLL.
- $i_{d,ref}$, $i_{q,ref}$, *cosref* and *sinref*: The reference d- and q-axis current values can be used as inputs to the PWM converter when the internal current controller of the PWM converter model is used. The current input variables are defined in a reference frame specified by *cosref* and *sinref*.
- $P_{m,in}$ and d_{phiu}: The magnitude and phase of $\bar{P}_m$ are used as inputs. This method is essentially equivalent to the P_{mr} and P_{mi} method.

- $P_{m,in}$ and f_0 : Here the magnitude of $\bar{P}_m$ and frequency of output signals can be specified.

The controlled voltage source model contain an optional internal current controller. The internal current controller is the simplest implementation of a current controller. The input currents i_d and i_q are simply the output AC currents of the PWM controller defined in a reference frame specified by *cosref* and *sinref*. Therefore, the output signals P_{md} and P_{mq}, which are also defined in the same reference frame, are transformed back to the global reference frame within the controller by using *cosref* and *sinref*. The additional input current signals, $i_{d,ref}$ and $i_{q,ref}$, are found through an active and reactive controller. Refer to Figure 36 for the block diagram of the internal current controller.

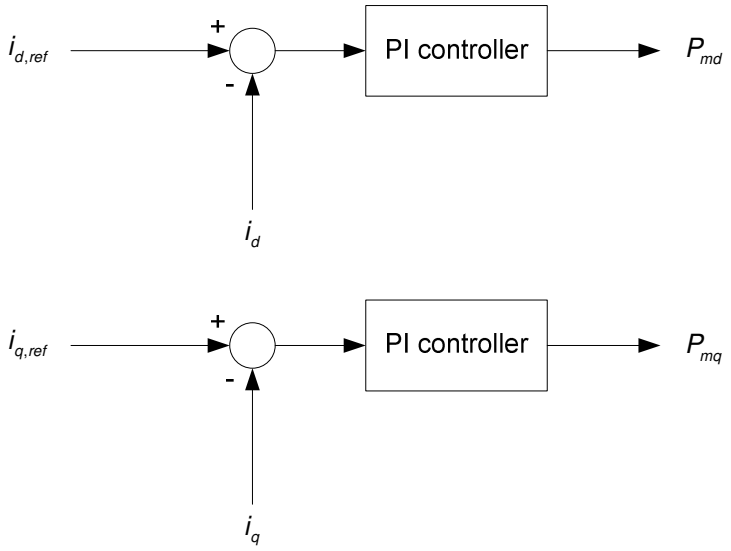

Figure 36: Block diagram of the built-in current controller in the PWM controller model

The controlled voltage source model can also be controlled through an external current controller and will be discussed in more detail where relevant. Losses can be added to the controlled voltage source model according to Section 3.3.1.1.

3.3.1.4. RMS and EMT control of PWM converter – detailed model

For the detailed model, the PWM converter is represented by a three-phase detailed VSC composed out of IGBT switches and is, therefore, similar to the three-phase VSI equivalent diagram as seen in Figure 19. The switching states u_a , u_b and u_c of the detailed PWM model can be externally controlled through a DSL model. These signals control the on/off states of the three-phase legs. A positive signal for u_a , u_b and u_c will connect the respective phase to the positive DC voltage V_{DC} and vice versa. It is important to note that the internal current

controller is not available for this approach, therefore, an external current controller must be designed and implemented with DSL.

3.3.1.5. PWM converter model limitations

The DIgSILENT PowerFactory PWM controller is a three-phase model, therefore, challenges exist in single-phase applications such as the control of single-phase active rectifiers. A method had to be investigated to overcome this limitation by controlling each phase separately. The implementation of the solution will be discussed in more detail in Section 3.5.1.

3.3.2. AC and DC cables

The AC overhead lines can all be defined as either short-length or medium-length lines as all of the relevant lines in the network are no longer than 240 km. Short-length and medium-length lines can be modelled using lumped parameters with a small effect on the accuracy of simulation as shown in [119]. The AC cable parameters are obtained from the Wind farm A original equipment manufacturer model of the renewable plant.

3.3.3. Built-in PLL model

DIgSILENT PowerFactory contain a built-in PLL DSL model that is supported for both RMS and EMT simulations within DIgSILENT PowerFactory. The PLL element (ElmPhi__pll) is used to measure the frequency and phase of the system voltage and then to output *cosphi* and *sinphi* as output signals to the rest of the control system.

3.3.4. Built-in sample and hold element

DIgSILENT PowerFactory contain a built-in sample and hold element (ElmSamp) that is supported for both RMS and EMT simulations within DIgSILENT PowerFactory. The sample and hold element is used to sample an analog signal for digital control purposes. The input analog signal is sampled at every rising edge of the clock pulse input signal and is held constant up to the next rising edge. Therefore, ElmSamp can be setup for symmetrical or asymmetrical regular sampling as described in Section 2.4.4.2 by controlling the clock pulse input signal.

3.3.5. Built-in voltage measurement element

DIgSILENT PowerFactory contain a built-in voltage measurement element (StaVmea) that is supported for both RMS and EMT simulations within DIgSILENT PowerFactory. The voltage measurement element can be used to measure AC or DC voltage at any selected terminal. The number of phases (three-phase or single-phase) for an AC measurement can be selected along with the voltage rating and frequency output. The measured voltage can then be fed as

a signal to the rest of the control system. The measured voltage are transformed into a fixed two-axis reference frame (αβ reference frame). Therefore, the following StaVmea output signals can be used in a control system during EMT simulations: real voltage (*ur*), imaginary voltage (*ui*), voltage magnitude (*u*), zero sequence voltage (*u*0) and the frequency (*fe*).

3.3.6. Built-in current measurement element

DIgSILENT PowerFactory contain a built-in current measurement element (StaImea) that is supported for both RMS and EMT simulations within DIgSILENT PowerFactory. The current measurement element can be used to measure AC or DC current at any selected cubicle of an element connected to a terminal. The number of phases (three-phase or single-phase) and current rating can be selected for an AC measurement. The measured current can then be fed as a signal to the rest of the control system. The measured voltage are transformed into a fixed two-axis reference frame (αβ reference frame). Therefore, the following StaImea output signals can be used in a control system during EMT simulations: real current (*ir*), imaginary current (*ii*), current magnitude (*i*) and zero sequence current (*u*0).

3.3.7. Built-in power measurement element

DIgSILENT PowerFactory contain a built-in power measurement element (StaPqmea) that is supported for both RMS and EMT simulations within DIgSILENT PowerFactory. The power measurement element can be used to measure the power flow of any element connected to a terminal. The number of phases (three-phase or single-phase), power rating and orientation can be selected. For EMT simulations the power measurement element will measure the phase voltages and currents and output the real power (*p*) and reactive power (*q*) as output signals to the control system.

3.4. CONTROL OF CONVERTER - POWER FLOW THEORY

An active rectifier is basically an inverter connected to a network through a series inductor. The control of an active rectifier or inverter has been described in various papers [120], [121]. A grid-connected inverter with a series reactance can be illustrated by two voltage sources and a pure inductance as seen in Figure 37 to derive the required power flow equations. The direction of the current $\overline{I}$ determine whether the converter is operating as an inverter or as a rectifier.

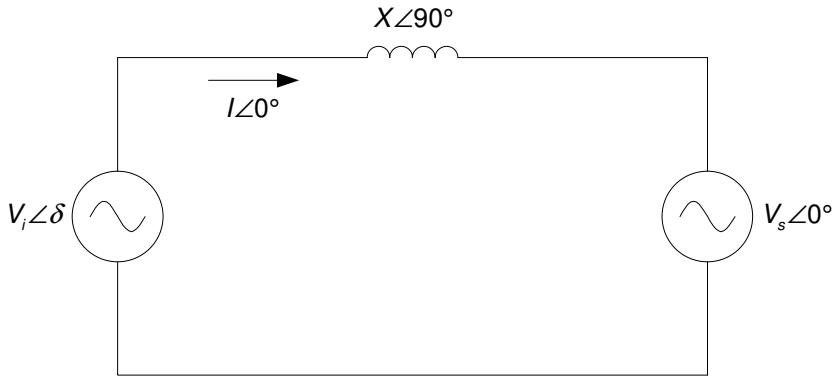

Figure 37: Power flow between two voltage sources

The inverter mode of operation is described below. The current flowing from an inverter $\overline{I}$ acting as voltage source $\overline{V_i}$ to the grid represented by $\overline{V_s}$ through the filter inductive reactance $\overline{X}$ can be calculated as follows:

$$\begin{aligned}\overline{I} &= \frac{\overline{V_i} - \overline{V_s}}{\overline{X}} = \frac{V_i\angle\delta - V_s\angle 0°}{X\angle 90°} \\ &= \frac{V_i}{X}\angle(\delta - 90°) - \frac{V_s}{X}\angle -90°\end{aligned} \tag{2.36}$$

The apparent power flowing from the inverter side $\overline{S_i}$ can be calculated as follows:

$$\begin{aligned}\overline{S_i} &= \overline{V_i}\,\overline{I}^{*} = V_i\angle\delta\left(\frac{V_i}{X}\angle(90° - \delta) - \frac{V_s}{X}\angle 90°\right) \\ &= \frac{V_i^2}{X}\angle 90° - \frac{V_iV_s}{X}\angle(90° + \delta)\end{aligned} \tag{2.37}$$

Per definition the real power at the inverter P_i can be calculated as follows:

$$\begin{aligned}P_i &= S_i\cos\phi = \frac{V_i^2}{X}\cos 90° - \frac{V_iV_s}{X}\cos(90° + \delta) \\ &= \frac{V_iV_s}{X}\sin(\delta)\end{aligned} \tag{2.38}$$

The reactive power at the inverter Q_i can be calculated as follows:

$$\begin{aligned}Q_i &= S_i\sin\phi = \frac{V_i^2}{X}\sin 90° - \frac{V_iV_s}{X}\sin(90° + \delta) \\ &= \frac{V_i^2}{X} - \frac{V_iV_s}{X}\cos(\delta)\end{aligned} \tag{2.39}$$

The apparent power flowing into the network $\overline{S_s}$ can be calculated as follows:

$$\begin{aligned}\overline{S_s} &= \overline{V_s}\left(-\overline{I}^*\right) = V_s\angle 0°\left(-\frac{V_i}{X}\angle(90° - \delta) + \frac{V_s}{X}\angle 90°\right) \\ &= -\frac{V_s V_i}{X}\angle(90° - \delta) + \frac{V_s^2}{X}\angle(90°)\end{aligned} \tag{2.40}$$

Per definition the real power flowing into the source P_s can be calculated as follows:

$$\begin{aligned}P_s &= S_s\cos\phi = -\frac{V_s V_i}{X}\cos(90° - \delta) + \frac{V_s^2}{X}\cos(90°) \\ &= -\frac{V_i V_s}{X}\sin(-\delta) + 0 = \frac{V_i V_s}{X}\sin\delta\end{aligned} \tag{2.41}$$

The reactive flowing into the source Q_s can be calculated as follows:

$$\begin{aligned}Q_s &= S_s\sin\phi = -\frac{V_s V_i}{X}\sin(90° - \delta) + \frac{V_s^2}{X}\sin(90°) \\ &= \frac{V_s^2}{X} - \frac{V_i V_s}{X}\cos(\delta)\end{aligned} \tag{2.42}$$

To inject power at unity power factor into the source the current should have the same angle as the voltage at the source. To illustrate this graphically, Figure 38 shows a scaled phasor diagram of a single-phase system in inverter mode of operation.

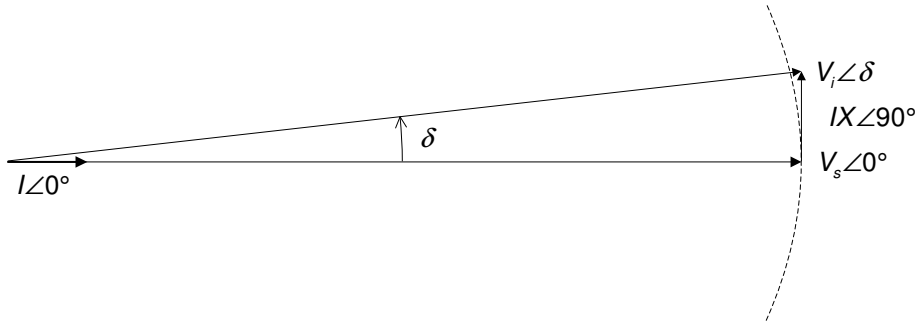

Figure 38: Voltage and current phasor diagram for inverter mode of operation

Figure 39 shows a scaled phasor diagram of a single-phase system in rectifier mode of operation.

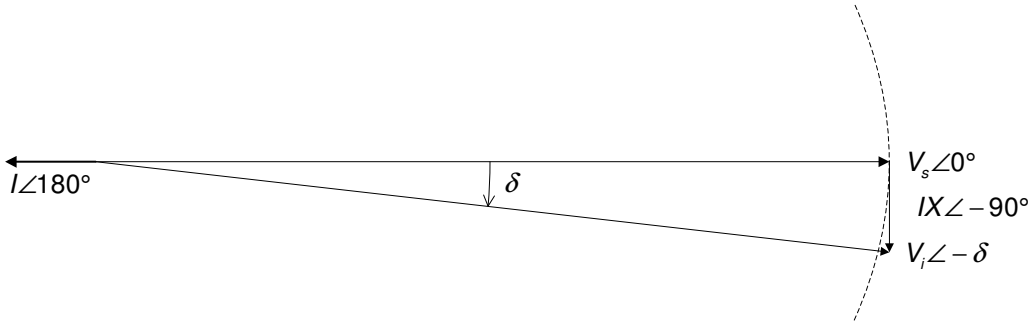

Figure 39: Voltage and current phasor diagram for rectifier mode of operation

The inverter voltage exceeds the grid voltage to produce the reactive power consumed by the reactance when transferring the required active power. The power factor can be controlled at unity by ensuring that all reactive power is consumed in the reactance and that the reactive power consumed at the grid is zero. The inverter voltage vector $\overline{V_i}$ magnitude and phase angle values for unity power factor at the grid interface are subsequently calculated.

By setting $\overline{I} = I\angle 0°$ in (2.36):

$$\begin{aligned} \overline{I} &= \frac{V_i}{X}\angle(\delta - 90°) - \frac{V_s}{X}\angle -90° = I\angle 0° \\ \Rightarrow & \frac{V_i\cos\delta - V_s}{X} = 0 \\ \Rightarrow & V_i = \frac{V_s}{\cos\delta} \end{aligned} \tag{2.43}$$

The value of δ for a required P_s can be calculated from (2.41):

$$\begin{aligned} P_s &= \frac{V_i V_s}{X}\sin\delta \\ &= \frac{V_s^2\sin\delta}{X\cos\delta} = \frac{V_s^2}{X}\tan\delta \\ \Rightarrow & \delta = \arctan\left(\frac{P_s X}{V_s^2}\right) \end{aligned} \tag{2.44}$$

Now the value of V_i can be calculated from (2.43):

$$V_i = \frac{V_s}{\cos\left(\arctan\left(\frac{P_s X}{V_s^2}\right)\right)} \tag{2.45}$$

The above power theory equations can also be used to model an active rectifier by changing direction of current flow and in turn changing δ to a negative value as illustrated in Figure 39 for rectifier mode of operation.

3.5. TRACTION LOAD (RECTIFIER) MODELLING

The aim of the modelling is to control the rectifier so that the rectifier is supplying power to the traction motors but in turn injecting harmonic currents into the grid. This will provide a method to study the effects of traction on the PQ under various supply conditions.

3.5.1. DIgSILENT PowerFactory active rectifier model

3.5.1.1. Overview

Locomotives on the 25 kV AC traction systems use single-phase active rectifiers to convert power to DC. Three-phase inverters in the form of variable speed drives use the DC to control AC motors on the axes of the locomotives. On the AC side the 25 kV voltage is converted to 1.5 kV by means of a single-phase transformer located in the locomotive. The DC bus between the rectifier and the drive has a nominal voltage of 3 kV. The rectifier has a nominal power rating of 12 MW (based on the actual maximum demand of the locomotives that are in service on the network), therefore, P_s is selected as -12 MW, i.e. nominal current I of -8 kA. A 50 Hz filter reactance of 15% short circuit impedance was arbitrary selected, i.e. an inductance of 0.09 mH. By using these values in (2.38), (2.39) and (2.42) the relationship between power and phase angle is plotted in Figure 40.

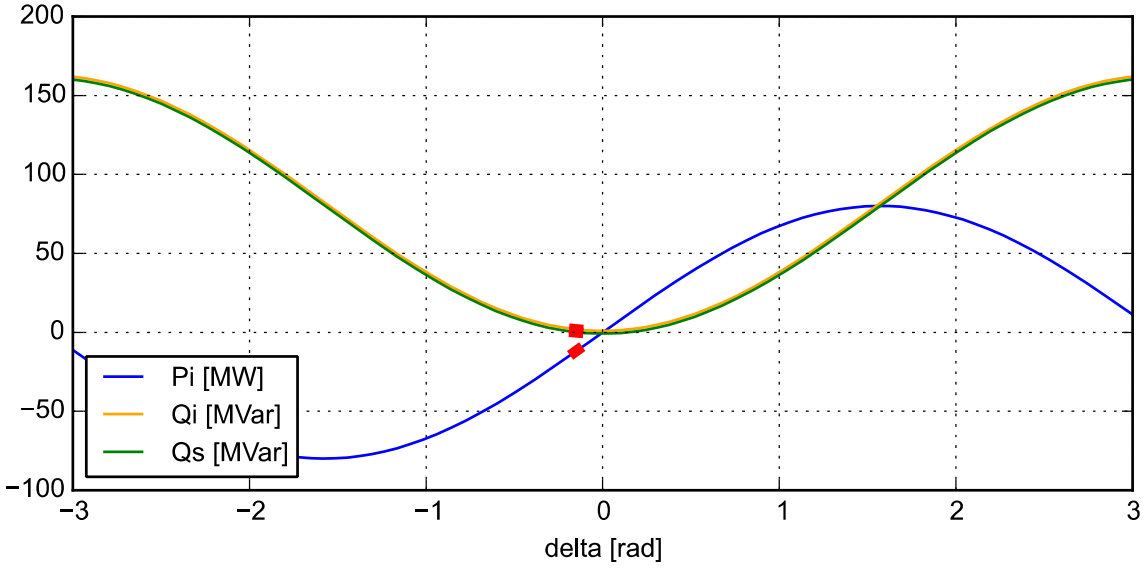

Figure 40: Active and reactive power magnitude as a function of δ

Figure 40 is further exposed around the operating point of this inverter and is shown in Figure 41. This is around the operating point (highlighted section) of $\delta = -0.1489\,\text{rad}$, from (2.44), where the inverter power $P_s = -12\,\text{MW}$. The negative power indicates that it is operating as an active rectifier. The inverter voltage is set to 1.5168 kV, calculated from (2.45) to generate the required reactive power ($Q_i = 1.8\,\text{MVAR}$) so that the reactive power at the source side can

be zero. Although power flows from the grid to the inverter, reactive power is still generated by the inverter as long as the inverter can generate a voltage magnitude that exceeds the grid voltage, i.e. it has a high enough DC voltage.

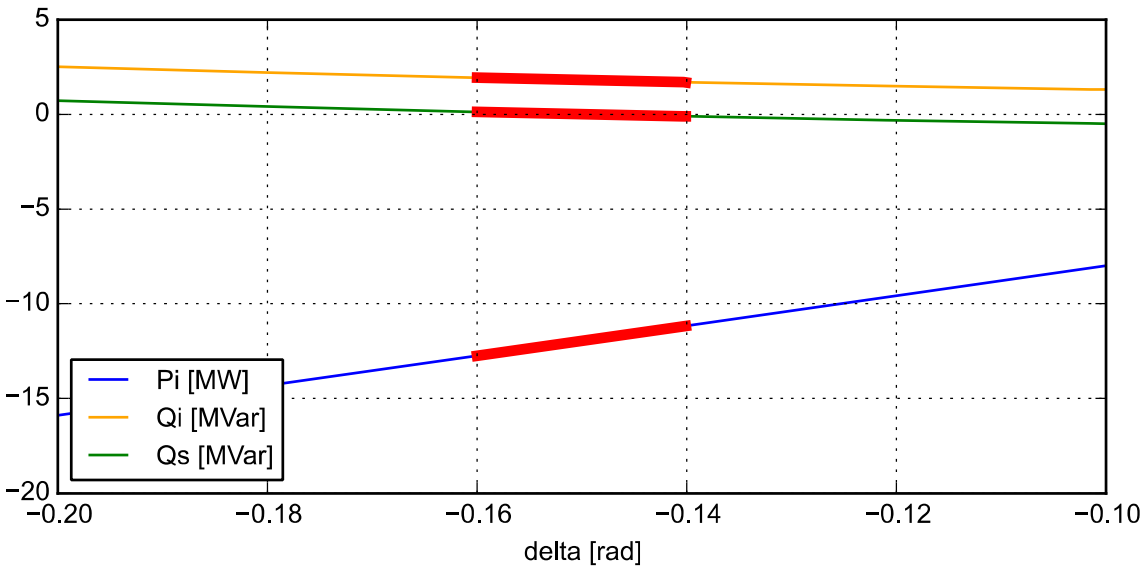

Figure 41: Active and reactive power magnitude as a function of δ around operating point of $\delta = -0.1489$ rad

Figure 42 shows the designed control layout of a single-phase active rectifier.

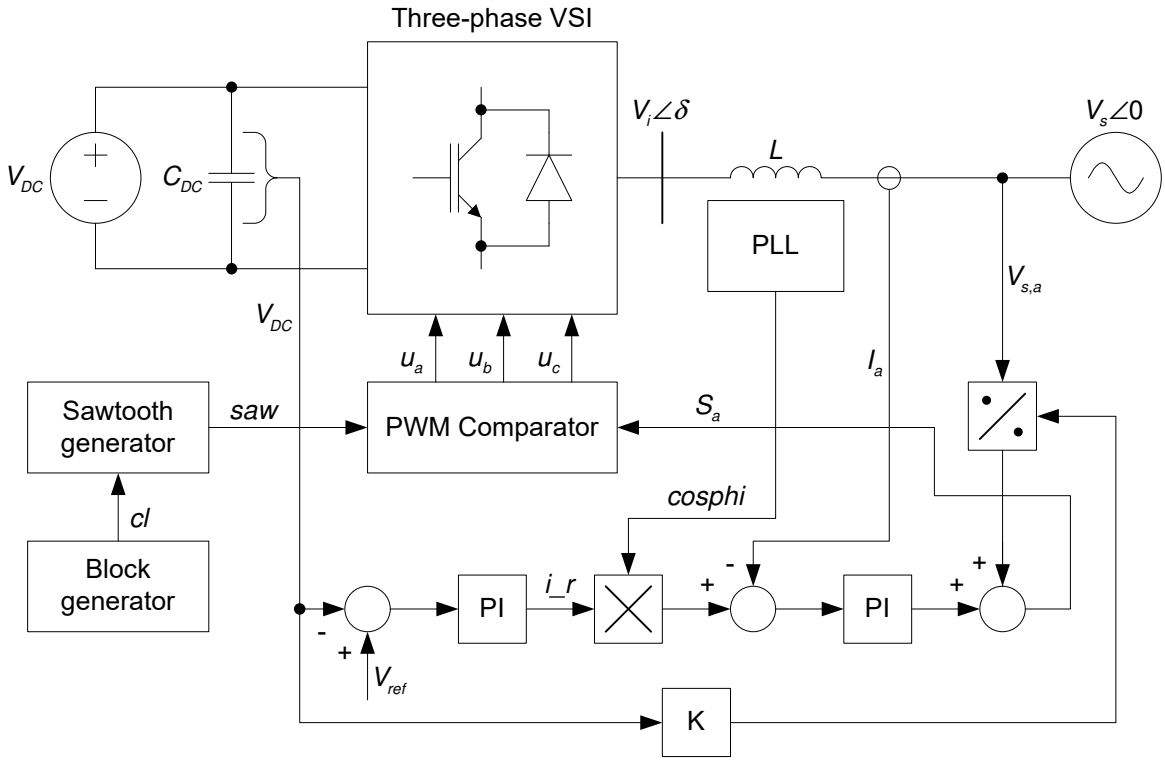

Figure 42: Designed control layout of a single-phase active rectifier

Basic functionality can be shown in the time domain using the DIgSILENT PowerFactory EMT tool.

3.5.1.2. Element layout in DIgSILENT PowerFactory

Figure 43 shows the network diagram of the system. Both the AC and DC sides are modelled by simple voltage sources. The network further consist of a single-phase 132/25 kV traction transformer, single-phase 25/1.5 kV locomotive transformer, an AC LC filter and DC capacitor. Refer to Figure 174 in the appendix for a photo of the traction transformer nameplate. The power that flows between these sources is a function of the selected phase angle.

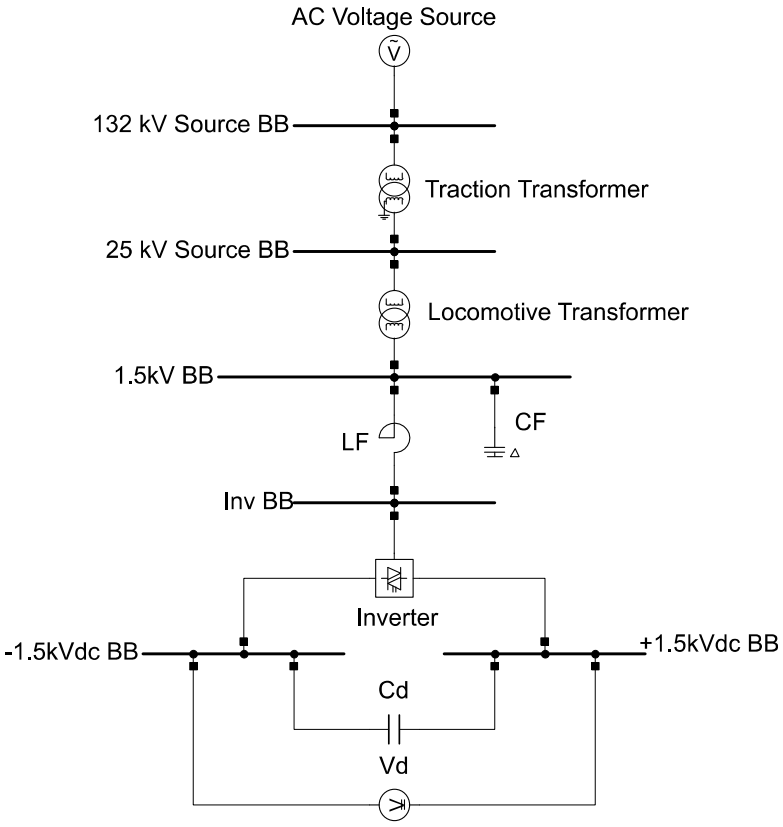

Figure 43: Network diagram of the single-phase active rectifier traction system

3.5.1.3. Composite model in DIgSILENT PowerFactory

Figure 44 shows the designed composite model of the active rectifier system consisting of a voltage measurement slot, a current controller, voltage controller, sample and hold element and the inverter.

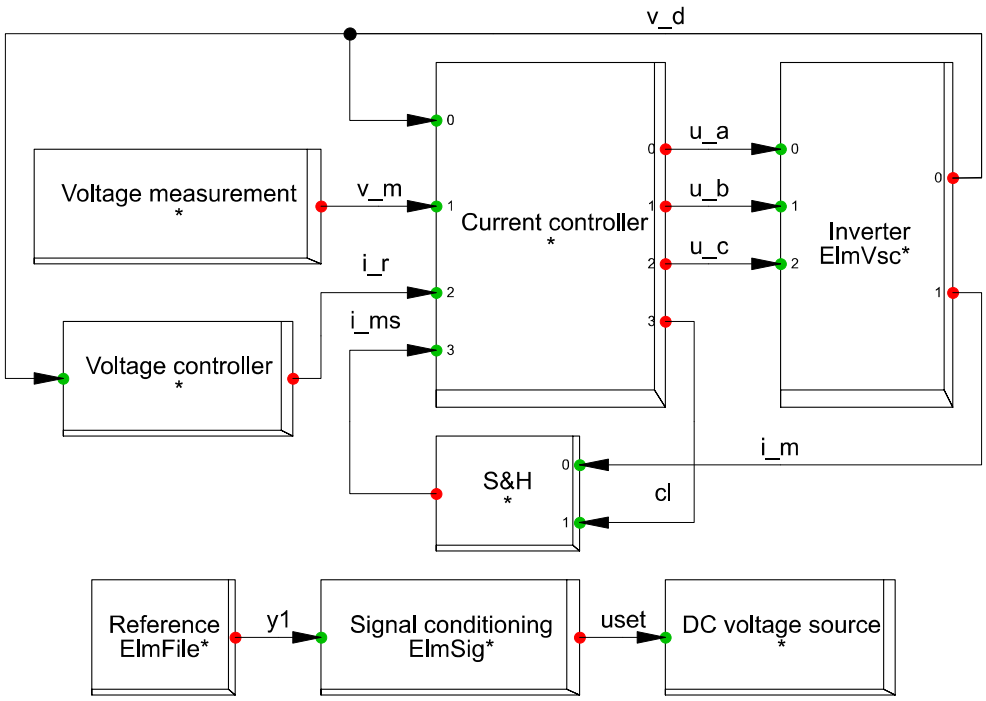

Figure 44: Designed composite model of the single-phase active rectifier in PowerFactory

The built-in PWM converter model (ElmVsc) discussed in Section 3.3.1 is used as the inverter model in the implementation. The detailed model of the PWM converter, as discussed in Section 3.3.1.4, is implemented due to the fact that the PWM converter lack the capability for single-phase control. Therefore, the internal current controller of the PWM model is not available for implementation in the single-phase active rectifier application and an external current controller had to be designed and implemented. The current controller and voltage controller is designed using DSL common models. The initialisation of these DSL models can be challenging due to stability issues. Therefore, the initial conditions need to be set up with great care to accurately evaluate the performance of the designed system during transient and steady state conditions.

The current controller generates pulse width modulated signals to drive the inverter. For optimal dynamic response, an inverter normally has an inner current control loop that follows a reference in phase with the grid voltage waveform. The current controller will be discussed in more detail in Section 3.5.1.5. A voltage vector on the rectifier AC terminals is synthesized by generating pulse width modulated signals at a switching frequency f_s. Note that the switching frequency is unknown and will thus be chosen by examining the frequency spectrum of the measured phase current in a traction substation which is shown Section 6.6.2. The voltage measurement element in Figure 44 measures the grid voltage, with the predefined built-in PLL model (ElmPhi__pll) discussed in Section 3.3.3, as a per unit value which is fed as a signal to the current controller. The measured AC current in kA is sampled twice per switching cycle, i.e. using asymmetrically regular sampling, and is then fed to the input of the current

controller. Asymmetrical regular sampling is done using the predefined built-in sample and hold element (ElmSamp) discussed in Section 3.3.4. The reference block can be used to import an external data file to change the nominal DC voltage in time domain to investigate the impact of the DC voltage on the control and harmonics.

3.5.1.4. DSL model of voltage controller in DIgSILENT PowerFactory

The designed voltage controller in Figure 45 receives the measured DC voltage signal as a per unit value and compare it to a reference voltage of 1 per unit. The per unit error is then scaled to a voltage value by multiplying the error with the nominal DC voltage of 3 kV. A reference current signal is then obtained by multiplying the error with a proportional integral (PI) controller.

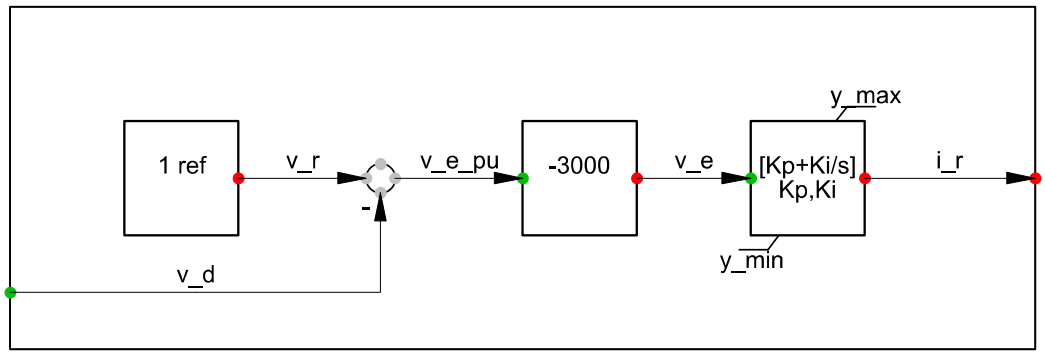

Figure 45: Designed active rectifier voltage controller DSL model in DIgSILENT PowerFactory

3.5.1.5. DSL model of current controller in DIgSILENT PowerFactory

The complexity of the current controller was prevented by only considering steady state operation. The current controller have the following input signals: the measured DC voltage in per unit, the measured AC grid voltage in per unit, a reference current and the measured sampled AC current in kA. The designed current controller shown in Figure 46 scales the measured grid voltage signal (v_m) in per unit to a signal with a voltage value (v_ac) by multiplying it with 2121 which is the peak value of the 1.5 kV AC grid voltage. The next step is to scale it to a value opposite to the gain of the inverter or $\frac{2121}{3000}$. The sampled measured AC current signal (i_ms) is multiplied by 1000 to scale the kA signal to an A signal (i_m). The current controller multiplies the measured per unit grid voltage (v_m) with the reference current (i_r) and compares this to i_m. A block wave generator generate a clock pulse signal (dir) that changes from 1 to -1 and vice versa every half of a switching period. The signal dir is, therefore, used as the input clock pulse signal for the sampling of the measured AC current within the sample and hold block in Figure 44. The saw tooth generator with a period T with a value of

$\frac{1}{(4\times f_s)}$ generates a triangular waveform (saw) with a frequency (f_s). By comparing the reference signal s to the triangle waveform signal saw, the pulse width modulated signals are generated for phases A and B, i.e. u_a and u_b. A positive signal switches on the top switch in a phase leg, while a zero signal switches on the bottom switch. Only two phases of the three-phase PWM inverter model is used and u_c is consequently kept at 0 V.

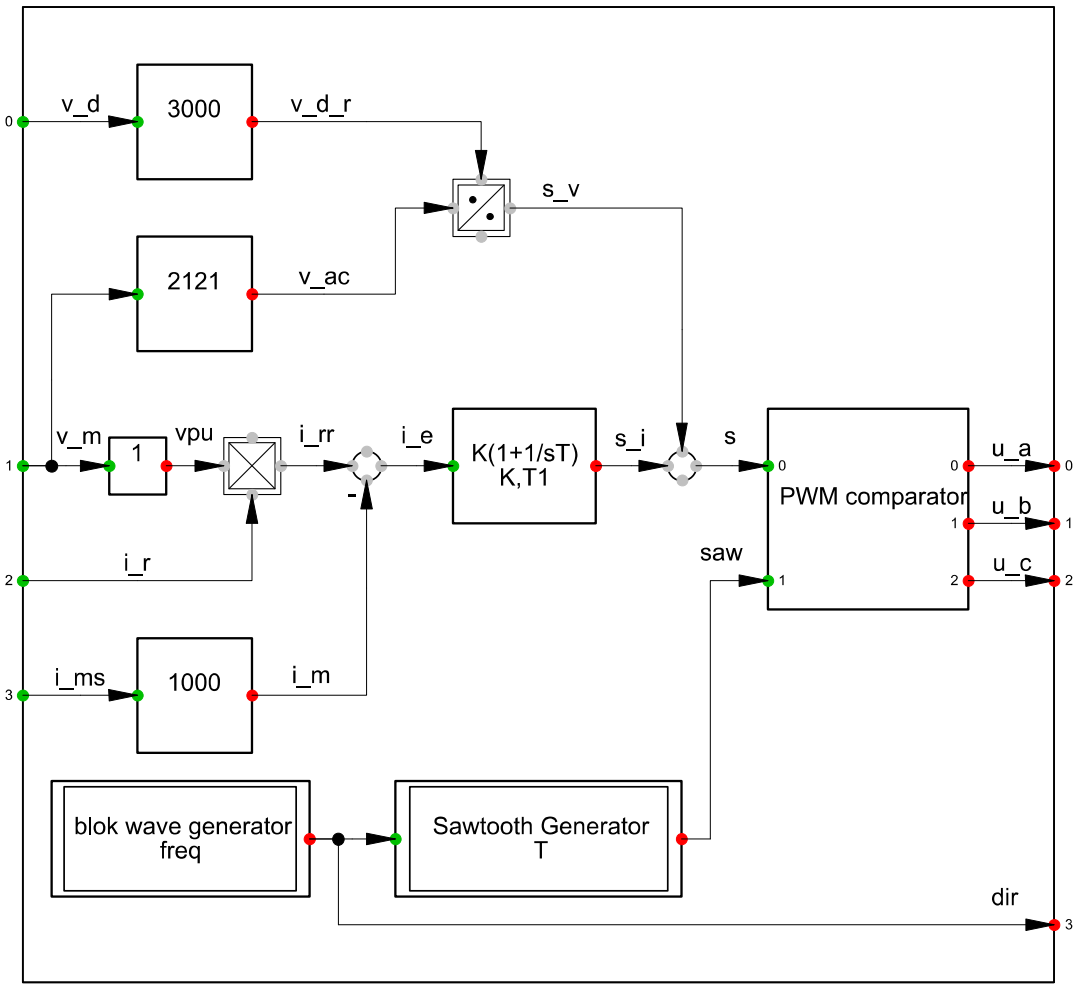

Figure 46: Designed active rectifier current controller DSL model in DIgSILENT PowerFactory

3.5.1.6. Working principle of an active rectifier in DIgSILENT PowerFactory

To illustrate the working principle of the active rectifier the switching frequency f_s is chosen as 5 kHz and thus the period T of the sawtooth generator is equal to 0.00005. Figure 47 shows the reference signal (s) which is compared to the generated triangular signal (saw) to generate the phase A leg switching state (u_a) in Figure 48.

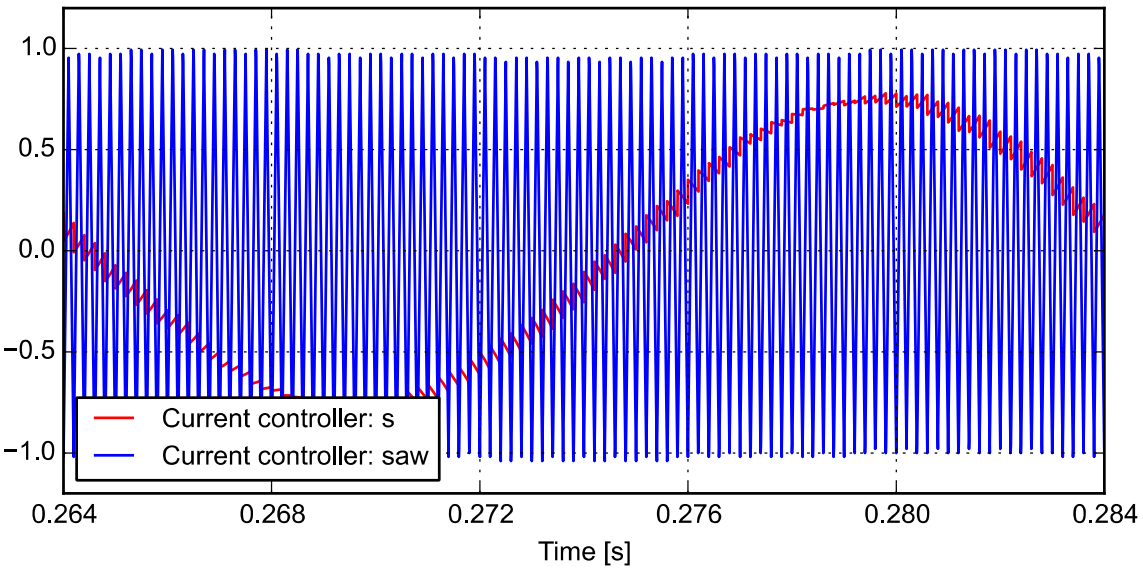

Figure 47: PWM generator reference and triangle signal

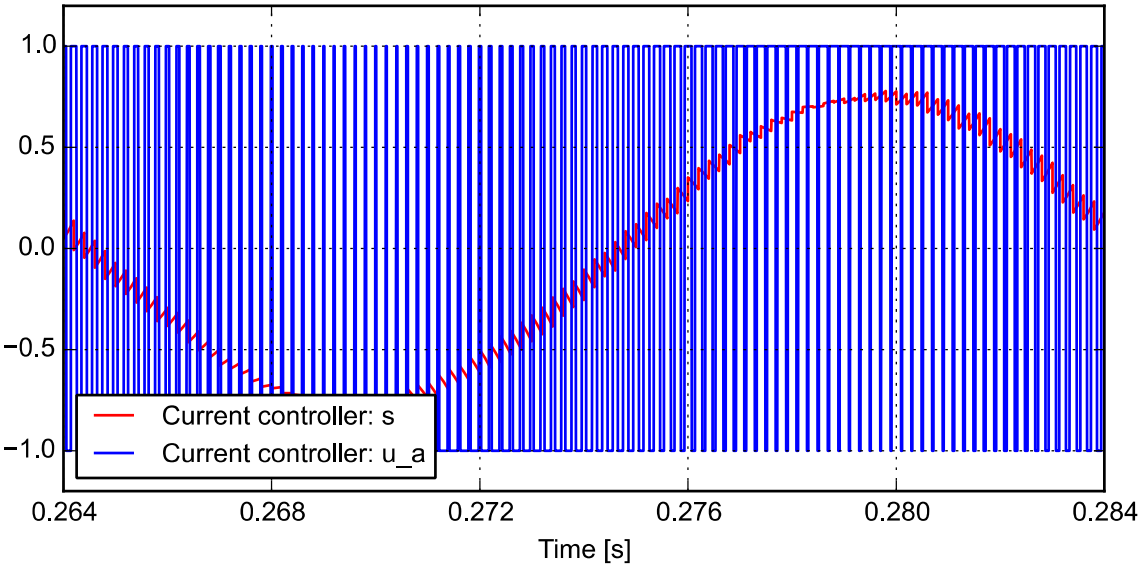

Figure 48: PWM generator reference and phase A switching signal

When the inverter is controlled as described above the current in Figure 49 is produced flowing between the grid and the inverter voltage sources. This is due to the inverter voltage that lags the grid voltage slightly that causes current to flow towards the inverter which is $180°$ out of phase with the voltage. Note that positive current was defined as current flowing out of the inverter. The measured inverter phase current waveform and grid voltage waveform is plotted in Figure 49 and Figure 50 respectively.

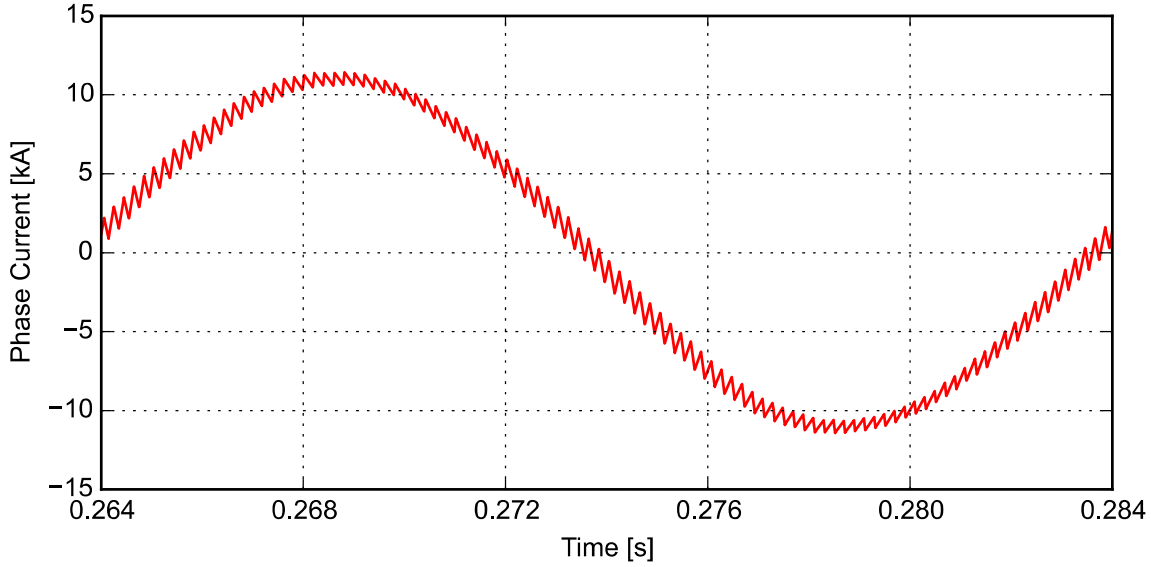

Figure 49: Inverter current waveform

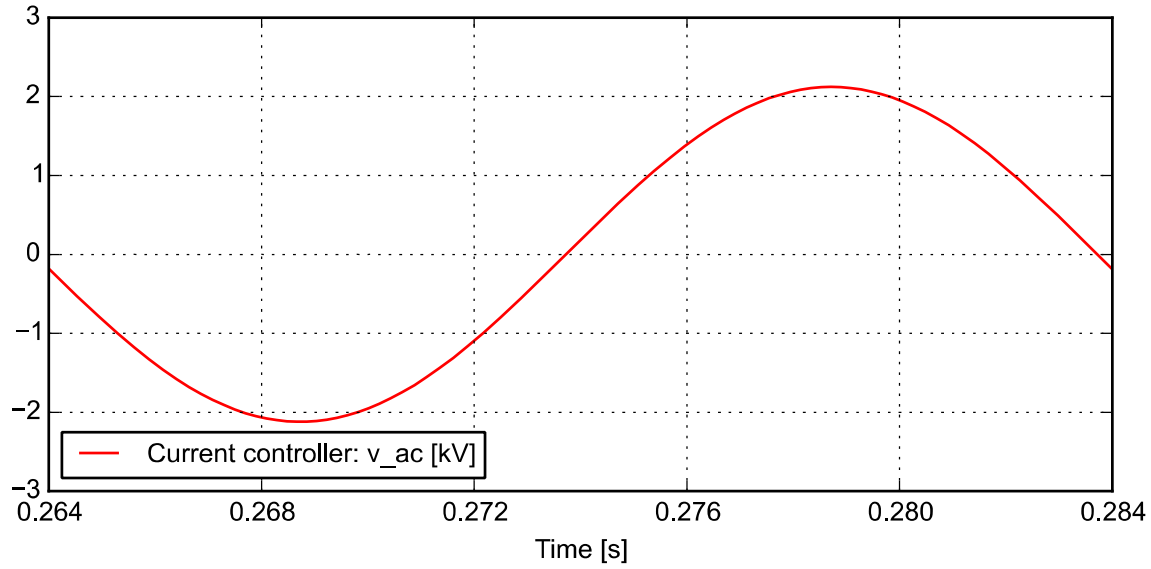

Figure 50: Grid voltage waveform

The voltage and current waveforms in Figure 49 and Figure 50 are multiplied to obtain the instantaneous power values as shown in Figure 51. The power has an average value of -12 MW that corresponds to designed value. It is shown that there is no reactive power present since the instantaneous power waveform never crosses zero on the vertical axis.

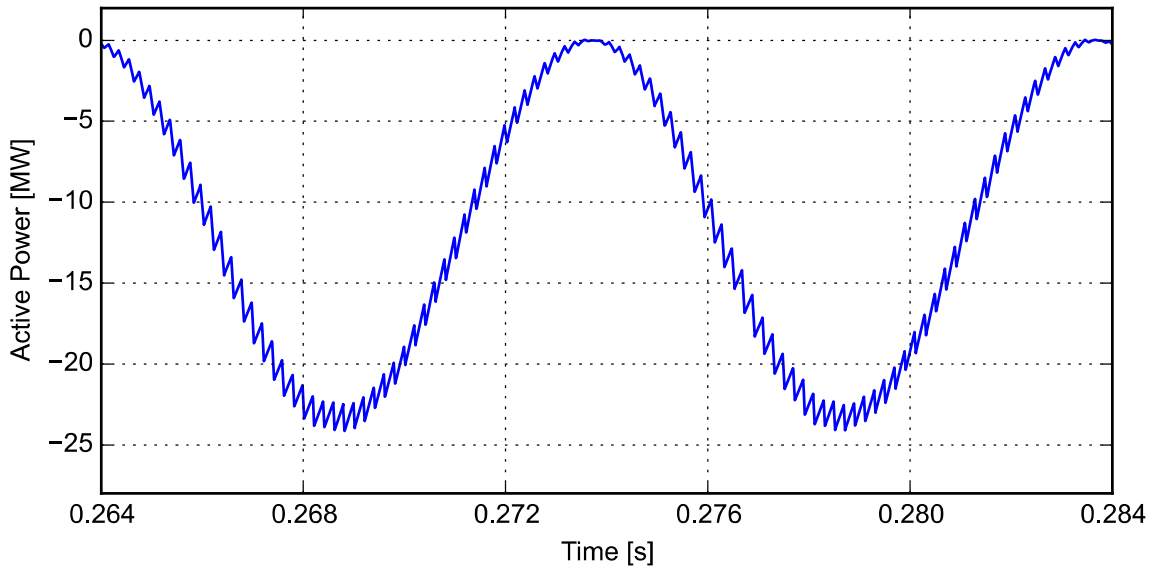

Figure 51: Inverter AC power waveform

The power in a single-phase circuit can be calculated as follows for small phase angles:

$$\begin{aligned} p(t) &= v(t)i(t) = \sqrt{2}V\sin(\omega t)\sqrt{2}I\sin(\omega t - \phi) \\ &= VI\left(\cos(\phi) - \sin(2\omega t - \phi)\right) \\ &\approx VI\left(1 - \sin(2\omega t)\right) \end{aligned} \tag{2.46}$$

The PQ analysis of an active rectifier will be shown in Section 6.6.2 and compared to measurement results.

3.5.2. DIgSILENT PowerFactory half-controlled thyristor rectifier model

3.5.2.1. Overview

A half-controlled thyristor rectifier traction system in Figure 10 can be modelled with the equivalent circuit shown in Figure 52. The DC motor is represented by a DC voltage source E_d, series resistor r_d and inductor L_d as seen in Figure 52 [18]. Most practical thyristor converters consist of an AC-side inductor and capacitor for power factor correction and is thus included in the diagram.

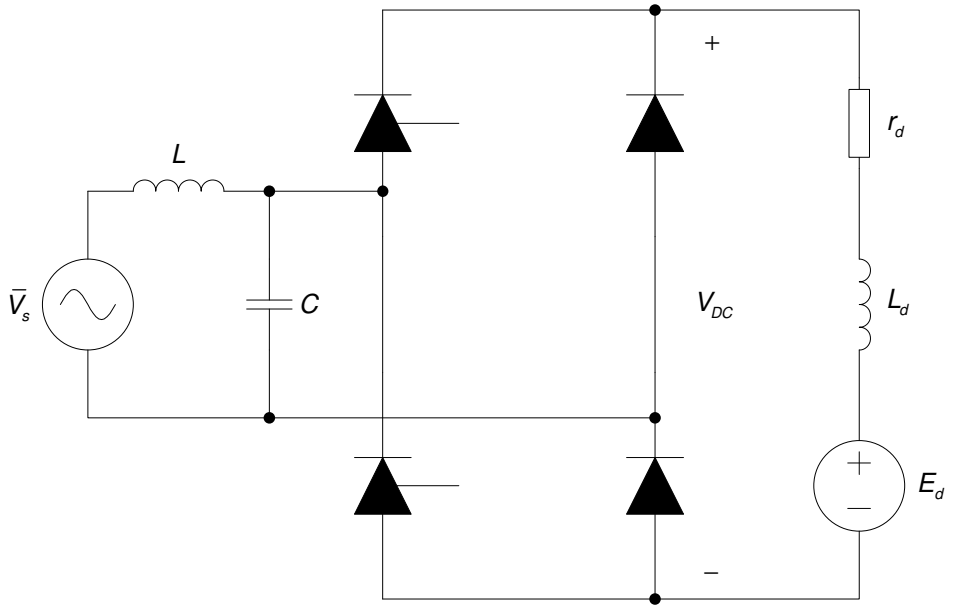

Figure 52: Simplified model of traction drive

3.5.2.2. Element layout in DIgSILENT PowerFactory

Figure 53 shows the network diagram of a single-phase half-controlled thyristor controlled system in DIgSILENT PowerFactory. Both the AC and DC sides are modelled as simple voltage sources. DIgSILENT PowerFactory does not contain a built-in model for a half-controlled thyristor rectifier and additionally does not allow the connection of a DC bus directly to an AC bus, therefore a solution was required to obtain the required functionality. To achieve this the inter-circuit fault event in EMT simulation was used to bridge DC and AC networks. DIgSILENT PowerFactory provide the user with the functionality to create an inter-circuit fault event which will generate a specified fault type at a specified time in EMT simulation. Therefore, at the start of the simulation a single-phase short circuit event is created which bridged the current flow from phase A of the AC bus (1.5 kV Source BB in Figure 53) to the DC bus (DC A in Figure 53) as well as the neutral phase of the AC bus to the DC bus (DC Neutral in Figure 53). Consequently, during EMT simulation the system is basically simulated as a grid-connected half-controlled thyristor rectifier with the DC network directly connected to the AC network. The network further consists of a single-phase 132/25 kV traction transformer, single-phase 25/1.5 kV locomotive transformer and AC filter. Refer to Figure 174 in the appendix for a photo of the traction transformer nameplate.

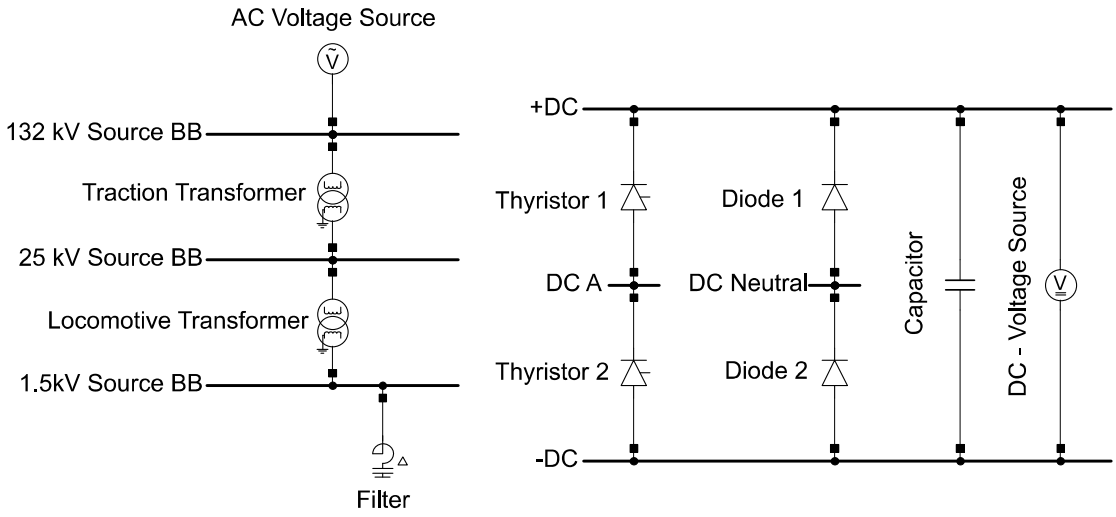

Figure 53: Network diagram of single-phase half-controlled thyristor controlled system in DIgSILENT PowerFactory

3.5.2.3. Composite model in DIgSILENT PowerFactory

Figure 54 shows the designed composite model of the rectifier system consisting of a voltage measurement element, a pulse generator and two thyristors. The real voltage (ur) is measured as a per unit value at the 25 kV terminal (25 kV Source BB in Figure 53) with the built-in voltage measurement element (StaVmea) discussed in Section 3.3.5. The Thyristor 1 and Thyristor 2 slots in Figure 54 are connected to the respective thyristor elements in Figure 53. The pulse generator generate the gate signals gate1 and gate2 which controls the switching states of Thyristor 1 and Thyristor 2 respectively.

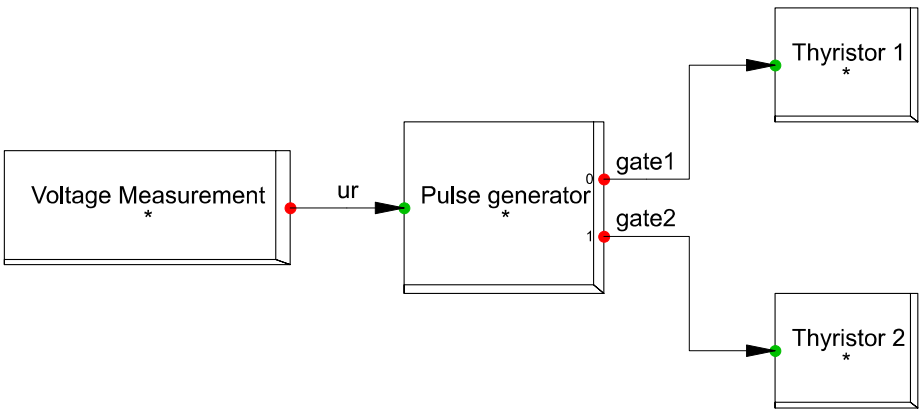

Figure 54: Designed composite model of half-controlled thyristor rectifier in DIgSILENT PowerFactory

3.5.2.4. DSL model of pulse generator in DIgSILENT PowerFactory

Figure 55 shows the designed DSL model of the single-phase pulse generator. The single-phase pulse generator is constructed to simply generate two pulse signals: gate1 and gate2 with a magnitude of 1 per unit (1.5 kV) and period of 500 µs. The pulse signal gate1 is phase shifted by the firing angle Alpha with respect to the input voltage ur and gate2 is phase shifted by 180º from gate1. The output signals gate1 and gate2 are then fed to Thyristor 1 and Thyristor 2 respectively as gate signals.

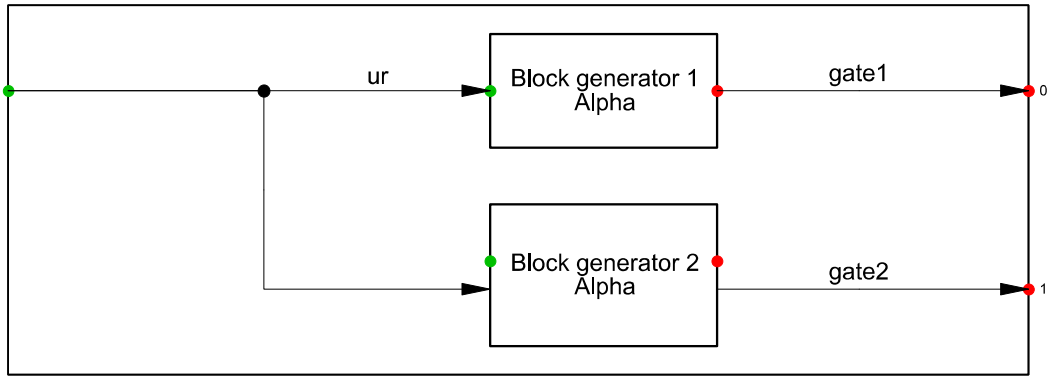

Figure 55: Designed pulse generator DSL model in DIgSILENT PowerFactory

3.5.2.5. Working principle of a half-controlled thyristor rectifier in DIgSILENT PowerFactory

Due to limited information regarding the equipment specifications, the values of the components within the model have arbitrary been chosen and then modified to generate waveforms similar to the practical waveforms measured on site. At this point in the thesis the measured results have not been shown yet, therefore, keep in mind that the equipment ratings must be chosen based on the measured results that will be shown in Section 6.7.1. To complete the discussion and implementation of the hysteresis traction loads in DIgSILENT PowerFactory there will be figures referenced in this section that will only be shown later on in the thesis. The measured current waveform that will be used to define the equipment ratings can be seen in Figure 146. By modifying the element values, certain observations could be made. By changing the DC voltage resistance (r_d) and keeping the DC voltage (E_d) constant the power demand can be changed to the required demand of the locomotive. By increasing the DC voltage inductance (L_d) the generated AC current waveform will become similar to that of a block wave. By adding an AC filter (Filter in Figure 53) with an inductor and capacitor a resonance frequency is introduced on the current waveform similar to the resonance frequency that can be seen in the measured phase current harmonic spectrum in Figure 148. The size of the inductor and capacitor will determine the resonance frequency according to (2.47).

$$f_{res} = \frac{1}{2\pi \times \sqrt{LC}} \tag{2.47}$$

By adding a damping resistance an increase in the decay of oscillation can be achieved which in turn will decrease the peak of the resonance frequency to obtain similar current and voltage waveforms compared to Figure 146 and Figure 147. For illustration purposes the AC filter is removed and the measured AC voltage ur is plotted with the thyristor gate signals gate1 and gate2 as seen in Figure 56.

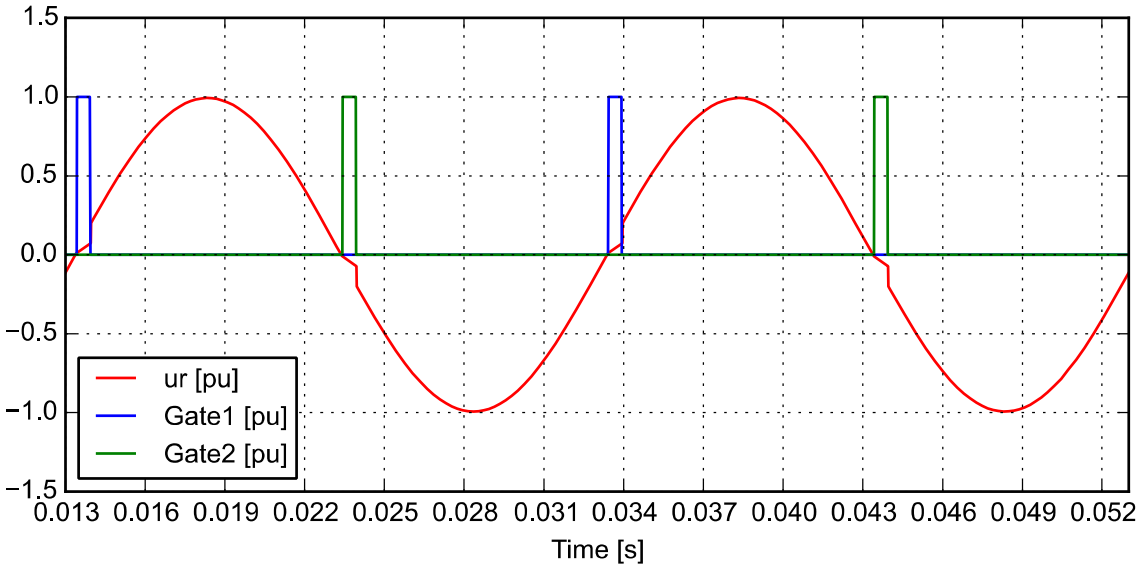

Figure 56: AC voltage waveform and thyristor gate signals

The PQ analysis of a half-controlled thyristor rectifier will be shown in Section 6.7.1 and compared to measurement results.

3.6. WIND FARM (INVERTER) MODELLING

Two local wind farms in South Africa are used as case studies. The DIgSILENT PowerFactory models are designed and constructed to reflect the physical system as closely as possible by using the actual equipment ratings of the passive filters installed at turbine level. Note that only the generic model of a singular wind turbine inverter is discussed in this section. The wind farm in case study 1 will be referred to as Wind farm A and the wind farm in case study 2 will be referred to as Wind farm B. This will be used throughout the rest of the thesis.

3.6.1. Inverter hardware – Wind farm A

The wind turbines in Wind farm A each have a power rating of 2.3 MW. The induction machine feeds power to the rectifier side of an inverter. The DC side of the rectifier stage is coupled to the inverter stage that feeds power to the grid through a LCL low pass filter with values of $22\ \mu\text{H}$, $311\ \mu\text{F}$, $38\ \mu\text{H}$ respectively. Only the line side inverter has an impact on the network and is subsequently investigated. Therefore, the rectifier and induction machine is replaced by a DC voltage source and capacitor. The inverter under investigation is an ABB inverter

consisting of three modules in parallel. The inverter modules are illustrated in Figure 172 of the Appendix. In addition, a photo of the inverter nameplate is shown in Figure 173 of the Appendix.

3.6.2. Inverter hardware – Wind farm B

The wind turbines in Wind farm B also have a power rating of 2.3 MW. The induction machine feeds power to the rectifier side of an inverter. The DC side of the rectifier stage is coupled to the inverter stage that feeds power to the grid through a main reactor with a value of $74\ \mu\text{H}$. The system further consist of LC passive filters that were designed to reduce the ripple at the switching frequency with respective values of $0.08\ mF$ and $50.6\ \mu\text{H}$, as well as the ripple at the first multiple of the switching frequency with filter values of $0.04\ mF$ and $26.4\ \mu\text{H}$. Only the line side inverter has an impact on the network and is subsequently investigated. Therefore, the rectifier and induction machine is replaced by a DC voltage source and capacitor. The inverter under investigation is a general electric (GE) inverter consisting of three modules in parallel.

3.6.3. DIgSILENT PowerFactory hysteresis inverter model – Wind farm A

3.6.3.1. Overview

The hysteresis current control method has been utilised at Wind farm A and must be investigated. The hysteresis current control approach provide high robustness and the fastest dynamic response of any VSI control method available [25]. The basic control strategy of the conventional hysteresis current control approach is to compare a reference current value to an actual measured current value for each phase to ensure that the current error is kept within a chosen hysteresis band by the inverter switching action. Within a conventional hysteresis current control approach the hysteresis band is kept constant and thus the switching frequency vary to ensure that the current ripple is maintained within the hysteresis band. This is the frequency characteristic of a conventional hysteresis inverter. In the conventional three-phase approach the three phases are not independent, therefore, the instantaneous switching of one phase leg can interfere with the voltage of the other phase legs [122]. This interference can lead to irregular switching of the inverter and current overshoot above the hysteresis limit as the single-phase current is not only dependent on the corresponding phase voltage but also on the other phase voltages [122], [123]. The interference can be compensated for by considering the current errors as space vectors as investigated in [124]–[126]. Various other adaptive hysteresis current control approaches have been proposed to solve the problem of variable switching frequency [127]–[131]. This is achieved by varying the hysteresis band depending on the output AC voltage and desired switching frequency to obtain a fixed switching frequency as investigated in [132]. However, due to the added complexity of these

methods and the limited information regarding the exact hysteresis control method utilised at Wind farm A the conventional hysteresis current control approach was implemented. The conventional hysteresis current controller for a three-phase system can be seen in Figure 57.

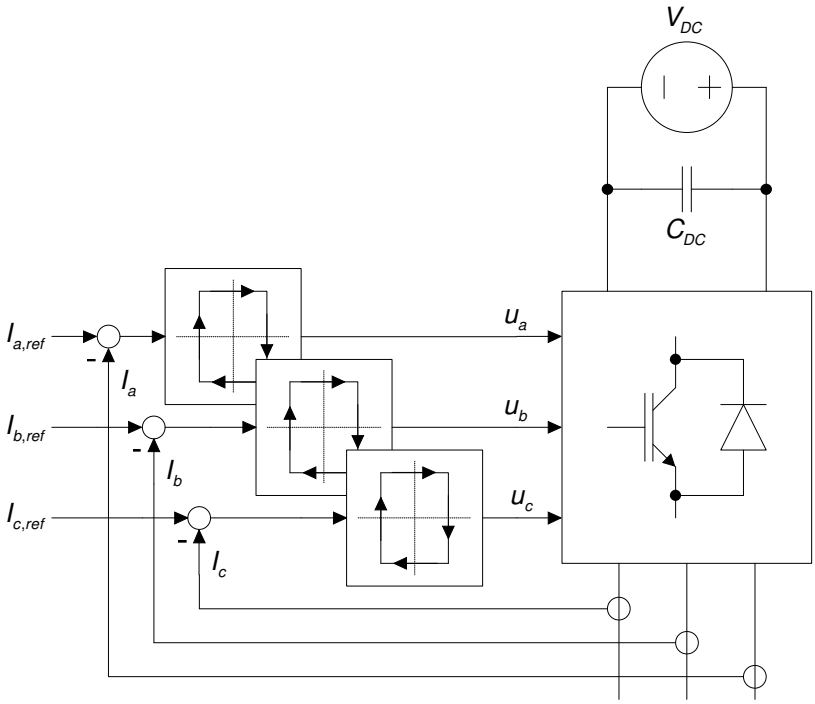

Figure 57: Conventional hysteresis current controller

The switching of the inverter is determined by the gate signals u_a, u_b and u_c. Each gate signal determine the state of the inverter switches for the corresponding inverter phase leg. The reference current can be expressed by the following equation:

$$i_{ref} = I_{ref} \sin \omega t \tag{2.48}$$

from which the upper and lower reference band can further be expressed as follows:

$$\begin{aligned} i_u &= i_{ref} + \Delta i \\ i_l &= i_{ref} - \Delta i \end{aligned} \tag{2.49}$$

where Δi is the maximum current error. Therefore, if the current error exceeds Δi the gate signal is turned low, and when the current error is smaller than $-\Delta i$ the gate signal is turned high. If the measured signal is between i_l and i_u the switching signals are unaltered and no switching occurs. The hysteresis control switching is illustrated in Figure 58.

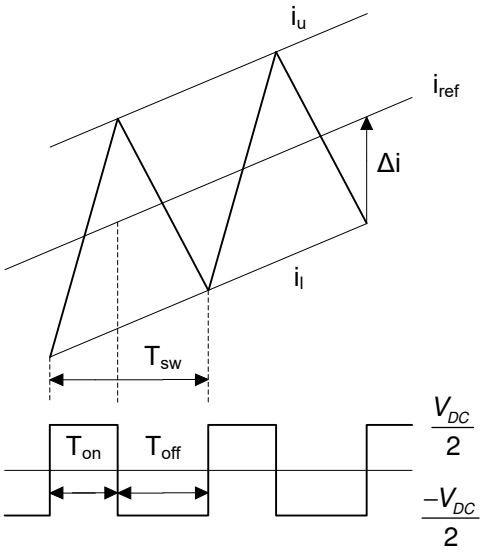

Figure 58: Conventional hysteresis current control switching diagram

The mathematical formulation of the hysteresis approach has been described in various papers [133], [134] and was also used in this thesis. The instantaneous output current i for an inverter connected to the grid through an inductor can generally be expressed by the following equation:

$$\frac{di}{dt} = \frac{v_{DC} - v_s}{L} \tag{2.50}$$

where v_{DC} is the instantaneous inverter DC voltage, v_s the instantaneous output voltage and L the output filter inductance.

The instantaneous inverter DC voltage v_{DC} can be expressed as the following during a switching period T_{sw} :

$$\begin{aligned} v_{DC} &= \frac{V_{DC}}{2} \text{ for } T_{on} \\ v_{DC} &= -\frac{V_{DC}}{2} \text{ for } T_{off} \end{aligned} \tag{2.51}$$

where

$$T_{sw} = T_{on} + T_{off} \tag{2.52}$$

as shown in Figure 58.

By using the above equations and investigating the single-phase operation one can define the output current slope during the on period:

$$\frac{di}{dt} = \frac{\frac{V_{DC}}{2} - v_s}{L} T_{on} \tag{2.53}$$

By using the hysteresis band limit Δi_h which is $2\Delta i$, (2.53) can be written as follows:

$$\frac{\Delta i_h}{T_{on}} = \frac{\frac{V_{DC}}{2} - v_s}{L} \tag{2.54}$$

The same can be done for the off period to obtain the following equation:

$$\frac{\Delta i_h}{T_{off}} = \frac{-\frac{V_{DC}}{2} - v_s}{L} \tag{2.55}$$

where $T_{sw} = \frac{1}{f_{sw}}$ and f_{sw} the switching frequency. By replacing T_{on} and T_{off} in (2.52) with T_{on} and T_{off} in (2.54) and (2.55) respectively the switching frequency f_{sw} can be calculated as:

$$f_{sw} = \frac{(\frac{V_{DC}}{2})^2 - v_s^2}{V_{DC} L \Delta i_h} \tag{2.56}$$

With the output voltage v_s a varying sinusoidal waveform at the fundamental frequency.

$$v_s = P_m \frac{V_{DC}}{2} \sin \omega t \tag{2.57}$$

with P_m the amplitude modulation index of the inverter. Therefore, with a fixed hysteresis band Δi_h the switching frequency f_{sw} depend on the output voltage v_s. The switching frequency will vary as the output voltage vary sinusoidally. If the output voltage v_s is equal to zero the maximum switching frequency can be obtained with the following equation:

$$f_{\max} = \frac{V_{DC}}{4 L \Delta i_h} \tag{2.58}$$

From which (2.56) can be further derived to the following:

$$\begin{aligned} f_{sw} &= f_{\max}\left(1 - P_m^2 \sin^2 \omega t\right) \\ &= f_{\max}\left(1 - \frac{P_m^2}{2} + \frac{P_m^2}{2} \cos 2\omega t\right) \end{aligned} \tag{2.59}$$

Therefore, the switching frequency will vary around an average value:

$$f_{avg} = f_{\max}\left(1 - \frac{P_m^2}{2}\right) \tag{2.60}$$

So by changing the DC voltage the modulation index will change and thus the frequency range will change.

For balanced three-phase systems the summation of three-phase currents are always zero:

$$i_a + i_b + i_c = 0 \tag{2.61}$$

Therefore, the phase current that contain the minimum switching frequency according to (2.59) at any given moment will depend on the value of the other two phases and this can cause overshoot in the phase that can exceed the hysteresis limit by $2\Delta i_h$.

3.6.3.2. Element layout in DIgSILENT PowerFactory

The wind plant model of a PWM controlled inverter system was built with predefined elements in DIgSILENT PowerFactory as seen in Figure 59. Both the AC and DC sides are modelled as simple voltage sources. The system further consists of a 132/33 kV transformer, 33/0.69 kV transformer, AC LCL filter and DC capacitor. The LCL filter values given in Section 3.6.1 are scaled so to model the combined filter values of the wind farm.

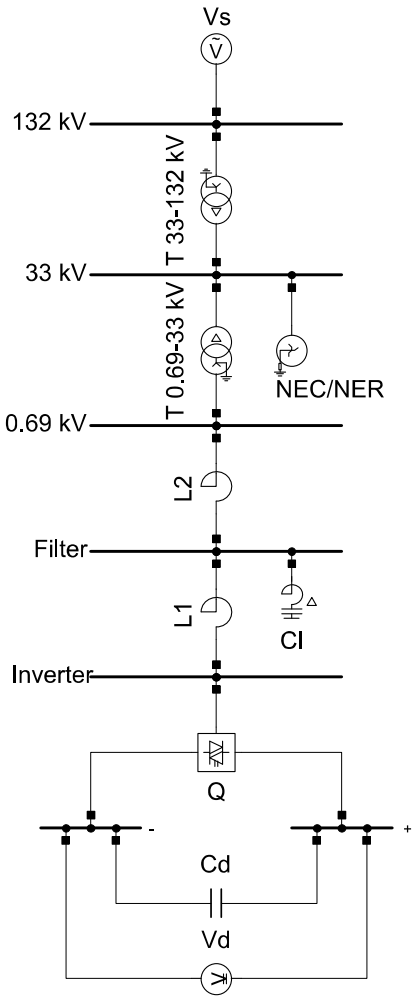

Figure 59: Network diagram of hysteresis wind farm system in DIgSILENT PowerFactory

3.6.3.3. Hysteresis inverter composite model

The hysteresis inverter control system is constructed as a composite model comprising of a voltage measurement element per phase, voltage controller, current controller and the inverter as shown in Figure 60. The inverter system is modelled by using the DSL feature of DIgSILENT PowerFactory. Therefore, DSL was used to implement the designed voltage controller and current controller. The initialisation of these DSL models can be challenging due to stability issues. Therefore, the initial conditions must be set up with great care to accurately evaluate the performance of the designed system during transient and steady state conditions.

Each voltage measurement slot measures the AC-voltage of that particular phase at the 0.69 kV bus on the AC grid with the use of a PLL. The design of a PLL DSL model was not necessary as DIgSILENT PowerFactory provides a more than adequate built-in PLL model (ElmPhi_pll) as discussed in Section 3.3.3. The PLL slot provide the cosphi signals of each phase and these are sent as signals to the current controller. The voltage controller receive the inverter DC voltage as an input signal and calculates the reference current which is sent as an input signal to the current controller. In addition, the inverter output currents are measured and sent as input signals to the current controller.

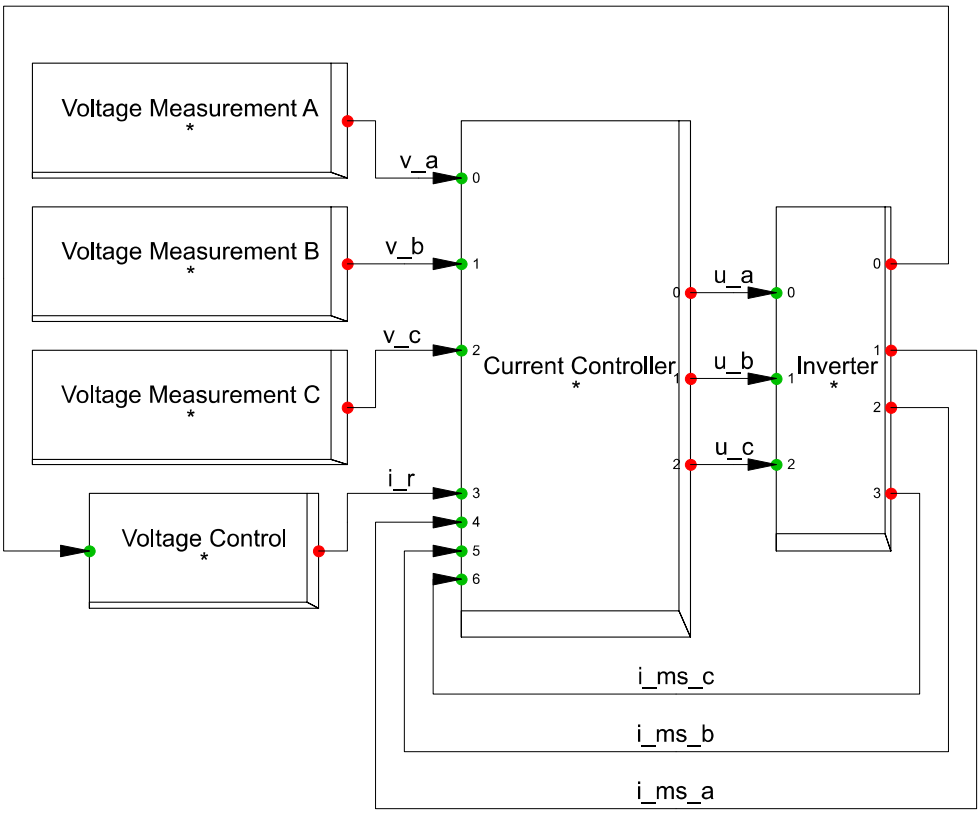

Figure 60: Designed composite model of hysteresis inverter model in DIgSILENT PowerFactory

The inverter slot consist of the built-in PWM converter (ElmVsc) element discussed in Section 3.3.1. The PWM converter is modelled as a detailed inverter with switches that contain on/off resistances and snubber-circuits. In addition, the PWM converter model was controlled using an external current controller rather than the built-in internal current controller discussed in Section 3.3.1.3. Therefore, none of the stability PWM converter control methods discussed in Section 3.3.1.3 was implemented for the hysteresis controlled inverter system. Consequently, the PWM converter was controlled by externally controlling the switching states of the three phase legs of the PWM converter using the inverter input signals u_a, u_b and u_c. The conventional hysteresis approach has a varying switching frequency, therefore, the PWM converter model parameters is set up differently. The implementation of the voltage and current controllers will be discussed in the following sections.

3.6.3.4. Voltage controller

The voltage controller in Figure 61 receives the measured DC voltage signal as a per unit value and compare it to a reference voltage of 1 per unit. The per unit error is then scaled to a voltage value by multiplying the error with the nominal DC voltage of 1.38 kV. A reference current signal is then obtained by multiplying the error with a PI controller.

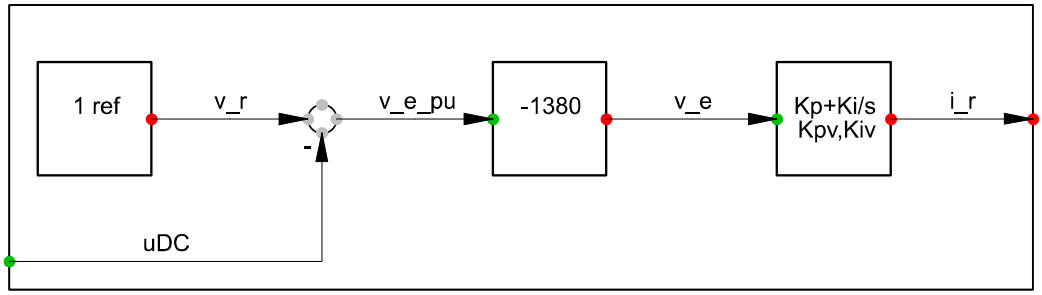

Figure 61: Hysteresis inverter voltage controller in DIgSILENT PowerFactory

The required reference current for a specific power generation is obtained with the relationship between the fixed internal resistance of the DC voltage source and the DC voltage set point. Therefore, by changing the DC voltage one can control the amount of active power generation of the wind farm due to the change in reference current.

3.6.3.5. Current controller

The current controller shown in Figure 62 multiplies the measured per unit three-phase grid voltage waveforms (vpu_a, vpu_b and vpu_c) with the reference current magnitude (i_r) to obtain the reference current waveforms (i_rr_a, i_rr_b and i_rr_c). The measured AC current signals (i_ms_a, i_ms_b and i_ms_c) are multiplied by 1000 to scale the kA signal to A signals (i_m_a, i_m_b and i_m_c). The measured current signals are then compared to the reference current waveforms to obtain the current errors (s1, s2 and s3) that can be compared to the fixed hysteresis band within the hysteresis comparator to determine the switching states of the

inverter phase legs (u_a, u_b and u_c). Note that each phase is controlled independently. The hysteresis comparator compares the measured current errors (s1, s2 and s3) to the defined current error Δi (HB in Figure 62) through DSL code. The hysteresis comparator basically implements (2.49). If one of the current errors (s1, s2 and s3) exceeds Δi the gate signal for that specific phase is turned low, and when the current error is smaller than $-\Delta i$ the gate signal is turned high. If the measured signal is between i_l and i_u the gate signals are unaltered and no switching occurs. A positive signal switches on the top switch in a phase leg, while a zero signal switches on the bottom switch. If the top switch is switched on the corresponding phase leg is connected to the positive DC voltage terminal while if the bottom switch is switched on the corresponding phase leg is connected to the negative DC voltage terminal. The hysteresis controller is stable with a reference signal, therefore, do not require the implementation of a PI controller.

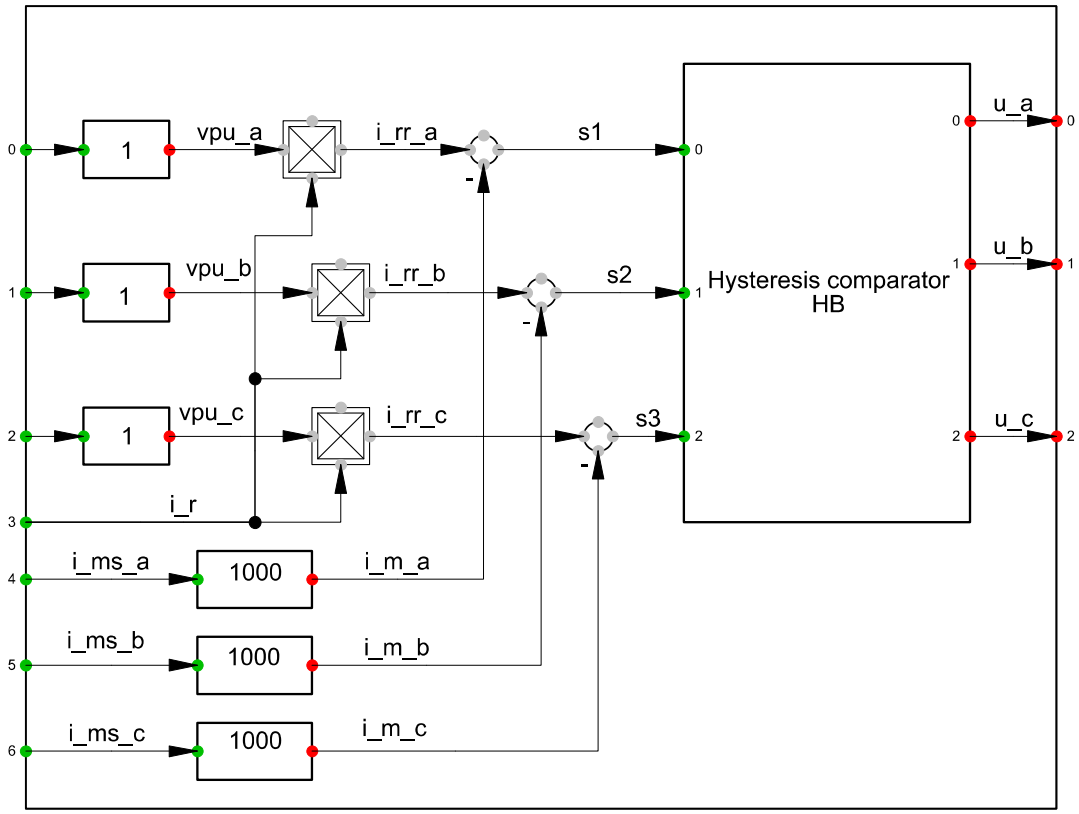

Figure 62: Hysteresis inverter current controller in DIgSILENT PowerFactory

3.6.3.6. Working principle of a three-phase hysteresis inverter in DIgSILENT PowerFactory

For an average 2.3 MW power generation the reference peak phase current is calculated as 2.72 kA. Therefore, for a hysteresis band limit of 10% at the peak of the reference current, HB is chosen as 272 A. The inverter reference current and measured output phase A current is shown in Figure 63.

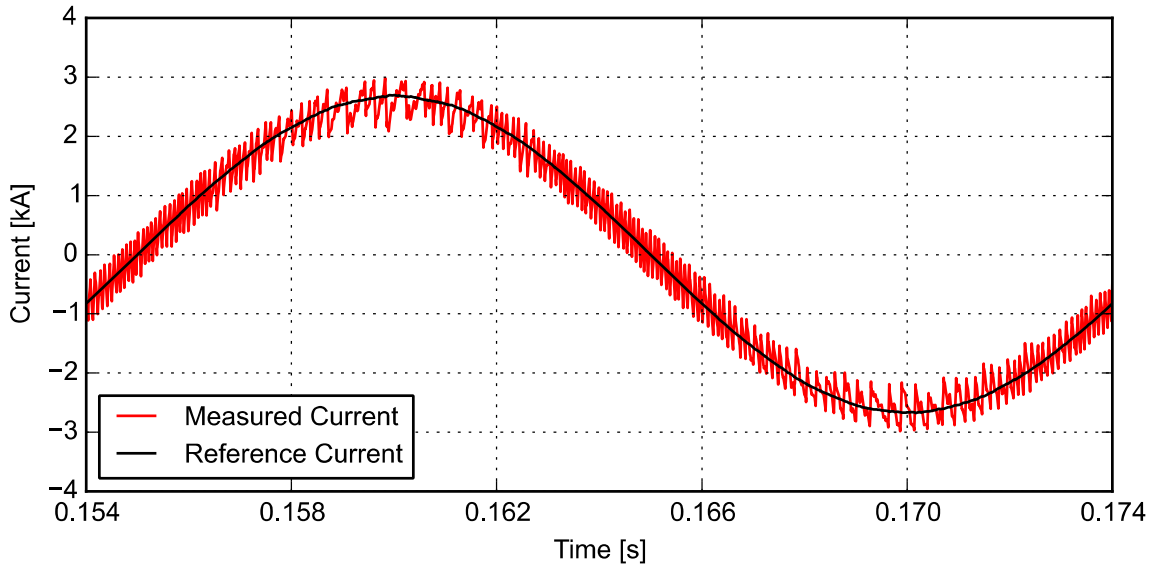

Figure 63: Measured inverter output phase A current (red) and reference current (black)

Figure 64 illustrates the drawbacks of the conventional hysteresis approach showing the measured phase A current compared to the hysteresis band limits. Current overshoot above and below the hysteresis limit is clearly visible all along the waveform. In addition, the drawback of irregular switching near the peak of the current waveform is also visible due to the interference of the current in phase B and phase C on the measured phase A.

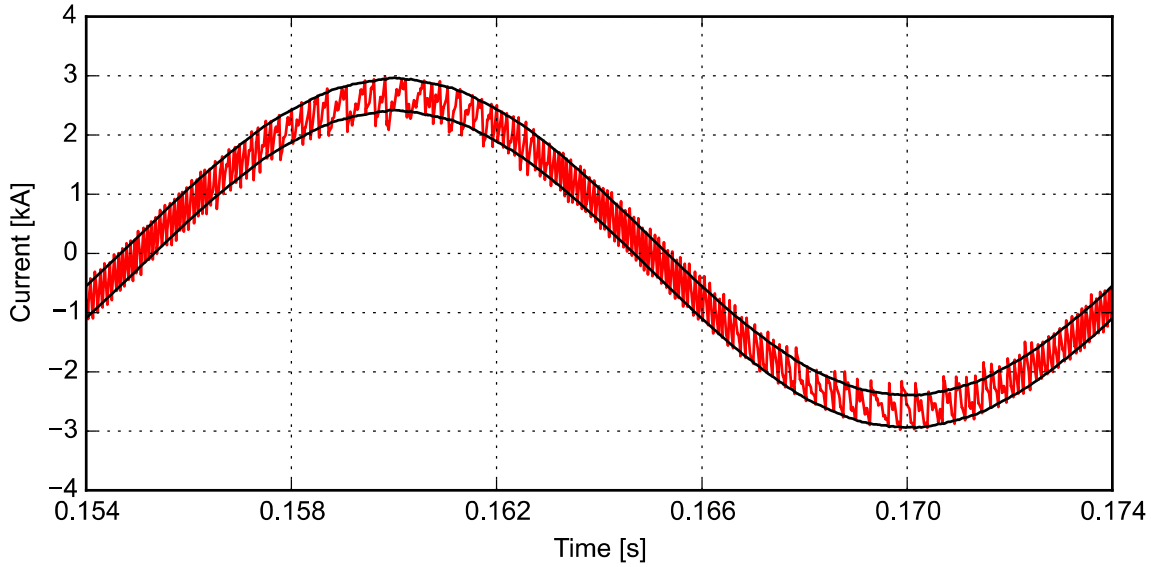

Figure 64: Inverter output measured phase A current compared to the hysteresis band

The PQ analysis of the above designed three-phase hysteresis inverter will be shown in Section 4.3.3 and compared to the measurement results in Section 4.3.4. Keep in mind that the hysteresis limit and controller values will be adjusted to replicate the measurement results as close as possible.

3.6.4. DIgSILENT PowerFactory conventional PWM inverter model – Wind farm B

3.6.4.1. Overview

The conventional PWM inverter is designed and implemented based on the vector current control method presented in [116], [135]. This method is widely used for grid-connected inverter systems [136]. The concept of vector control implies the independent control of the power and reactive power injected into the grid through a feedback PI current controller. To improve the dynamic response of the PI controller and to remove the steady state error in voltage and currents, the controller was implemented in the rotating reference frame (dq reference frame). The rotating reference frame refers to the mapping of the three-phase inverter values onto a two-axis synchronous rotating reference frame (dq reference frame) rather than a fixed two-axis reference frame (αβ reference frame) [25]. The AC voltages and currents are measured and transformed into the dq (direct and quadrature) reference frame by means of the Clarke transformation followed by the Park transformation. The single-line equivalent diagram of a typical three-phase grid-connected VSI is shown in Figure 65. For the purpose of explaining the control a three-phase grid-connected VSI, the VSI is connected to the grid through a series reactor with an inductor (L) and resistor (R).

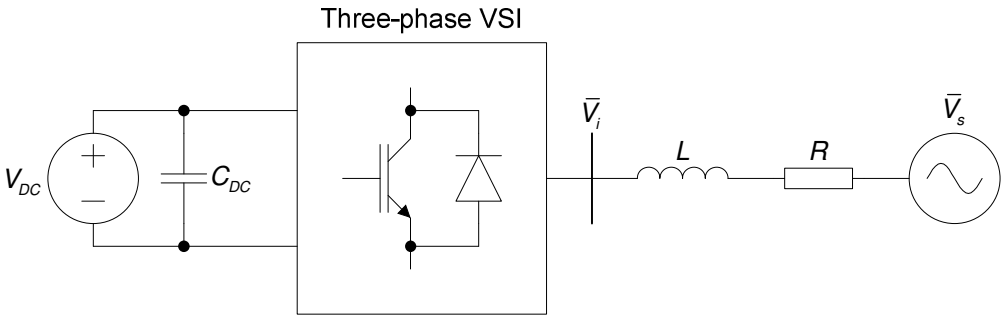

Figure 65: Single-line equivalent circuit of three-phase grid-connected VSI

Figure 66 shows the vector control layout of a grid-connected VSI with the power controller, inner close loop current controller and a PLL.

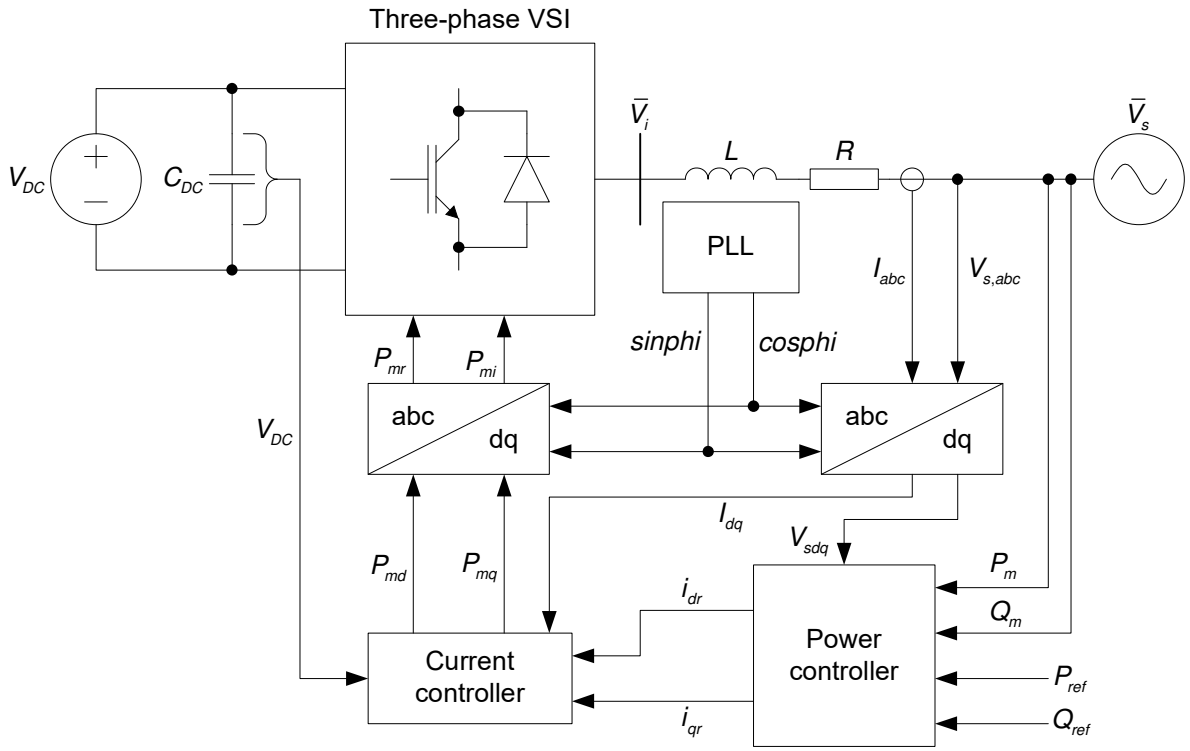

Figure 66: Designed control layout of grid-connected VSI

3.6.4.2. Element layout in DIgSILENT PowerFactory

The wind plant model of a PWM controlled inverter system was built with predefined elements in DIgSILENT PowerFactory as shown in Figure 67. Both the AC and DC sides are modelled as simple voltage sources. The system further consists of a 132/33 kV transformer, 33/0.69 kV transformer, a grid reactor and passive filters.

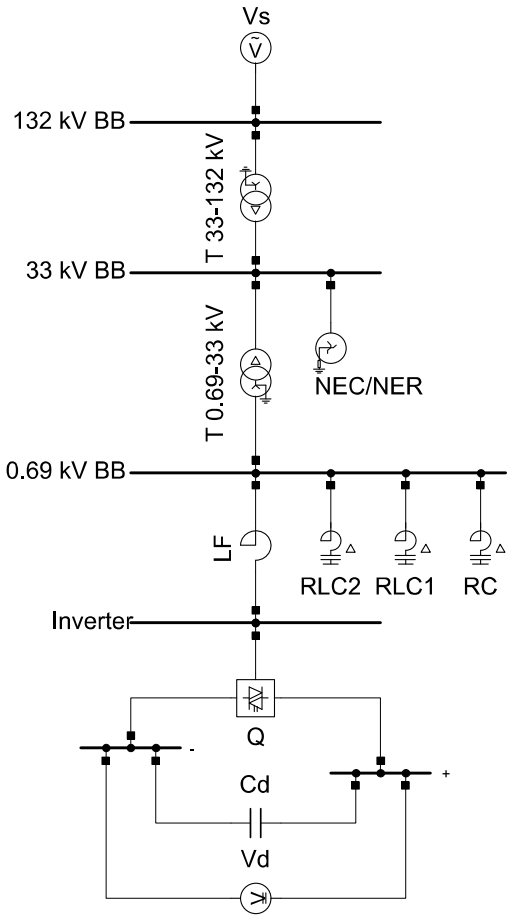

Figure 67: Network diagram of PWM wind farm system in DIgSILENT PowerFactory

3.6.4.3. PWM inverter composite model

The PWM inverter control system in Figure 66 is constructed as a composite model comprising of a voltage measurement element, power measurement element, current measurement element, a PLL, various sample and hold blocks, a power controller, current controller and the inverter as shown in Figure 68. The inverter system is modelled by using the DSL feature of DIgSILENT PowerFactory. The feature allows the dynamic modelling of both linear and non-linear systems. Thus, DSL was used to implement the designed power controller and current controller. The initialisation of these DSL models can be challenging due to stability issues. Therefore, the initial conditions need to be set up with great care to accurately evaluate the performance of the designed system during transient and steady state conditions.

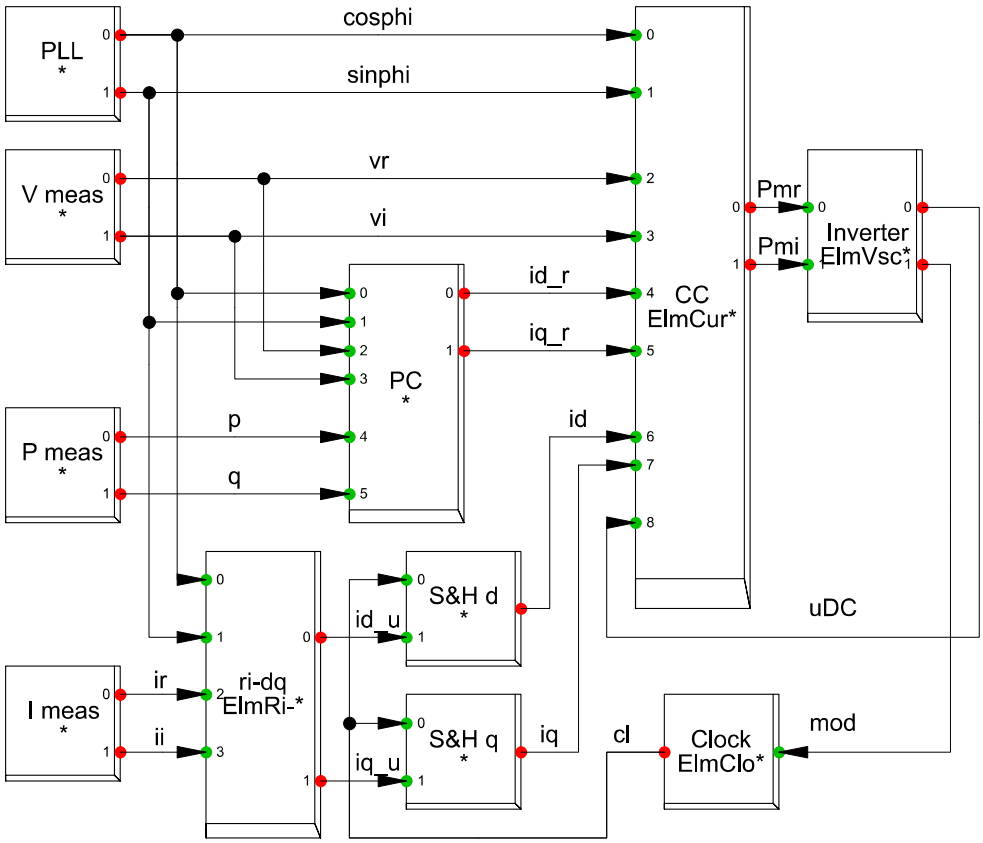

Figure 68: Composite model of PWM inverter model in DIgSILENT PowerFactory

The voltage measurement element measures the AC-voltage at the 0.69 kV bus on the AC grid with the use of the built-in voltage measurement (StaVmea) element discussed in Section 3.3.5. The real and imaginary values of the voltage are sent as signals to the power controller and current controller respectively. The power measurement element measures the real and reactive power that flows on the AC side of the inverter with the use of the built-in power measurement (StaPqmea) element discussed in Section 3.3.7. The design of a PLL DSL model was not necessary as DIgSILENT PowerFactory provides a more than adequate built-in PLL model (ElmPhi_pll) as discussed in Section 3.3.3. The PLL slot, provide the cosphi and sinphi signals used for αβ to dq transformation and vice versa and are measured at the 0.69 kV bus. The current measurement slot measures the AC-current at the output of the inverter with the use of the built-in current measurement (StaImea) element discussed in Section 3.3.6. The real and imaginary values of the current are sent as signals to the αβ to dq transformation slot. The αβ to dq transformation slot consist of a DSL model that convert the αβ currents to dq currents using the Park transformation as follows:

$$\begin{aligned} i_d &= i_r \cos phi + i_i \sin phi \\ i_q &= -i_r \sin phi + i_i \cos phi \end{aligned} \tag{2.62}$$

The direct current (id_u), quadrature current (iq_u) and clock pulse are sent as signals to two sample and hold elements (S&H d and S&H q). The clock element generates a clock pulse

signal that alternates between high and low values with the frequency or period of the clock pulse signal equal to that of the inverter switching frequency and period. The sample and hold elements perform regular symmetrical sampling on the direct and quadrature current values using the predefined built-in sample and hold element (ElmSamp) discussed in Section 3.3.4. The sampled direct and quadrature current values are then sent as signals to the inverter current controller for further control.

The inverter slot consist of the built-in PWM converter (ElmVsc) element discussed in Section 3.3.1. The P_{mr} and P_{mi} PWM converter control method as discussed in Section 3.3.1.3 was implemented for the PWM controlled inverter system. The implementation of the different controllers will be discussed in the following sections.

3.6.4.4. Power controller (labelled as PC in Figure 68)

The primary function of the inverter is normally to transfer all generated power to the grid. This is normally done at a specified power factor or alternatively reactive power is specified by a power system voltage control algorithm. Control of active and reactive power is established by the inverter outer loop control system as shown in Figure 69.

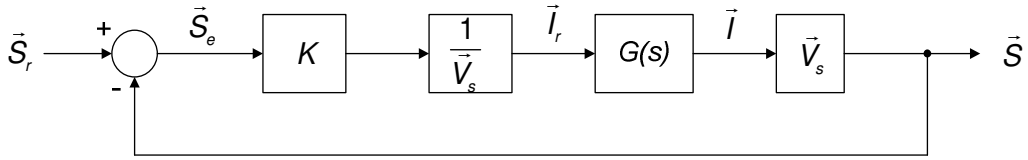

Figure 69: Power control loop block diagram

For the purpose of the power controller design it is assumed that the current controller is ideal, i.e. it follows its input without an error and responds much faster than the power controller. It can, therefore, be assumed that $G(s) = 1$. The power controller does not need to respond fast to perturbations, but accuracy at steady state is a priority. The selected controller, therefore, has a small proportional term of $K_p = 0.5$ that would not do much about steady state error, for which purpose an integral term is selected. The integral gain (K_i) is inversely proportional to the integration time constant. It takes a period of approximately five time constants for the error to decay to zero. It was decided to reach steady state within one fundamental cycle of 20 ms, for a fast set point response due to the long simulation time when doing EMT simulation. K_i was selected as 100, which gives a time constant of 10 ms. An integrator adds an open loop pole at the origin of the s-plain and a close loop pole located at $-K_i$ on the real axis. That means the system is stable and its response time is determined by the value of K_i.

An inverter transfers power in the form of a controlled current source into the grid. Voltage is predominately governed by the grid. The current vector required for a desired apparent power

vector can be calculated by applying the instantaneous power theory in three-phase, three-wire systems.

$$\begin{aligned}\bar{S} &= \bar{V} \times \bar{I}^{*} \\ &= \left(v_{\alpha} + jv_{\beta}\right)\left(i_{\alpha} - ji_{\beta}\right) \\ &= \underbrace{\left(v_{\alpha} i_{\alpha} + v_{\beta} i_{\beta}\right)}_{p} + j\underbrace{\left(v_{\beta} i_{\alpha} - v_{\alpha} i_{\beta}\right)}_{q}\end{aligned} \tag{2.63}$$

The active and reactive powers are:

$$\begin{bmatrix} p \\ q \end{bmatrix} = \begin{bmatrix} v_{\alpha} & v_{\beta} \\ -v_{\beta} & v_{\alpha} \end{bmatrix} \begin{bmatrix} i_{\alpha} \\ i_{\beta} \end{bmatrix} \tag{2.64}$$

where p and q are the reference real and reactive power that the inverter must inject into the grid at steady state conditions. To produce required active and reactive power, the alpha and beta components of the current reference can be calculated as follows:

$$\begin{bmatrix} i_{\alpha} \\ i_{\beta} \end{bmatrix} = \frac{1}{v_{\alpha}^{\,2} + v_{\beta}^{2}} \begin{bmatrix} v_{\alpha} & v_{\beta} \\ v_{\beta} & -v_{\alpha} \end{bmatrix} \begin{bmatrix} p \\ q \end{bmatrix} \tag{2.65}$$

Since the alpha and beta components are still quantities that vary at the fundamental frequency, the use of an integral term in the current controller causes undesirable phase delay. By transforming quantities to the rotating reference frame, i.e. i_d and i_q, the fundamental frequency component becomes a direct current component and an integral term can be applied. Therefore, (2.64) can be written in the dq reference frame as follows:

$$\begin{bmatrix} p \\ q \end{bmatrix} = \begin{bmatrix} v_{d} & v_{q} \\ -v_{q} & v_{d} \end{bmatrix} \begin{bmatrix} i_{d} \\ i_{q} \end{bmatrix} \tag{2.66}$$

From the above equation the direct and quadrature components of the current controller reference current can be calculated as follows:

$$\begin{bmatrix} i_{dr} \\ i_{qr} \end{bmatrix} = \frac{1}{v_{sd}^{\,2} + v_{sq}^{2}} \begin{bmatrix} v_{sd} & v_{sq} \\ v_{sq} & -v_{sd} \end{bmatrix} \begin{bmatrix} p \\ q \end{bmatrix} \tag{2.67}$$

The PLL is used to align the dq reference frame with the rotating voltage vector so that zero steady state error can be achieved through the PI controller. Thus, the PLL measures the voltage phase angle to lock the dq reference frame axes to this phase angle. Therefore, if the alignment was done correctly the quadrature voltage v_{sq}, will equal zero as shown in (2.68).

$$v_{sd} = v \text{ and } v_{sq} = 0 \tag{2.68}$$

To simplify calculations variables with per unit values are used throughout the current controller, keeping in mind that the base parameters are set in the inverter object in the network

diagram. That means the first part of (2.67) is unity, because $\sin^2 phi + \cos^2 phi = 1$ which will then further simplify the current controller reference current values in (2.67) to:

$$\begin{bmatrix} i_{dr} \\ i_{qr} \end{bmatrix} = \begin{bmatrix} \frac{1}{v_{sd}} \\ -\frac{1}{v_{sd}} \end{bmatrix} \begin{bmatrix} P_{ref} \\ Q_{ref} \end{bmatrix} \tag{2.69}$$

Therefore, it is shown that the active and reactive power controller can be developed through a simple open loop controller. The active and reactive power controller can be made more accurate through a close loop controller that feed the measured active power and reactive power back as shown in Figure 70. However, this is not needed in this thesis as the accuracy of the open loop controller was considered adequate.

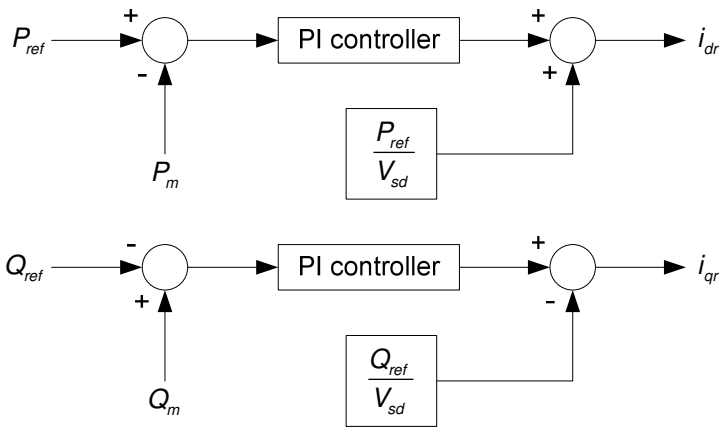

Figure 70: Closed loop active and reactive power controller

The above equations and theory is implemented in the DIgSILENT PowerFactory DSL model of Figure 71 to calculate the reference current values.

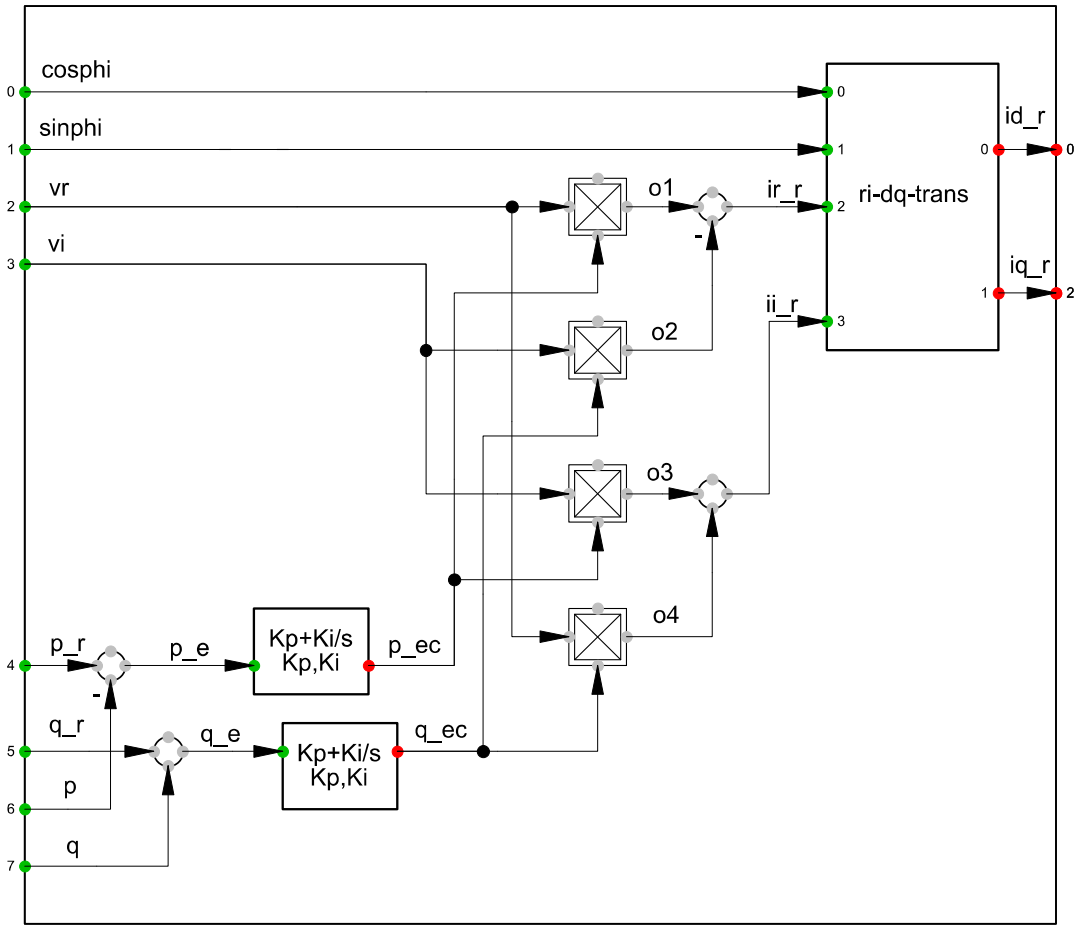

Figure 71: Designed inverter power controller for PWM inverter in DIgSILENT PowerFactory

The per unit active and reactive power reference values p_r and q_r in Figure 71 are set as initial conditions in the power controller DSL code.

3.6.4.5. Current controller

It is possible to implement the DIgSILENT PowerFactory built-in PWM converter current controller as discussed in Section 3.3.1.3 for a simple current control method. The built-in current controller was, however, not implemented as it lacks feed forward voltage and cross coupling compensation, which is necessary in this application based on the derivations in (2.71) to (2.73). Consequently, a current controller need to be designed to achieve the accuracy and response required for this thesis.

An inverter with current control, functions by applying a voltage on its terminals to force a current through its filter inductor. Since the other side of this inductor is connected to the grid, the instantaneous grid voltage also affects the inductor current.

Figure 65 can be used to write the required voltage equations. The required applied voltage vector $\vec{v}_{i,\alpha\beta}$ to achieve a desired current change, can be calculated using the current derivative in the rotating reference frame as follows [76], [137]:

$$\vec{v}_{i,\alpha\beta} = L\frac{d\vec{i}_{\alpha\beta}}{dt} + \vec{v}_{g,\alpha\beta} \tag{2.70}$$

The transformation from the stationary reference frame to the rotating reference frame involves a time dependant function. To transform $\frac{d\vec{i}_{\alpha\beta}}{dt}$ to the rotating reference frame, the derivative of the transformation needs to be done as follows [25], [137]:

$$\begin{aligned}
&\frac{d}{dt}\left\{\begin{bmatrix}\cos\omega t & \sin\omega t\\ -\sin\omega t & \cos\omega t\end{bmatrix}\begin{bmatrix}i_\alpha\\ i_\beta\end{bmatrix}\right\}\\
&=\begin{bmatrix}\frac{di_\alpha}{dt}\cos\omega t + \frac{di_\beta}{dt}\sin\omega t - \omega\sin\omega t\, i_\alpha + \omega\cos\omega t\, i_\beta\\ -\frac{di_\alpha}{dt}\sin\omega t + \frac{di_\beta}{dt}\cos\omega t - \omega\cos\omega t\, i_\alpha - \omega\sin\omega t\, i_\beta\end{bmatrix}\\
&=\begin{bmatrix}\frac{di_\alpha}{dt}\cos\omega t + \frac{di_\beta}{dt}\sin\omega t\\ -\frac{di_\alpha}{dt}\sin\omega t + \frac{di_\beta}{dt}\cos\omega t\end{bmatrix}+\begin{bmatrix}-\omega\sin\omega t\, i_\alpha + \omega\cos\omega t\, i_\beta\\ -\omega\cos\omega t\, i_\alpha - \omega\sin\omega t\, i_\beta\end{bmatrix}\\
&=\begin{bmatrix}\cos\omega t & \sin\omega t\\ -\sin\omega t & \cos\omega t\end{bmatrix}\frac{d}{dt}\begin{bmatrix}i_\alpha\\ i_\beta\end{bmatrix}+\begin{bmatrix}-\omega\sin\omega t + \omega\cos\omega t\\ -\omega\cos\omega t - \omega\sin\omega t\end{bmatrix}\begin{bmatrix}i_\alpha\\ i_\beta\end{bmatrix}\\
&=\frac{d}{dt}\begin{bmatrix}i_d\\ i_q\end{bmatrix}+\begin{bmatrix}0 & \omega\\ -\omega & 0\end{bmatrix}\begin{bmatrix}\cos\omega t & \sin\omega t\\ -\sin\omega t & \cos\omega t\end{bmatrix}\begin{bmatrix}i_\alpha\\ i_\beta\end{bmatrix}\\
&=\frac{d\vec{i}_{dq}}{dt}+\begin{bmatrix}0 & \omega\\ -\omega & 0\end{bmatrix}\vec{i}_{dq}
\end{aligned} \tag{2.71}$$

then (2.70) now becomes:

$$\vec{v}_{i,dq} = L\frac{d\vec{i}_{dq}}{dt} + \begin{bmatrix}0 & \omega L\\ -\omega L & 0\end{bmatrix}\vec{i}_{dq} + \vec{v}_{g,dq} \tag{2.72}$$

The ωL represent the cross-coupling between the direct and quadrature axis, thus the two axes are no longer independent from each other. The cross-coupling term can be considered as a control disturbance that needs to be corrected to achieve accurate control. Therefore, a decoupling feed-forward path must be included in the close loop current controller and (2.72) can be further derived as follows:

$$\begin{aligned}
&\mathcal{L}\left(\vec{v}_{i,dq}\right) = \mathcal{L}\left(L\frac{d\vec{i}_{dq}}{dt} + \begin{bmatrix} 0 & \omega L \\ -\omega L & 0 \end{bmatrix}\vec{i}_{dq} + \vec{v}_{g,dq}\right) \\
&\Rightarrow \vec{V}_{i,dq} = sL\vec{I}_{dq} + \begin{bmatrix} 0 & \omega L \\ -\omega L & 0 \end{bmatrix}\vec{I}_{dq} + \vec{V}_{g,dq} \\
&\Rightarrow \vec{D}_{dq}V_d = sL\vec{I}_{dq} + \begin{bmatrix} 0 & \omega L \\ -\omega L & 0 \end{bmatrix}\vec{I}_{dq} + \vec{V}_{g,dq} \\
&\Rightarrow \vec{I}_{dq} = \vec{D}_{dq}\frac{V_d}{sL} - \frac{\vec{I}_{dq}}{sL}\begin{bmatrix} 0 & \omega L \\ -\omega L & 0 \end{bmatrix} - \frac{\vec{V}_{g,dq}}{sL}
\end{aligned} \tag{2.73}$$

Equation (2.73) states that the inverter current in the rotating reference frame is shaped by the duty cycle, cross-coupling between the d and q components and the grid voltage as shown in Figure 72. In addition, (2.73) also shows that the applied voltage includes a component that decouples the direct and quadrature axes from one another as derived in [25].

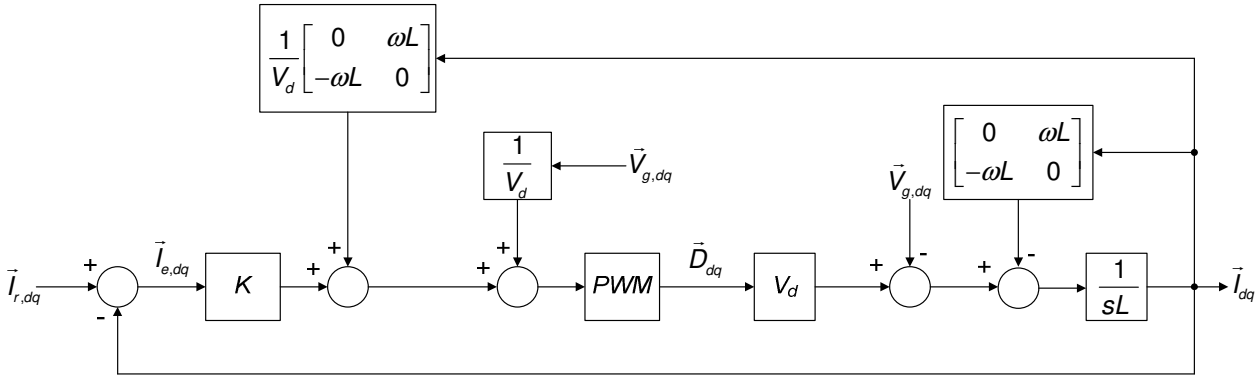

Figure 72: Inverter control block diagram in the frequency domain with feedforward of grid voltage and current to cancel their effect on output

When the duty cycle is calculated, the secondary influences on the current waveform should be taken into account as follows:

$$\vec{D}_{dq} = \frac{sL\vec{I}_{dq}}{V_d} + \frac{\vec{I}_{dq}}{V_d}\begin{bmatrix} 0 & \omega L \\ -\omega L & 0 \end{bmatrix} + \frac{\vec{V}_{g,dq}}{V_d} \tag{2.74}$$

When these terms are feed forward as shown in Figure 72 the feedback system can be reduced to the model in Figure 73.

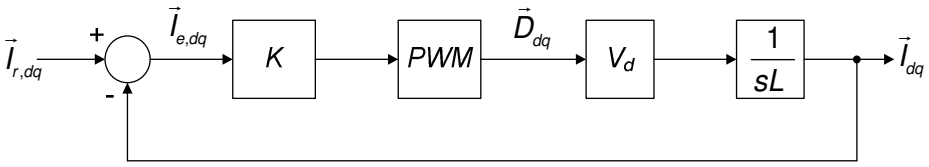

Figure 73: Reduced model of inverter control block diagram in the frequency domain with feedforward of grid voltage and current to cancel their effect on output

The linearized open loop transfer function can be calculated as follows:

$$\begin{aligned}\vec{I}_{dq} &= \frac{1}{sL}\left(\left(\vec{I}_{e,dq}K(s)+\frac{\vec{V}_{g,dq}}{V_d}\right)PWM(s)\,V_d-\vec{V}_{g,dq}\right)\\ &= \frac{1}{sL}\left(\vec{I}_{e,dq}K(s)\,PWM(s)\,V_d+\vec{I}_{dq}\begin{bmatrix}0 & \omega L\\ -\omega L & 0\end{bmatrix}PWM(s)+\vec{V}_{g,dq}\,PWM(s)-\vec{I}_{dq}\begin{bmatrix}0 & \omega L\\ -\omega L & 0\end{bmatrix}-\vec{V}_{g,dq}\right)\\ &\approx \frac{1}{sL}\vec{I}_{e,dq}(s)K(s)\,PWM(s)\,V_d\end{aligned}$$

(2.75)

The open loop transfer function $G_{OL}(s)$ include a controller $K(s)$ and the non-linear effect of pulse width modulation $PWM(s)$. The $PWM(s)$ function is assumed to be a simplified delay function using Padé approximation in (2.76).

$$\text{PWM}(s) = e^{-T_d s} = \frac{1-\frac{T_d s}{2}}{1+\frac{T_d s}{2}} \tag{2.76}$$

The open loop transfer function now becomes:

$$\begin{aligned}G_{OL}(s) &= \frac{I_{dq}(s)}{I_{e,dq}(s)} = K(s)\frac{PWM(s)V_d}{sL}\\ &= K(s)\frac{1-\frac{T_d s}{2}}{1+\frac{T_d s}{2}}\frac{V_d}{sL}\\ &= K(s)\frac{-V_d T_d s+2V_d}{LT_d s^2+2Ls}\end{aligned} \tag{2.77}$$

It was decided to implement a PI controller by plotting a locus of the closed loop poles from knowledge of the open loop transfer function. If it is assumed that the inverter switches at 5 kHz and samples twice per switching cycle then $T_d = 100\ \mu\text{s}$. The DC voltage is arbitrary chosen large enough for linear operation and is thus chosen as 1200 V with a filter inductance of 38 μH. $K(s)$ is substituted in (2.77) by $K_p+\frac{K_i}{s}$ as follows:

$$\begin{aligned}G_{OL}(s) &= K(s)\frac{-V_d T_d s+2V_d}{LT_d s^2+2Ls}\\ &= \left(K_p+\frac{K_i}{s}\right)\frac{-V_d T_d s+2V_d}{LT_d s^2+2Ls}\\ &= \frac{-K_p V_d T_d s^2+(2K_p V_d-K_i V_d T_d)s+2K_i V_d}{LT_d s^3+2Ls^2}\\ &= K_p\frac{-V_d T_d s^2+(2V_d-\frac{K_i}{K_p}V_d T_d)s+2\frac{K_i}{K_p}V_d}{LT_d s^3+2Ls^2}\end{aligned} \tag{2.78}$$

In the equation above the value of K_i was selected as 1000 times the value K_p to make sure it is larger than the integral term value in the power controller so that its reaction time is much faster. A value for K_p was selected by investigating the root locus plot of Figure 74. The locus shows that the maximum controller gain that can be selected before the system controller becomes unstable is 0.00059. Since the controller in PowerFactory uses per unit values, a conversion factor equal to the current base value of 1924 A should be used to calculate the controller gain to obtain a maximum value of 1.154. The gain value $K_p = 0.6$ (0.0003 on locus) was selected to obtain good damping ratio of 0.36 and about 30% overshoot. The corresponding integrator gain is $K_i = 600$ that gives settling time of approximately 2 ms.

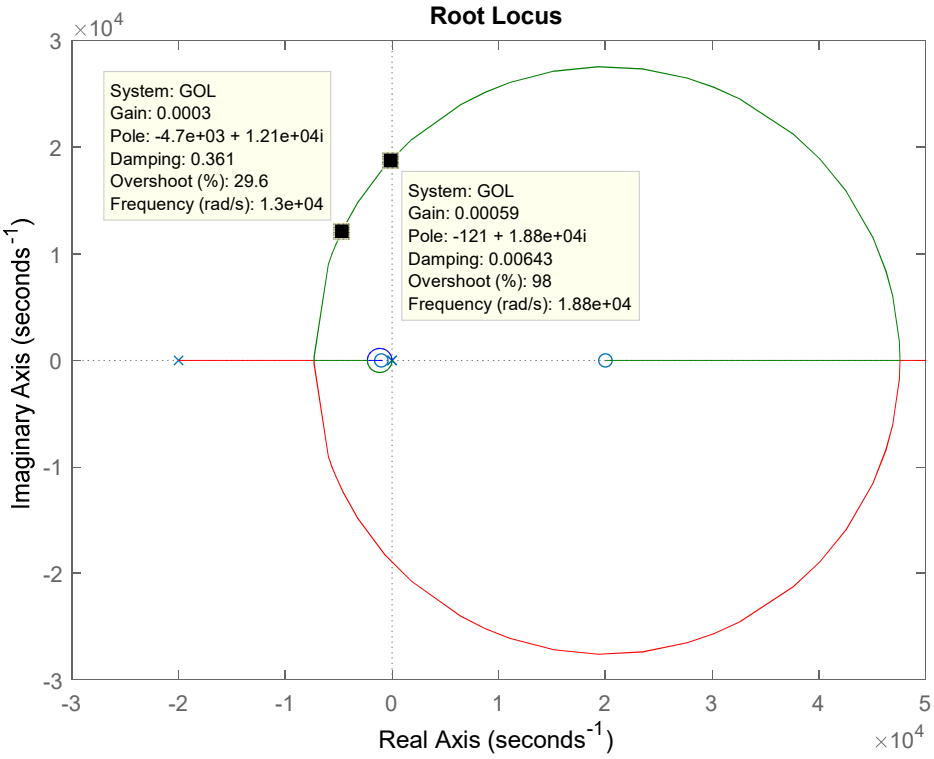

Figure 74: Root locus plot of the current controller

Figure 75 shows the block diagram of the current controller in DIgSILENT PowerFactory.

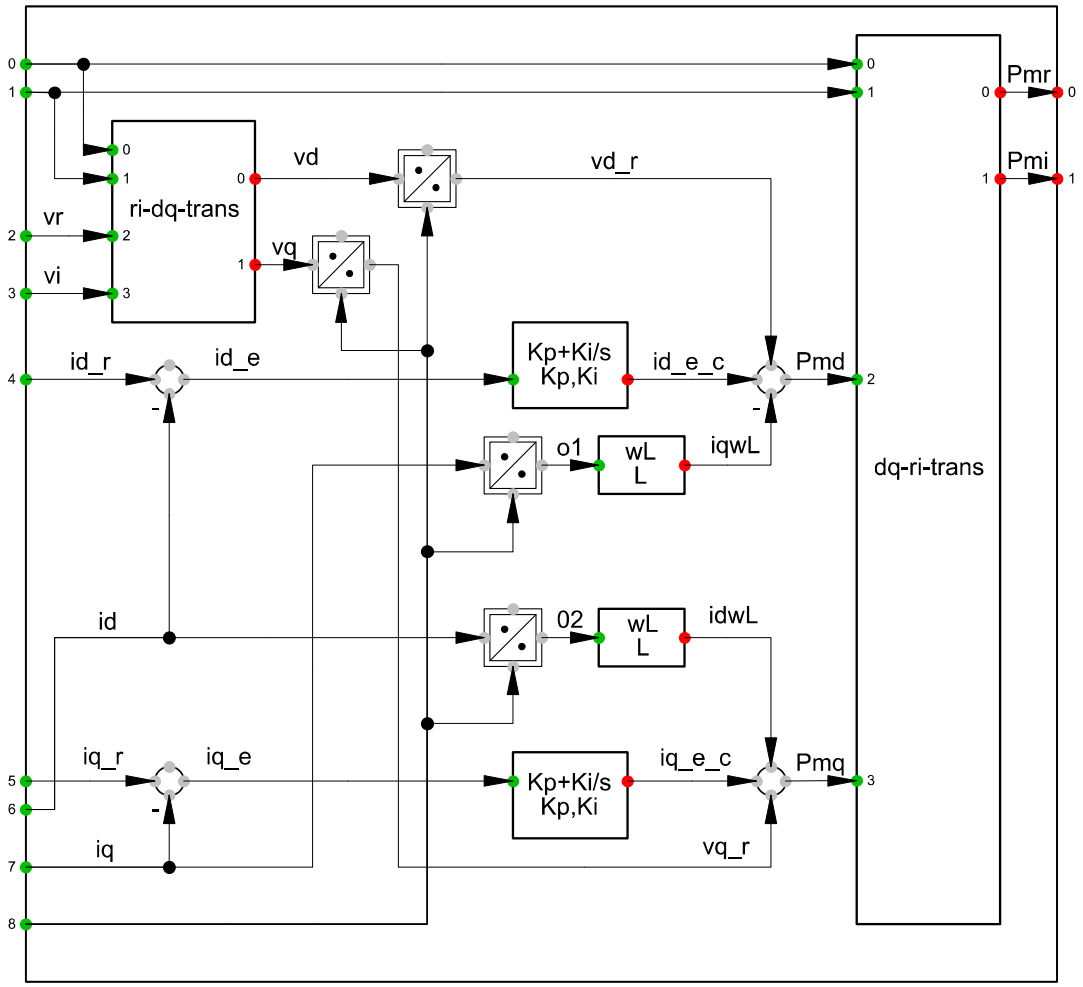

Figure 75: Current controller block diagram in DIgSILENT PowerFactory

3.6.5. DIgSILENT PowerFactory interleaved PWM inverter model – Wind farm B (revised)

3.6.5.1. Overview

The method used to control the conventional three-phase PWM inverter as described in Section 3.6.4 cannot be used for an interleaved converter due to the fact that the method in DIgSILENT PowerFactory does not allow for the control of the triangular waveform. This is important because for an interleaved inverter with three parallel inverters the triangular waveform of each inverter must be phase shifted by 120 degrees. Therefore, an interleaved PWM inverter system can be modelled by controlling each inverter individually but ensuring that the reference triangular waveform of each inverter is phase shifted by 120 degrees. A single three-phase PWM inverter can be modelled based on the control theory described in Section 3.4. The aim of the modelling is to control the inverter so that the inverter is supplying power to the grid and in turn injecting harmonic currents into the grid. The power generation of each individual inverter within the interleaved inverter system must be equal to a third of the total power generation of the interleaved inverter. This will provide a method to study the effects

of an interleaved inverter system on the PQ of the system. A single-line diagram of a PWM interleaved inverter system connected to the grid is shown in Figure 76.

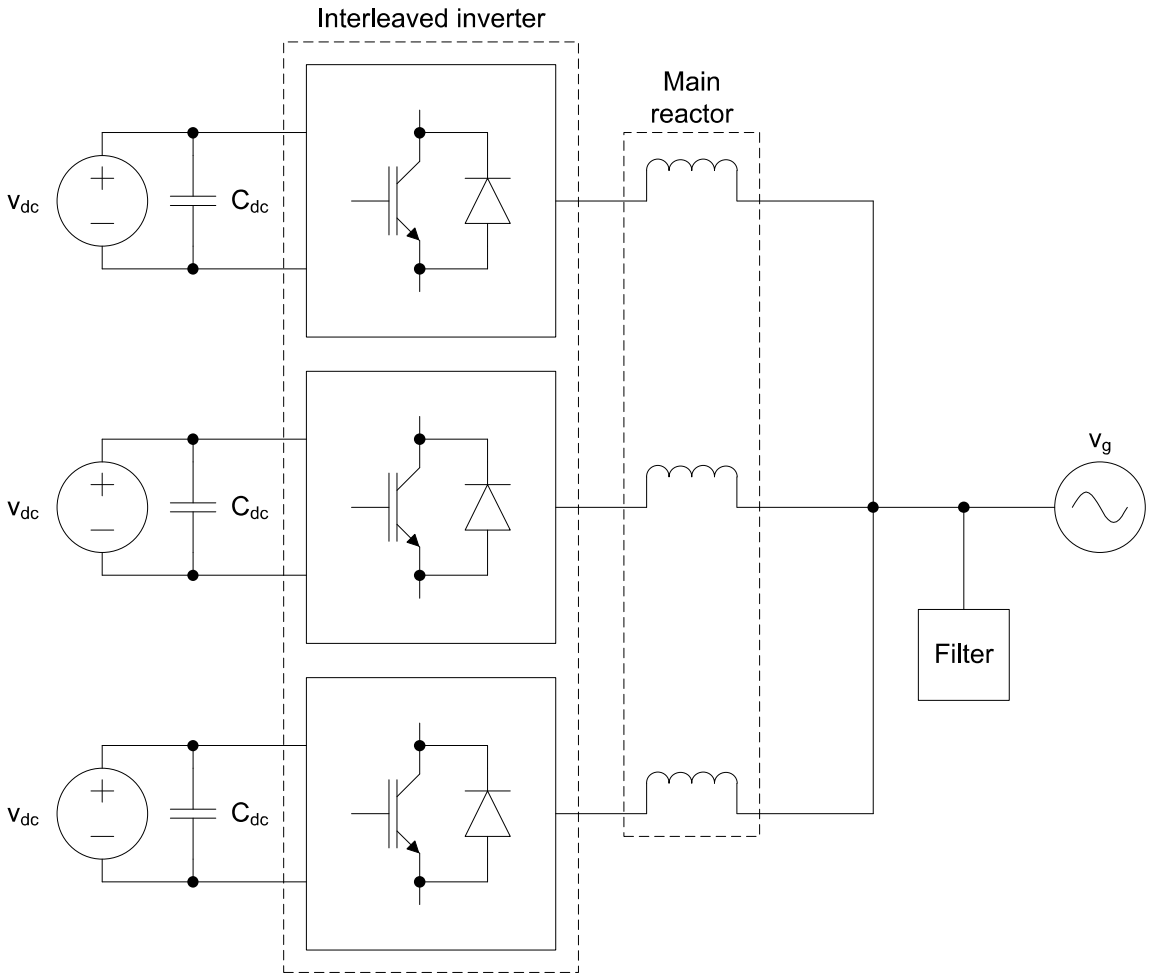

Figure 76: Single-line diagram of interleaved inverter connected to grid

3.6.5.2. Element layout in DIgSILENT PowerFactory

The wind plant model of an interleaved PWM controlled inverter system was built with predefined elements in DIgSILENT PowerFactory as shown in Figure 77. As with the conventional PWM wind farm system both the AC and DC sides are modelled as simple voltage sources and the system further consists of a 132/33 kV transformer, 33/0.69 kV transformer, a grid reactor and passive filters. However, with the interleaved PWM inverter system, the inverter is modelled as three parallel inverters each connected to the grid through a grid reactor.

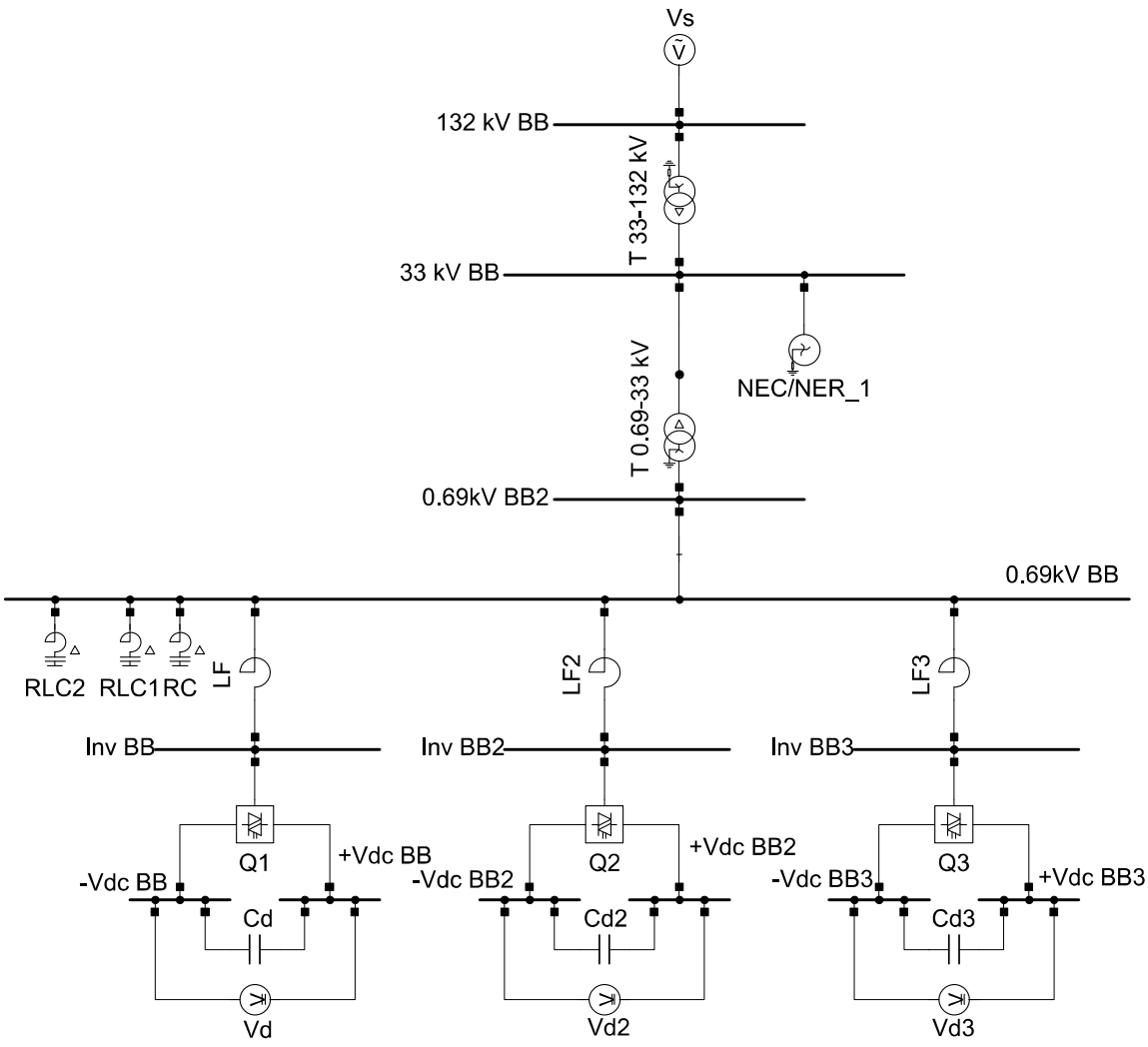

Figure 77: Network diagram of interleaved PWM inverter in DIgSILENT PowerFactory

3.6.5.3. Composite model of a single three-phase PWM inverter

The control of a single inverter of an interleaved inverter in DIgSILENT PowerFactory is similar to that described in Section 3.5.1 but for a three-phase system. Therefore, only small adjustments to the system in Section 3.5.1 had to be made to compensate for three-phase control. The composite model of a single three-phase PWM inverter is shown in Figure 78.

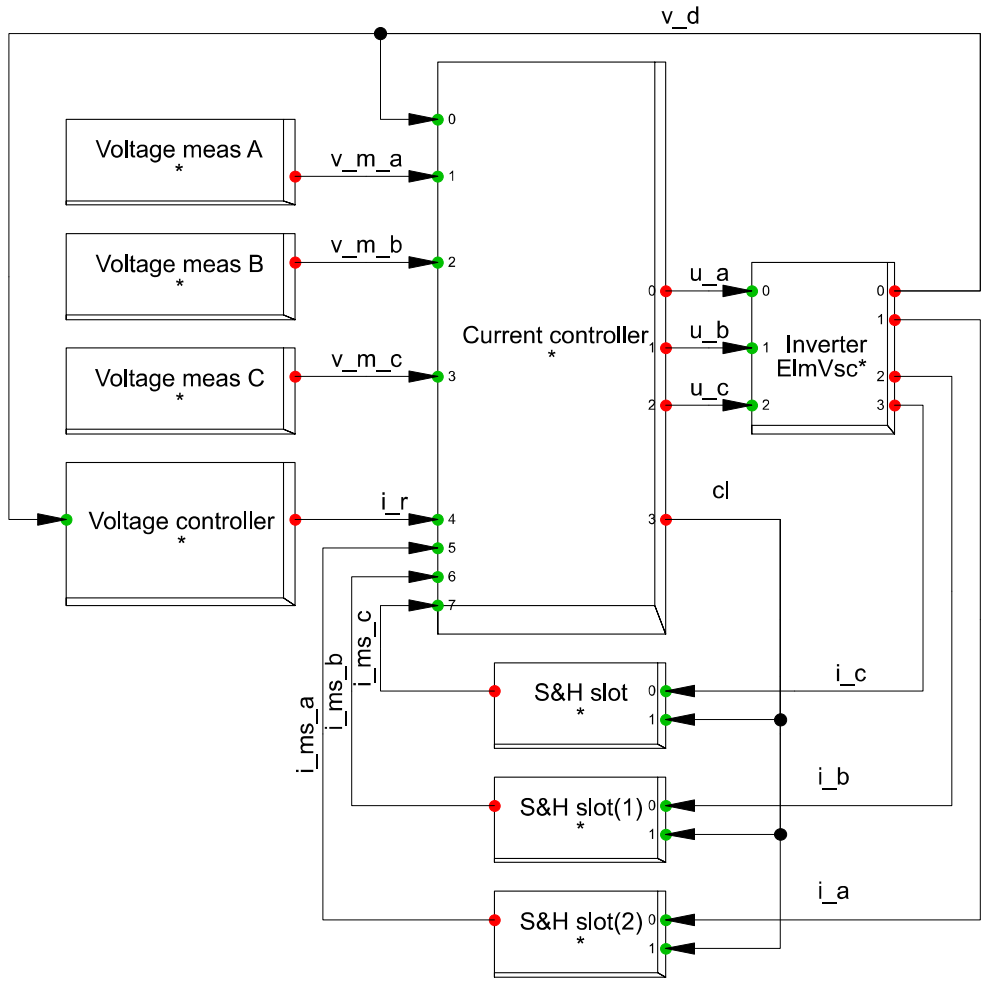

Figure 78: Composite model of PWM inverter in DIgSILENT PowerFactory

For a three-phase PWM inverter the grid phase voltages are measured, with the predefined built-in PLL model (ElmPhi__pll) discussed in Section 3.3.3, as a per unit value and compared to the measured sampled three-phase currents. The measured AC current in kA is sampled twice per switching cycle, i.e. using asymmetrically regular sampling, and is then fed to the input of the current controller. Asymmetrical regular sampling is done using the predefined built-in sample and hold element (ElmSamp) discussed in Section 3.3.4. Therefore, three control signals are obtained that can be compared to the triangular waveform to control the on and off states of the PWM switches of each phase. Due to repetitiveness this will not be discussed in more detail. The PQ analysis of the above designed three-phase interleaved inverter will be shown Section 4.4.3 and will be compared to the measurement results. Keep in mind that the switching frequency and relevant controller values will be adjusted to replicate the measurement results as close as possible.

3.7. CONCLUSION

In this chapter the functionality of DIgSILENT PowerFactory was explained. The built-in PWM converter model and its internal control functions for RMS and EMT simulations were

presented. All of the necessary built-in elements that were used in simulation models were discussed.

Traction load customers do not provide details on the control of their rectifiers, therefore, it was deemed necessary to model rectifiers so to completely understand the principles and control of traction loads on a network. The design and implementation of these generic rectifier models, in particular for EMT simulation, is relevant to this project to investigate the PQ impact of traction loads on the network. The theory, control, modelling and implementation of the two main locomotives technologies types in South Africa were presented. The power flow theory along with its implementation to control an active rectifier or PWM inverter was discussed. A generic model of an active rectifier was implemented and the basic functionality in DIgSILENT PowerFactory in EMT simulation was shown. DIgSILENT PowerFactory lack the functionality to simulate a half-controlled thyristor rectifiers and do not permit the connection of a DC bus directly to an AC bus. Therefore, a method was devised on how a half-controlled thyristor rectifier can be implemented in DIgSILENT PowerFactory. A generic model of a half-controlled thyristor rectifier was implemented and the basic functionality in DIgSILENT PowerFactory in EMT simulation was shown. These models can be compared to actual traction load systems for future PQ studies and network planning.

Customers and RPPs do not provide details on the control of their inverters, therefore, it was deemed necessary to model inverter so to completely understand the principles and control of grid-connected inverters. The design and implementation of these generic inverter models, in particular for EMT simulation, is relevant to this project to investigate PQ in RPPs. The control of the wind farm inverters for the two case studies was discussed. The conventional hysteresis control in Wind farm A was investigated and mathematically analysed. A generic conventional hysteresis inverter model, with the actual filter equipment installed at Wind farm A, was designed and implemented in DIgSILENT PowerFactory for EMT simulation. The illustration of the implementation of the model in Section 3.6.3.6 shows the drawbacks to the implementation of the conventional hysteresis inverter. The conventional PWM control approach in RPPs was investigated and mathematically analysed. A generic conventional PWM inverter model was designed and implemented in DIgSILENT PowerFactory for EMT simulation. The interleaved PWM control approach in Wind farm B was investigated. A method was devised on how an interleaved inverter can be implemented in DIgSILENT PowerFactory. A generic interleaved PWM inverter model, with the actual filter equipment installed in Wind farm B, was designed and implemented in DIgSILENT PowerFactory for EMT simulation. These models can be compared to actual wind farm systems for future PQ studies and network planning. The reliability of each model will be investigated by comparing simulation results to measurement results in the following chapter.

CHAPTER 4
THE IMPACT OF WIND FARMS ON NETWORK HARMONICS

4.1. INTRODUCTION

In this chapter the voltage waveforms, current waveforms and the harmonic content generated by Wind farm A and Wind farm B will be presented. The purpose of this chapter is to determine the switching frequency of the inverters, harmonic spectrum and the amplitude of the harmonics injected into the grid. Measurement results taken at turbine level for both Wind farm A and Wind farm B will be shown to obtain a general idea of the switching frequency of the inverters and the harmonics generated by the inverters. The designed models in Section 3.6.3, Section 3.6.4 and Section 3.6.5 will then be adjusted to reflect the measurement results as closely as possible and lastly be compared to the measurement results to validate the generic models.

4.2. MEASURMENT SETUP AT WIND FARMS

Wind farm A and Wind farm B can be represented by the single-line diagram in Figure 79. In Wind farm A, a 33 kV ring feed is connected to the main grid by means of a 90 MVA, 132 kV to 33 kV transformer. Each turbine inverter is connected to the 33 kV line by means of a 2.7 MVA, 33 kV to 690 V transformer. In Wind farm B, a 33 kV ring feed is connected to the main grid by means of a 80 MVA, 132 kV to 33 kV transformer. Each turbine inverter is connected to the 33 kV line by means of a 2.6 MVA, 33 kV to 690 V transformer. For measurement purposes an oscilloscope was used for short-term snapshots of the voltage and current waveforms as well as their respective harmonic spectrums. In addition, an Elspec PQ class A measurement instrument was installed to record data for a period of few hours. The Elspec and oscilloscope was installed at the inverter AC terminals. The Elspec was connected through voltage transformers (VTs) and current transformers (CTs). Figure 79 shows the location where the Elspec and oscilloscope measurements were taken.

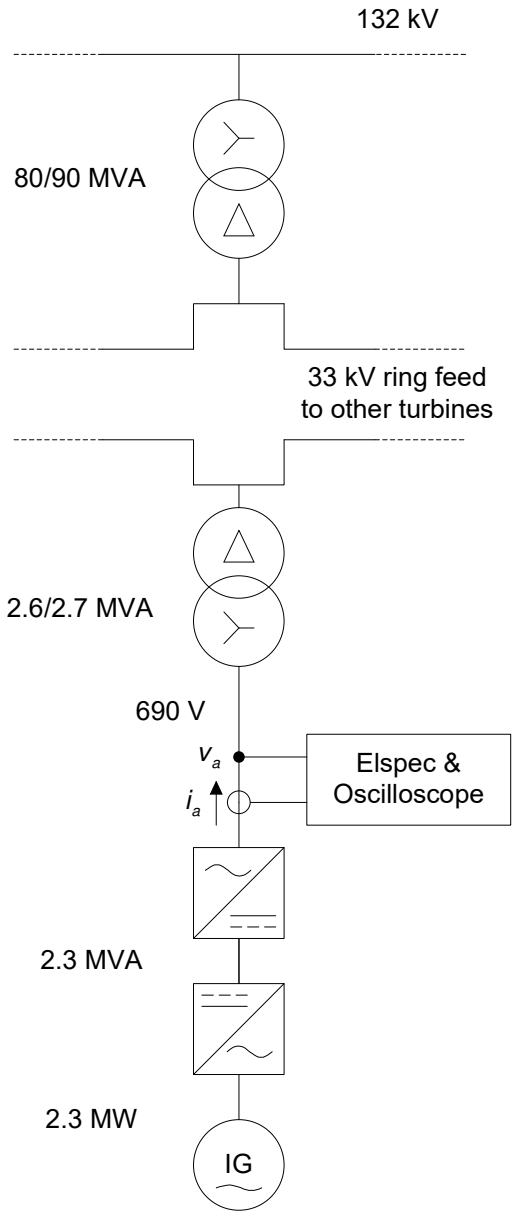

Figure 79: Single-line diagram of the wind farm installation

The electrical diagram of the Elspec installation at the inverter AC terminals is shown in Figure 80. Three voltage clamps are connected to the L1, L2 and L3 ports of the Elspec and to the three voltage transformer connections in the measurement panel. Another voltage clamp is connected to the earth port of the Elspec and grounded on the measurement panel. Three current probes are connected to the I1, I2 and I3 ports of the Elspec and are clamped over the phase A, phase B and phase C cable of the CT in the measurement panel.

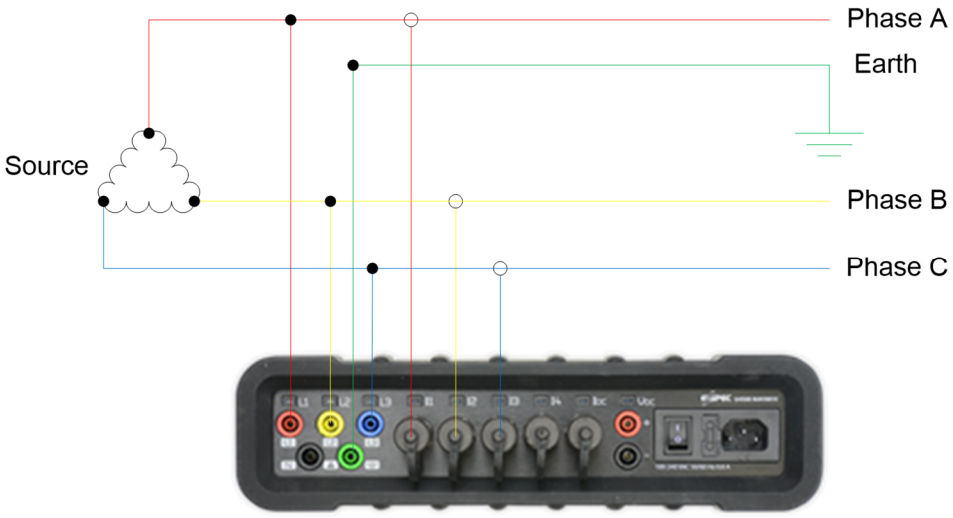

Figure 80: Three-phase delta 3 wire Elspec connection diagram

The Elspec must further be setup to ensure that the measurement data are recorded as expected. The Elspec connection configuration must be setup to use the delta 3 wire connection type. The VT and CT ratios must be changed according to those on site. The Elspec meet the measurement specifications and standards discussed in Section 2.5.3.

4.3. WIND FARM A – HYSTERESIS INVERTER

4.3.1. Measurement results – Oscilloscope

Figure 81 and Figure 82 show the inverter phase voltage and phase current waveform at the Wind farm A. The measurements in Figure 81 and Figure 82 were taken on the secondary of a CT on the inverter AC terminals that has a 2500:1 ratio i_a. The voltage is directly measured at the 690 V Padmount transformer bus bars.

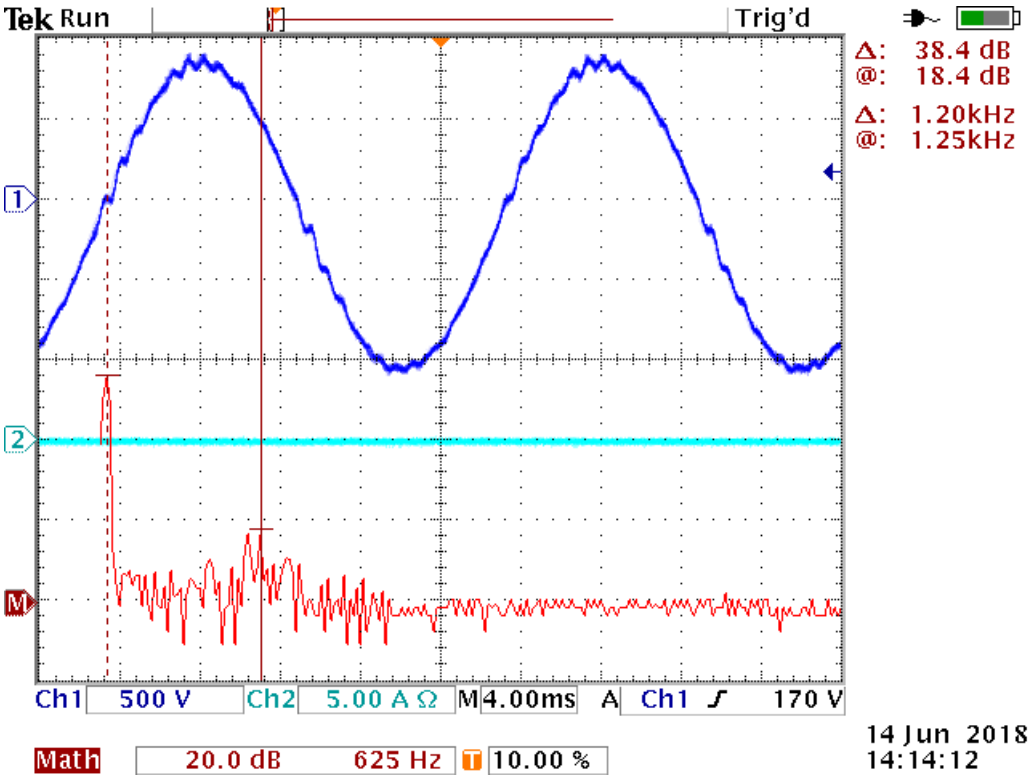

Figure 81: Inverter phase voltage (blue) and phase voltage harmonic spectrum (red) (snapshot 1) measured by oscilloscope

Figure 81 shows that the switching frequency is not well defined, but changes in a band from 0.75 kHz to 1.5 kHz. This is the typical characteristic of a hysteresis controller. The switching ripple amplitude is 18.4 dB or 8.31 V at 1.15 kHz. The fundamental phase voltage amplitude is 56.8 dB or 691.83 V, therefore, resulting in a 1.2% switching ripple injected into the grid. At the time of this measurement, no low frequencies were present in the phase voltage waveform. This will most probably change with time as traction loads are connected and changes on the connected railway system.

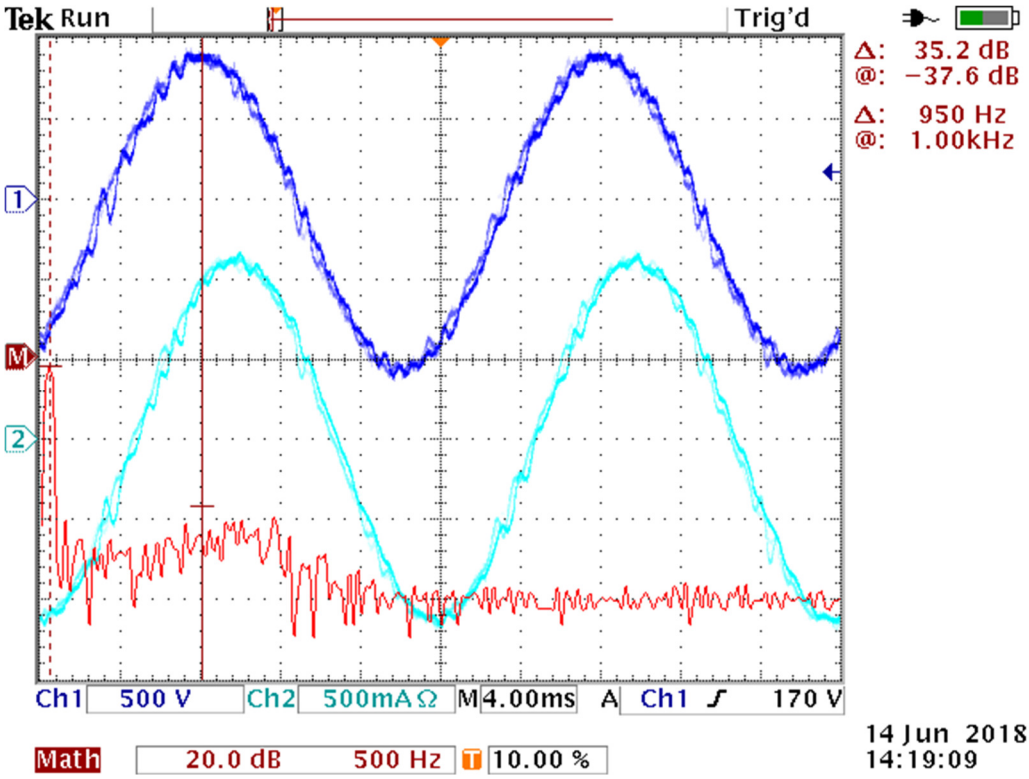

Figure 82: Inverter phase voltage waveform (blue), current waveforms (cyan) and phase current harmonic spectrum (red) (snapshot 2) measured by oscilloscope

Figure 82 shows that there is a band of harmonics from 0.75 kHz to 1.5 kHz with amplitudes around -41 dB or 8.9125 mA that transforms to 22.28 A on the primary side of the CT. The fundamental phase current amplitude is -2.4 dB or 0.7585 A amplitude that transforms to 1896.44 A on the primary side of the CT, therefore, resulting in a 1.175% switching ripple injected into the grid.

From a low frequency harmonic perspective the 3rd, 5th, 7th, 11th and 13th are present with amplitudes around -43 dB or 7 mA on the secondary side of the CT that transforms to 17.7 A on the primary side. That is a 17 A / 880 A = 1.9% emission per harmonic into the grid.

4.3.2. Measurement results – Elspec

For the Elspec measurement results the current and voltage harmonic spectrums will be analysed over different time windows to obtain a clear picture of the generated harmonics.

4.3.2.1. One-cycle window harmonics

The captured phase current waveform for a one-cycle window and phase current harmonic spectrum are shown in Figure 83 and Figure 84 respectively.

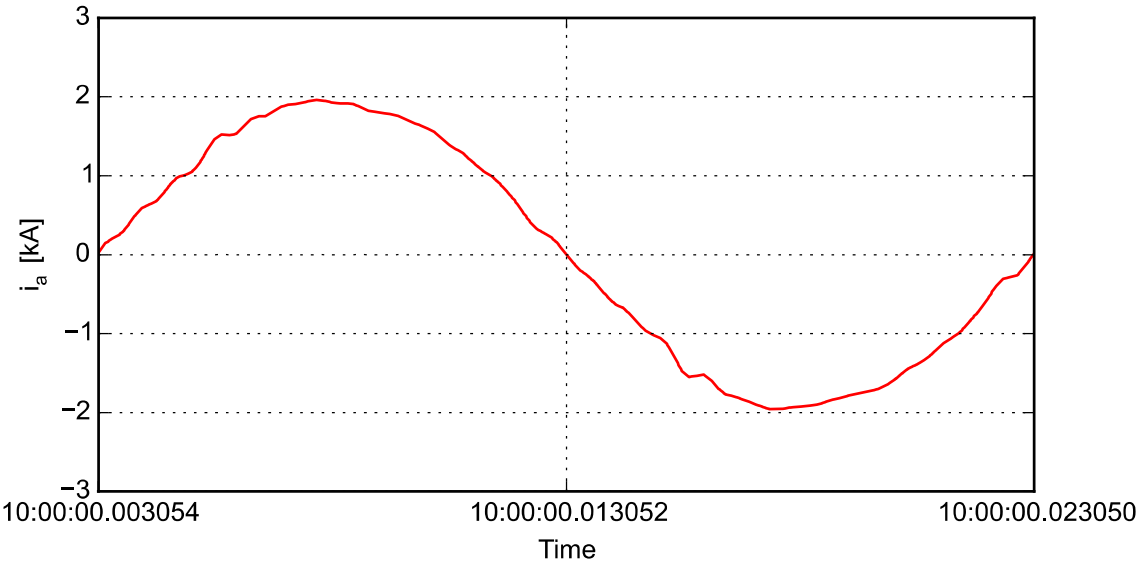

Figure 83: Inverter phase current waveform recorded by Elspec

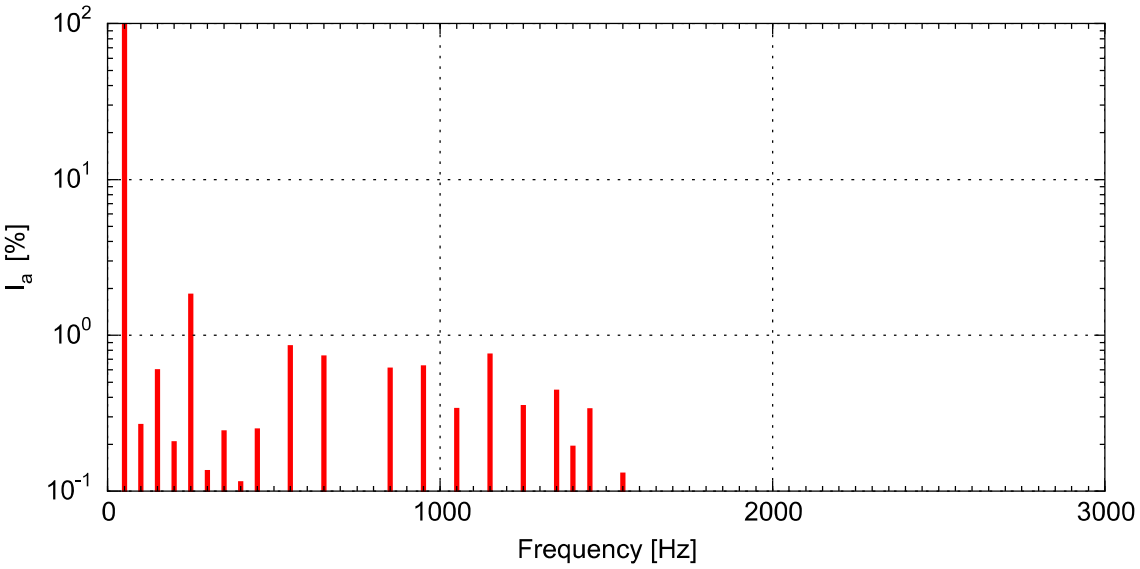

Figure 84: Harmonic spectrum of inverter phase current recorded by Elspec for one-cycle window

The captured phase voltage waveform for a one-cycle window is shown in Figure 85.

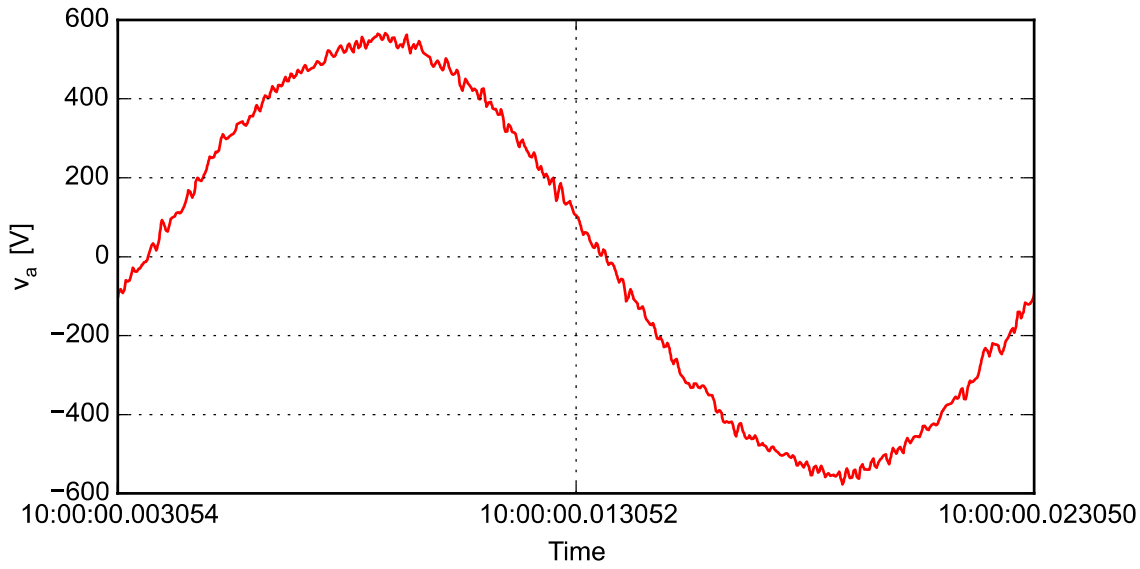

Figure 85: Inverter phase voltage waveform recorded by Elspec

The phase voltage harmonic spectrum up to 10 kHz for a one-cycle window is shown Figure 86.

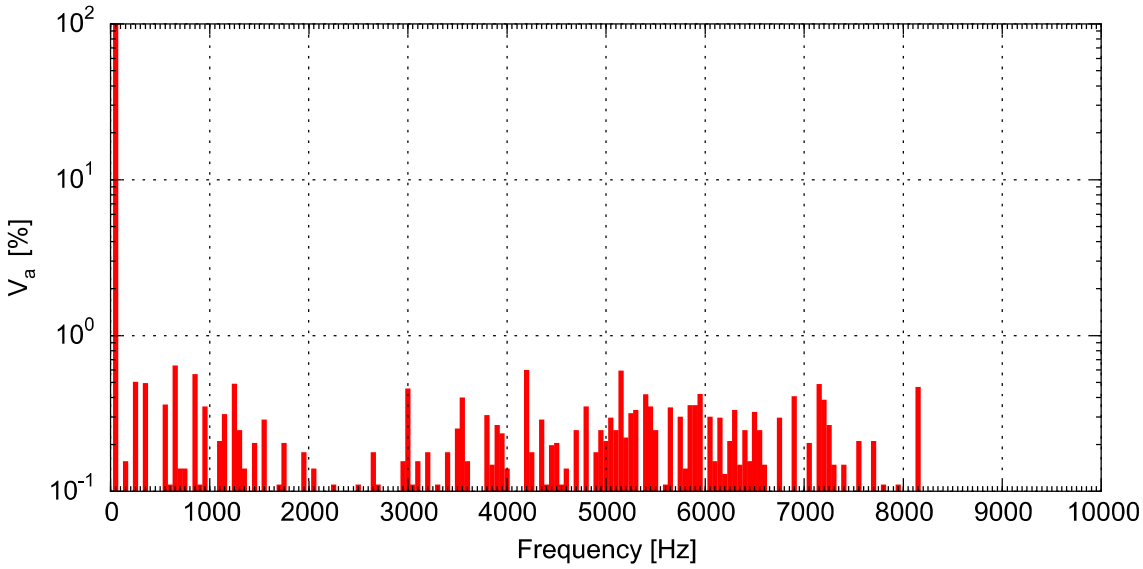

Figure 86: Harmonic spectrum of inverter phase voltage recorded by Elspec for one-cycle window

The harmonics in the range of 3 kHz to 8 kHz as shown in Figure 86 is characteristic of a hysteresis controller, this band will change as one analyses the harmonics for longer time windows. It is important to note that the current harmonic spectrum only shows harmonic content up to the 63rd harmonic or 3.15 kHz because the current sampling rate of the Elspec was set to 128 samples/cycle. The voltage sampling rate is, however, 1024 samples/cycle which will record voltage harmonic content up to the 512th harmonic or 25.6 kHz. Consequently, the high-order harmonics above 3.15 kHz as shown in the phase voltage harmonic spectrum

will not be visible on the phase current waveform. The value of the DC voltage, filter reactance and hysteresis band will all influence the switching frequency of a hysteresis inverter as explained in Section 3.6.3.1. To investigate the lower harmonics the phase voltage harmonic spectrum is plotted up to 3 kHz as shown in Figure 87.

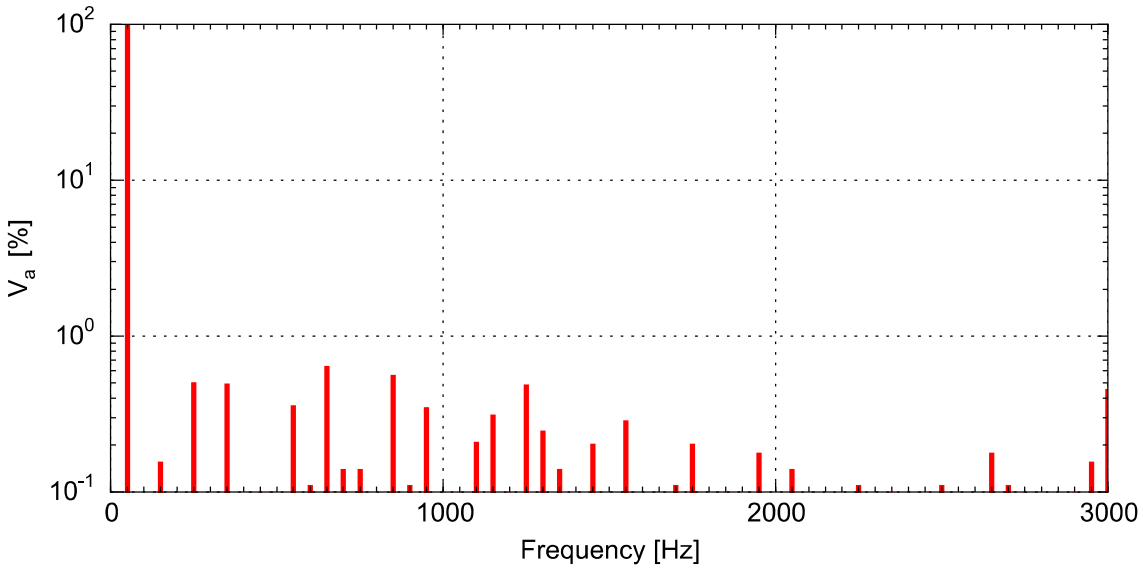

Figure 87: Harmonic spectrum of inverter phase voltage recorded by Elspec for one-cycle window (detailed)

Figure 84 and Figure 87 clearly show the harmonic content at the 3rd, 5th, 7th, 11th and 13th harmonic. By just looking at the harmonic spectrum for a one-cycle window it is hard to determine the cause of the harmonic content at the low frequencies and for the band of harmonics from the 15th up to the 30th harmonic.

4.3.2.2. 3-second window harmonics

The phase current harmonic spectrum up to 3 kHz for a 3-second window is shown Figure 88.

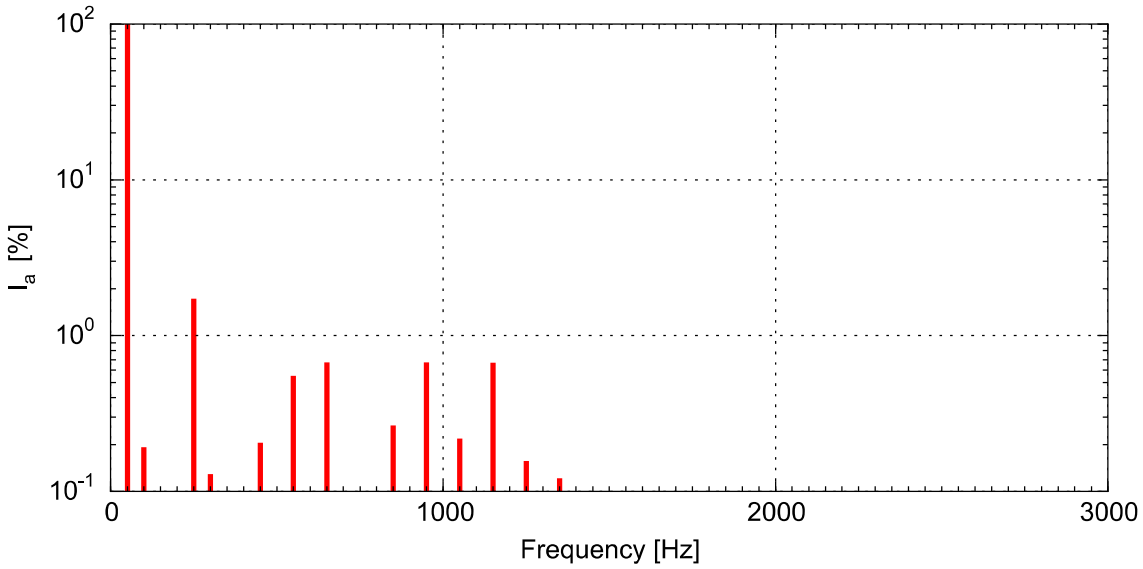

Figure 88: Harmonic spectrum of inverter phase current recorded by Elspec for 3-second window

The phase voltage harmonic spectrum up to 10 kHz for a 3-second window is shown Figure 89.

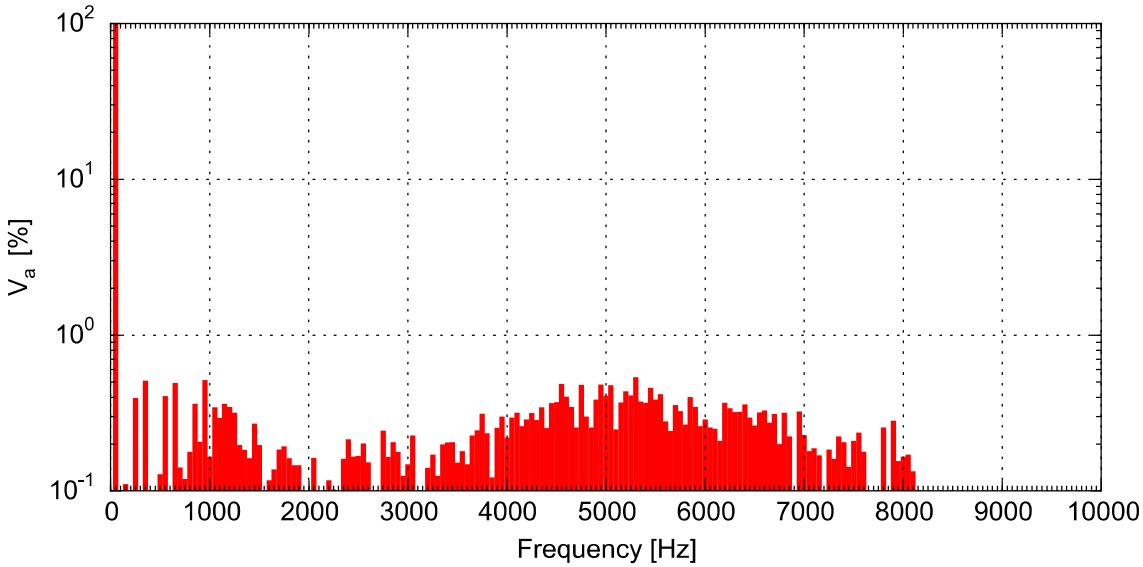

Figure 89: Harmonic spectrum of inverter phase voltage recorded by Elspec for 3-second window

The phase voltage harmonic spectrum up to 3 kHz for a 3-second window is shown Figure 90.

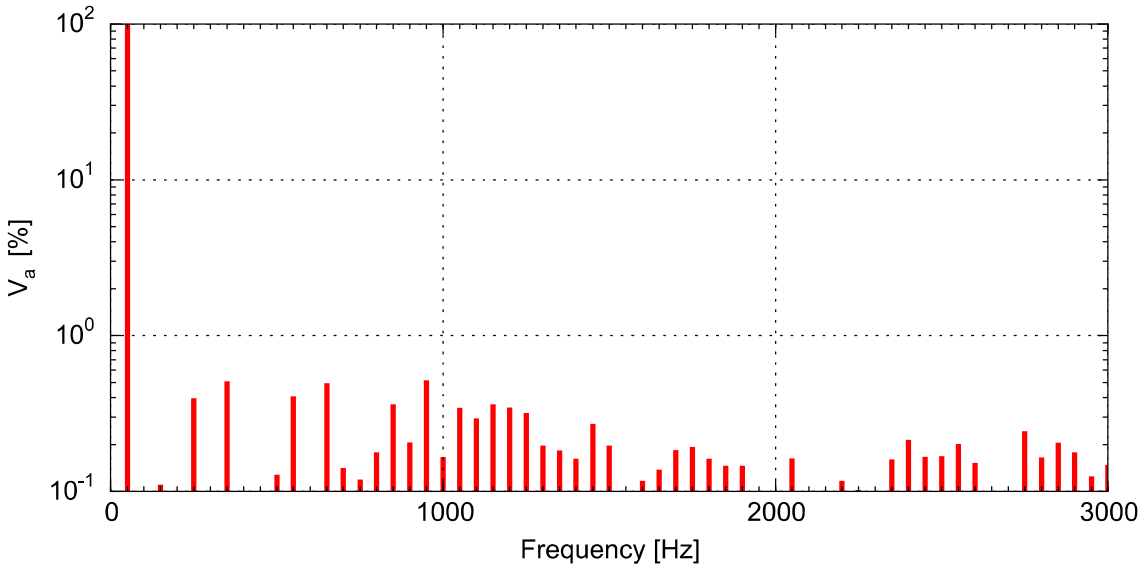

Figure 90: Harmonic spectrum of inverter phase voltage recorded by Elspec for 3-second window (detailed)

Figure 89 and Figure 90 suggest that the harmonics at and around the 23rd harmonic are produced by a parallel resonance at that point as explained in Section 2.7.4. It is well known that a hysteresis controller generate a large range of harmonics. Therefore, even small harmonic content at and around the 23rd harmonic will be enhanced significantly by the presence of a parallel resonance.

4.3.2.3. 10-minute window harmonics

The phase current harmonic spectrum up to 3 kHz for a 10-minute window is shown Figure 91.

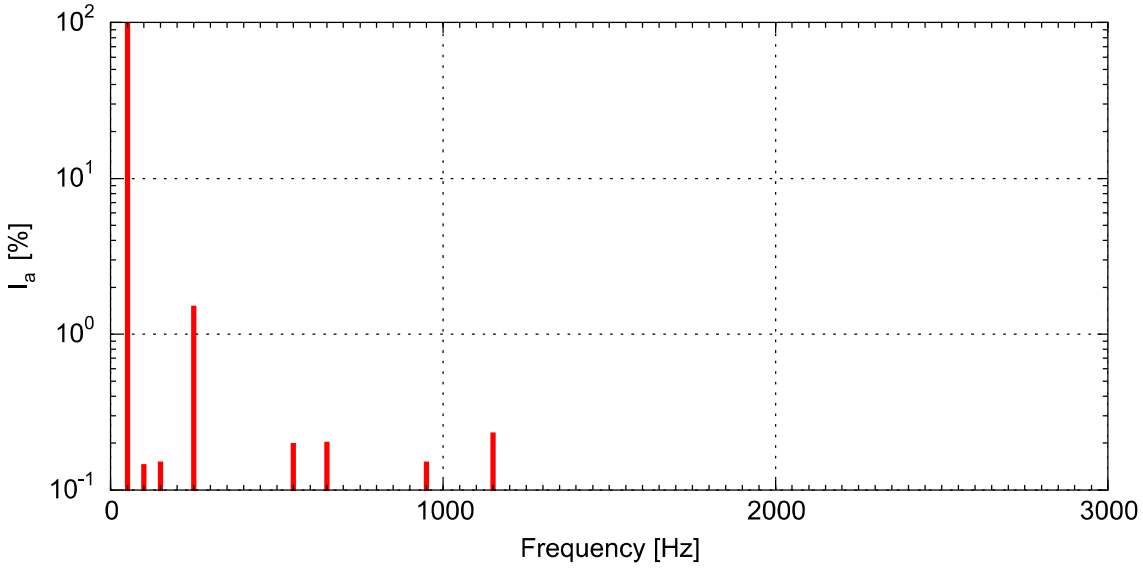

Figure 91: Harmonic spectrum of inverter phase current recorded by Elspec for 10-minute window

The phase voltage harmonic spectrum up to 10 kHz for a 10-minute window is shown Figure 92.

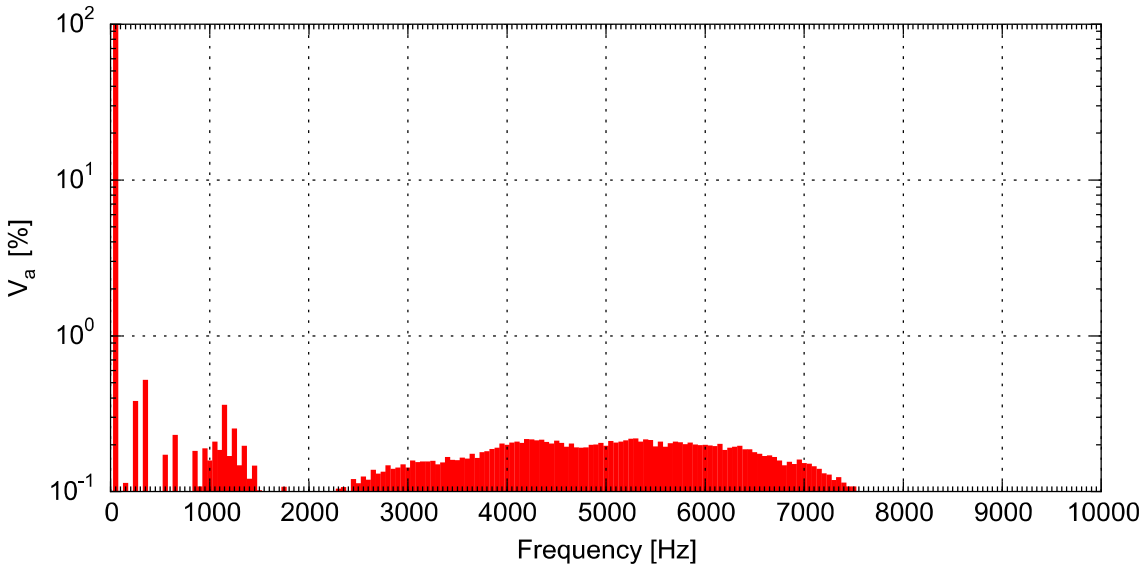

Figure 92: Harmonic spectrum of inverter phase voltage recorded by Elspec for 10-minute window

The phase voltage harmonic spectrum up to 3 kHz for a 10-minute window is shown Figure 93.

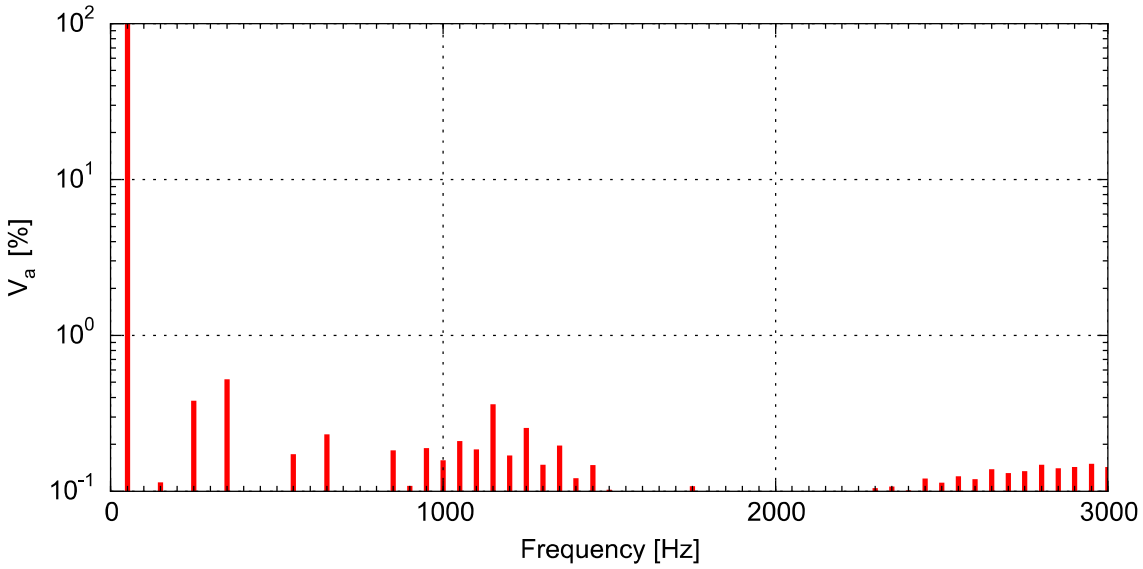

Figure 93: Harmonic spectrum of inverter phase voltage recorded by Elspec for 10-minute window (detailed)

Figure 91, Figure 92 and Figure 93 further suggests that the harmonics at and around the 23rd harmonic are produced by a parallel resonance at that point as explained in Section 2.7.4.

4.3.3. Simulation results - Wind farm A

4.3.3.1. Parallel resonance

To investigate whether a parallel resonance is the cause for the harmonics at and around the 23rd harmonic the complete wind farm must be modelled to reflect the physical system. Therefore, the equipment ratings of the wind farm transformers, cables and turbine filters must be modelled as accurately as possible using DIgSILENT PowerFactory. The network layout of all these equipment in DIgSILENT PowerFactory will not be shown due to the mere size of the wind farm network. The network in DIgSILENT PowerFactory is constructed as shown in Figure 79 with the ring feed of turbines connected with cables and at some places overhead lines. The 132 kV bus is simulated as a slack bus using the external grid element in DIgSILENT PowerFactory with no background harmonics. The turbine is simulated using the generic inverter model presented in Section 3.6.3. A frequency sweep of the network is done and the network impedance at the 0.69 kV terminal is shown in Figure 94.

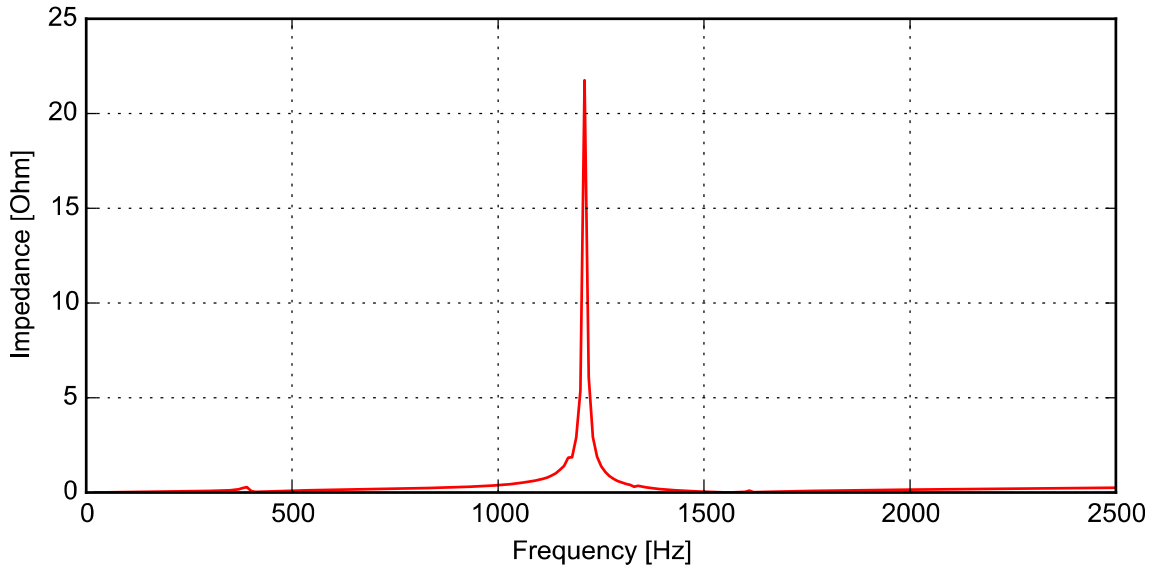

Figure 94: Network impedance at 0.69 kV terminal

The measured and simulated harmonic spectrum can be compared to the network impedance in Figure 94. There is a parallel resonance at the 24th harmonic (1.2 kHz) which explain the harmonics content at and around the 24th harmonic. The network impedance at the 132 kV terminal is shown in Figure 95.

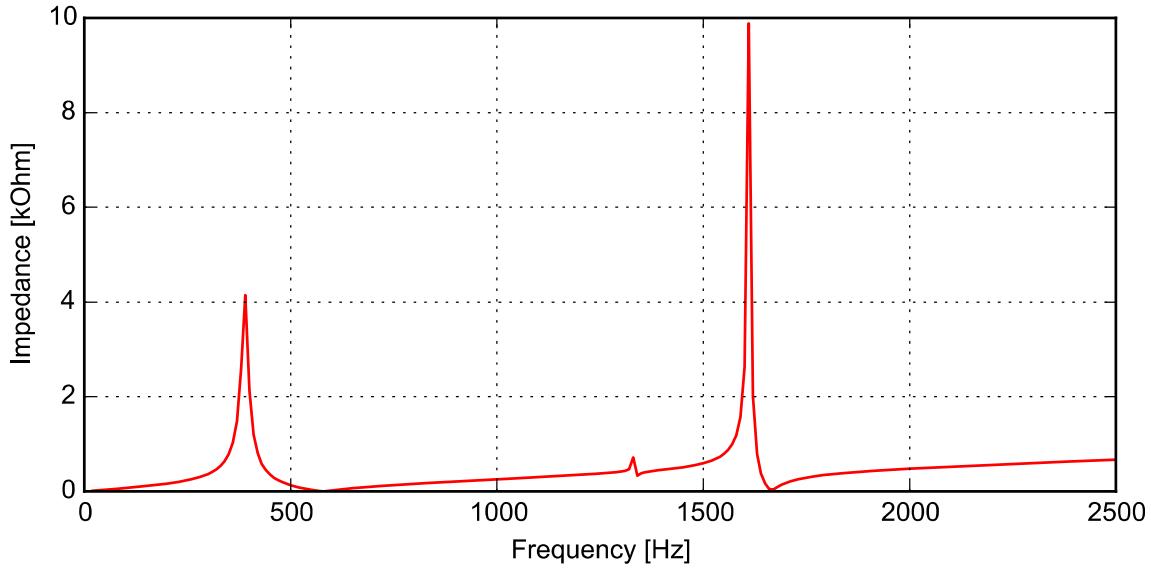

Figure 95: Network impedance at 132 kV terminal

Figure 95 shows a parallel resonance at 350 Hz (7th harmonic) and 1.65 kHz (33rd harmonic) without any other loads connected to the network. The addition of non-linear traction loads which produce harmonics at the parallel resonance locations can lead to distortion problems on the network. This is investigated in Section 6.8 of the thesis.

4.3.3.2. Waveform and harmonic analysis

The simulation results for the hysteresis inverter approach were obtained using the model presented in Section 3.6.3. A single turbine was simulated at rated power, 2.3 MW, and the output phase current of the inverter is shown in Figure 96. The hysteresis band, Δi, was chosen as 5% of the peak current.

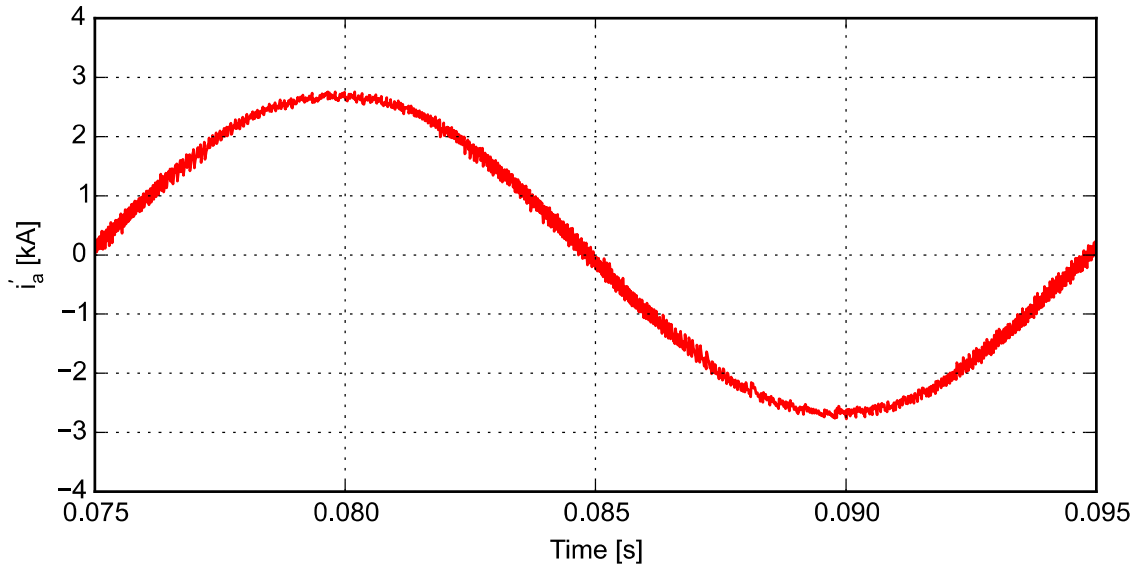

Figure 96: Hysteresis inverter phase current waveform in DIgSILENT PowerFactory

The grid phase current after the grid LCL filter, with values given in Section 3.6.1, is shown in Figure 97.

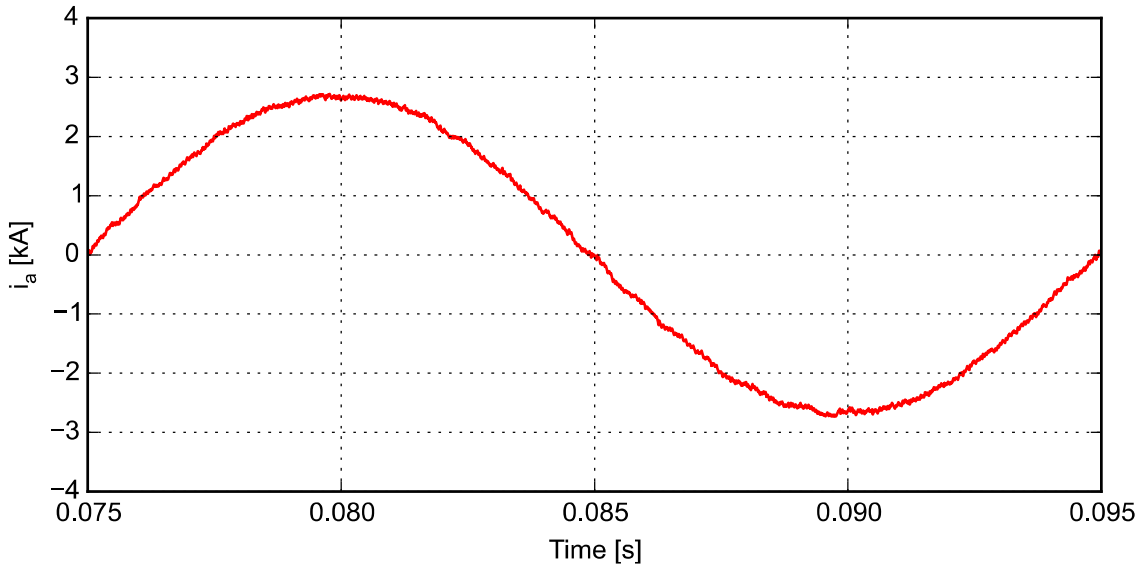

Figure 97: Grid phase current waveform in DIgSILENT PowerFactory

The current harmonic spectrum of the grid phase current is shown Figure 98.

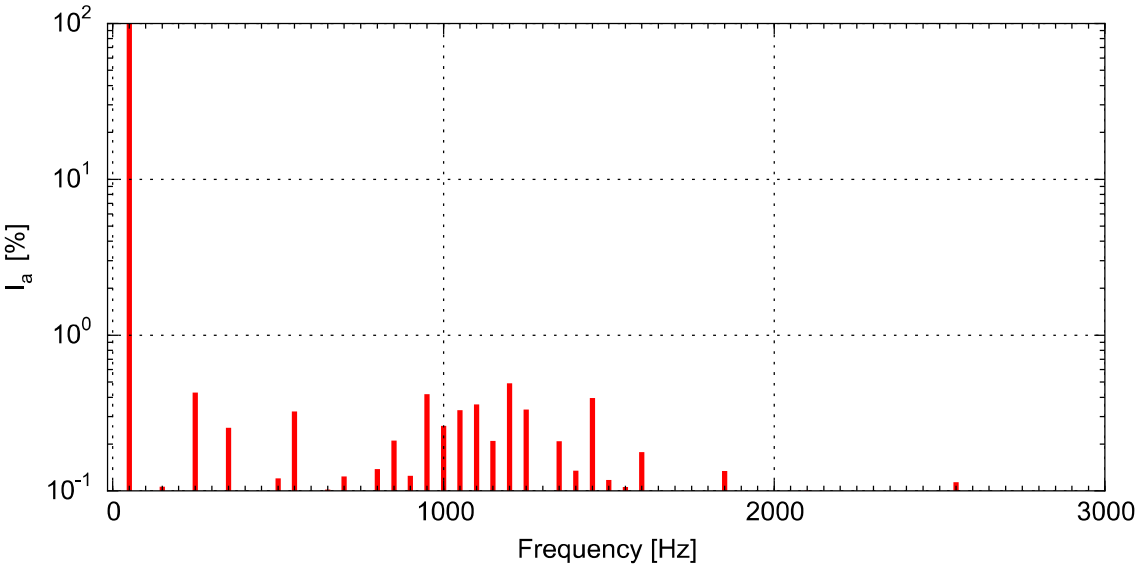

Figure 98: Harmonic spectrum the grid phase current in DIgSILENT PowerFactory

4.3.4. Comparison of measurement and simulation results - Wind farm A

It is shown that both the measured and simulated results contain low-order harmonics which are largely caused by a low DC voltage or high modulation index. The presence of the 3rd harmonic suggests that the method of third harmonic injection is used to increase the modulation index to 1.155 without entering the overmodulation region as explained in [25], [27]. The 5th, 7th, 11th and 13th harmonics are not cancelled due to the sampling method used

[27]. These low-order harmonics are increased due to the implementation of third harmonic injection as explained in Section 2.4.5. Therefore, highlighting the importance of the sampling method used in digital control of inverters.

4.4. WIND FARM B – PWM INVERTER

4.4.1. Measurement results – Oscilloscope

The measurements in Figure 99 and Figure 100 were taken on the secondary of a CT on the inverter AC terminals that has a 2500:1 ratio i_a. The voltage v_a is directly measured at the 690 V Padmount transformer bus bars. By taking this ratio into account the operating point of the inverter is around 880 A. By looking at the harmonic spectrum in Figure 99 it is shown that the inverter switches at 2.5 kHz with a -45 dB or 5 mA RMS amplitude that transforms to 14 A on the primary side of the CT. That is a 14 A / 880 A = 1.6% switching ripple injected into the grid.

From a low frequency harmonic perspective the 5th and 7th are present with amplitudes around -43 dB or 7 mA on the secondary side of the CT that transforms to 17.7 A harmonic on the primary side. That is a 17 A / 880 A = 1.9% emission per harmonic into the grid.

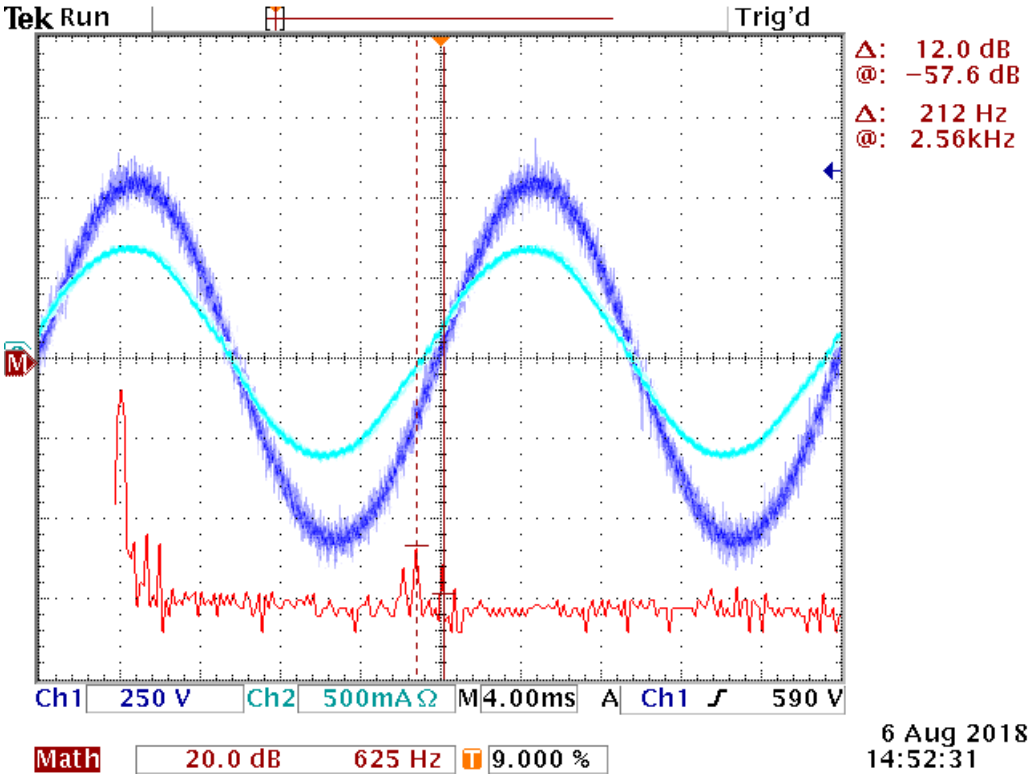

Figure 99: Inverter phase voltage waveform (blue), current waveform (cyan) and phase current harmonic spectrum (red) (snapshot 1) measured by oscilloscope

The phase voltage waveform in Figure 99 and Figure 100 was measured with a voltage probe that was earthed on the inverter panel, since a neutral terminal was not readily available. For this reason it contains significant noise and cannot be used for sensible voltage harmonic analysis.

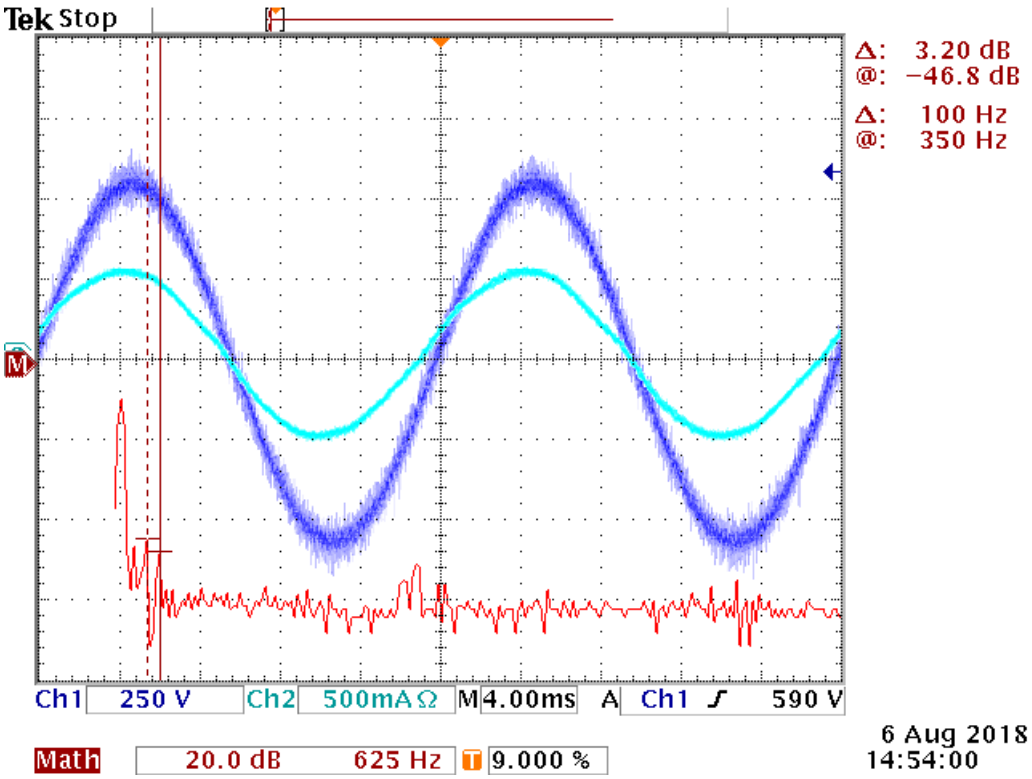

Figure 100: Inverter phase voltage waveform (blue), current waveform (cyan) and phase current harmonic spectrum (red) (snapshot 2) measured by oscilloscope

4.4.2. Measurement results – Elspec

An Elspec PQ recorder was installed at the same location and waveforms were recorded for a period of a few hours. The captured phase voltage waveform, phase voltage harmonic spectrum and a detailed phase voltage harmonic spectrum with values are shown in Figure 101, Figure 102 and Figure 103 respectively. The harmonics correspond with the harmonic spectrums measured with the oscilloscope.

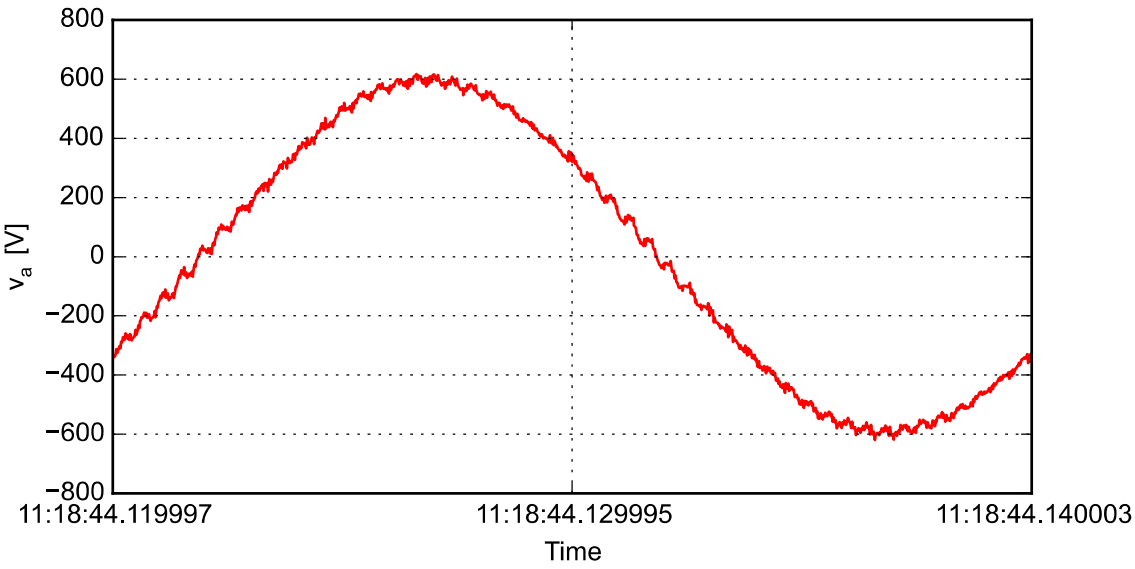

Figure 101: Inverter phase voltage recorded by Elspec (detailed) for one cycle

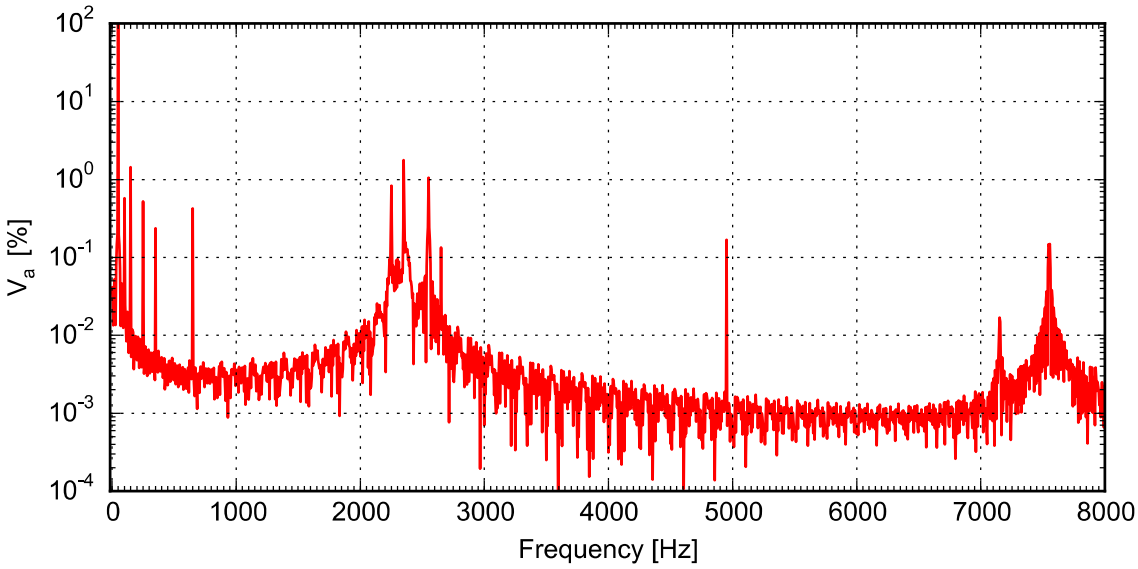

Figure 102: Harmonic spectrum of inverter phase voltage as a percentage of the fundamental voltage recorded by Elspec

From Figure 102 the harmonic content at 7.5 kHz is important to note as the reason for these high-order harmonics will be discussed in Section 4.4.3.

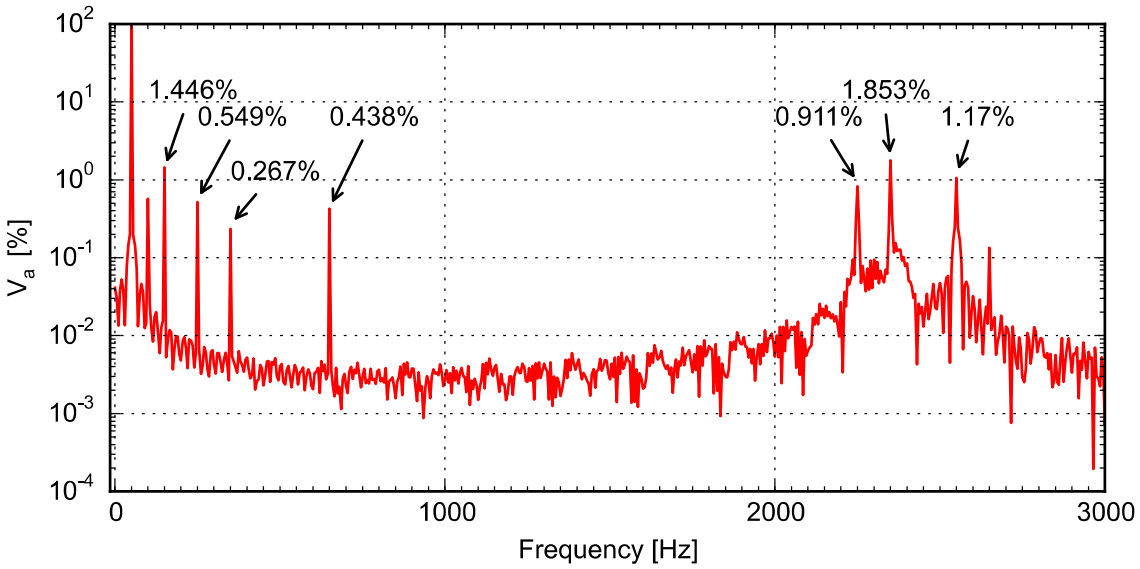

Figure 103: Harmonic spectrum of inverter phase voltage as a percentage of the fundamental voltage recorded by Elspec (detailed)

From Figure 103 the 2nd harmonic voltage component valued at 0.597% of the fundamental is important to note. Even harmonics are caused by equipment having asymmetrical i-v characteristics, such as a transformer that is operating towards one side of the B-H curve. This aspect should be investigated further in future work to determine if there is a DC component in the current that will require a Hall-effect current sensor. To measure low magnitude DC current on a high magnitude AC waveform requires high accuracy. The current waveform and its harmonic spectrum shows the same 2nd harmonic component, but much higher in relative magnitude, i.e. more than 1%. This is an indication that the inverter generates an asymmetrical current waveform that causes the voltage to distort at this frequency. This will, however, not be investigated further in this thesis but need to be analysed in the future as this will certainly impact PQ assessments being done in the future.

The captured phase current waveform for one cycle, phase current harmonic spectrum and a detailed phase current harmonic spectrum with values are shown in Figure 104, Figure 105 and Figure 106 respectively.

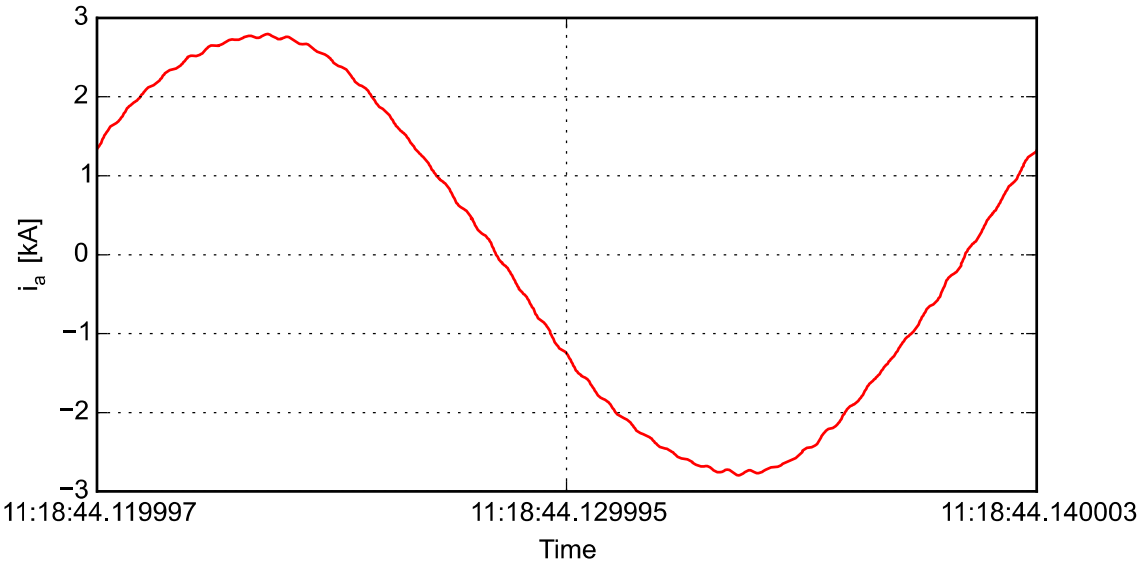

Figure 104: Inverter phase current recorded by Elspec (detailed) for 1 cycle

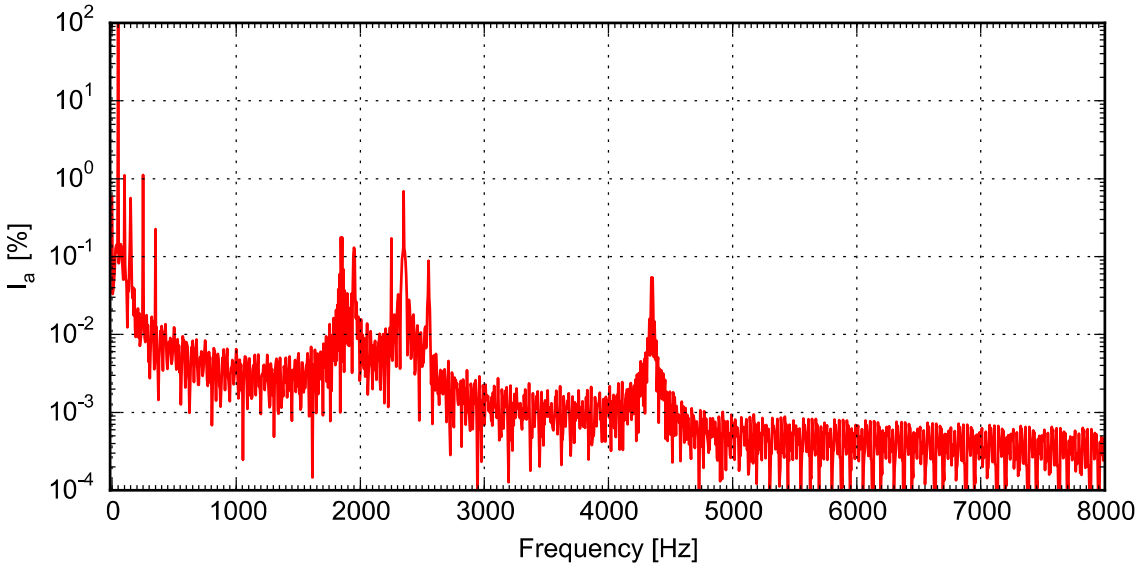

Figure 105: Harmonic spectrum of inverter phase current as a percentage of the fundamental current recorded by Elspec

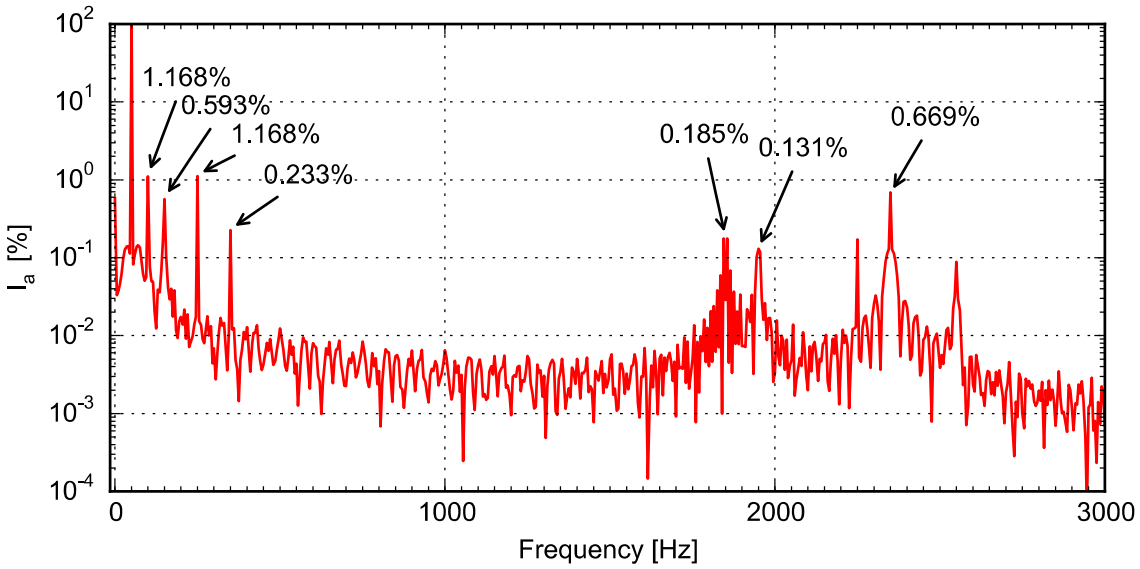

Figure 106: Harmonic spectrum of inverter phase current as a percentage of the fundamental current recorded by Elspec (detailed)

By looking at the harmonic spectrum of the voltage and current waveforms recorded by the Elspec in Figure 103 and Figure 106 it is shown that the inverter switches at 2.5 kHz and inject a 1.853% phase voltage switching ripple and 0.669% phase current switching ripple into the grid.

4.4.3. Simulation results – Wind farm B

The simulation results for the conventional PWM inverter model approach with the filter values chosen in Section 3.6.2 do not correlate with the measured results in Section 4.4.1 and Section 4.4.2. The high-order harmonic content greatly exceeds that of the measured results. After further investigation it was found that Wind farm B utilises an interleaved PWM inverter approach to reduce the high frequency harmonic content in the phase voltages and currents. This explains the high voltage harmonic content at 7.5 kHz as seen in Figure 102 since the switching frequency of an interleaved inverter is shifted to a multiple of the switching frequency which is dependent on the number of parallel modules within an interleaved inverter. Therefore, with this specific case study, with three parallel modules each with a switching frequency of 2.5 kHz the switching frequency of the interleaved inverter will be 7.5 kHz. It is, however, important to note that the 7.5 kHz harmonic content is not visible on the current harmonic spectrum in Figure 105, because the current sampling rate of the Elspec is 256 samples/cycle which only records the harmonics up to the 127th harmonic or up to 6.35 kHz. The simulation results of the conventional PWM inverter model will not be shown in this thesis as it is not relevant to Wind farm B. The DIgSILENT PowerFactory model, however, can still be used for future studies of RPPs that implement the conventional PWM approach.

The simulation results for the interleaved PWM inverter approach were obtained using the model presented in Section 3.6.5. A single turbine was simulated at rated power, 2.3 MW, and the phase current of one individual inverter within the interleaved inverter is shown in Figure 107.

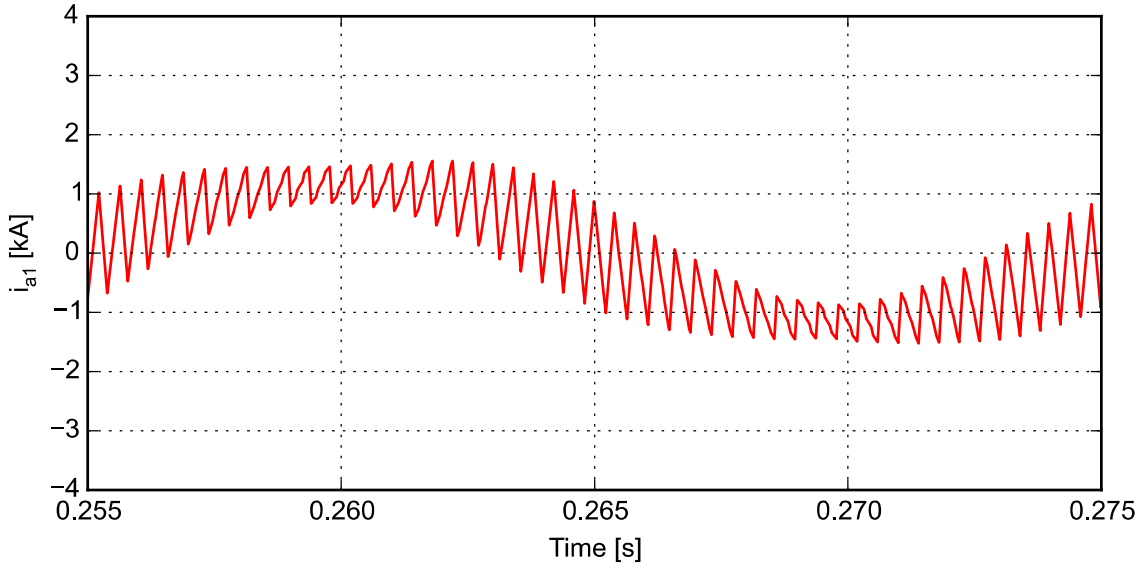

Figure 107: Phase current of each individual inverter module in DIgSILENT PowerFactory

The current harmonic spectrum of the phase current for one individual inverter within the interleaved inverter is shown in Figure 108.

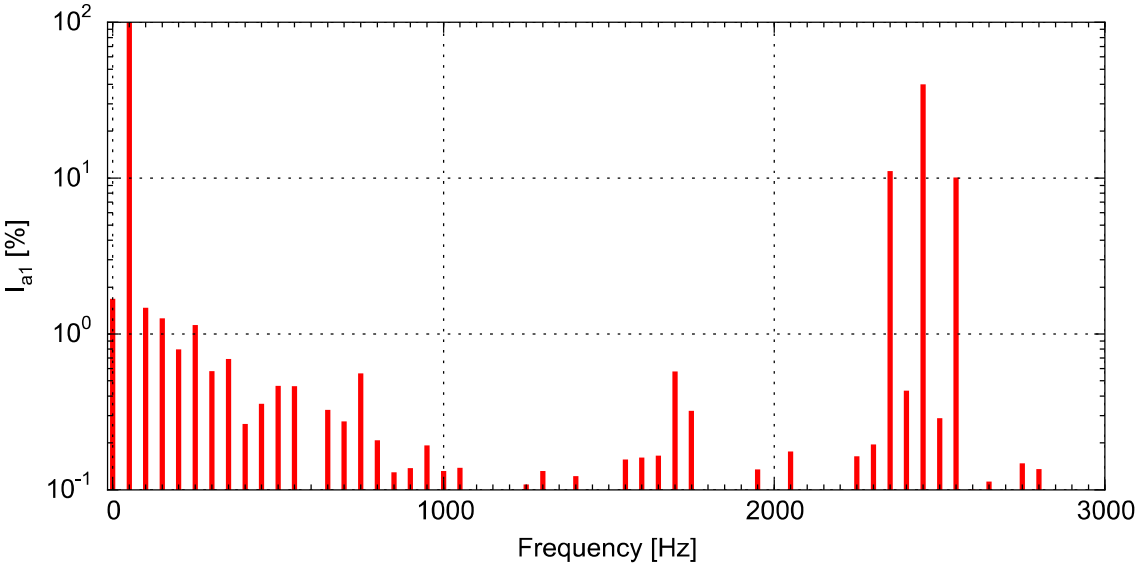

Figure 108: Harmonic spectrum of the phase current as percentage of fundamental current of each individual inverter module in DIgSILENT PowerFactory

By looking at the harmonic content of the phase current in Figure 108 it is shown that the inverter switches at 2.5 kHz with high harmonic content at and around the switching frequency.

The phase currents of each individual inverter within the interleaved inverter is shown in Figure 109 which demonstrates the effect caused by the phase shift between the inverter reference triangular waveform.

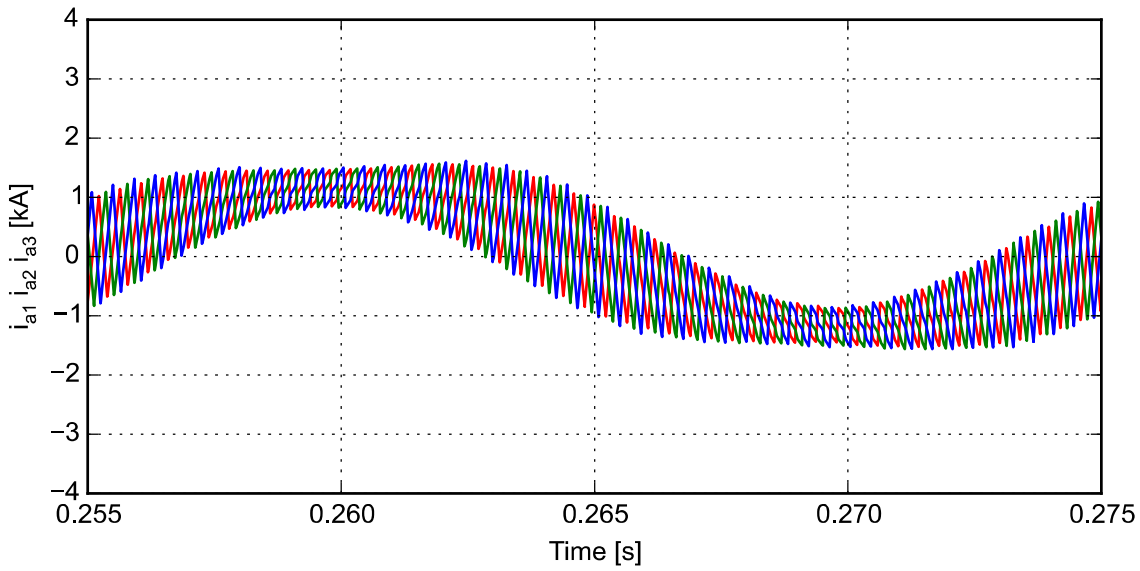

Figure 109: Phase currents of the three individual inverter modules in DIgSILENT Powerfactory

The total output phase current of the interleaved inverter is shown in Figure 110.

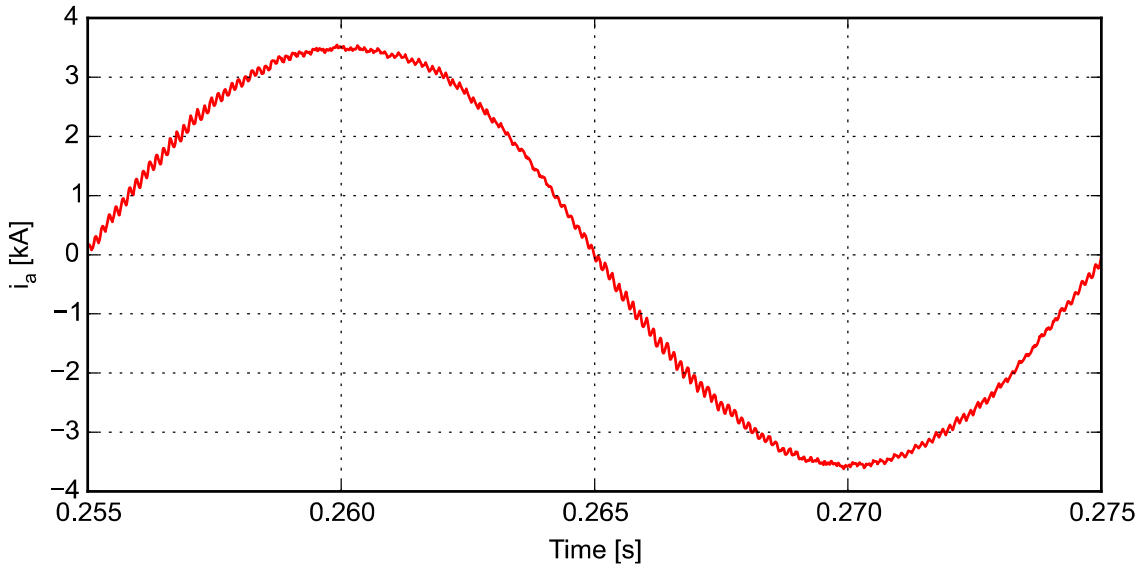

Figure 110: Phase current of interleaved inverter in DIgSILENT PowerFactory

The current harmonic spectrum of the output phase current of the interleaved inverter is shown Figure 111.

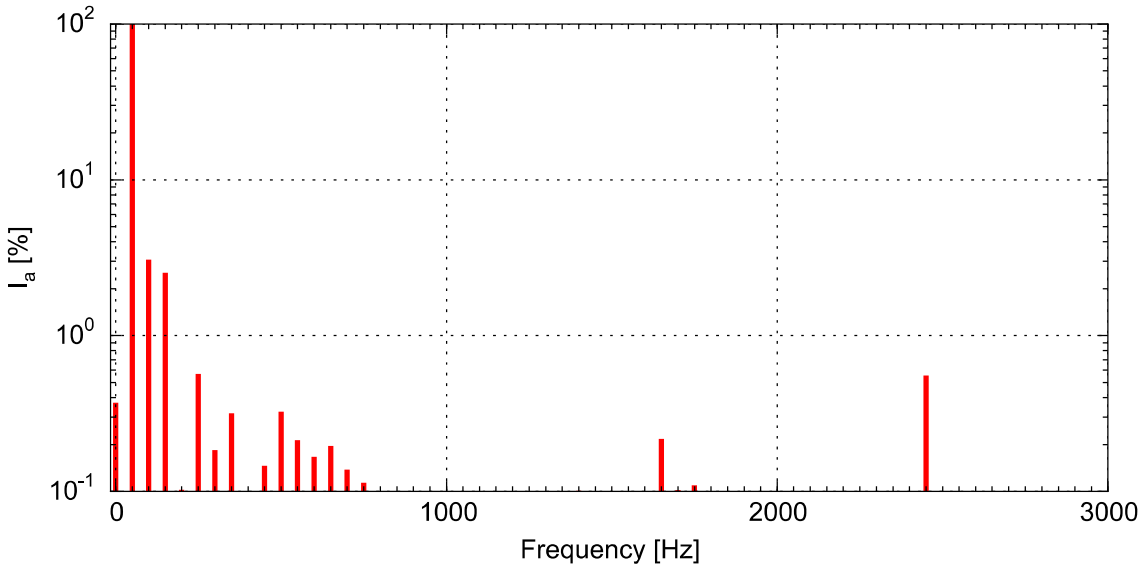

Figure 111: Harmonic spectrum the phase current of the interleaved inverter in DIgSILENT PowerFactory

By looking at Figure 110 and Figure 111 it is shown that the interleaved PWM inverter approach reduces the harmonic content at and around the switching frequency significantly. It is, however, important to note that the grid reactor inductance of each individual inverter was not chosen to be exactly the same as this will completely remove the harmonic content at the switching frequency. Therefore, the grid reactor inductance of each inverter was chosen as 78 µH, 74 µH and 70 µH respectively to illustrate the effect this will have on the harmonic content and thus more closely represent the model under practical conditions. The interleaved inverter switches at 2.5 kHz and inject a 0.55% switching ripple into the grid. The harmonic content of 0.218% at 1.65 kHz is due to a parallel resonance caused by the passive filters, transformer inductances and cable capacitances in the wind farm. This resonance can cause excessive distortion at the POC if non-linear loads such as traction loads inject harmonic content at the resonance frequency.

4.4.4. Comparison of measurement and simulation results

The simulated model of case study 1 produce similar results compared to the measured results. The simulated switching ripple, 0.55%, can be increased to reflect the measured 0.669% switching ripple by further adjusting the grid reactor inductance in the DIgSILENT PowerFactory model. The simulated parallel resonance is not located at the same location as that of the measured results as the simulated model is largely a generic model that do not accurately reflect the cable equipment ratings and transformer impedance ratings. At the time of writing limited information was known with regards to the equipment ratings and thus was not deemed that important for this thesis as it would require a large amount of time to produce an exact replica of the wind farm. It was deemed more important to show the general working

principles of an interleaved inverter wind farm system, to obtain a better understanding about the approach and show the basic PQ characteristics of such a system. It is shown that both the measured and simulated results contain low-order harmonics which are largely caused by the regular symmetrical sampling of the PWM reference waveform where the reference waveform is sampled at the negative peak of the triangular carrier waveform [27]. In addition, regular symmetrical sampling produces additional sideband harmonics at the switching frequency as shown in Figure 108 and this reflect the modulation theory explained by Lipo [27] as described in Section 2.4.4.

4.5. CONCLUSION

In this chapter the PQ in terms of voltage waveforms, current waveforms and respective harmonic content generated by Wind farm A and Wind farm B were investigated using measurements results and designed DIgSILENT PowerFactory simulation models. It is difficult to understand the control of RPPs and to describe PQ by only investigating the measurement results. The measurement results recorded by an Elspec and an Oscilloscope connected to the 0.69 kV terminals of a single turbine were shown. The DIgSILENT PowerFactory simulation results of the generic inverter models of Wind farm A and Wind farm B were shown. The simulated results were compared to the measured results to validate the accuracy the respective DIgSILENT PowerFactory models. The models provide similar results to the actual measured results but is not 100% accurate due to the assumptions that was made. These models provided important insight on the control of RPPs. It was possible to show the effect of sampling and third harmonic injection on current harmonic content. It can be stated that these models provide a good baseline for future PQ studies and with more information can be updated to provide models that can be used in network planning and PQ assessment.

CHAPTER 5
THE IMPACT OF TRACTION LOADS ON NETWORK VOLTAGE UNBALANCE

5.1. INTRODUCTION

This chapter will analyse the impact of traction loads on the network voltage unbalance by evaluating measurement results obtained by installing two Elspec class A PQ measurement instruments. A local traction network with Wind farm A connected to the network has been chosen as case study. The network geographical layout of the network can be seen in Figure 1. Firstly, the measurement setup and installation will be discussed followed by a brief examination on the voltage unbalance emissions caused by Wind farm A. Thereafter, the voltage unbalance conditions to which a RPP, connected to a traction network, will be exposed to, will be investigated by analysing the measured data for a weekly (long-term) assessment and for a short-term assessment. The contribution of traction loads to the measured voltage unbalance will be investigated by determining when a locomotive is present on the network and then analysing the voltage unbalance during that time period. In addition, a DIgSILENT PowerFactory EMT simulation that consist of the Wind farm A model in Section 3.6.3 in combination with the half-controlled thyristor model in Section 3.5.2 will be done to determine the simulated voltage unbalance. The simulated voltage unbalance will then be compared to the measured results to determine the reliability of the simulation results. Lastly, the inverter trip levels will be compared to the simulated voltage unbalance values to determine if RPPs can expect inverter trip events when connected to a traction network.

5.2. MEASUREMENT INSTALLATION AND SETUP

Wind farm A has a maximum power generation of 79 MW and is connected to the 132 kV network via a 132 kV/33 kV 90 MVA step-up transformer. Elspec A was installed at the POC of Wind farm A while Elspec B was installed at a nearby traction substation. Both Elspecs were connected through VTs and CTs. The voltage is measured using voltage clamps and the current is measured using current probes. The current probes have a measurement range of 6/60 AAC and an output signal of 100 mV/A. Refer to Figure 112 for a single-line diagram showing the locations of the installed Elspecs.

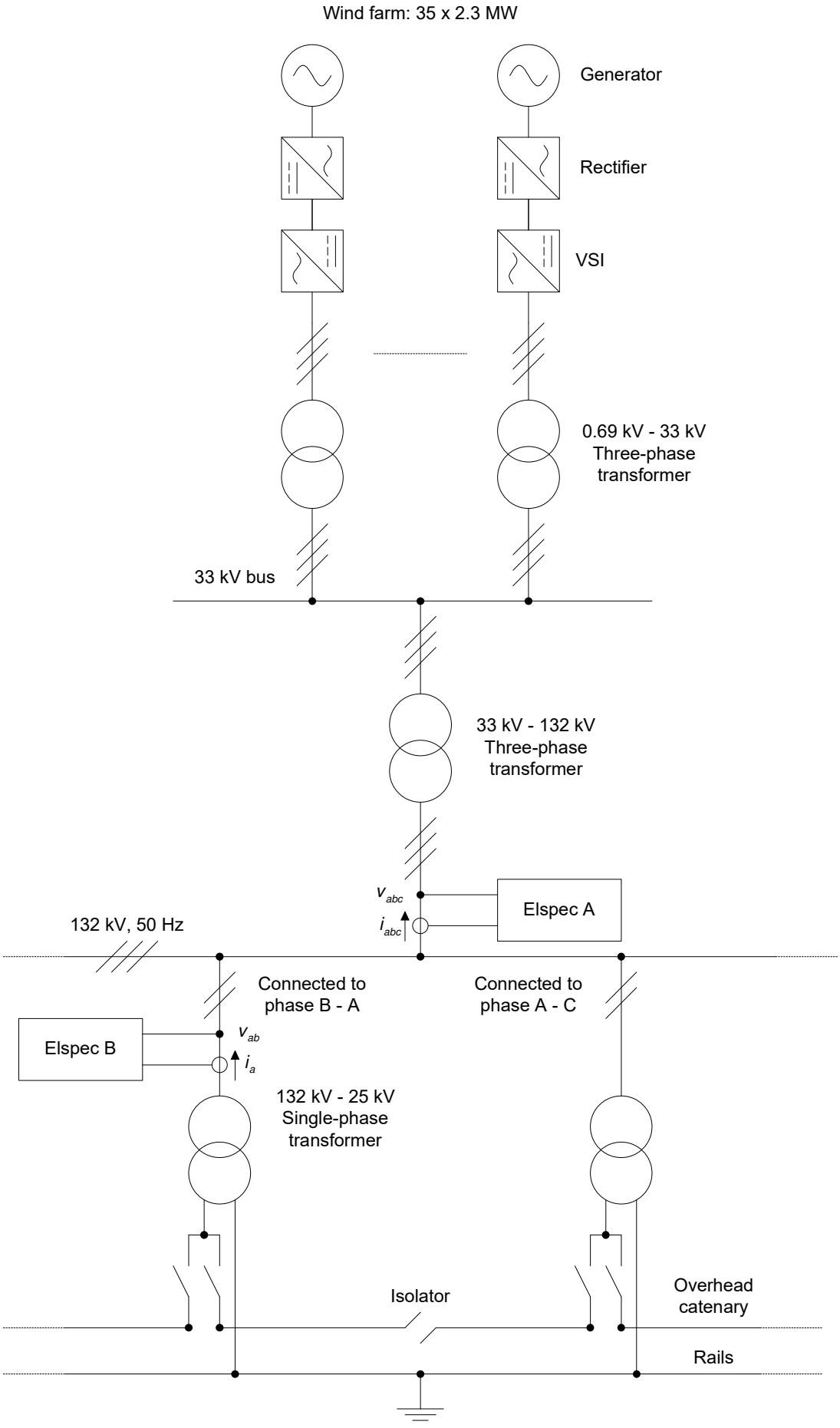

Figure 112: Single-line network diagram with the locations of the Elspec installations

The electrical diagram of the Elspec installation at the traction substations can be seen in Figure 113.

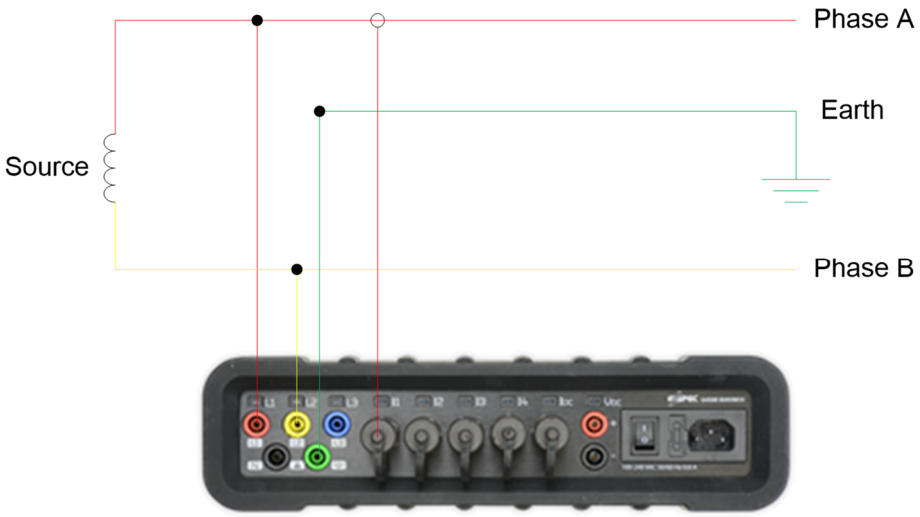

Figure 113: Single-phase Elspec connection diagram

Two voltage clamps are connected to the L1 and L2 ports of the Elspec and to the two voltage transformer connections in the measurement panel. Another voltage clamp is connected to the earth port of the Elspec and grounded on the measurement panel. A current probe is connected to the I1 port of the Elspec and was clamped over the phase A cable of the CT in the measurement panel.

The electrical diagram of the Elspec installation at the POC of Wind farm A can be seen in Figure 114.

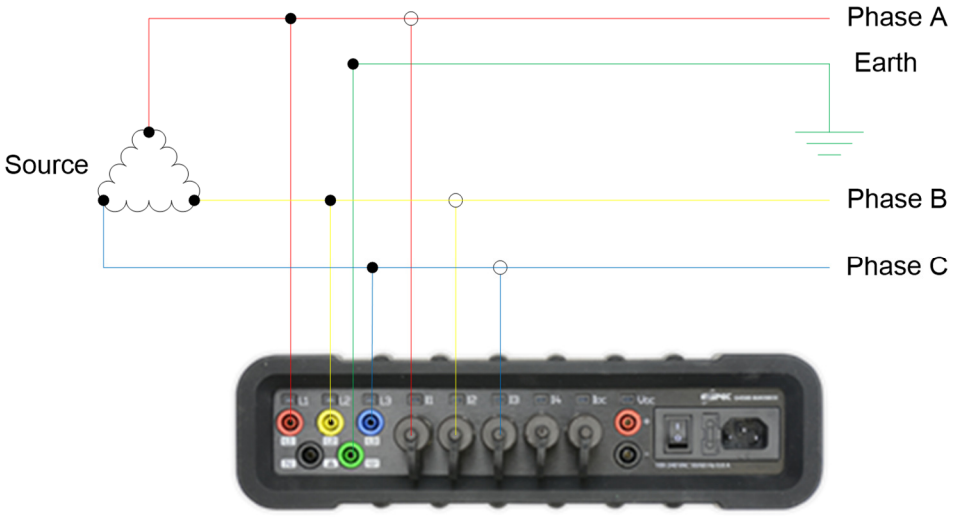

Figure 114: Three-phase delta 3 wire Elspec connection diagram

Three voltage clamps are connected to the L1, L2 and L3 ports of the Elspec and to the three VT connections in the measurement panel. Another voltage clamp is connected to the earth port of the Elspec and grounded on the measurement panel. Three current probes are

connected to the I1, I2 and I3 ports of the Elspec and are clamped over the phase A, phase B and phase C cable of the CT in the measurement panel. The physical voltage clamps and current probes connections can be seen in Figure 115 and Figure 116 respectively.

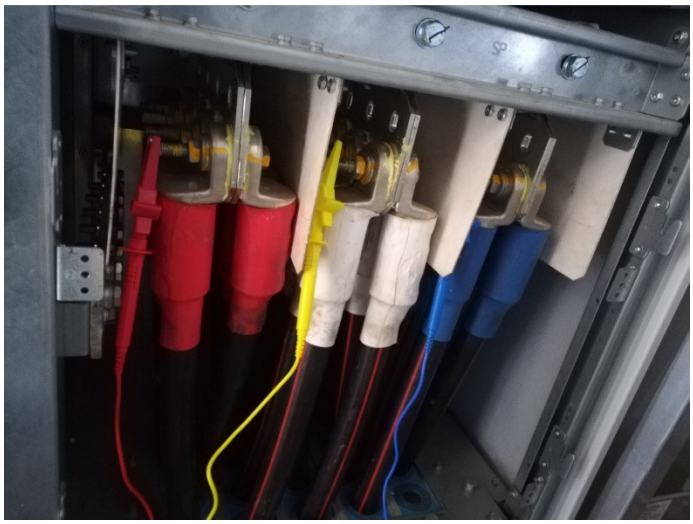

Figure 115: Physical voltage clamps connections

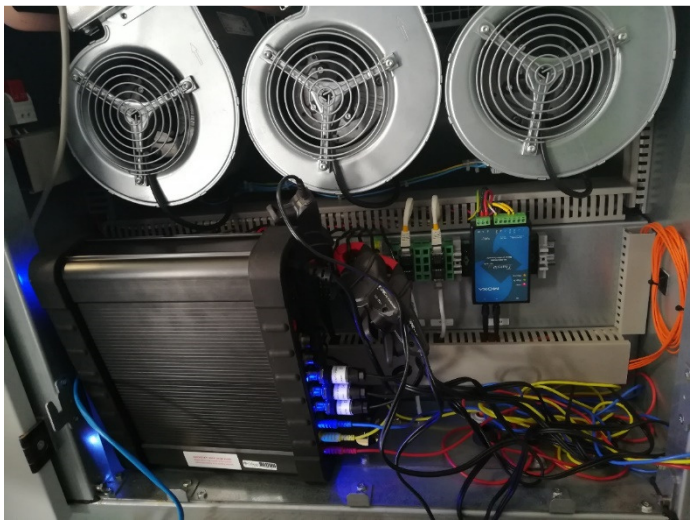

Figure 116: Physical current probes connections

The Elspec is further setup to ensure that the measurement data is as expected. The Elspec connection configuration must be changed to either the single-phase connection or the delta 3 wire connection depending on the Elspec location. The VTs and CTs ratios must be changed according to those on site. It was decided that GPS units must be installed at both Elspec A and Elspec B to ensure that the measurements are time synchronised so that the data can be directly compared.

5.3. VOLTAGE UNBALANCE EMMISIONS BY WIND FARM A

A voltage unbalance assessment report at the POC of Wind farm A investigated and compared the quality of supply at the POC to the PQ limits specified in the Eskom distribution connection

and use-of-system agreement with generators (DCUOSA). The voltage unbalance emissions caused by the RPP was evaluated using the voltage assessment techniques described in Section 2.6.3.4. The investigation showed that by taking the 95th percentile voltage unbalance pre-connection value of 1.66% and 95th percentile voltage unbalance post-connection value of 2.09% and substituting the values into (2.20) that Wind farm A is not contributing to the voltage unbalance on the network, therefore, the voltage unbalance on the network is largely caused by the non-linear single-phase traction loads. The unbalance caused by traction loads will, therefore, be investigated in the following sections.

5.4. MEASUREMENT RESULTS

The data used for this analysis was obtained from a monthly continuous recording in 2018, from which a single week (03/06/2018 - 10/06/2018) of data was chosen for evaluation. This time period was chosen to evaluate the data according to the NRS 048-2 assessment period requirement. One week of data will ensure that a clear profile is obtained under normal load conditions.

5.4.1. Weekly (long term) PQ assessment

5.4.1.1. Voltage unbalance

The measured data recorded by Elspec A was used for a PQ assessment at the 132 kV POC of Wind farm A. The weekly 95th percentile 10-minute aggregated voltage unbalance values were used for the PQ assessments as per the NRS 048-2 standard requirements. This 10-minute aggregated data was obtained using PQSCADA software.

The weekly PQ assessment as generated by PQSCADA indicates that the measured 95th percentile 10-minute voltage unbalance value is 1.79% which does not exceed the 2% limit set in the NRS 048-2. This, however, cannot be said for the maximum 10-minute voltage unbalance value of 3.11% which exceed the 3% limit set in the NRS 048-2 [81]. It is important to note that the 3% voltage unbalance limit is still under consideration by the NRS [81] and at the time of writing is not used for PQ assessment. It will, however, be used in the thesis as a reference value for short-term PQ assessment.

5.4.1.2. Voltage fluctuations

During the time of investigation, eight voltage dip events were recorded as shown by the dots in Figure 117. The dip categories also shown in Figure 117 are defined in the NRS 048-2 [81].

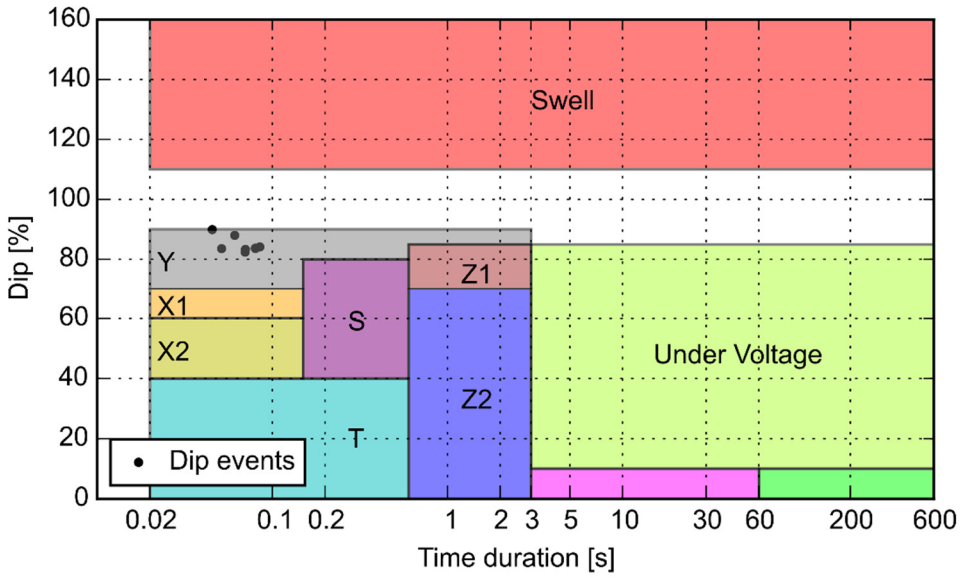

Figure 117: Voltage dip events

At the time of writing, it is unclear whether these dip events are caused by traction loads on the network. However, it is shown that all of these dips fall in the Y, fast voltage dip, category and consequently within area A of the VRTC of RPPs as shown in Figure 29. Therefore, even if one of these events were cause by a traction load, for any of the reasons explained in Section 2.7.5, it is clear that it will have no PQ impact on RPPs that employ the VRTC explained in Section 2.7.5. Therefore, this will not be further investigated in this thesis.

5.4.2. Worst case (short term) PQ assessment

Voltage unbalance can cause voltage swells and sags that persist on the network for longer periods of time and can still be of great concern to nearby RPPs. To investigate whether traction loads contributed to the weekly PQ problems it was decided to investigate the largest 10-minute aggregated voltage unbalance and to determine whether the unbalance was caused by traction loads. To accurately determine whether a traction load was present on the network, the data obtained from Elspec B was used in combination with the measured data of Elspec A at the POC on the network.

5.4.2.1. Voltage unbalance

The maximum 10-minute negative sequence voltage unbalance for the weekly period was obtained and is plotted and compared to the 3% NRS 048-2 limit in Figure 118.

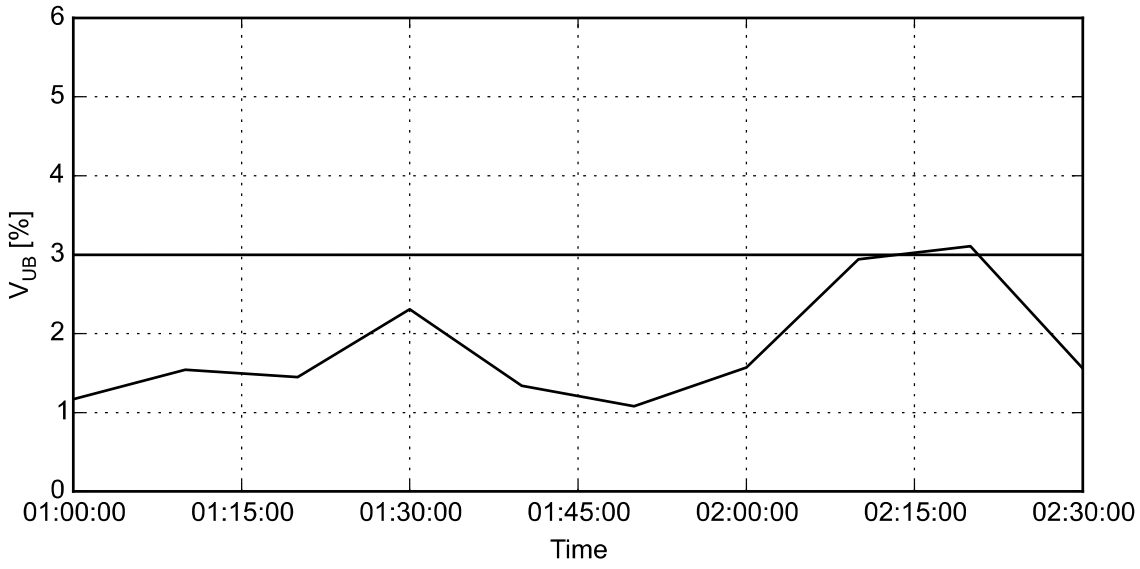

Figure 118: 10-minute negative sequence voltage unbalance at Wind farm A

Although the 95th percentile of the voltage unbalance limit was not exceeded for the total period of assessment it is clearly shown that this is not the case when investigating the voltage unbalance for short periods of time. The voltage unbalance V_{UB} reach a 10-minute maximum aggregated value of 3.1% which exceed the 100% indices limit of 3% which is under consideration by the NRS [81].

Figure 119 shows the current drawn by a traction load and thus support this investigation as it clearly shows that a locomotive was present on the network during the period (1:00:00 PM to 2:30:00 PM) in Figure 118.

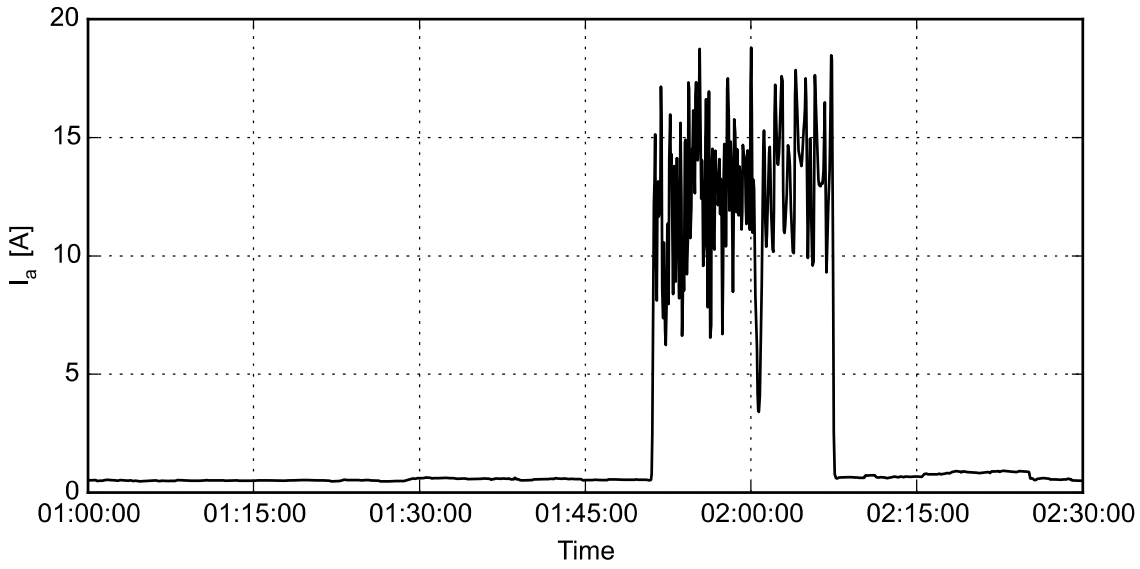

Figure 119: RMS phase current at traction substation

It is important to mention that the current was only measured on one of the three phases. Therefore, the sudden increase and decrease in current as the locomotive move passed neutral sections and are connected to different phases of the three-phase system. Moreover, the voltage unbalance immediately start to increase after the current in the measured phase decreased to approximately zero which shows that a large load is still present. Therefore, it can be assumed that the traction load is the cause of the maximum voltage unbalance. This sudden increase in the voltage unbalance could be due to a number of causes as traction loads are dynamic. The dynamic effects produce a time varying power consumption that is determined by a number of variables such as the locomotive tractive efforts, position, mass, slope etc. The harmonic emissions become time varying and depend on the operating conditions of the locomotive. Another reason could be the aggregated PQ issues from a number of running locomotives where each locomotive produce harmonic current emissions on the system that propagates through the network. The instantaneous voltage unbalance values during the period are plotted and compared to the NRS 048-2 limit in Figure 120.

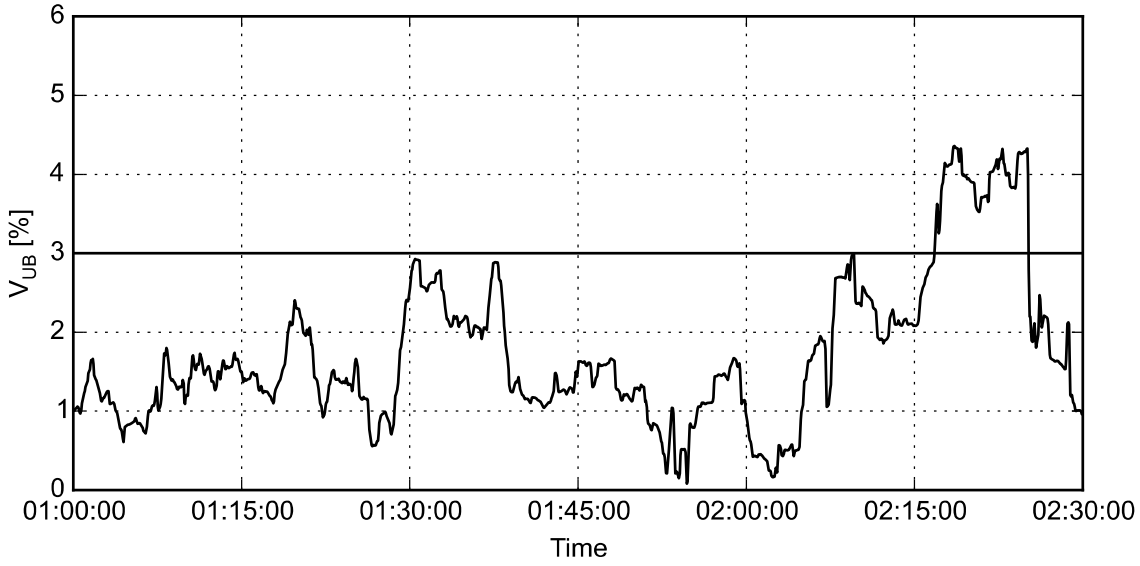

Figure 120: Measured negative sequence unbalance at Wind farm A

From Figure 120 it is clear that the maximum instantaneous voltage unbalance V_{UB} of 4.36% is higher than the maximum 10-minute aggregated value 3.1%. The maximum instantaneous voltage unbalance V_{UB} exceeds the 100% indices limit of 3% which is under consideration by the NRS [81]. The corresponding RMS phase voltages for the period while a traction load is present on the network are plotted in Figure 121. From Figure 121 the movement of the locomotive on the network is visible. The dip in phase voltage indicates on which phases the traction load is connected to. The continuous dip in voltages in different phases indicates the movement of the locomotive past neutral sections on the network. This is shown by the highlighted sections in Figure 121.

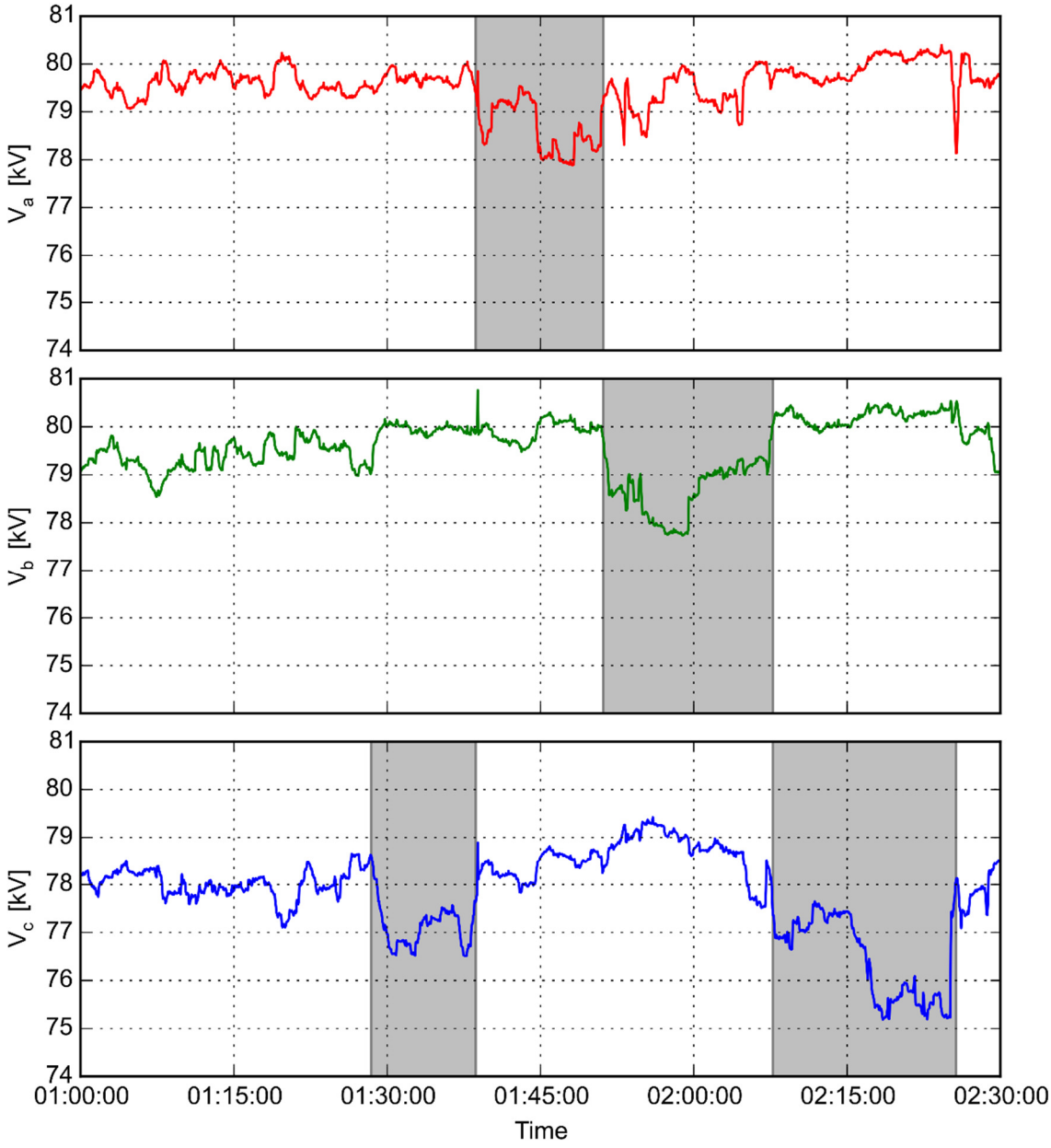

Figure 121: RMS phase voltages of phase A (a), phase B (b) and phase C (c) at Wind farm A

Figure 121 shows that the voltage unbalance is much larger when the locomotive is connected to phase C compared to phase A and B. This is due to the dynamic effects that are characteristic of traction loads as discussed in Section 2.3.

5.5. SIMULATION SETUP

A high level diagram of the network layout in DIgSILENT PowerFactory which was used for a dynamic voltage unbalance simulation in this thesis is shown in Figure 122. The external grid elements are modelled with the three-phase fault level which was agreed upon by Eskom and Wind farm A in the DCUOSA to run the simulation under practical conditions. Traction substation A in Figure 122 represents the DIgSILENT PowerFactory active rectifier locomotive model designed in Section 3.5.1. By exposing the DIgSILENT PowerFactory model of Wind

farm A designed in Section 3.6.3 to these conditions the PQ impact and response of the wind farm under various operating scenarios can be investigated. For the purposes of this thesis the movement of a locomotive was not implemented but must be studied and implemented in future work as the movement of a dynamic load includes a new level of challenges in DIgSILENT PowerFactory EMT simulations.

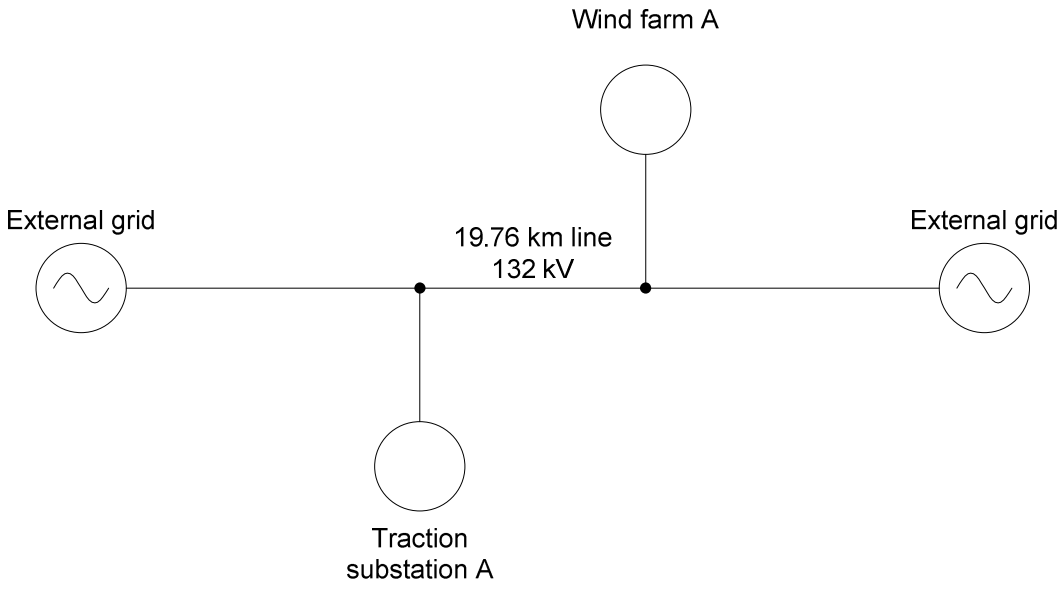

Figure 122: High level network diagram in DIgSILENT PowerFactory

5.6. SIMULATION RESULTS

The dynamic voltage unbalance effect as shown in Figure 120 was simulated by performing an EMT simulation of the network in Figure 122. The EMT simulation was also used to support the peak voltage unbalance value of 4.36% obtained in Figure 120. The traction load was set to 12 MW which is approximately the maximum power consumption of the traction loads under investigation. The peak simulated voltage unbalance is 5.61% and the voltage unbalance when reaching steady state conditions is 4.07% as shown in Figure 123. This correlates well with the measurement results obtained from Figure 120. Note that the simulation is run with the external grid elements three-phase fault level values set to 408 MVA which is the three-phase fault level of the network under weakened operating conditions. Therefore, by increasing the three-phase fault level value of the network to normal operating conditions values will decrease the peak simulated voltage unbalance which will then decrease the simulated maximum voltage unbalance closer to the measured 4.36% according to (2.30). By comparing the dynamic response of the voltage unbalance a similar response is found in simulation compared to the measured voltage unbalance response.

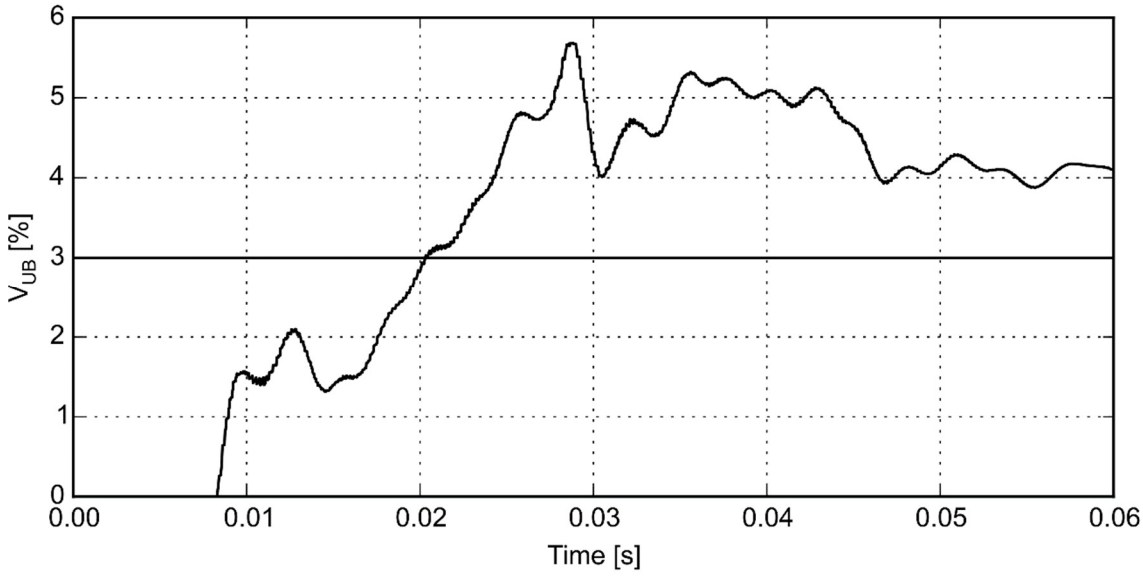

Figure 123: Simulated negative sequence unbalance

The simulated and measured RMS phase voltages are shown in Figure 124 and Figure 125 respectively. A similar dynamic response and percentage change from the nominal voltage could be observed.

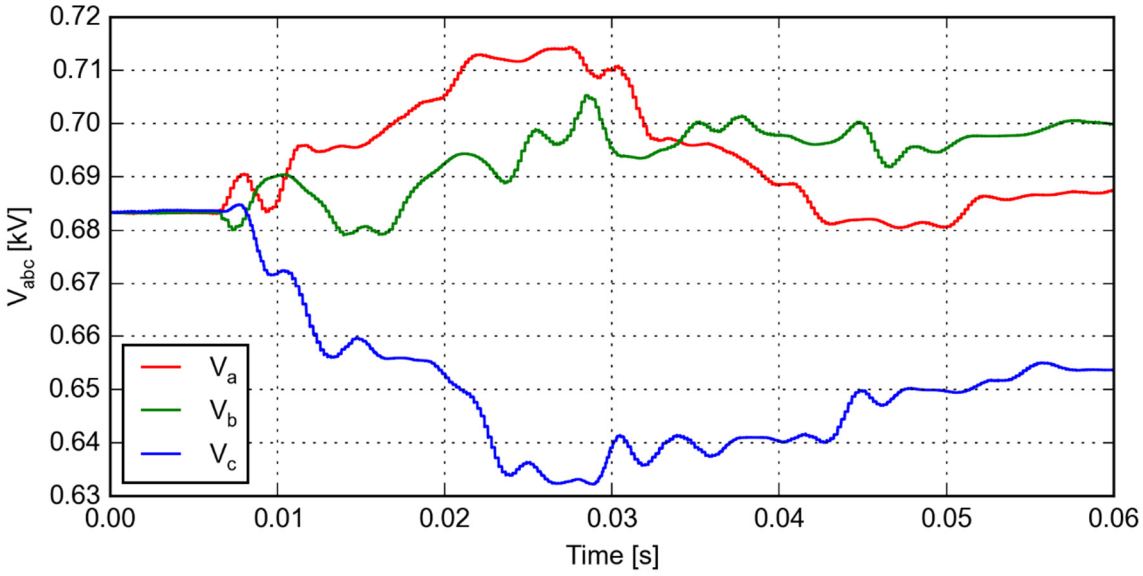

Figure 124: Simulated RMS phase voltages at the 0.69 kV terminal

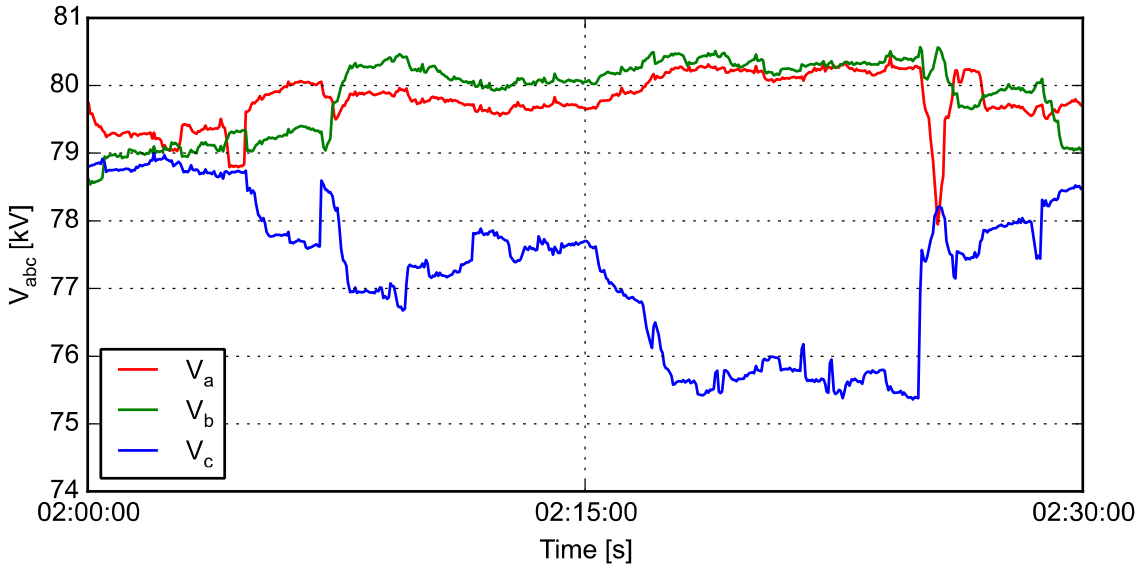

Figure 125: Measured RMS phase voltages at Wind farm A

5.7. THE EFFECT OF VOLTAGE UNBALANCE ON WIND FARM

The above phase voltages which are subjected to the above voltage unbalance levels will be compared to the voltage trip levels of Wind farm B due to the fact that at the time of writing the trip levels of Wind farm A was unavailable. Table 4 contains the inverter trip settings for Wind farm B. The voltage limits in the table is relative to the nominal voltage of the inverter which is 690 V (1 p.u.). The voltage limits indicate the value at which the inverter will trip if the voltage cannot recover within the respective time. Note that these limits are specific to Wind farm B and can change for other wind farms. For the purpose of this thesis the simulated RMS phase voltages in Figure 124 will be compared to the limits in Table 4 which are also plotted in Figure 126 and Figure 127. Note that the measured phase voltages in Figure 125 cannot directly be compared to voltage limits as it was measured at the POC which has a nominal voltage of 132 kV.

Table 4: Inverter trip settings

Lower voltage trip limits	**Voltage limit (p.u.)**	**Time (s)**
1	0.15	0.85
2	0.4	1.6
3	0.7	2.6
4	0.85	11
5	0.9	200
Upper voltage trip limits	**Voltage limit (p.u.)**	**Time (s)**
1	1.3	0.002
2	1.2	0.15

3	1.1	2

Figure 126 shows the inverter voltage limit in the time range 0 - 5 seconds.

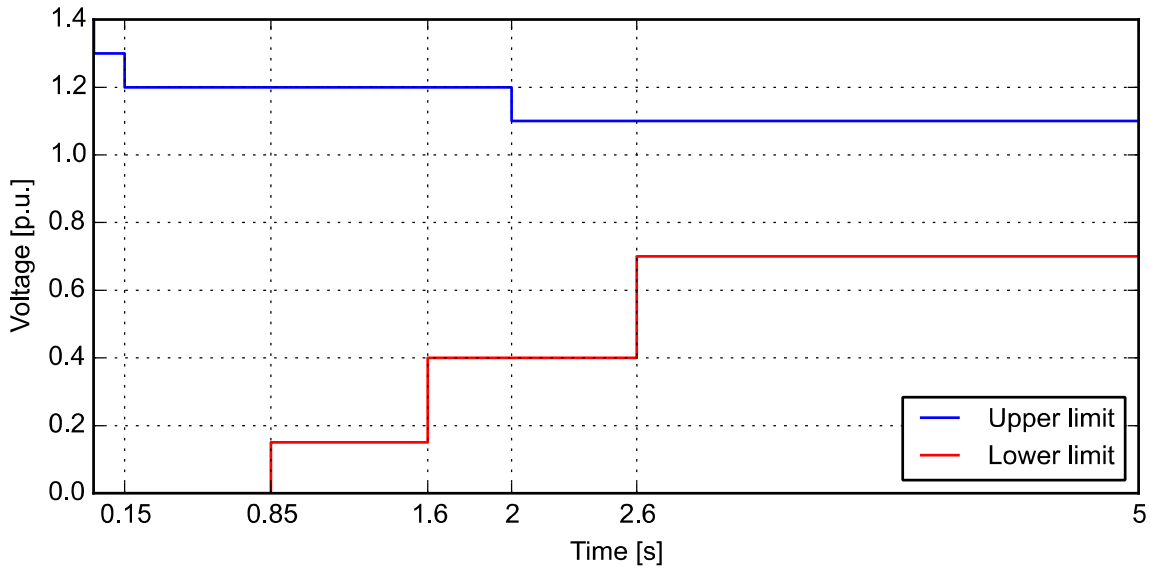

Figure 126: The upper (blue) and lower (red) voltage limits for a wind turbine inverter

Figure 127 shows the inverter voltage limit in the time range 5 - 300 seconds.

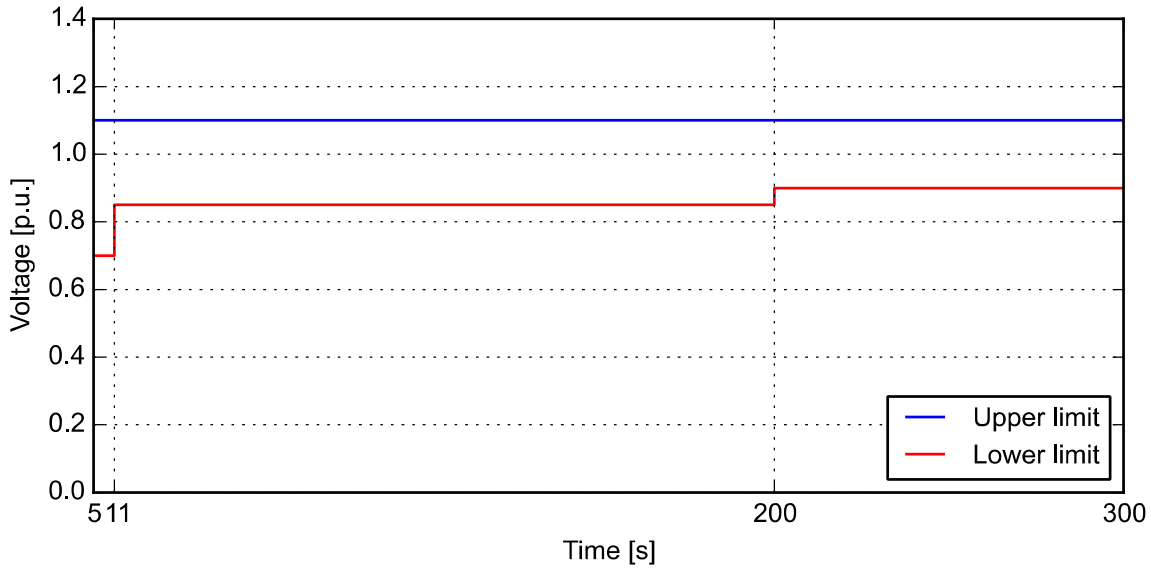

Figure 127: The upper (blue) and lower (red) voltage limits for a wind turbine inverter

By inspecting the simulated RMS phase voltages in Figure 124 it is shown that the lowest point of V_c is 0.631 kV or 0.914 p.u. at the maximum voltage unbalance. This will not cause the inverter to trip but is close to the 0.9 p.u. lower voltage limit although only for a short period of time. It is important to mention that a conventional traction substation in South Africa has a power rating of 20 MVA as shown on the nameplate of a traction transformer in Figure 174

and, thus, the risk of inverter trips still exist. The constant rise in demand for high power locomotives increase the possibility for higher demand locomotives up to 20 MW in the future. Consequently, the 12 MW maximum demand assumed in this thesis may become a conservative assumption in the future. Furthermore, networks with lower three-phase fault levels will experience larger voltage unbalance levels and can lead to inverter trips. By substituting the three-phase fault level of Wind farm A which is 408 MVA and a possible future traction load with a power demand of 20 MVA into (2.30) an estimated voltage unbalance V_{UB} can be calculated as 4.9% which is higher than the measured and simulated steady state voltage unbalance and can lead to inverter trips at RPPs.

5.8. CONCLUSION

It was observed that various conditions such as the traction load type, operating conditions and control of the traction load, power demand of the traction loads and three-phase fault level will impact the voltage unbalance caused by traction loads. The acceleration operating conditions of traction loads will cause larger power demand and, therefore, lead to larger voltage unbalance on the network. Therefore, network planners must reconsider the placement of RPP on traction network, placing a RPP close to a traction station will inherently lead to large voltage unbalance at that point due to the frequent stop and start of locomotives at traction stations. In addition, national service providers and traction load customers must also consider installing and implementing voltage unbalance mitigation methods at points of interest on the network close to RPPs where the voltage unbalance is inherently high due to the dynamic effects of traction loads voltage unbalance caused by the network configuration, geographical influences of slope and railway curvature and locomotive operating conditions. A recommendation would be to implement self-balancing transformers at the identified traction substations in the network where voltage unbalance is a large problem. In this specific case, a self-balancing transformer can be installed at the traction substation where the traction load is connected to phase C as the voltage unbalance is consistently high when the traction load is connected to that substation during the entire week of assessment. This, however, is not investigated in this thesis, therefore, a more thorough investigation must be done to determine the value that the mitigation methods discussed in Section 2.8 will have for Eskom.

CHAPTER 6
THE IMPACT OF TRACTION LOADS ON NETWORK HARMONICS

6.1. INTRODUCTION

This chapter will analyse the impact of traction loads on the network harmonics by evaluating measurement results that were obtained by installing two Elspec class A PQ measurement instruments as well as simulation results in DIgSILENT PowerFactory. A weekly PQ assessment at the POC will be done according to the NRS 048-2 assessment guidelines described in Section 2.6. Thereafter, a short-term assessment will be done to investigate the harmonic content of traction loads by using measurement data as well as the results obtained from the simulation models designed in Section 3.5. Lastly, this chapter aims to determine if traction loads influence the harmonic assessment results of RPPs. Therefore, a two-point measurement approach will be followed based on the IEC 61000-3-6 guidelines by measuring at the POC of Wind farm A as well as at a nearby traction substation.

The data used for this analysis was obtained from a monthly continuous recording in 2018, on both Elspec A and Elspec B, from which a single week (03/06/2018 - 10/06/2018) of data was chosen for evaluation. This time period was chosen to evaluate the data according to the NRS 048-2 assessment period requirements discussed in Section 2.6.2. One week of data will ensure that a clear profile is obtained under normal load conditions. Note that this is the same time period as used for voltage unbalance studies in CHAPTER 5. The Elspecs were GPS time synchronized to ensure that a direct comparison of the measurement results could be done.

The weekly PQ assessment is done using the weekly 10-minute aggregated data as per the NRS 048-2 standard requirements discussed in Section 2.6.2. The 10-minute aggregated values were recorded by Elspec A which was installed at the POC of Wind farm A as shown in Figure 112. This 10-minute aggregated data was analysed using PQSCADA software.

6.2. MEASUREMENT SETUP

Refer to Section 5.2 for the description of the measurement setup.

6.3. VOLTAGE THD ASSESSMENT (WEEKLY (LONG-TERM) ASSESSMENT)

The voltage THD is used to obtain insight into the voltage harmonic distortion present at the POC. The weekly PQ assessment indicates that the voltage THD at the POC exceeded the voltage THD limit defined in the NRS 048-2. The 95th percentile three-phase voltage THD values for the assessment period are compared to the NRS 048-2 limit as shown in Table 5.

Table 5: The measured 95th percentile THD voltages of phase A, B and C

Parameter	Regulation limit (%)	Measured max (%)
V_a THD	4	4.18
V_b THD	4	3.04
V_c THD	4	5.62

Table 5 shows that the voltage THD on phase C is significantly higher than the voltage THD on phase A and phase B. This is typical characteristics of single-phase traction loads. Therefore, by only observing the weekly PQ voltage THD assessment it will appear as if single-phase traction loads effect the voltage distortion at the POC as the network mainly consist of traction loads. To support this statement the voltage THD for a short period when a traction load is present on the network will be investigated in the following section.

6.4. VOLTAGE THD ASSESSMENT (SHORT-TERM)

For the short-term voltage THD assessment the same time period as used for the voltage unbalance short-term assessment in CHAPTER 5 was used due to the fact that it was already determined that a locomotive was present during that time. The 10-minute aggregated three-phase voltage THD values are shown and compared to the NRS 048-2 voltage THD limit in Figure 128. The voltage THD is used to obtain insight into the voltage harmonic distortion caused by the train during that period of time. The measured peak voltage THD for the 10-minute aggregated values as shown in Figure 128 is 5.8% for phase C and thus exceeds the NRS 048-2 limit of 4%. Note that this is only for comparison purposes and cannot directly be used for PQ assessment purposes.

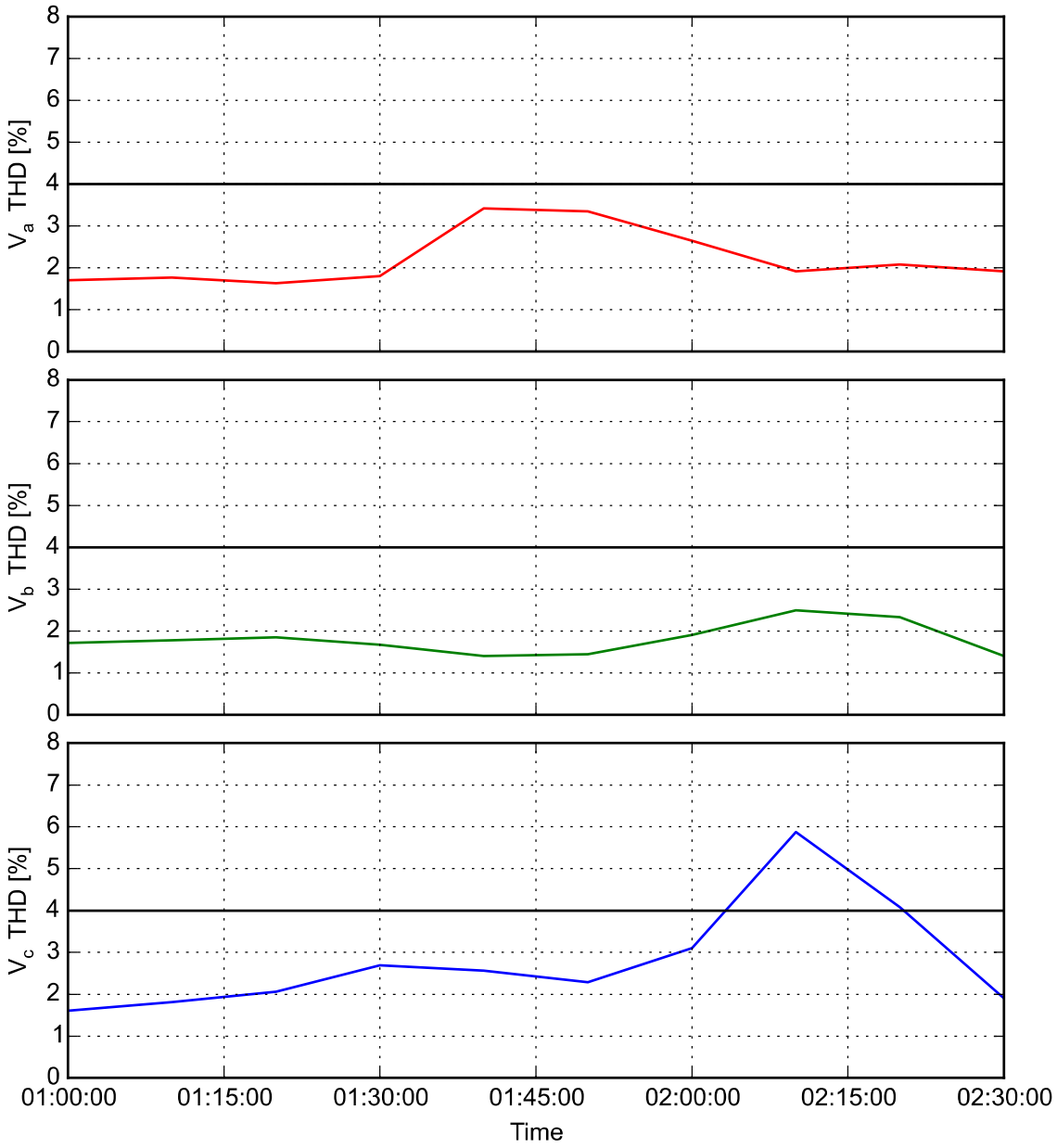

Figure 128: Measured 10-minute voltage THD of phase A (a), phase B (b) and phase C (c) at Wind farm A

The instantaneous measured voltage THD values are plotted and compared to the NRS 048-2 voltage THD limit in Figure 129. With a resolution of 1024 samples per cycle. The measured peak voltage THD value is 7.37%.

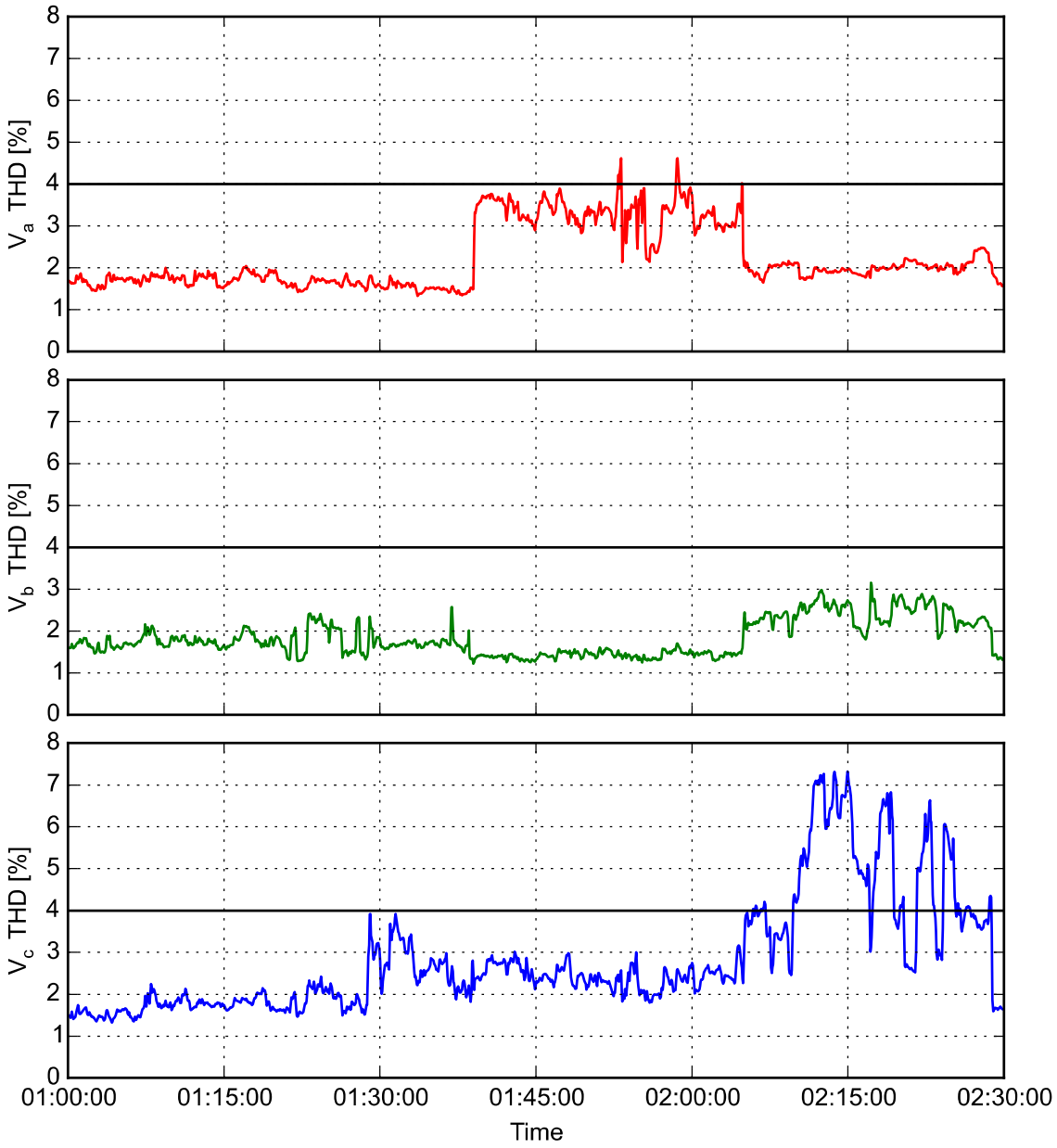

Figure 129: Measured instantaneous voltage THD of phase A (a), phase B (b) and phase C (c) at Wind farm A

Figure 129 show that the instantaneous voltage THD, for the phase on which the traction load is connected, is significantly higher than the instantaneous voltage THD on the other phases. Therefore, traction loads clearly have an impact on the voltage harmonics and must be further investigated by analysing the individual harmonic contribution of traction loads to the network.

6.5. INDIVIDUAL VOLTAGE HARMONIC ASSESSMENT (WEEKLY (LONG-TERM) ASSESSMENT)

The weekly PQ assessment also indicates that some individual voltage harmonics component limits defined in the NRS 048-2 and NRS 048-4 were exceeded. The maximum measured three-phase voltage harmonic content are shown in Figure 130.

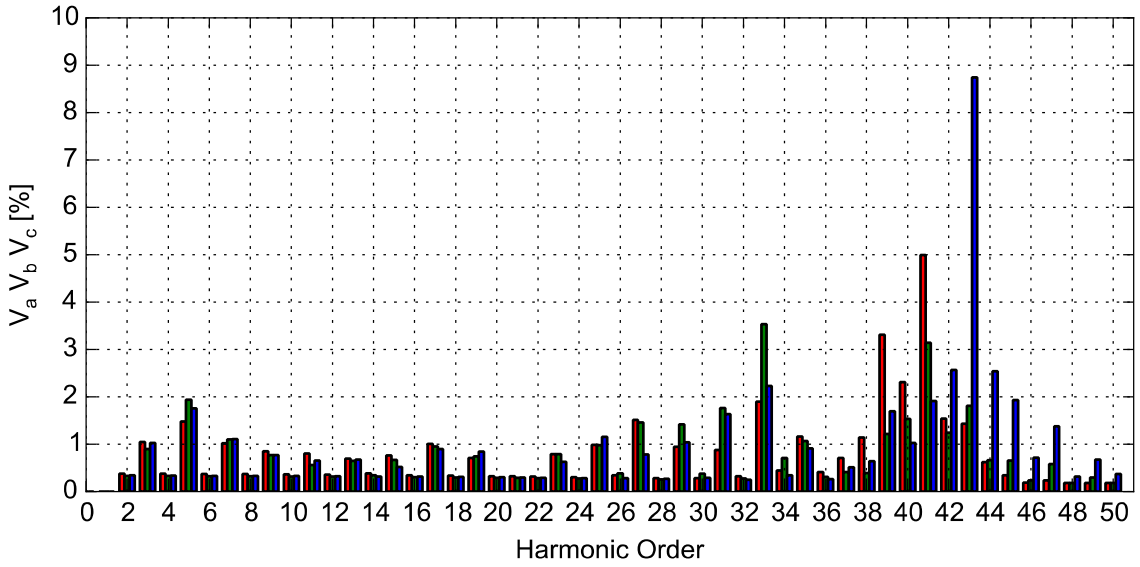

Figure 130: The maximum measured voltage harmonic content of phase A (red), phase B (green) and phase C (blue)

The 95th percentile three-phase harmonic voltage content of phase A, B and C with corresponding individual harmonic limits are shown in Figure 131, Figure 132 and Figure 133 respectively.

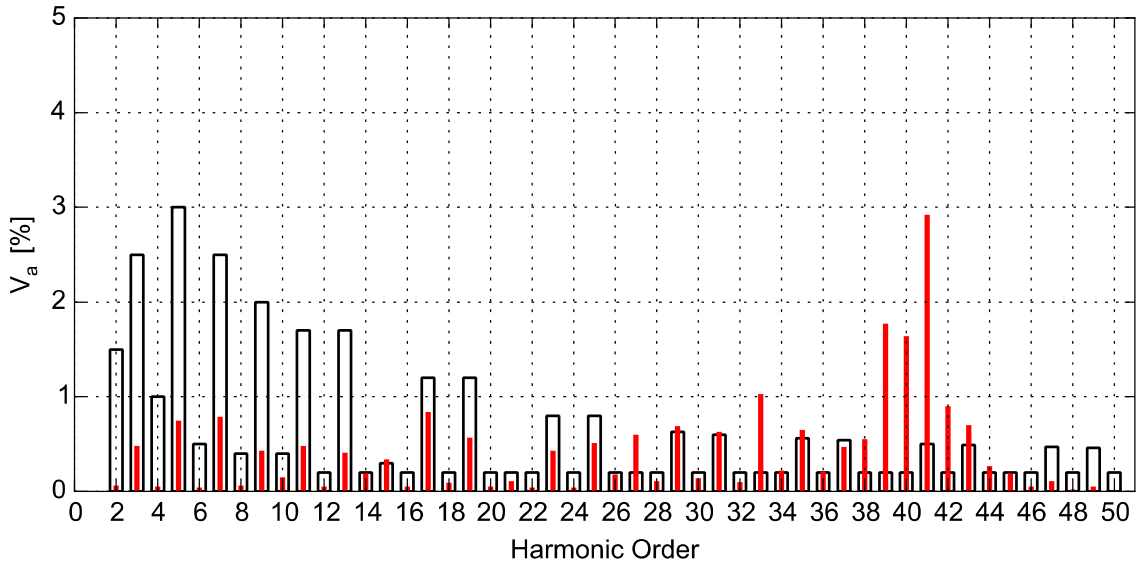

Figure 131: The 95th percentile measured voltage harmonic content of phase A (red) compared to the corresponding harmonic limit (black)

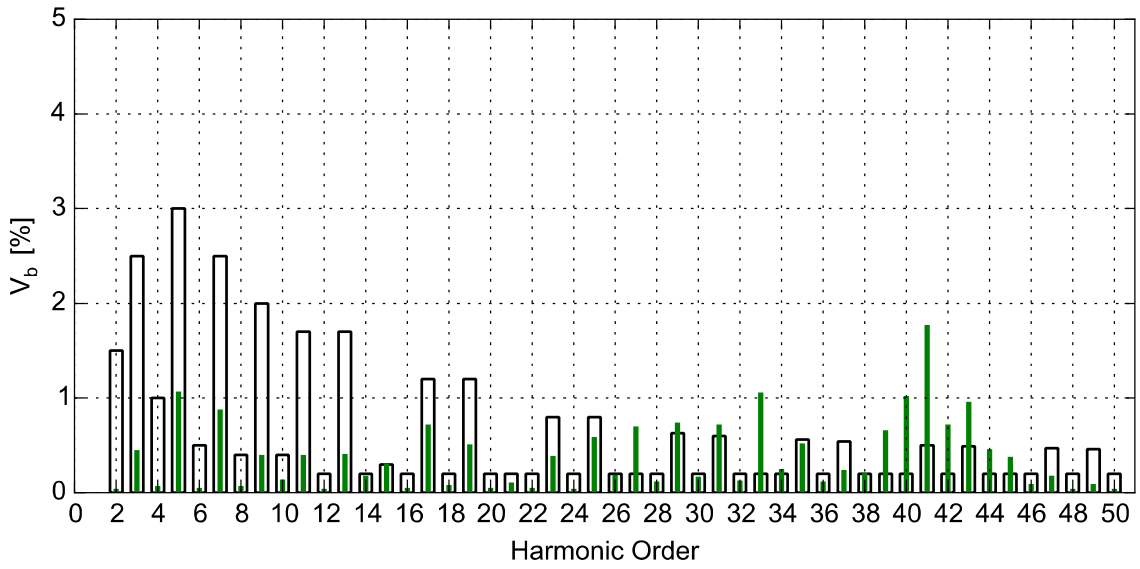

Figure 132: The 95th percentile measured voltage harmonic content of phase B (green) compared to the corresponding harmonic limit (black)

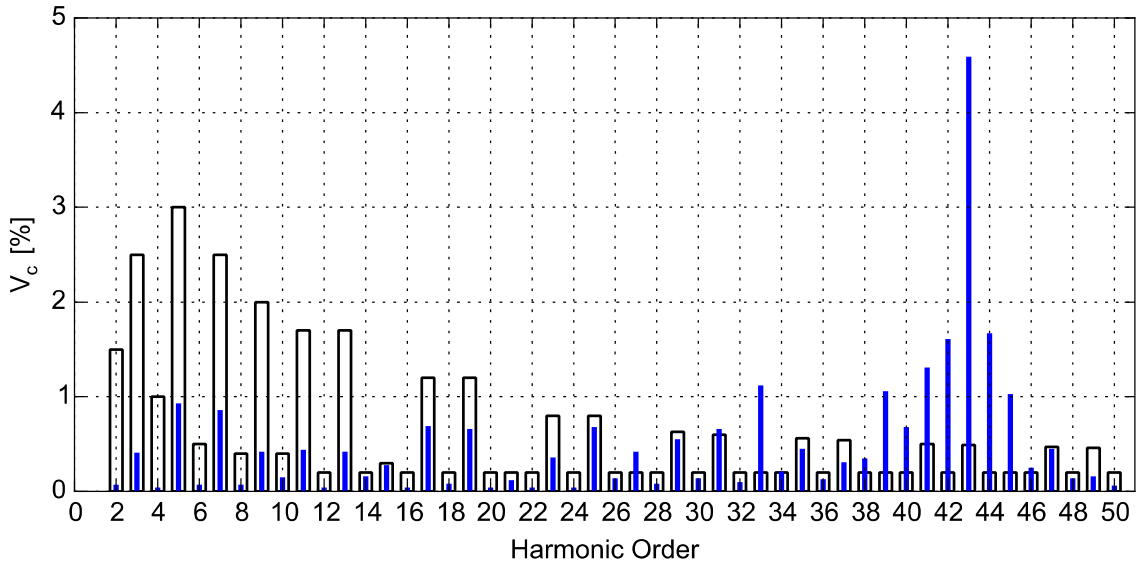

Figure 133: The 95th percentile measured voltage harmonic content of phase C (blue) compared to the corresponding harmonic limit (black)

From in Figure 131, Figure 132 and Figure 133 the individual voltage harmonics that exceeded the NRS 048-2 limits in one or more of the phases is shown in Table 6. The highlighted values are the specific values that exceeded the limits.

Table 6: The 95th percentile measured three-phase voltage harmonic that exceeded the NRS 048-2 limits

Harmonics	**NRS Limits (%)**	**Values V_a (%)**	**Values V_b (%)**	**Values V_c (%)**	**Average (%)**
15	0.3	**0.34**	**0.31**	0.28	0.31
27	0.2	**0.6**	**0.7**	**0.42**	0.573
29	0.63	**0.69**	**0.74**	0.55	0.66
31	0.6	**0.63**	**0.72**	**0.66**	0.67
33	0.2	**1.03**	**1.06**	**1.12**	1.07
34	0.2	**0.22**	**0.25**	**0.21**	0.227
35	0.56	**0.65**	0.52	0.45	0.54
36	0.2	**0.21**	0.12	0.13	0.153
38	0.2	**0.55**	**0.21**	**0.35**	0.37
39	0.2	**1.77**	**0.66**	**1.06**	1.163
40	0.2	**1.64**	**1.02**	**0.68**	1.113
41	0.5	**2.92**	**1.77**	**1.31**	2
42	0.2	**0.9**	**0.72**	**1.61**	1.077
43	0.49	**0.7**	**0.96**	**4.59**	2.083
44	0.2	**0.27**	**0.46**	**1.67**	0.8

45	0.2	0.19	**0.38**	**1.03**	0.533
46	0.2	0.05	0.09	**0.25**	0.13

Table 6 shows that there is a wide band of voltage harmonics, from the 27th harmonic up to 46th harmonic that exceeded the limits. There are significantly large voltage harmonic content at the 33rd harmonic and at frequencies between the 39th and 45th harmonic. This can be due to the combination of high-order harmonics sources such as PWM inverters within energy sources (RPPs) and active rectifier traction loads on the distribution network. Therefore, higher-order harmonics are of great concern on a traction network with RPPs and it becomes important to determine how traction loads contribute to the high-order harmonics in addition to low-order harmonics. There is often resonance points at these frequencies which cause significant voltage distortion.

Specific individual voltage harmonics will now be analysed by plotting the individual harmonics for the assessment period. Only the harmonics with significant voltage distortion will be discussed in this section. Therefore, from a low-order harmonic point of view only the 3rd, 5th and 7th harmonic will be analysed, which are characteristic of diode and thyristor rectifiers. From a high-order point of view only the 39th and 41st harmonic will be analysed, which is characteristic of active rectifiers. The 10-minute aggregated 3rd voltage harmonic at the POC is observed for the period of one week and is plotted as a percentage of the fundamental voltage as shown in Figure 134.

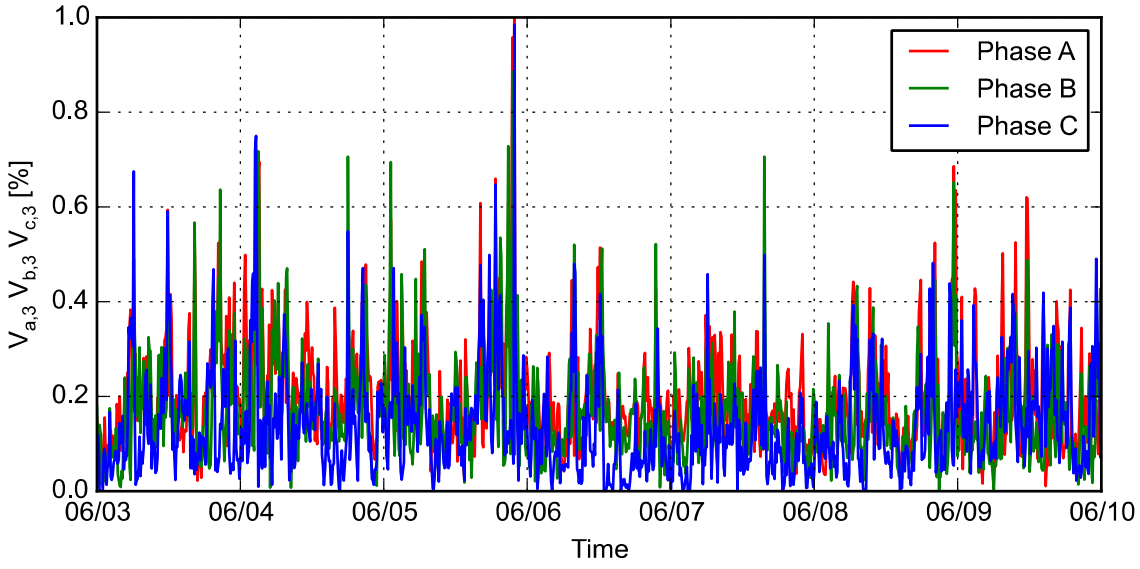

Figure 134: Measured 10-minute aggregated 3rd voltage harmonic at POC

The large spikes in the 3rd harmonic suggests that these low-order harmonics are generated by diode/thyristor traction loads. It can also be observed that the spikes usually occur on two of the three phases which is a further indication that the spikes are contributed by traction

loads. Therefore, it will appear as if the 3rd harmonic current generated by thyristor/diode rectifier will impact the voltage distortion at the POC. The 10-minute aggregated 5th voltage harmonic at the POC is observed for the period of one week and is plotted as a percentage of the fundamental voltage as shown in Figure 135.

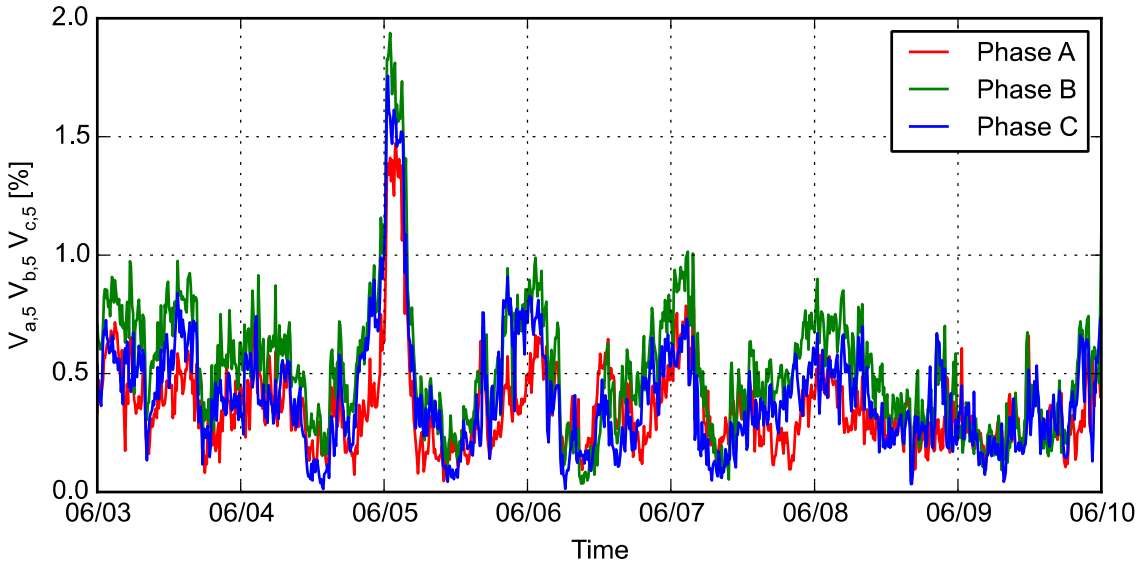

Figure 135: Measured 10-minute aggregated 5th voltage harmonic at POC

Figure 135 shows that the 5th voltage harmonic is approximately equal in all three phases due to the fact that the 5th harmonic is characteristic for the loads in a distribution network as well as for the railway system [138]. The 5th voltage harmonic increase significantly when the RPP is operating in reactive power control mode, i.e. when the RPP is not generating any active power. This is the reason for the high harmonics values at the start of 5 June 2018. It can be seen that the 5th harmonic current generated by thyristor/diode rectifiers, therefore, does not impact the voltage THD at the POC as significantly as with the 3rd harmonic component. The 10-minute aggregated 7th voltage harmonic at the POC is observed for the period of one week and is plotted as a percentage of the fundamental voltage as shown in Figure 136.

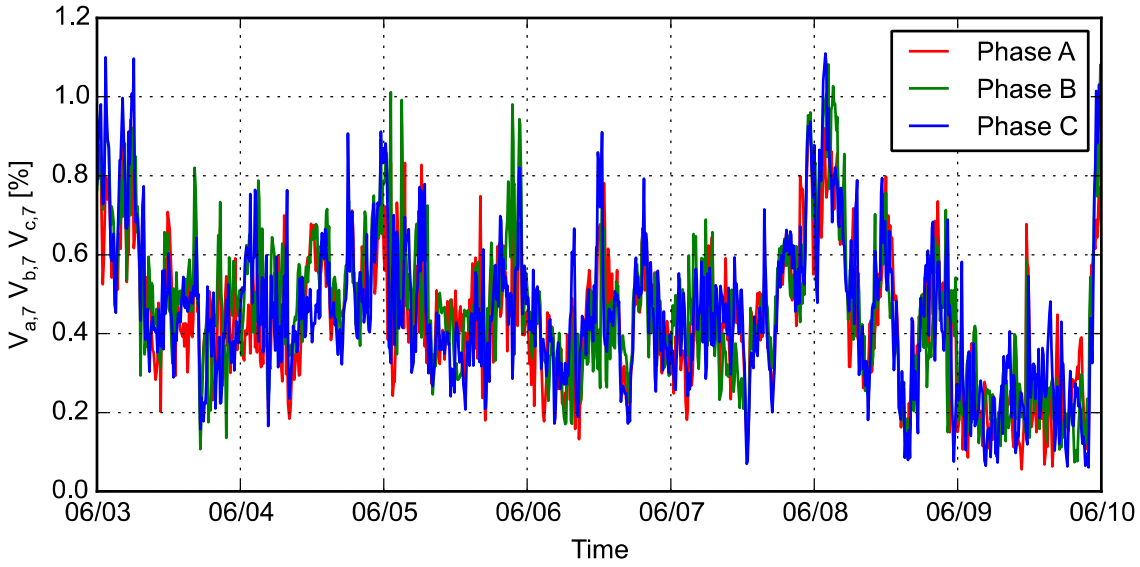

Figure 136: Measured 10-minute aggregated 7th voltage harmonic at POC

The 7th voltage harmonic in this case is related to the magnitude of the power generation from the RPP, a large power generation leads to lower 7th voltage and current harmonics and vice versa. Therefore, it will appear as if the 3rd harmonic component of thyristor/diode rectifier have the largest impact on the voltage distortion from a low-order harmonic point of view. However, it is important to mention that the 95th percentile 3rd voltage harmonic component did not exceed the respective NRS 048-2 limit.

Table 6 shows that the 38th, 39th, 40th and 41st harmonics in the observed period of one week are significantly higher on phase A than on phase B and phase C which can be due to resonance at that point and the typical high-order switching harmonics associated with single-phase active rectifier locomotives in that region. This is shown in Figure 137 for the 10-minute aggregated 39th harmonic voltage as a percentage of the fundamental voltage at the POC.

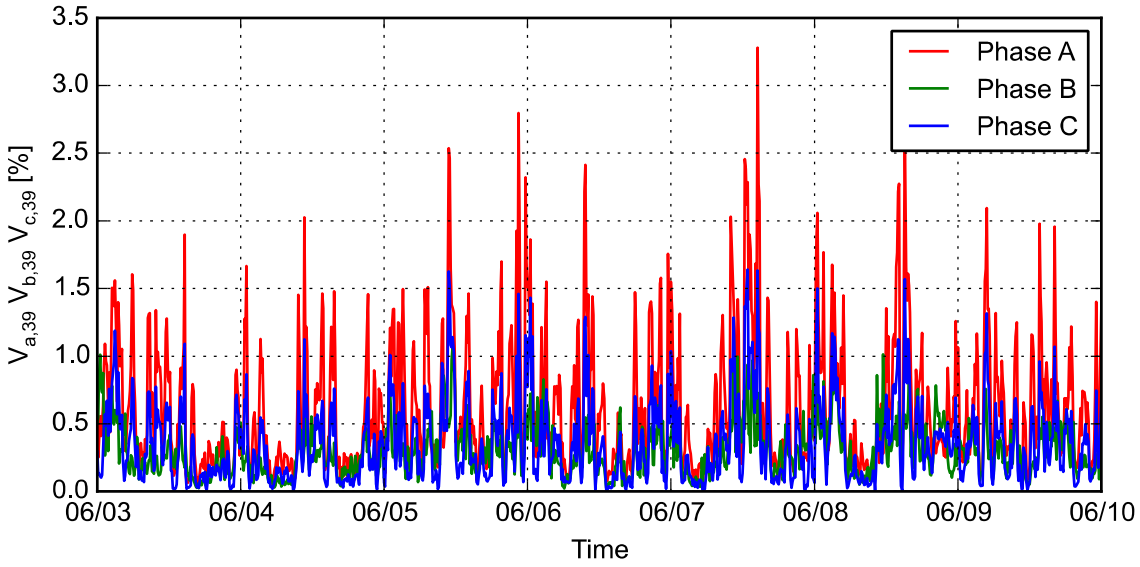

Figure 137: Measured 10-minute aggregated 39th voltage harmonic at POC

To prove the presence of a parallel resonance on the network, the DIgSILENT PowerFactory Wind farm A model was connected to the DIgSILENT PowerFactory Eastern Cape distribution network model which is constantly updated by Eskom. Due to the large size of the distribution network the network layout in DIgSILENT PowerFactory will not be shown. A frequency sweep is simulated and the results at the POC is shown in Figure 138.

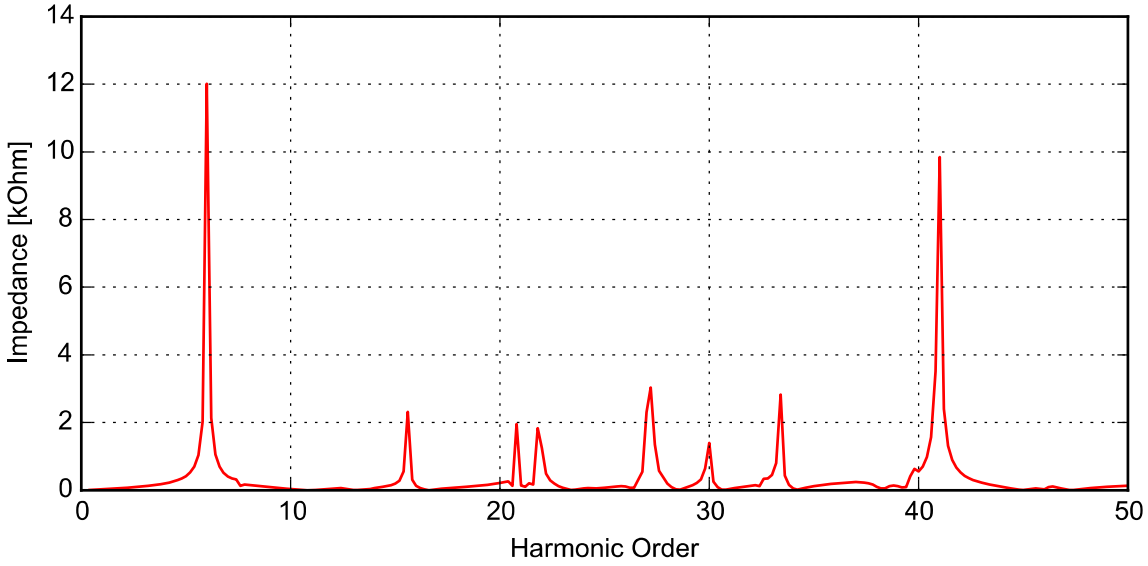

Figure 138: Simulated parallel resonance at POC

Figure 138 shows that there is parallel resonance points at the following harmonic components: 7th, 15th, 21st, 23rd, 27th, 30th, 33rd and 41st harmonic. This explains the high voltage distortion at the 33rd, 39th and 41st harmonic as small currents generated by active rectifier locomotives can cause large voltage distortion at these frequencies especially at the 39th and 41st harmonic due to the significant high resonance point.

The 39th harmonic current for all three phases as shown in Figure 139 clearly shows that the 39th current harmonic of phase B is zero and that the 39th voltage harmonics for phase A and phase C are significantly larger. Furthermore, it shows that small current harmonics can lead to large voltage harmonics when the harmonics are in the proximity of a parallel resonance which was shown in Figure 138.

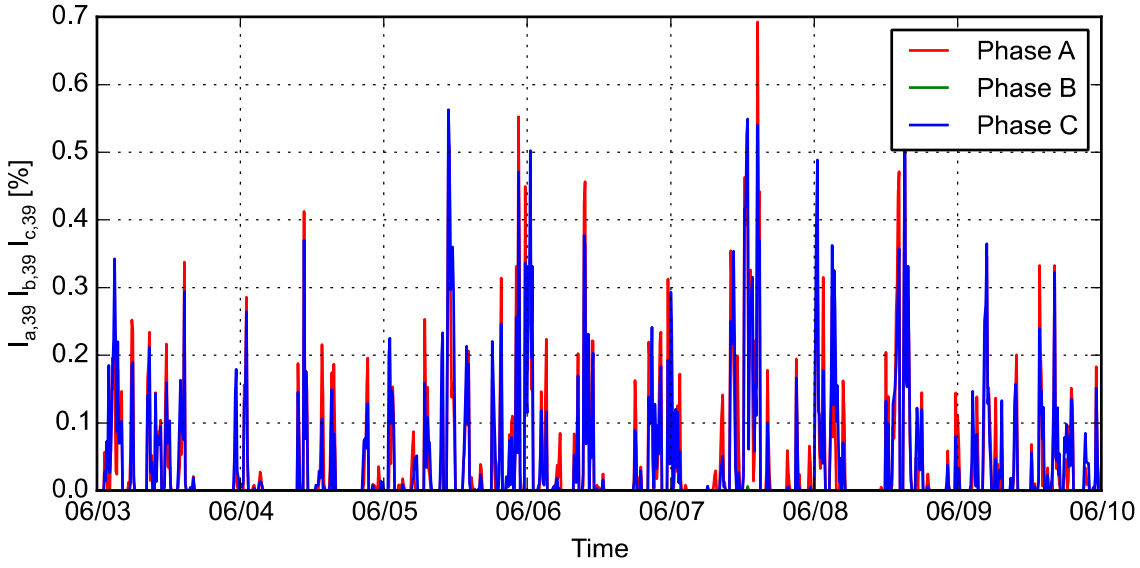

Figure 139: Measured 10-minute aggregated 39th current harmonic at POC

Similarly, the 43rd, 44th, 45th and 46th harmonics in the observed period of one week are significantly higher on phase B and phase C than on phase A and is shown in Figure 140 for the 10-minute aggregated 43rd harmonic as a percentage of the fundamental voltage at the POC. This can be due to the resonance that shifts as the locomotive move from traction substation to traction substation as the power system and traction system topology changes as discussed in Section 2.7.4.2.

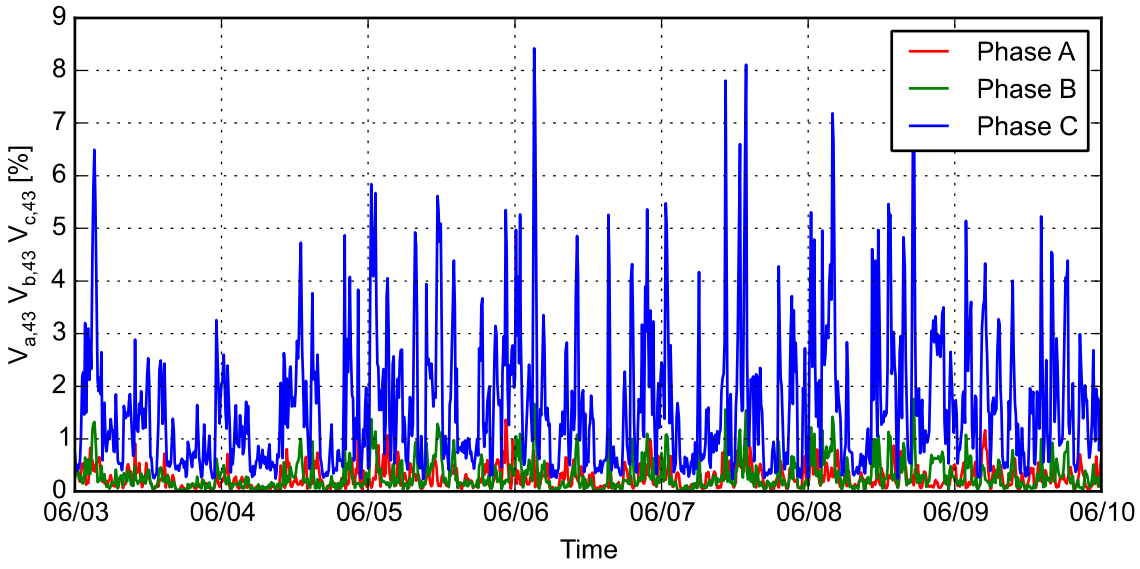

Figure 140: Measured 10-minute aggregated 43rd voltage harmonic at POC

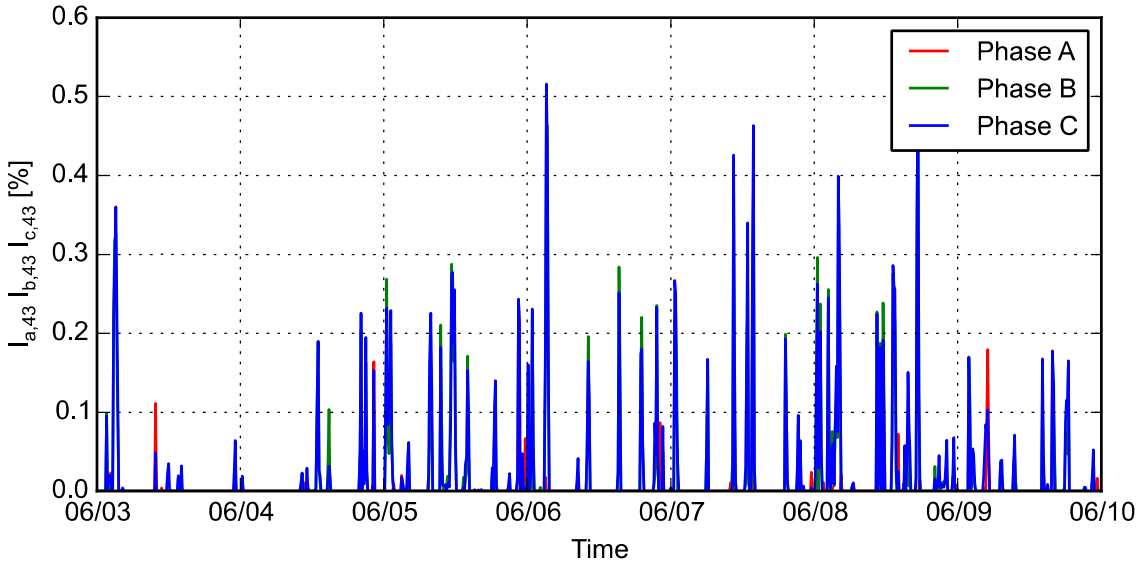

Figure 141: Measured 10-minute aggregated 43rd current harmonic at POC

The sudden increase and decrease in the 39th and 43rd voltage and current harmonics suggests that these high-order harmonics are generated by active rectifier locomotives. Therefore, it will appear as if small higher-order current harmonic components of active rectifiers can have a large impact on the voltage distortion at the POC when the harmonics is in the vicinity of a parallel resonance.

6.6. MEASURED LOCOMOTIVE INDIVIDUAL HARMONIC EMISSIONS

To investigate the effect that traction loads can have on the RPP assessment and the voltage distortion at the POC the individual harmonic content of traction loads will be investigated in this section. By investigating the harmonic spectrum of locomotives on the network it can be

determined which harmonics can influence the current emissions of RPPs. A second Elspec PQ recorder, Elspec B, is installed at a nearby traction substation to overcome the short comings with the single-point assessment approach discussed in Section 2.6.4.3.

6.6.1. Half-controlled thyristor rectifiers

The 132 kV phase voltages and single-phase locomotive current waveforms were measured at the traction substation with Elspec B. A number of snapshots were taken at different times during the day to determine the locomotive technology types and to get a better understanding of the dynamic effect of traction loads and the wide variety of load conditions that RPPs are subjected to on a traction power system. Figure 142 shows the single-phase current waveform drawn by a thyristor or diode rectifier locomotive for the first time period.

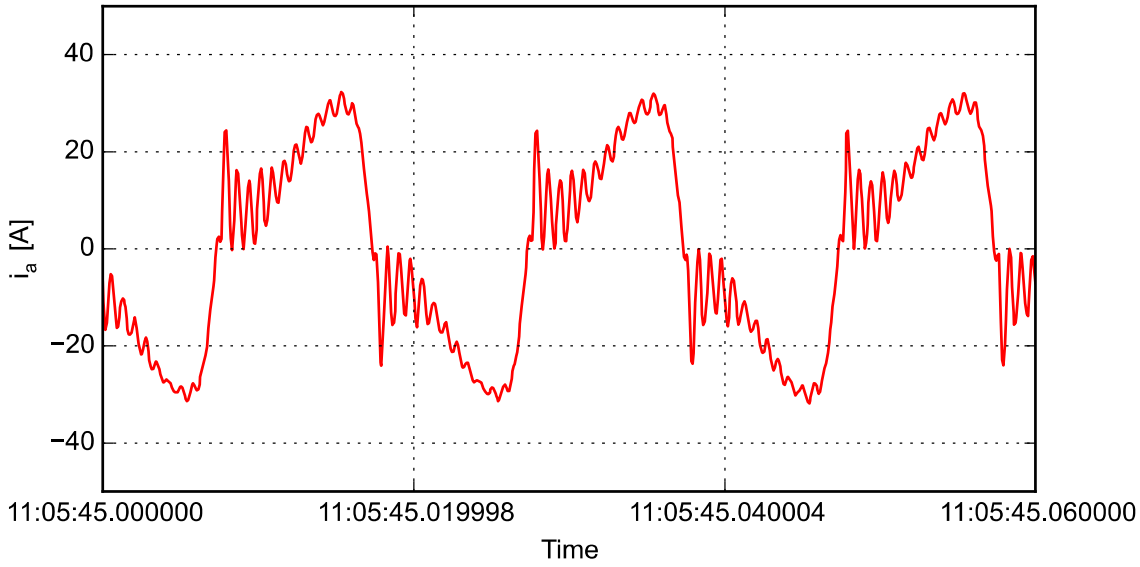

Figure 142: Measured single-phase current waveform on 132 kV side of traction substation transformer (snapshot 1)

Figure 143 shows the current harmonic spectrum of the single-phase current measured at the 132 kV side of the traction substation transformer for the first time period.

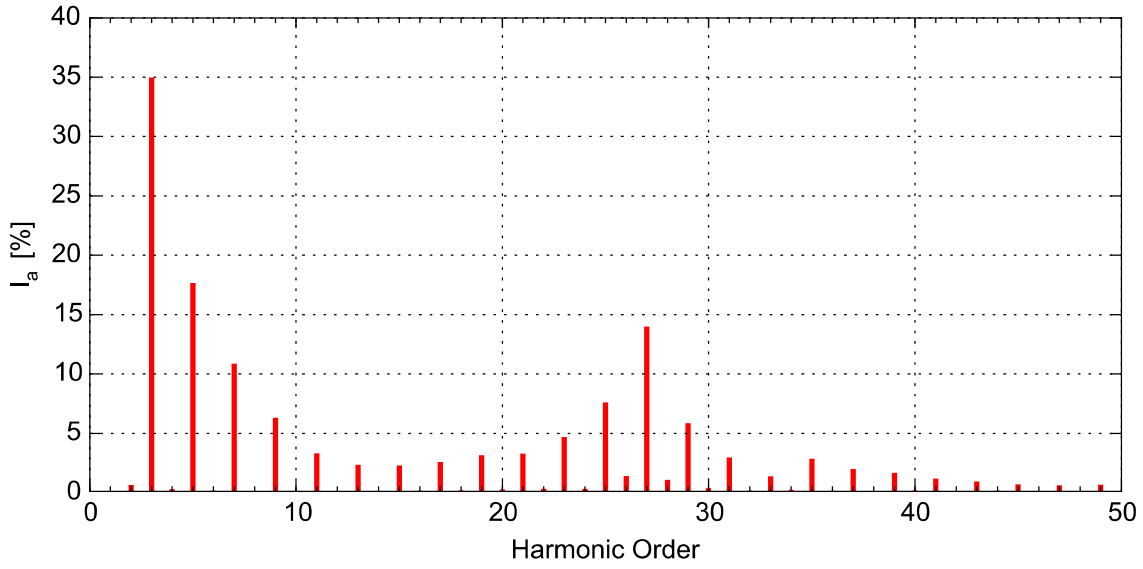

Figure 143: Measured current harmonics as a percentage of the fundamental current magnitude on 132 kV side of traction substation transformer (snapshot 1)

The low-order 3rd, 5th and 7th harmonic are characteristic of a half-controlled thyristor controlled locomotive. There is also significant higher-order harmonics at and surrounding 1.35 kHz which is generated due to the resonance effect of the on-board locomotive capacitor and grid impedance as shown in Section 6.7.1. The higher-order ripple is clearly visible in the current waveform. Figure 144 shows the phase voltage waveform at the 132 kV side of the traction transformer for the first time period.

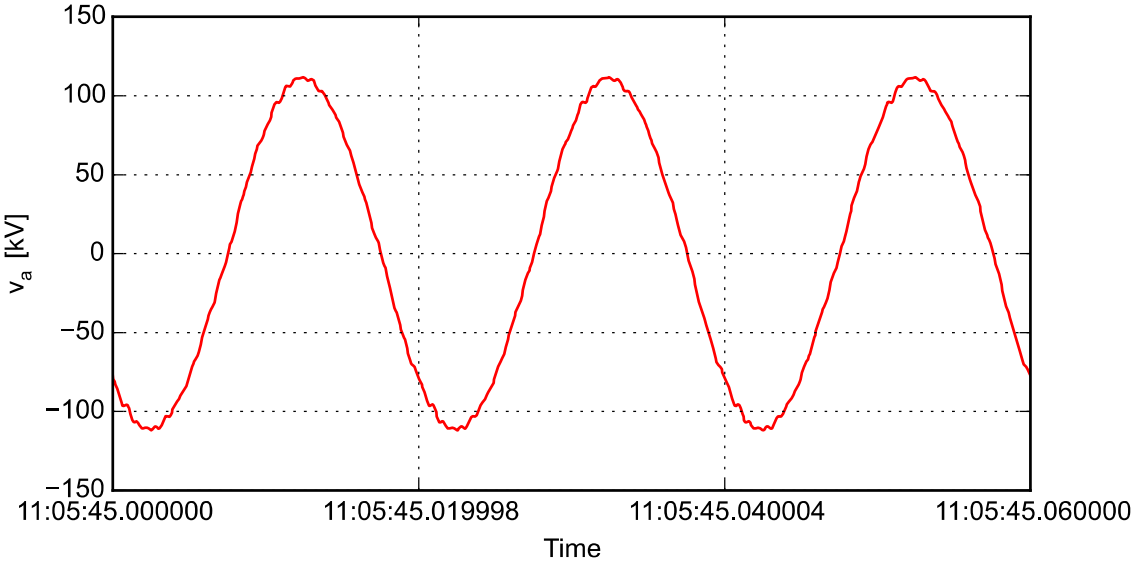

Figure 144: Measured phase voltage waveform on 132 kV side of traction substation transformer (snapshot 1)

Figure 145 shows the voltage harmonic spectrum of the phase voltage measured at the 132 kV side of the traction substation transformer for the first time period.

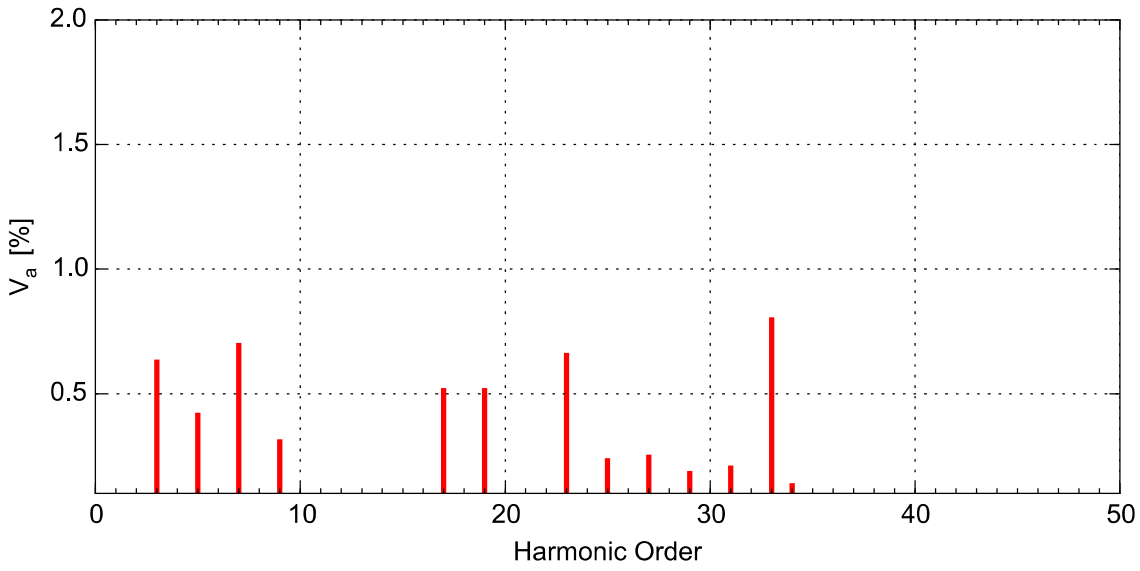

Figure 145: Measured voltage harmonics as a percentage of the fundamental voltage magnitude on 132 kV side of traction substation transformer (snapshot 1)

The half-controlled thyristor controlled locomotive causes voltage distortion on the 25 kV side of the traction substation transformer and is passed through to the 132 kV side of the transformer. Figure 146 shows the single-phase current waveform drawn by a thyristor or diode rectifier locomotive and Figure 147 the phase voltage waveform at the 132 kV side of the traction transformer for a second time period but for the same locomotive in Figure 142 and Figure 144.

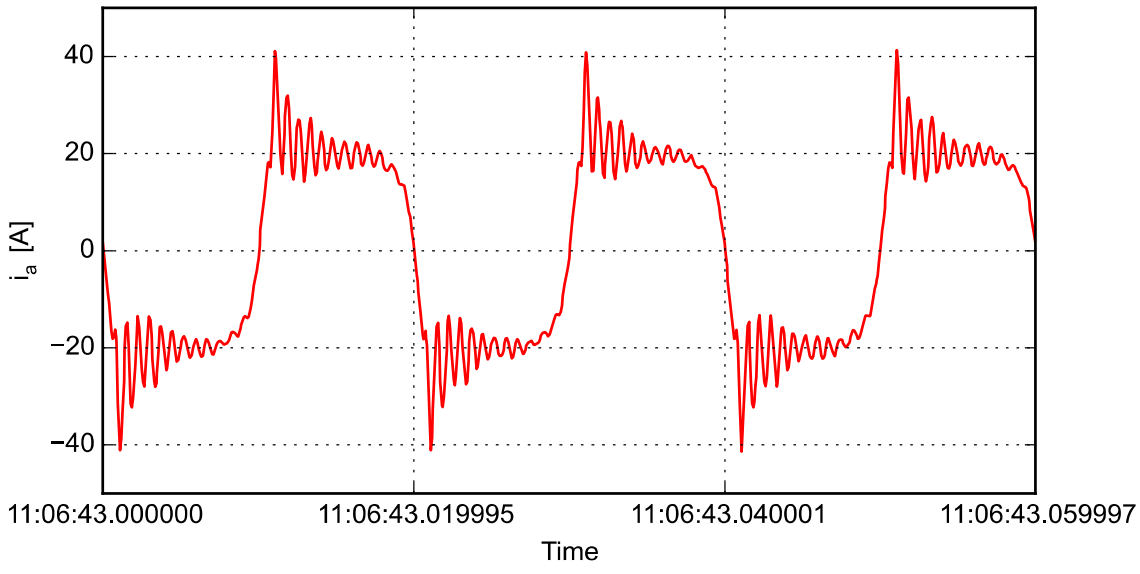

Figure 146: Measured single-phase current waveform on 132 kV side of traction substation transformer (snapshot 2)

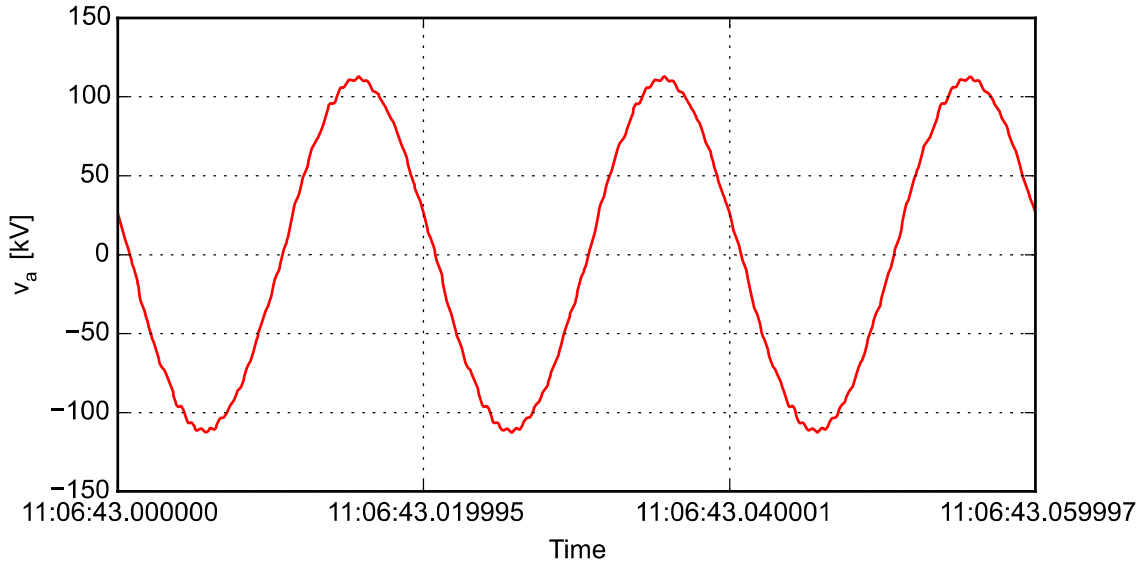

Figure 147: Measured phase voltage waveform on 132 kV side of traction substation transformer (snapshot 2)

Figure 148 shows the current harmonic spectrum of the single-phase current measured at the 132 kV side of the traction substation transformer for the second time period.

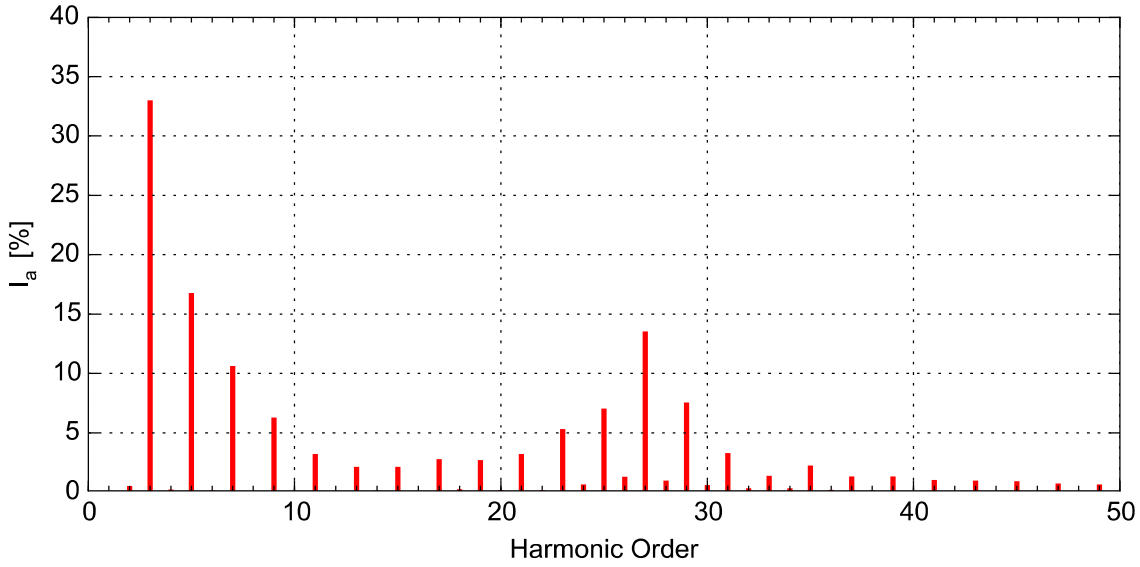

Figure 148: Measured current harmonics as a percentage of the fundamental current magnitude on 132 kV side of traction substation transformer (snapshot 2)

The phase current and voltage harmonics for snapshot 2 is similar to that of snapshot 1. The change in the current waveform is due to the control of the rectifier such as the change in firing angles of the thyristors as the operating mode of the locomotive changes. Figure 149 shows the voltage harmonic spectrum of the phase voltage measured at the 132 kV side of the traction substation transformer for the second time period.

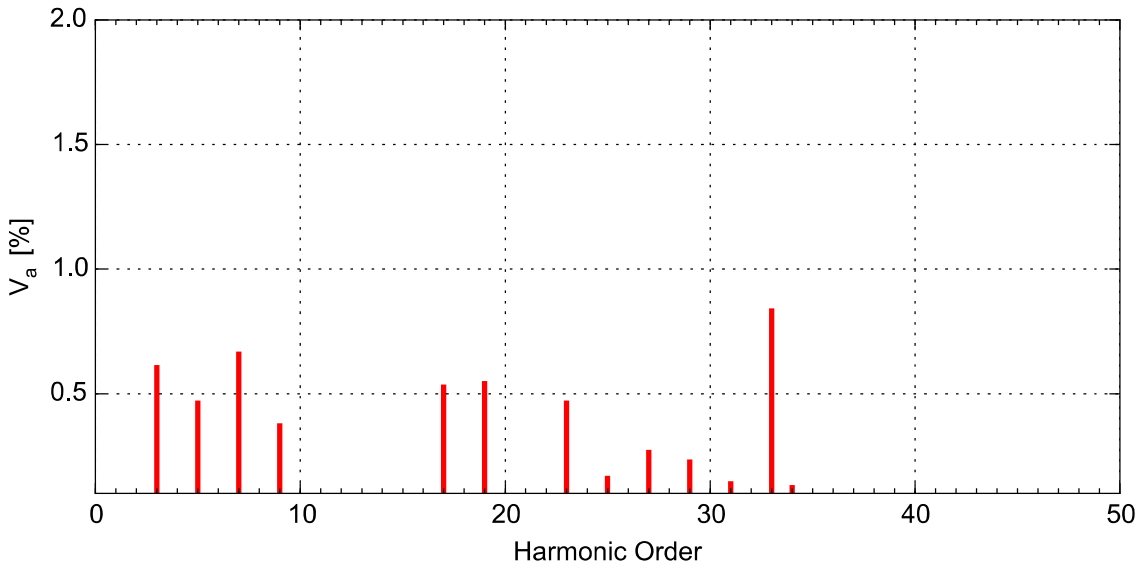

Figure 149: Measured voltage harmonics as a percentage of the fundamental voltage magnitude on 132 kV side of traction substation transformer (snapshot 2)

Figure 150 shows the single-phase current waveform drawn by a thyristor or diode rectifier locomotive and Figure 151 the phase voltage waveform at the 132 kV side of the traction transformer for a third time period. It is unclear whether the snapshot 3 measurement results was obtained from the same locomotive in snapshot 1 and snapshot 2 but this clearly shows the wide range of loads and the effect of the loads on PQ in traction power systems.

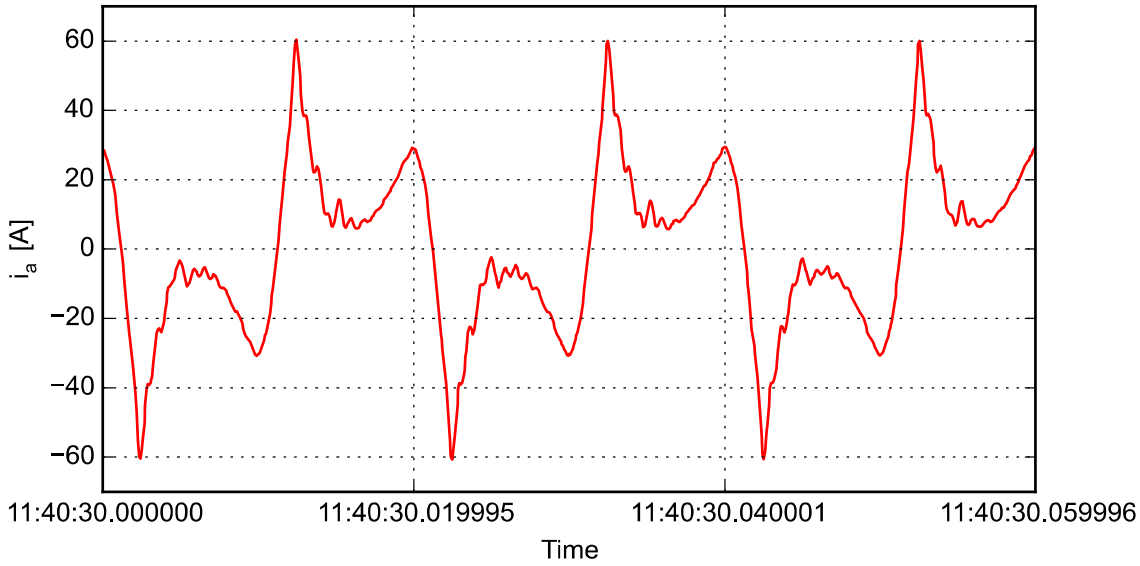

Figure 150: Measured single-phase current waveform on 132 kV side of traction substation transformer (snapshot 3)

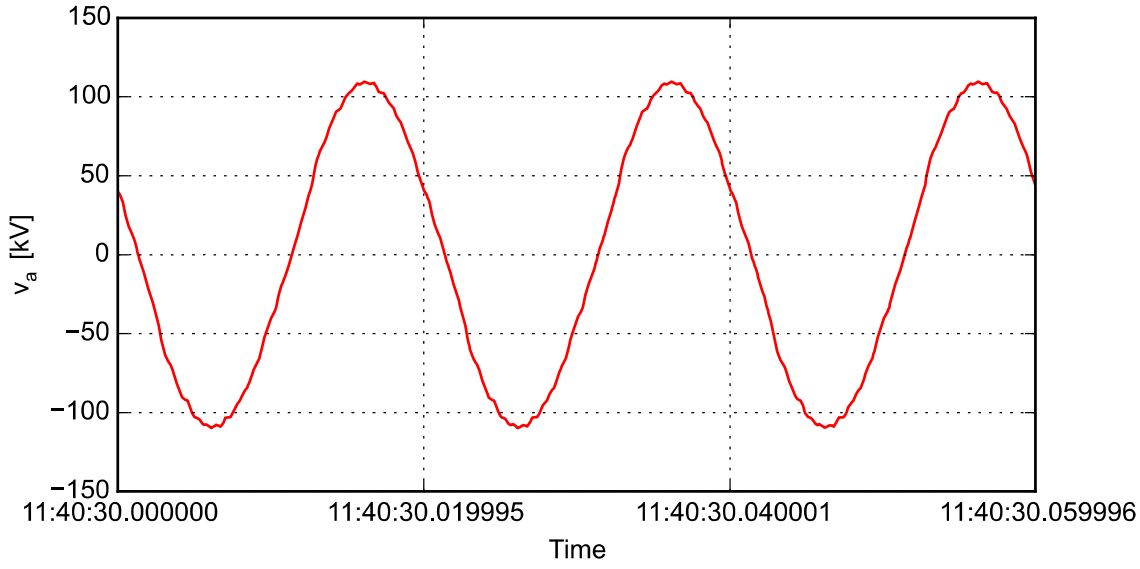

Figure 151: Measured phase voltage waveform on 132 kV side of traction substation transformer (snapshot 3)

Figure 152 shows the current harmonic spectrum of the single-phase current measured at the 132 kV side of the traction substation transformer for the third time period.

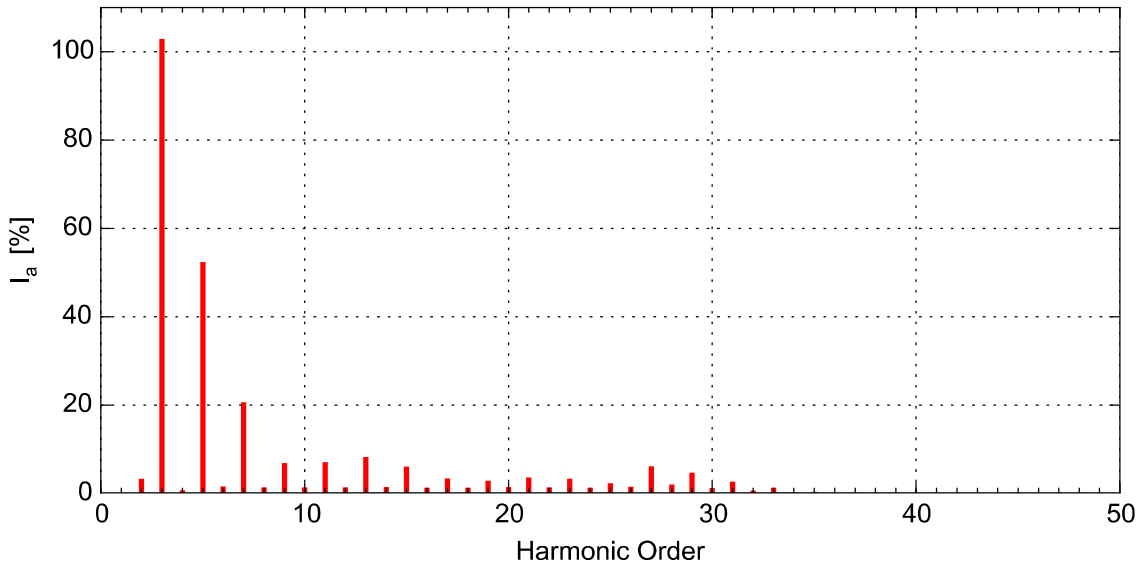

Figure 152: Measured current harmonics as a percentage of the fundamental current magnitude on 132 kV side of traction substation transformer (snapshot 3)

The 3rd, 5th and 7th harmonic are significantly larger than that measured for snapshot 1 and snapshot 2. This can be due to the resonance effect caused by large power factor correction capacitors installed on-board in addition to the typical low-order harmonics associated with thyristor or diode rectifier locomotives. Figure 149 shows the voltage harmonic spectrum of the phase voltage measured at the 132 kV side of the traction substation transformer for the third time period.

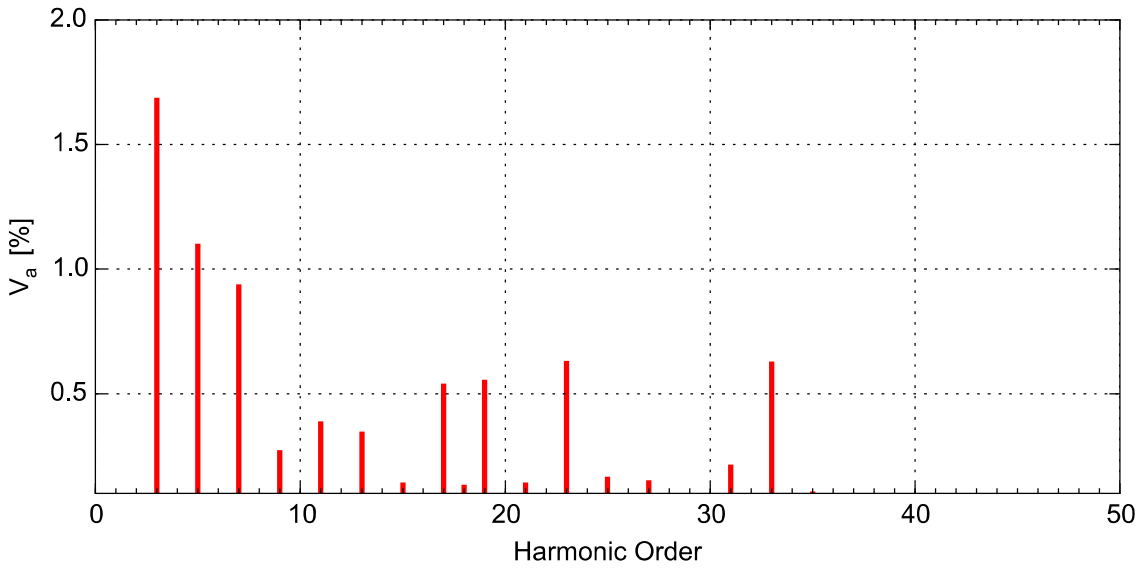

Figure 153: Measured voltage harmonics as a percentage of the fundamental voltage magnitude on 132 kV side of traction substation transformer (snapshot 3)

The magnitude of the generated low-order current harmonics clearly have an impact on the low-order voltage harmonics. The low-order voltage harmonics for the third time period is significantly larger than that of snapshot 1 and 2 while the higher-order harmonics are similar in comparison.

6.6.2. Active rectifiers

Figure 154 shows the single-phase current waveform drawn by an active rectifier locomotive and Figure 144 the phase voltage waveform at the 132 kV side of the traction transformer.

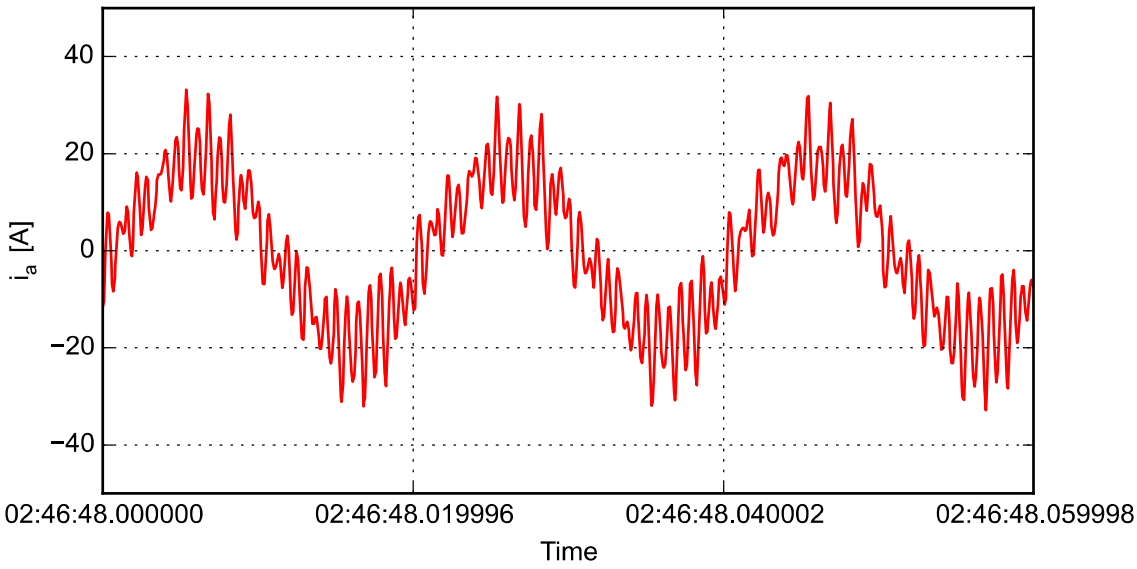

Figure 154: Measured single-phase current waveform on 132 kV side of traction substation transformer (snapshot 4)

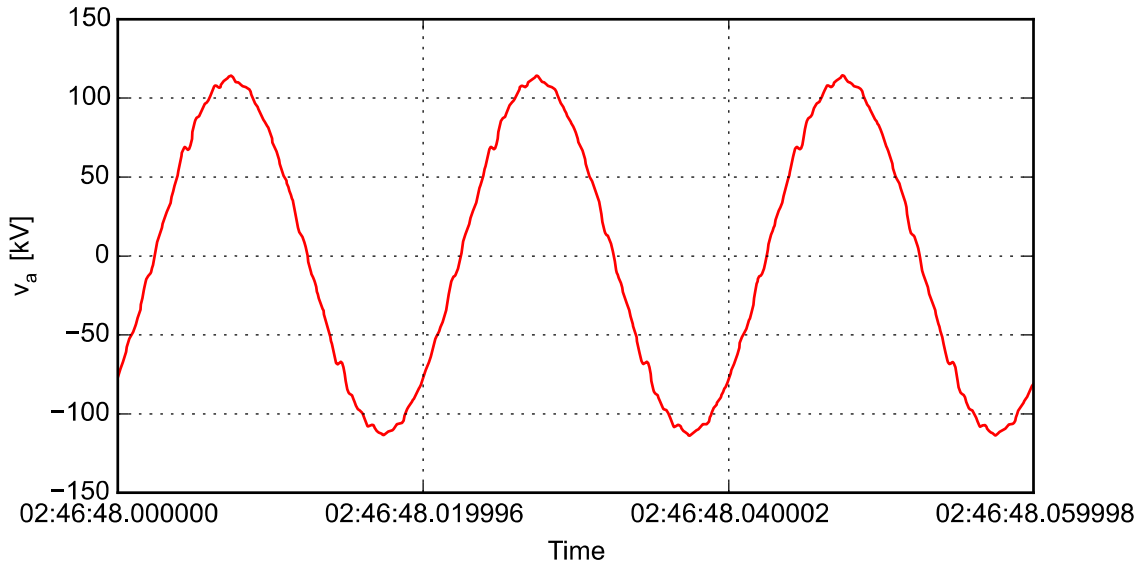

Figure 155: Measured phase voltage waveform on 132 kV side of traction substation transformer (snapshot 4)

Figure 156 shows the current harmonic spectrum of the single-phase current measured at the 132 kV side of the traction substation transformer for the fourth time period.

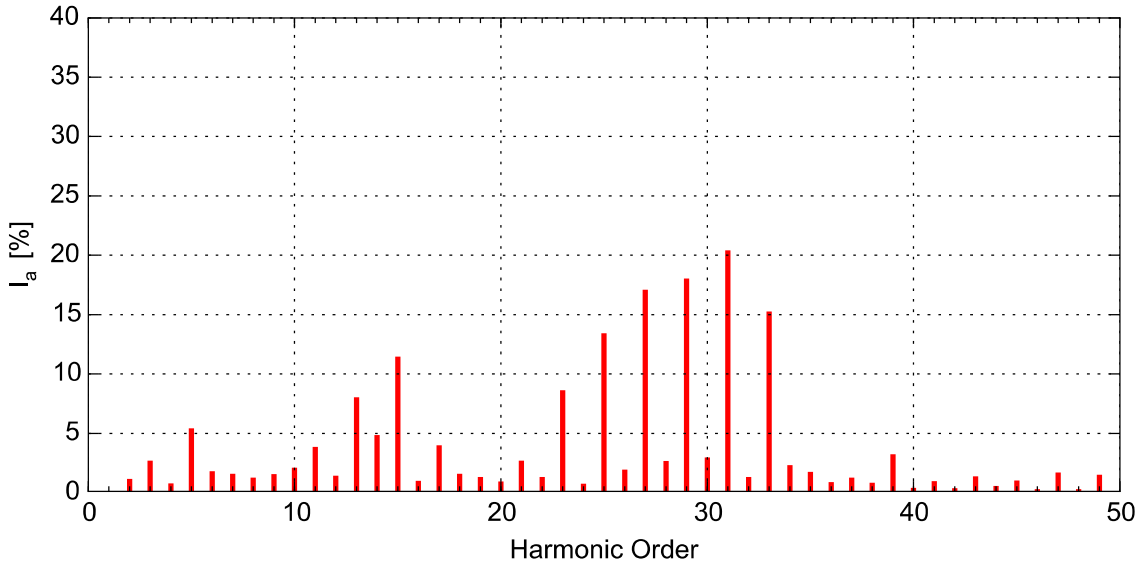

Figure 156: Measured current harmonics as a percentage of the fundamental current magnitude on 132 kV side of traction substation transformer (snapshot 4)

The current waveform in Figure 154 with significant high-order harmonic surrounding 1.5 kHz (30th harmonic) are characteristic of an active rectifier locomotive with a switching frequency of 1.5 kHz. The harmonic components at 650 Hz (13th harmonic) and 750 Hz (15th harmonic) is most likely caused by a parallel resonance in the traction network. The low-order harmonics for an active rectifier locomotive is significantly lower than that of a thyristor locomotive. Figure 157 shows the voltage harmonic spectrum of the phase voltage measured at the 132 kV side of the traction substation transformer for the fourth time period.

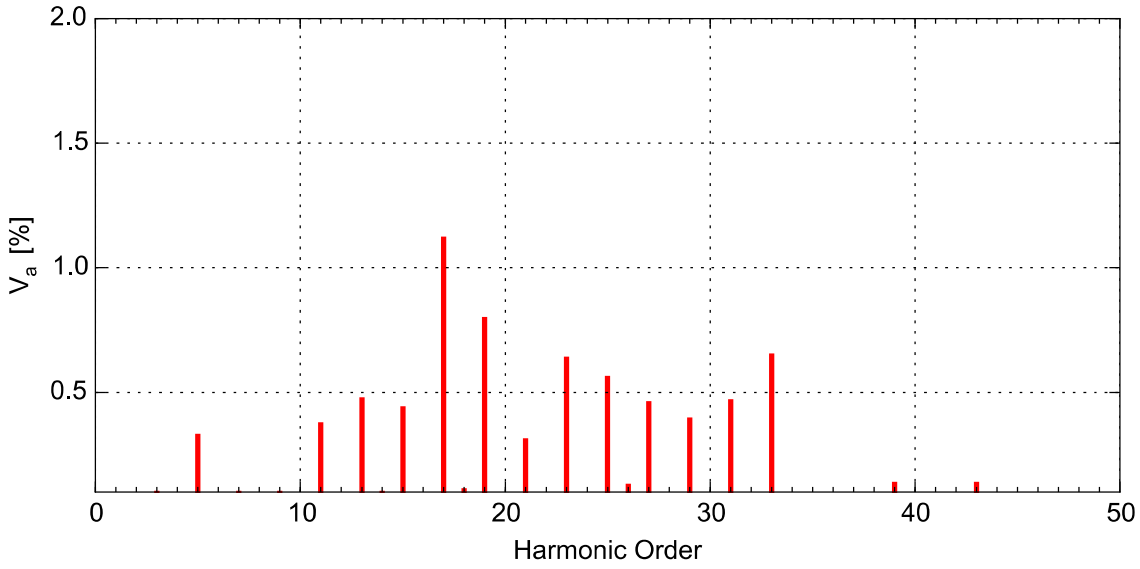

Figure 157: Measured voltage harmonics as a percentage of the fundamental voltage magnitude on 132 kV side of traction substation transformer (snapshot 4)

The low-order voltage harmonics when an active rectifier locomotive is present are significantly smaller than that of the low-order voltage harmonics produced by thyristor locomotives as shown in Figure 145, Figure 149 and Figure 153. The higher-order harmonics, however, have increased due to the current harmonics injected by the active rectifier locomotive at and around the switching frequency.

6.7. SIMULATED INDIVIDUAL HARMONIC EMISSIONS

In this section the current waveforms and respective harmonic spectrums in Section 6.6 will be compared to the simulation results of the designed active rectifier and half-controlled thyristor rectifier models designed in Section 3.5. The aim is to validate the simulation models and compare the simulated results to the measured results so to determine whether these models can be used as reliable dynamic models for future PQ studies in the time domain.

6.7.1. Half-controlled thyristor rectifier

The simulation results for the half-controlled thyristor rectifier were obtained using the model presented in Section 3.5.2. The grid is simulated using an external grid with no background harmonics. The simulated single-phase current waveform on the 132 kV side of the traction transformer is shown in Figure 158.

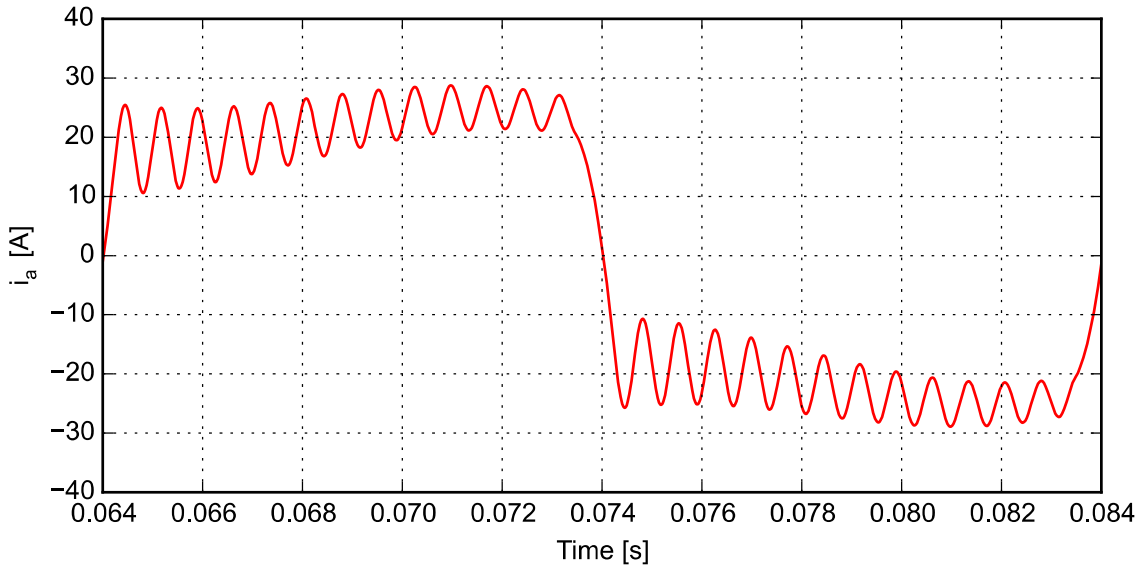

Figure 158: Simulated single-phase current waveform on 132 kV side of traction substation transformer

Figure 159 shows the simulated current harmonic spectrum of the simulated single-phase current measured at the 132 kV side of the traction substation transformer.

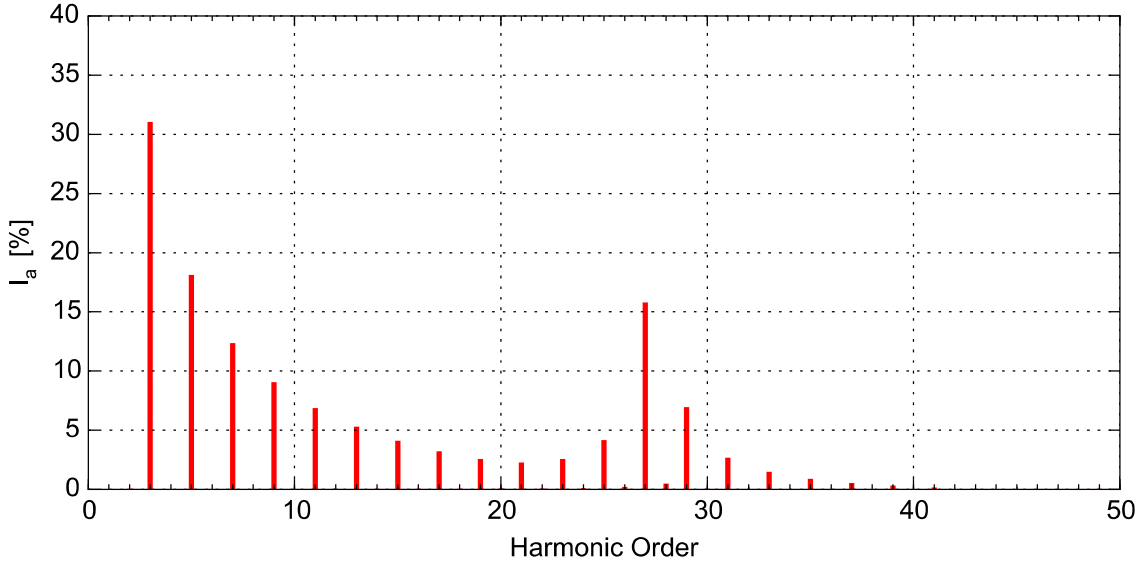

Figure 159: Simulated current harmonics as a percentage of the fundamental current magnitude on 132 kV side of traction substation transformer

Figure 160 shows the parallel resonance in the traction system.

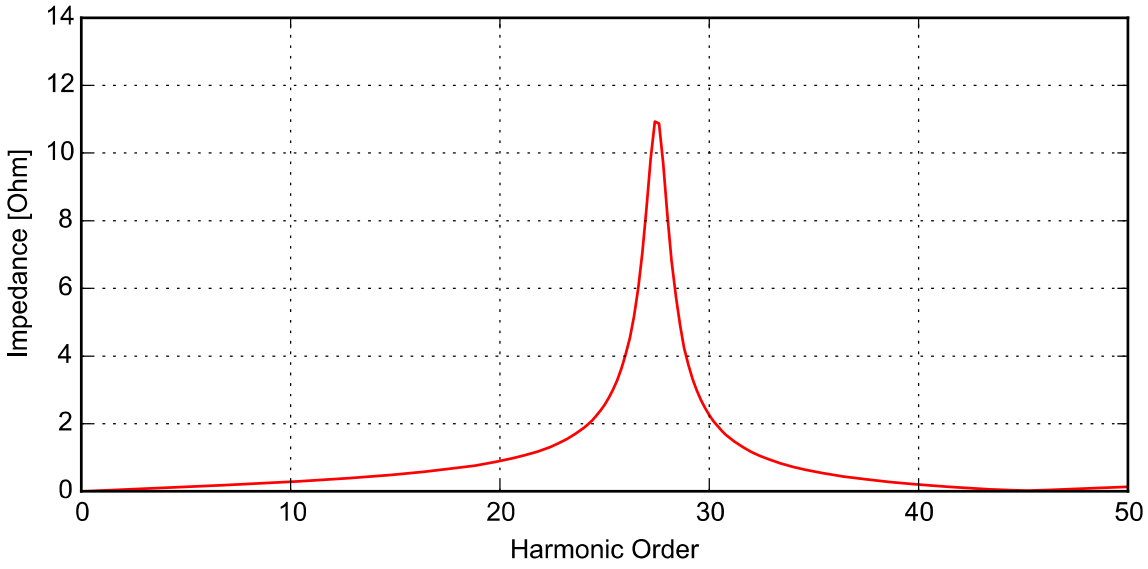

Figure 160: Simulated parallel resonance in traction system

It is clear that the higher-order current harmonics at and around 1.35 kHz in Figure 143, Figure 148 and Figure 159 are generated by the parallel resonance in the traction network. The half-controlled thyristor locomotive model provide adequate harmonic results and can thus be used for reliable future PQ studies.

6.7.2. Active rectifier

The simulation results for the active rectifier were obtained using the model presented in Section 3.5.1. The grid is simulated using an external grid with no background harmonics. The

simulated single-phase current waveform on the 132 kV side of the traction transformer is shown in Figure 161.

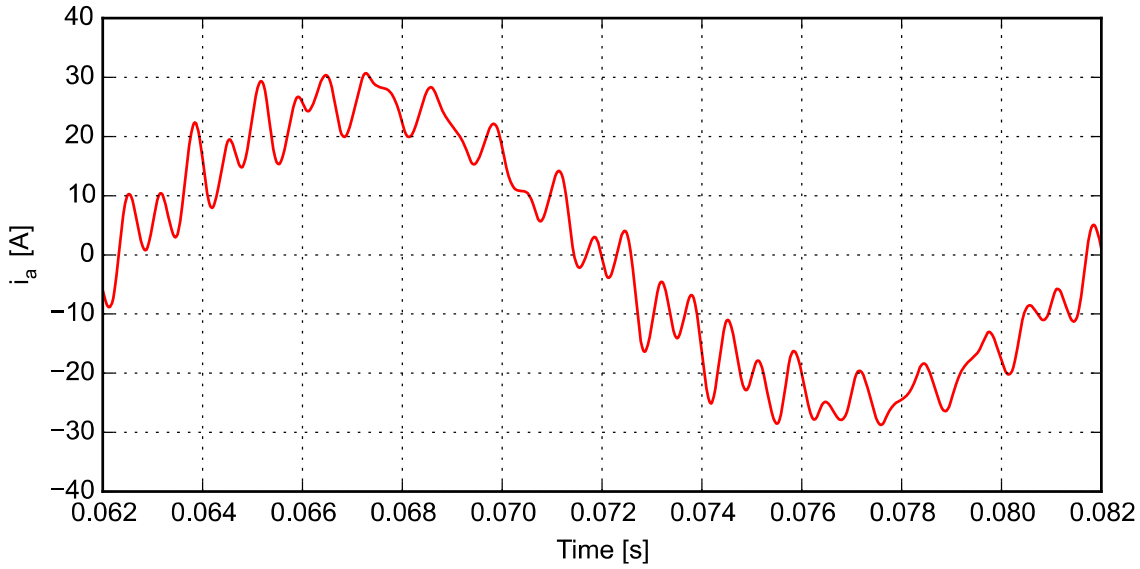

Figure 161: Simulated single-phase current waveform on 132 kV side of traction substation transformer

Figure 159 shows the simulated current harmonic spectrum of the simulated single-phase current measured at the 132 kV side of the traction substation transformer.

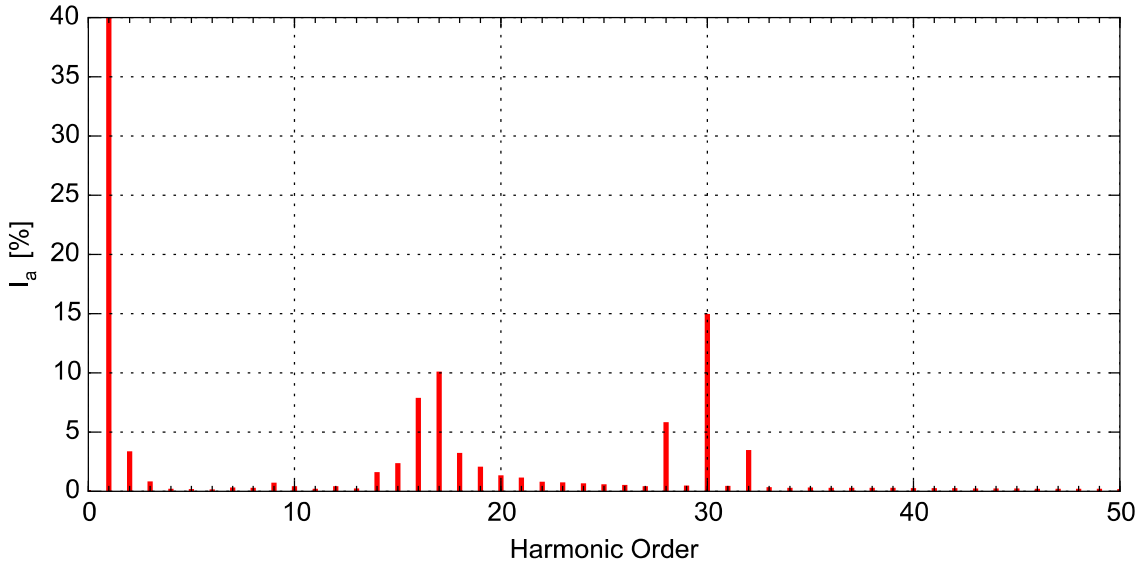

Figure 162: Simulated current harmonics as a percentage of the fundamental current magnitude on 132 kV side of traction substation transformer

The simulated harmonic spectrum in Figure 162 is similar to the measured results in Figure 156. It is important to note that the simulated magnitude of the individual harmonics at the switching frequency, 1.5 kHz, is smaller. This is due to the assumptions made surrounding the AC filter. Therefore, it can be said that the active rectifier locomotive model can provide

adequate harmonic results but require more information about the equipment ratings so that the model can be used for reliable future PQ studies in time domain.

6.8. THE IMPACT OF IMPEDANCE AND BACKGROUND HARMONICS ON EMISSION LEVELS OF RPP

This section will be investigated by using the calculation of harmonic emissions of RPPs for compliance assessment theory described in Section 2.6.4.3. The effect of the consumer impedance $\bar{\bar{Z}}_{hc}$ and background harmonics $\bar{V}_{h0}$ when connecting inverters to LV networks need to be modelled. Single-phase half-controlled thyristor or diode rectifiers typically produce third harmonic distortion as shown in Section 6.6.1 and Section 6.7.1. The effect of this harmonic will subsequently be investigated when present in circuits containing inverter loads. A simple investigation is done using Matlab/Simulink. The inverter output filter capacitance is arbitrary selected as 1 nF.

The effect of $\bar{I}_h$ on the network can be determined by setting $\bar{V}_{h0} = 0$ V in Figure 163. The harmonic spectrum in Figure 164 marked by 'o', shows the harmonic components at the switching frequency. When background harmonics is added in the form of a 3% component of the third harmonic, the consequence is shown by the harmonic spectrum marked by 'x'. The only additional component at the installation voltage is a third harmonic with a 3% amplitude. This means very little third harmonic current was caused by the background harmonic voltage source to flow into the inverters output stage to cause additional distortion at the inverter terminals. This can be expected when calculating the impedance of the output filter capacitance (1 nF) of the inverter:

$$\left|\bar{\bar{Z}}_{hc}\right| = \frac{1}{\omega C} = \frac{1}{2\pi 150.1.10^{-9}} = 1000\,\text{k}\Omega \tag{5.1}$$

By using this value in (2.26), reveals that negligible distortion is caused by lower-order background harmonics. To investigate when background harmonics become more significant, inverter capacitance was increased by a factor 1000, i.e. to $1\,\mu\text{F}$.

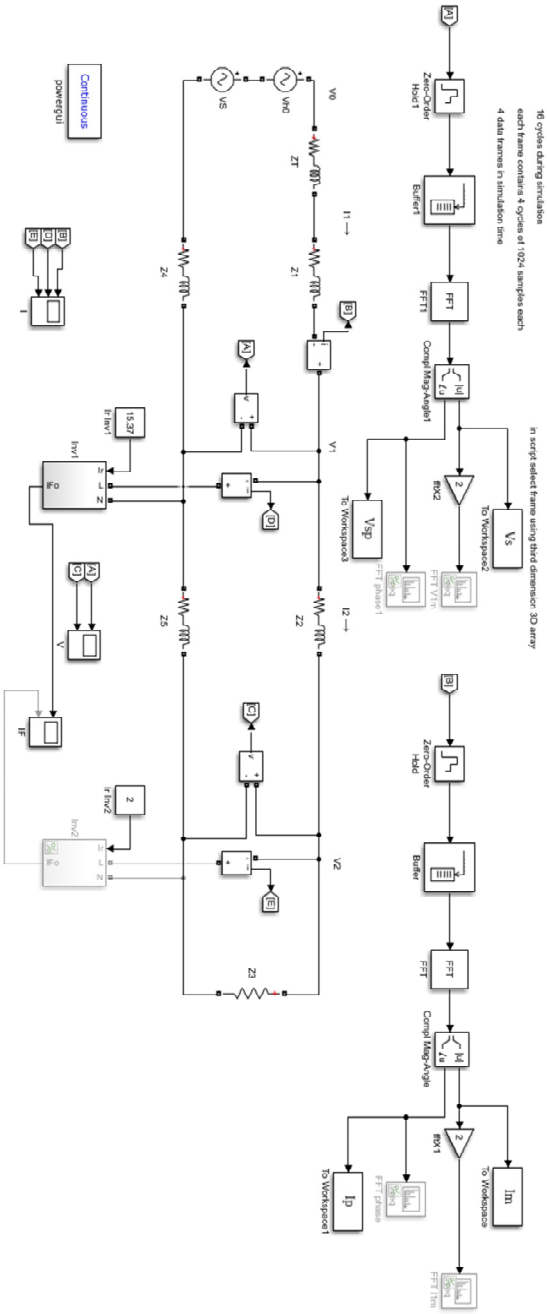

Figure 163: Simulink model of inverters connected to a simple LV feeder

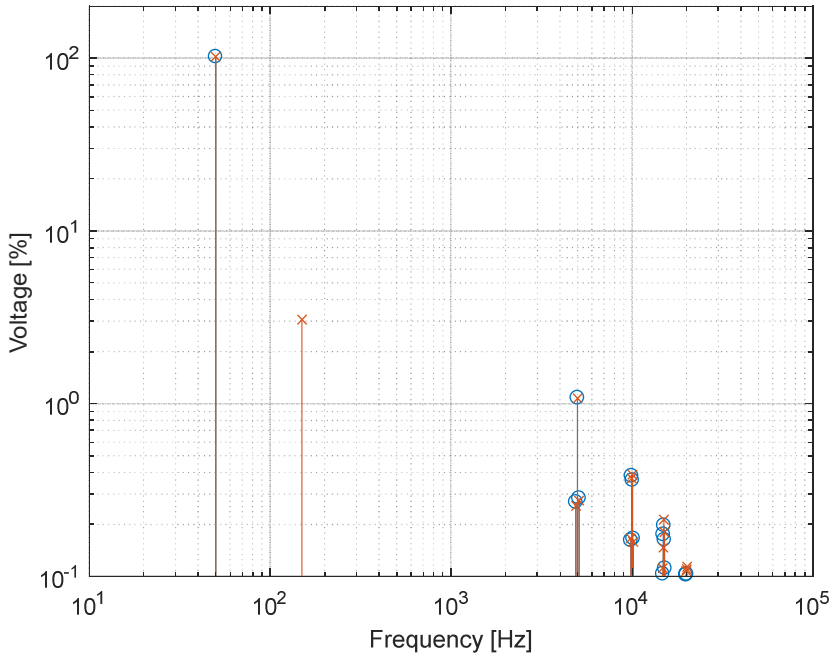

Figure 164: Harmonic spectrum of voltage at installation 1 without background harmonics ‘o’ and with third order background harmonic ‘x’

By increasing the inverter filter capacitance from 1 nF to 1 μF, the third harmonic distortion caused by the background source is slightly increased, while there is a significant effect on filtering switching frequency harmonics as shown in Figure 165. Contrary to the expectation of lower switching frequency harmonics from a larger low pass filter, the switching frequency harmonics increased. The reason for this finding is that the larger filter capacitance value of 1 μF has a parallel resonance frequency of 7.5 kHz with the line inductance which was arbitrary selected as 0.44 mH. The impedance at 5 kHz is, therefore, actually increased by the filter capacitance. By using the 1 nF filter capacitance value the resonant frequency moves up to 240 kHz, that results in much lower impedance at 5 kHz.

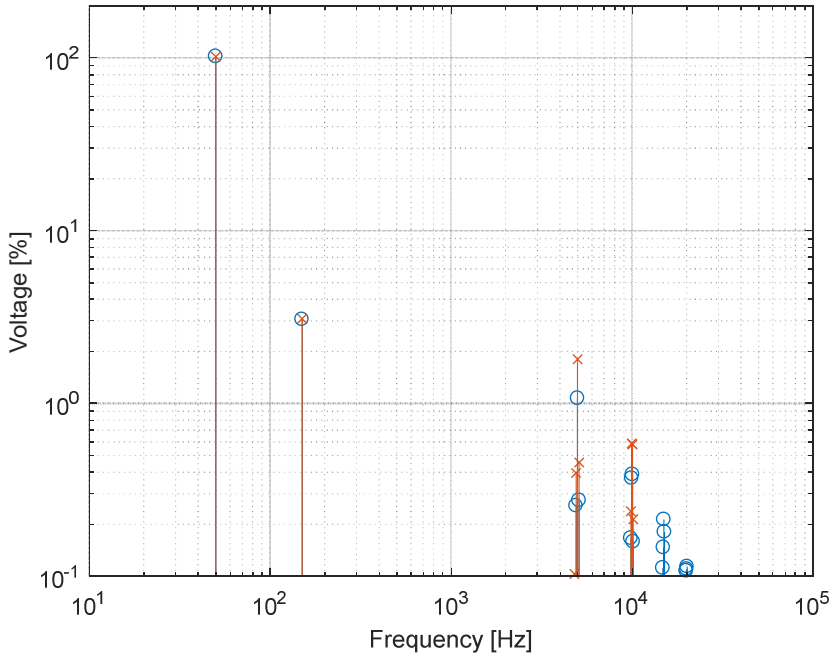

Figure 165: Harmonic spectrum of voltage at installation 1 with third order background harmonic and 1 nF filter capacitance ‘o’ and 1 μF filter capacitance ‘x’

The same analysis can be done for higher frequency background harmonics that can typically be generated by other inverters or single-phase active rectifier locomotive in the system. A 2 kHz voltage source, representing another inverter in the network, with amplitude of 1% of the fundamental voltage is used as background harmonic. Emission is evaluated at inverter filter capacitor values of 1 nF to 1 μF as shown in Figure 166.

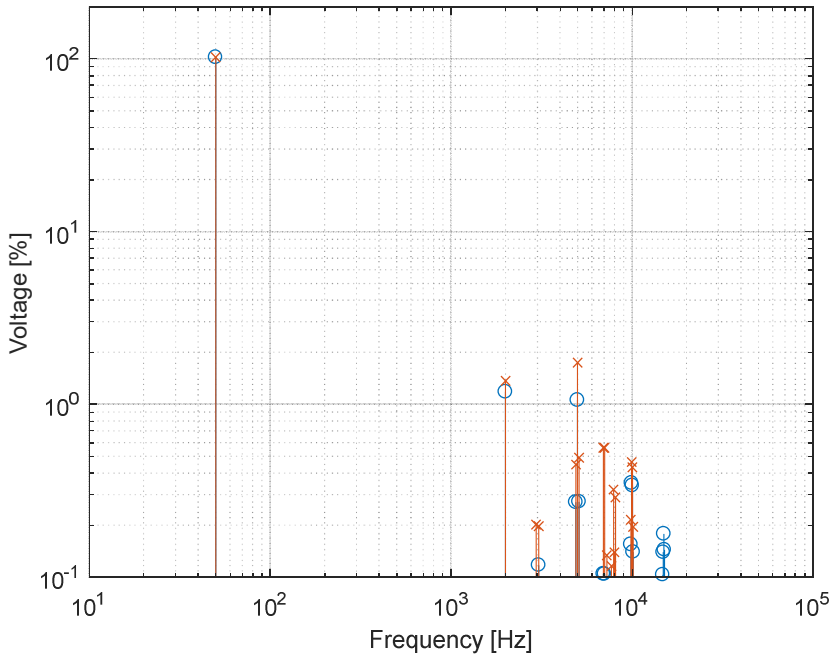

Figure 166: Harmonic spectrum of voltage at installation 1 with 2 kHz background harmonic and 1 nF filter capacitance ‘o’ and 1 μF filter capacitance ‘x’

From Figure 166 it is evident that the emission from the background harmonic of 2 kHz increased when the filter capacitance value was increased from 1 nF to 1 μF, because $|\bar{Z}_{hc}|$ is reduced. It is expected that the switching frequency harmonics should remain the same, since $|\bar{Z}_h|$ remains constant if (2.25) is valid. However, the emissions from the harmonic current sources $\bar{I}_{hc}$ at the switching frequency harmonics increased. This effect is evaluated by using the parallel combination of the system impedance and the consumer impedance $|\bar{Z}_p|$, instead of assuming that the consumer impedance can be regarded as insignificant. $|\bar{Z}_p|$ can be calculated as follows:

$$
\begin{aligned}
\bar{Z}_p &= \bar{Z}_h \| \bar{Z}_{hc} \\
&= \frac{\bar{Z}_h \bar{Z}_{hc}}{\bar{Z}_h + \bar{Z}_{hc}} \\
&= \frac{(R_h + jX_h)(R_{hc} + jX_{hc})}{(R_h + jX_h) + (R_{hc} + jX_{hc})} \\
&= \frac{(R_h R_{hc} - X_h X_{hc}) + j(R_h X_{hc} + R_{hc} X_h)}{(R_h + R_{hc}) + j(X_h + X_{hc})} \\
&= \frac{a + jb}{c + jd} \\
&= \frac{(a + jb)(c - jd)}{c^2 + d^2} \\
&= \frac{ac + bd}{c^2 + d^2} + j\frac{bc - ad}{c^2 + d^2}
\end{aligned}
$$

where

$$
\begin{aligned}
a &= R_h R_{hc} - X_h X_{hc} \\
b &= R_h X_{hc} + R_{hc} X_h \\
c &= R_h + R_{hc} \\
d &= X_h + X_{hc}
\end{aligned}
\qquad (5.2)
$$

Impedance magnitude at different frequencies can be calculated by setting the following values to the parameters in (5.2):

$$
\begin{aligned}
R_h &= 0.534\ \Omega \\
X_h &= \omega L_h = 2\pi f 414.10^{-6}\ \Omega \\
R_{hc} &= 0\ \Omega \\
X_{hc} &= \frac{-1}{\omega C_f} = \frac{-1}{2\pi f 1.10^{-9}}\ \Omega \text{ and } \frac{-1}{2\pi f 1.10^{-6}}\ \Omega
\end{aligned}
\qquad (5.3)
$$

The impedance plots in Figure 167 shows that for a filter capacitance of 1 nF, the assumption in (2.25) is valid, but if the combination of line inductance and filter capacitance forms a resonant circuit at frequencies in the same order as the switching frequency harmonics, the assumption is not valid and the equivalent impedance can be much higher. Therefore, the increase in emissions from $\overline{I}_{hc}$ in Figure 166 is experienced.

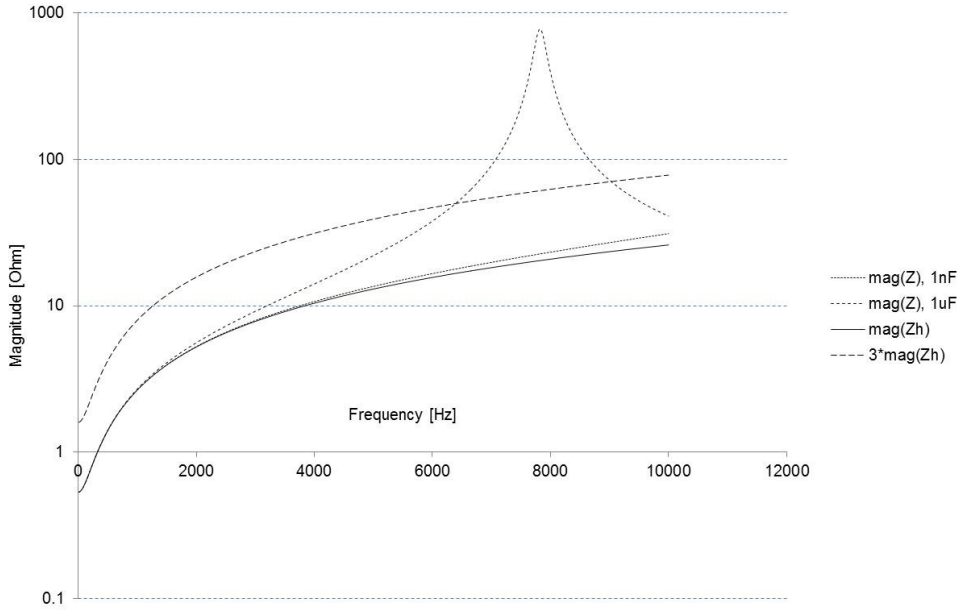

Figure 167: Impedance plots $\left|\overline{Z}_p\right|$ for $C_f = 1\,\text{nF}$ and $C_f = 1\,\mu\text{F}$ and $\left|\overline{Z}_h\right|$ and $\left|\overline{Z}_h\right| \times 3$

The simplified method of calculating impedances as described by CIGRE/CIRED C4.109 working group [50] to establish harmonic contribution will not always be valid, especially when having inverters as harmonic sources. It will be accurate when $\overline{Z}_h$ and $\overline{Z}_{hc}$ are both inductive and $\overline{Z}_{hc} \gg \overline{Z}_h$, or if $X_{hc} = -X_h$ at frequencies well above the highest frequency harmonic present in the system.

The effect of consumer impedance and background harmonics on Wind farm A current harmonic emissions will now be shown by investigating the two-point measurement approach. From the recorded data on Elspec B it can be determined when a locomotive was present on the network and what current harmonics were generated and thus be able to investigate whether the measured current emissions from Elspec A at the POC of Wind farm A are influenced by the current emissions of the traction load.

An internal RPP harmonic assessment report at the POC of Wind farm A investigated and compared the quality of supply at the POC to the PQ limits specified in the DCUOSA. From the investigation the current harmonic components shown in Table 7 all exceeded their respective DCUOSA limits. Note that only the individual harmonics and their respective limits for those that exceeded the emission limits are shown. These harmonic emission level values

were calculated by using the apportioned voltage emission levels assigned to the RPP and by using the method described in Section 2.6.4.3 to obtain the current emission levels.

Table 7: Individual current harmonic emission levels

Harmonic order	Current Emission (A)	DCOUSA emission level (A)	150% emission limit (A)
3	1.946	0.795	1.192
5	4.696	0.954	1.43
7	1.751	0.681	1.022
11	1.489	0.488	0.731
13	1.618	0.413	0.619
17	1.385	0.35	0.525
19	1.84	0.35	0.525
21	0.54	0.35	0.525
23	1.788	0.35	0.525
25	1.385	0.35	0.525
27	0.77	0.35	0.525
29	1.655	0.35	0.525
31	1.181	0.35	0.525
33	1.112	0.35	0.525
35	0.774	0.35	0.525
39	0.424	0.35	0.525

The investigation further determined which of the above harmonics was either absorbed or injected by the RPP or at some instances if that is not clear. The results is shown in Table 8.

Table 8: Results from investigation

Harmonic order	Injected by RPP	Absorbed by RPP	Not clear
3			Yes
5		Yes	
7			Yes
11		Yes	
13		Yes	
17		Yes	

19			Yes
21			Yes
23	Yes		Yes
25			Yes
27		Yes	
29			Yes
31	Yes		
33		Yes	
35		Yes	
39			Yes

To show that the harmonic assessment is not always accurate the 31st current harmonic will be investigated. From the investigation it was determined that the 31st harmonic has a current emission of 1.181 A which is injected by the RPP according to the IEC 61000-3-6 guidelines. From the weekly period of investigated in this thesis the 95th 10-minute aggregated 31st current harmonic is 1.215 A which is close to the value obtained from the internal harmonic assessment of Wind farm A. This value can, however, be influenced by the current emission of traction loads. By only looking at the IEC 61000-3-6 assessment guidelines and the results in Table 8 it will appear as if the RPP is the only source of the 31st current harmonic. It was already shown in Figure 156 that active rectifier locomotives on the network generate current harmonics surrounding 1.5 kHz (30th harmonic) and will, therefore, influence current emission assessment at these frequencies. The phase A 10-minute aggregated 31st current harmonic at the traction substation as measured by Elspec B for a period of one week is plotted in Figure 168. The spikes represent the times when a locomotive is in service and connected to the specific traction substation where Elspec B was installed.

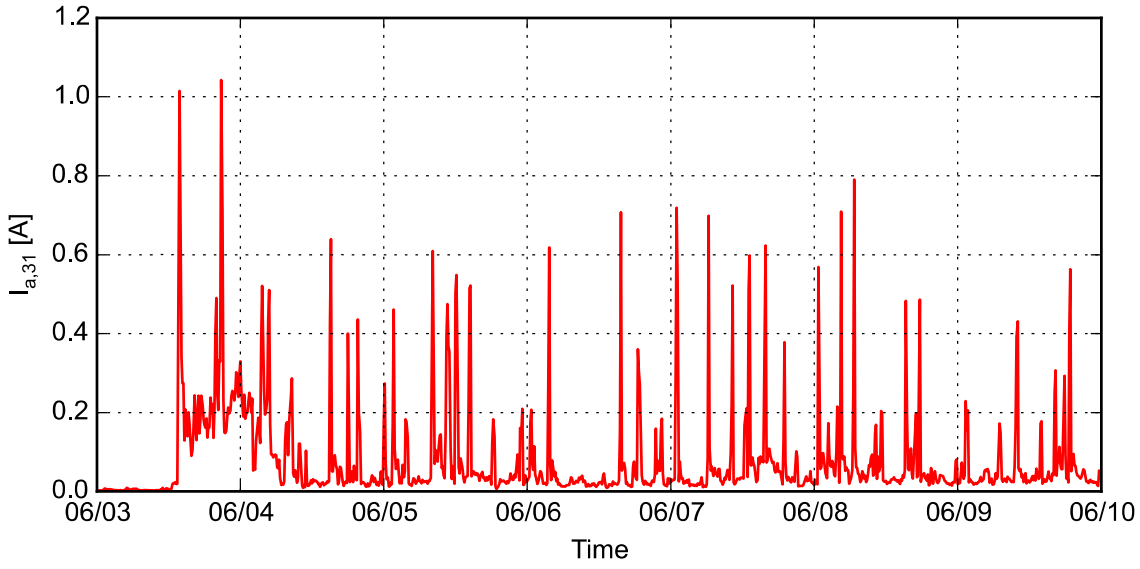

Figure 168: Measured 10-minute aggregated 31st current harmonic at traction substation

The three-phase 10-minute aggregated 31st current harmonic at the POC as measured by Elspec A for a period of one week is plotted in Figure 169.

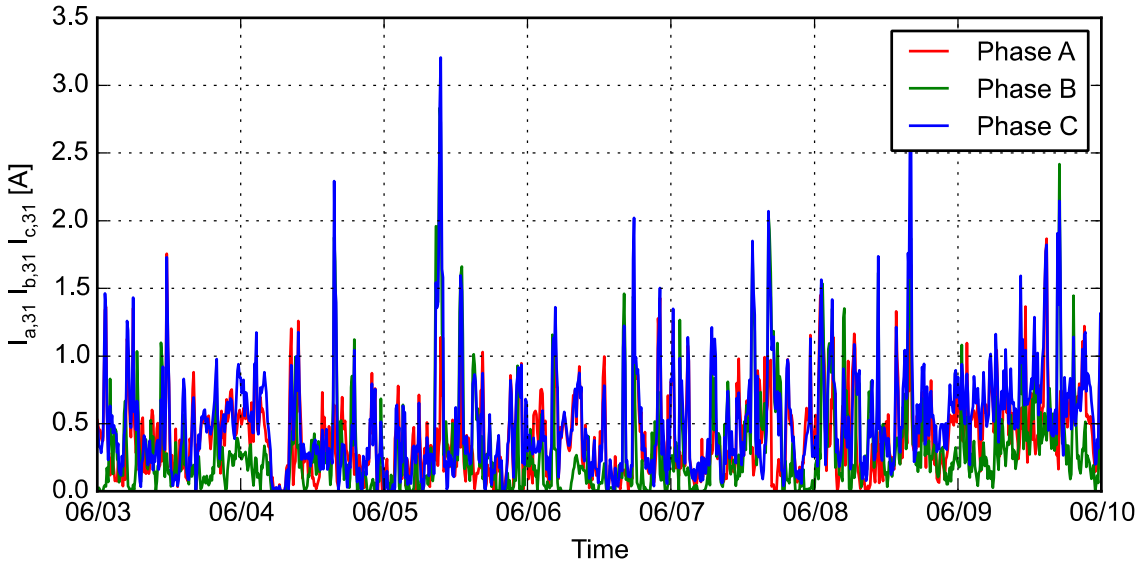

Figure 169: Measured 10-minute aggregated 31st current harmonic at POC

To determine to what degree the locomotives will influence the harmonic current emissions of RPPs it becomes necessary to determine the total time that a locomotive is injecting harmonics into the grid for the one week period. This provides challenges as data was only obtained at one traction substation and it is difficult to determine when a locomotive is injecting harmonics at other nearby traction substations as well. Therefore, a method will be presented to approximate current emissions of the RPP without the impact of the traction load current emissions on the calculation.

Figure 169 shows that the traction loads have unbalanced current emissions which cause the spikes in one or two of the phases when a traction load is injecting the 31st harmonic. Figure 170 shows the measured instantaneous 31st current harmonic at the POC during a time period when a traction load is injecting 31st harmonic. From Figure 170 the impact of traction load current emissions on the RPP harmonic emissions is visible.

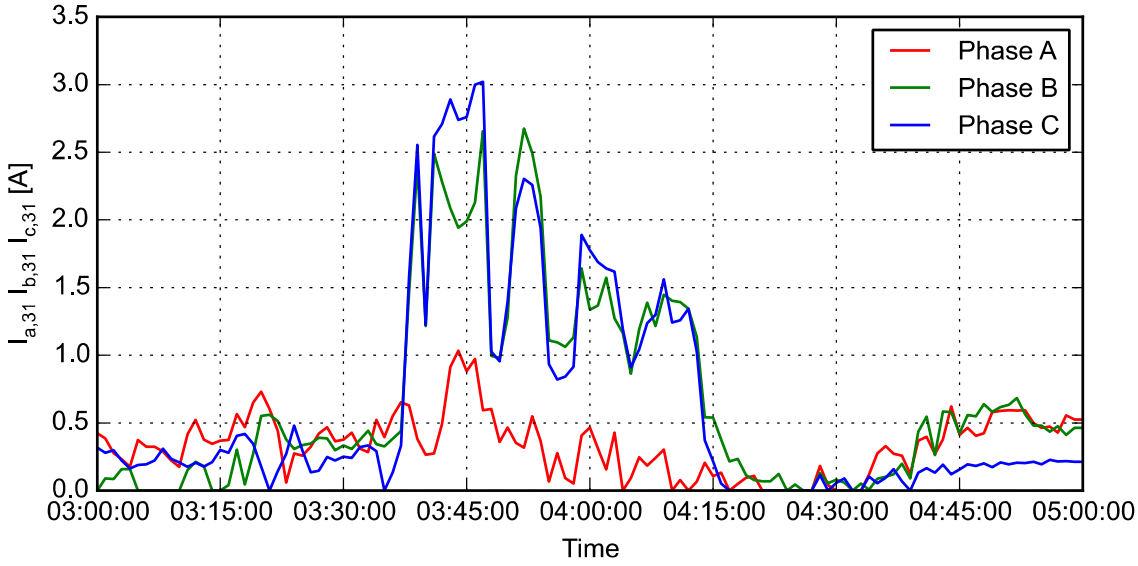

Figure 170: Measured instantaneous 31st current harmonic at the POC

By only assuming for the purposes of this thesis that a locomotive is injecting current harmonics at the traction substation where Elspec B is installed then the total time that a locomotive is injecting harmonics can be determined. This is done by counting the amount of 10-minute values that exceed a value of 0.1 A in Figure 168 and comes to 211 10-minute values. The average 10-minute 31st harmonic current injected by the traction load for the 211 10-minute values can then be calculated as 0.27 A. By taking the average 10-minute value over the week period for the 10-minute values in Figure 169 then the average 10-minute 31st harmonic current for phase A, phase B and phase C comes to 0.402 A, 0.305 A and 0.512 A respectively. The average 10-minute 31st current harmonic for all three phase can then be calculated as 0.406 A. By assuming that all 10-minute values above 0.406 A + 0.27 A = 0.676 A is caused by traction loads then the approximated amount of times that a traction load is injecting the 31st current harmonic comes to 319. This is a realistic value as it is more than 211 as expected. It is, however, a conservative value as all the data for the entire investigation period including times when a locomotive is injecting current harmonics was used to calculate the average 10-minute 31st harmonic for all three phase which is 0.406 A. Therefore, 0.406 A is expected to be lower when removing the data for the times when a traction load is injecting harmonics. The amount of times that a traction load is injecting the 31st current harmonic can thus be expected to be more than 319 times. By removing the 319 instances where it is assumed a locomotive is injecting current harmonics then a new approximated dataset is obtained that presents the

current harmonics of the RPP. The approximated 95th percentile 10-minute 31st current harmonic then becomes 0.612 A which is significantly lower than 1.215 A. Therefore, showing the impact that traction loads can have on current harmonic emissions of RPPs. It is important to note that this is only an approximated statistical approach to exclude traction load data and cannot be used for assessment purposes in the industry. For this thesis, however, this was deemed adequate to show the effect of locomotives on the current emissions of RPPs.

6.9. CONCLUSION

The impact of traction loads on the network voltage distortion was investigated. A weekly assessment on the voltage THD and individual voltage harmonics was done using the NRS 048-2 standards and guidelines. From the assessment it was determined that traction loads contribute to voltage distortion at the POC and that small current harmonics emissions of traction loads can generate large voltage distortion at the presence of a parallel resonance. The impact of impedance and background harmonics was investigated by modelling a simple Matlab/Simulink inverter model under various background harmonic and impedance conditions. The results showed that the simplified method of calculating impedances as described by CIGRE/CIRED C4.109 working group to establish harmonic contribution will not always be valid, especially when having inverters as harmonic sources. Lastly, the impact of traction load current emissions on the assessment of RPP current emission was investigated. A method was presented to approximate current emissions of the RPP without the impact of the traction load current emissions on the assessment. The method involve using a two point measuring approach and to determine when a traction loads is injecting current emission so to remove the times when a traction load is injecting harmonics from the assessment data. From the results it was shown that traction loads do impact the harmonic assessment of RPPs and will, therefore, not always be accurate.

CHAPTER 7
CONCLUSION

7.1. SYNOPSIS

This thesis investigated the PQ impact of AC traction loads on RPPs. A local wind farm connected to a traction network was used as a case study for the investigation. Different locomotive technologies in South Africa was explored and the two main technologies namely active rectifier and half-controlled thyristor rectifiers were identified and chosen as case studies for the investigation. Firstly, the main PQ issues associated with AC traction loads were explored.

A powerful simulation tool was required for the time domain analysis of Eskom's large distribution network. DIgSILENT PowerFactory offers a stand-alone software solution that is widely used for power system simulations, network planning and PQ studies and has become the industry standard in utility and RPP simulations in South Africa. DIgSILENT PowerFactory is easy to use with advanced solution algorithms combined with comprehensive and flexible modelling capabilities that include a large suite of libraries and electrical power equipment models. It features support for time domain (EMT) simulations of inverter and rectifier models. The built-in PWM converter model and its internal control functions for EMT simulations were presented. All of the necessary built-in elements that were used in simulation models were discussed.

To understand the PQ impact of traction loads on the network and on RPPs it was necessary to model locomotive rectifiers in detail, so to investigate various effects that a rectifier can have on the network. The theory, control, modelling and implementation of the two main locomotives technology types were presented. An active rectifier model and half-controlled thyristor rectifier model was designed and implemented in DIgSILENT PowerFactory. DIgSILENT PowerFactory, however, does not contain a built-in model for half-controlled thyristor rectifier and thus a method was explored to obtain the required functionality. This problem was further increased by a lack in DIgSILENT PowerFactory to simulate the combination of an AC and DC systems. This was addressed by developing a model that implements the inter-circuit fault event in EMT simulation to bridge separated DC and AC networks. It was important that the simulation models reflect the physical system as closely as possible, therefore, the models were compared to simulation results obtained on site by the installation a class A PQ recorder at a traction substation. These traction load models provided insight on the working principles and harmonic emissions of different traction loads on the network. The traction load models presented provided adequate results and can be compared to actual traction load systems for future PQ studies and network planning.

Customers and RPPs do not provide details on the control of their inverters, therefore, it was deemed necessary to model inverters so to completely understand the principles and control of grid-connected inverters. These models provide means of investigating PQ in RPPs. Different inverter control methodologies in South Africa were identified. The conventional hysteresis control was investigated and mathematically analysed. A generic conventional hysteresis inverter model was designed and implemented in DIgSILENT PowerFactory for EMT simulations. The illustration of the conventional hysteresis inverter showed the drawbacks to the implementation. The conventional PWM control approach in RPPs was investigated and mathematically analysed. A generic conventional PWM inverter model was designed and implemented in DIgSILENT PowerFactory for EMT simulation. The interleaved PWM control approach was investigated. A method was devised on how an interleaved inverter could be implemented in DIgSILENT PowerFactory. A generic interleaved PWM inverter model was designed and implemented in DIgSILENT PowerFactory for EMT simulation. The reliability of each model was investigated by comparing simulation results to measurement results obtained by installing a class A PQ recorder at the POC. The models presented provided adequate results and can be compared to actual wind farm inverters for future PQ studies and network planning.

The impact of traction loads on the network voltage unbalance was investigated. It was observed that various conditions such as the traction load types, operating conditions of traction loads, control of the traction loads, power demand of the traction loads, network layout, geographical variables and three-phase fault level will all impact the voltage unbalance caused by traction loads. Thyristor locomotives will have a higher impact on the network voltage unbalance due to the large low-order current harmonic components in particularly the 3rd harmonic. A weekly assessment on the voltage unbalance was done using the NRS 048-2 standards and guidelines. The measured and simulated results showed that traction loads can cause inverters to trip under certain network conditions. Network planners must reconsider the placement of RPP on traction network, placing a RPP close to a traction station will inherently lead to large voltage unbalance at that point due to the frequent stop and start of locomotives at traction stations. The national service providers and traction load customers must also consider installing and implementing voltage unbalance mitigation methods at points of interest on the network close to RPPs where the voltage unbalance is inherently high due to the dynamic effects of traction loads.

The impact of traction loads on the network voltage distortion was investigated. A weekly assessment on the voltage THD and individual voltage harmonics was done using the NRS 048-2 standards and guidelines. From the assessment it was determined that traction loads contribute to voltage distortion at the POC and that small current harmonics emissions of traction loads can generate large voltage distortion at the presence of a parallel resonance.

The impact of impedance and background harmonics was investigated by modelling a simple Matlab/Simulink inverter model under various background harmonic and impedance conditions. The results showed that the simplified method of calculating impedances as described by CIGRE/CIRED C4.109 working group to establish harmonic contribution will not always be valid, especially when having inverters as harmonic sources. Lastly, the impact of traction load current emissions on the assessment of RPP current emission was investigated. A method was presented to approximate current emissions of the RPP without the impact of the traction load current emissions on the assessment. The method involve using a two point measuring approach and to determine when a traction loads is injecting current emission so to remove the times when a traction load is injecting harmonics from the assessment data. From the results it was shown that traction loads do impact the harmonic assessment of RPPs and will, therefore, not always be accurate. Further investigations into possible practical harmonic measurement approaches to evaluate the harmonic emissions of RPPs once commissioned is definitely justified.

7.2. FUTURE WORK

The main problem that needs to be investigated, although this is not related to traction loads, is the cause for the large increase in harmonic emissions at RPP as the power generation increases as this is currently a big problem at various RPPs in South Africa. The following aspects should also be explored in future work:

- The designed AC traction models and generic inverter models must be combined to simulate the interaction between the two harmonic sources for detailed EMT analysis in DIgSILENT PowerFactory and future PQ studies.
- A method must be investigated to simulate moving AC traction loads on a traction network for detailed EMT analysis in DIgSILENT PowerFactory and future PQ studies.
- The traction rectifier models must be further improved and developed after obtaining more information regarding the equipment ratings of different locomotives in South Africa.
- The RPP generic inverter models must be further improved and developed for different sampling methods and control conditions.
- The impact of voltage unbalance on harmonic emission form RPPs must be analysed.
- The presence of 2nd harmonic component at PWM inverters need to be further analysed to determine the cause of the emission as this will impact the harmonic assessment of RPPs in the future.

References

[1] K. Kenosi and K. Phora, “Droerivier Report,” 2013.

[2] N. Esterhuysen, L. Bok, and M. Mathosa, “Kalkbult PV investigation report,” 2016.

[3] V. Matta and G. Kumar, “Unbalance and voltage fluctuation study on AC traction system,” in *2014 International Conference on Computation of Power, Energy, Information and Communication (ICCPEIC)*, 2014, pp. 315–320.

[4] T. Boonseng and N. Sarasiri, “Dynamic railway simulation using DIgSILENT programming language,” in *2016 19th International Conference on Electrical Machines and Systems (ICEMS)*, 2016, pp. 1–4.

[5] NRS, *NRS 048-2: 2015 Electricity Supply — Quality of Supply Part 2 : Voltage characteristics, compatibility levels, limits and assessment methods*, 4th ed. 2015.

[6] Z. He, Z. Zheng, and H. Hu, “Power quality in high-speed railway systems,” *Int. J. Rail Transp.*, vol. 4, no. 2, pp. 71–97, 2016.

[7] R. E. Morrison, “Power quality issues on AC traction systems,” in *Ninth International Conference on Harmonics and Quality of Power. Proceedings (Cat. No.00EX441)*, 2000, vol. 2, pp. 709–714.

[8] “South African Class 20E,” 2018. [Online]. Available: https://en.wikipedia.org/wiki/South_African_Class_20E. [Accessed: 14-Feb-2018].

[9] “Class 20E Electric Locomotive for South Africa,” 2016. [Online]. Available: http://www.crrcgc.cc/en/g5185/s12937/t264599.aspx. [Accessed: 20-Feb-2018].

[10] “South African Class 7E,” 2018. [Online]. Available: https://en.wikipedia.org/wiki/South_African_Class_7E.

[11] S. Lee, S. Member, J. Kim, S. Member, and H. Jung, “Analysis of Catenary Voltage of an AT-Fed AC HSR System,” vol. 53, no. 6, pp. 1856–1862, 2004.

[12] C. Lee, H. Lee, C. Lee, G. Jang, and S. Kwon, “Harmonic Analysis of the Korean High-Speed Railway Using the Eight-Port Representation Harmonic Analysis of the Korean High-Speed Railway Using the Eight-Port Representation Model,” no. May 2006, 2014.

[13] A. Nash and D. Huerlimann, “Railroad simulation using OpenTrack.”

[14] R. Hsr, T. Power, P. Hsi, S. Chen, and S. Member, “Electric Load Estimation Techniques for High-Speed,” vol. 50, no. 5, pp. 1260–1266, 2001.

[15] S. H. Hosseini and F. Shahnia, “Load Flow Calculation and Short Circuit Fault Transients in AC Electrified Railways,” pp. 4–7.

[16] S. Kejian, W. Mingli, V. G. Agelidis, and W. Hui, “Line current harmonics of three-level neutral- point-clamped electric multiple unit rectifiers : analysis , simulation and testing,” vol. 7, no. September 2013, pp. 1850–1858, 2014.

[17] G. W. Chang, H. Lin, and S. Chen, “Modeling characteristics of harmonic currents generated by high-speed railway traction drive converters,” *IEEE Trans. Power Deliv.*, vol. 19, no. 2, pp. 766–773, 2004.

[18] N. Mohan, T. M. Undeland, and W. P. Robbins, *Power Electronics: Converters, Applications and Design*, 3rd ed. John Wiley and Sons, Inc, 2003.

[19] “No Title,” pp. 1–21.

[20] G. Garcia and G. Ramos, “A Power Demand Simulator of Electric Transportation Systems for Distribution Utilities,” no. v, 2009.

[21] M. A. Ríos, G. Ramos, and U. D. L. Andes, “Power System Modelling for Urban Massive Transportation Systems.”

[22] R. J. Hill, “Electric railway traction. Part 1: Electric traction and DC traction motor drives,” *Power Eng. J.*, vol. 8, no. 1, pp. 47–56, 1994.

[23] S. A. Azmi, K. H. Ahmed, S. J. Finney, and B. W. Williams, “Comparative analysis between voltage and current source inverters in grid-connected application,” *Renew. Power Gener. (RPG 2011), IET Conf.*, pp. 1–6, 2011.

[24] D. Josi, “Comparison of a three phase single stage PV system in PSCAD and PowerFactory,” 2012.

[25] S. Buso and P. Mattavelli, *Digital Control in Power Electronics*, 2nd ed. Morgan & Claypool, 2006.

[26] R. W. Erickson and D. Maksimovic, *Fundamentals of Power Electronics*, 2nd ed. Springer US, 2001.

[27] D. G. Holmes and T. A. Lipo, *Pulse Width Modulation For Power Converters Principles and Practice*. Wiley, IEEE Press, 2003.

[28] D. A. Grant, “Technique for pulse dropping in pulse-width modulated inverters,” *IEE Proc. B - Electr. Power Appl.*, vol. 128, no. 1, pp. 67–72, 1981.

[29] J. A. Houldsworth and D. A. Grant, “The Use of Harmonic Distortion to Increase the Output Voltage of a Three-Phase PWM Inverter,” *IEEE Trans. Ind. Appl.*, vol. IA-20, no. 5, pp. 1224–1228, 1984.

[30] D. A. Grant, J. A. Houldswirth, and K. N. Lower, “A New High-Quality PWM AC Drive,” *IEEE Trans. Ind. Appl.*, vol. IA-19, no. 2, pp. 211–216, 1983.

[31] M. H. Rashid, *Power electronics handbook*, 3rd ed. Elsevier, 2011.

[32] M. A. A. Badran, A. M. Tahir, and W. F. Faris, “Digital Implementation of Space Vector Pulse Width Modulation Technique Using 8-bit Microcontroller,” vol. 21, pp. 21–28, 2013.

[33] M. Kubeitari, A. Alhusayn, and M. Alnahar, “Space Vector PWM Simulation for Three Phase DC / AC Inverter,” *Int. J. Electr. Comput. Eng.*, vol. 6, no. 12, pp. 1402–1407, 2012.

[34] H. W. van der Broeck, H. Skudelny, and G. V. Stanke, “Analysis and Realization of a Pulsewidth Modulator Based on Voltage Space Vectors,” *IEEE Trans. Ind. Appl.*, vol. 24, no. 1, pp. 142–150, 1988.

[35] S. Tahir, J. Wang, M. H. Baloch, and G. S. Kaloi, “Digital Control Techniques Based on Voltage Source Inverters in Renewable Energy Applications : A Review,” *Electronics*, vol. 7, no. 2, 2018.

[36] M. P. Kazmierkowski and L. Malesani, “Current control techniques for three-phase voltage-source PWM converters: a survey,” *IEEE Trans. Ind. Electron.*, vol. 45, no. 5, pp. 691–703, 1998.

[37] NERSA, “South African Grid Connection Code for Renewable Power Plants Connected to the Electricity Transmission System or the Distribution System in South Africa,” vol. 2, no. 9. 2016.

[38] NRS, *NRS 048-4: 2009 Electricity Supply - Quality of Supply: Part 4 : Application practices for licensees*. 2009.

[39] NRS, *NRS 048-7 : 2012 Electricity Supply — Quality of Supply Part 7: Application practices for end-customers*, 1st ed. 2012.

[40] South African Bureau of Standards, *SANS 1816: 2013 Electrical supply - Quality of supply: Power Quality monitoring instruments specification*, 2nd ed., no. 2. 2013.

[41] IEC, *Electromagnetic Compatibility (EMC) - Part 4-30 : Testing and measurement techniques - Power quality measurement methods*, 2nd ed. 2015.

[42] S. Sewchurran, J. Kalichuran, and S. Maphumulo, “SA grid code compliance for medium-high voltage renewable power plants,” in *2016 65th AMEU Convention*, 2016, pp. 44–52.

[43] South African Bureau of Standards, *SANS 61000-4-30 : Electromagnetic compatibility (EMC) Part 4-30 : Testing and measurement techniques — Power quality measurement methods*, 2nd ed. 2009.

[44] South African Bureau of Standards, *SANS 61000-4-7 : Electromagnetic compatibility (*

EMC) Part 4-7 : Testing and measurement techniques - General guide on harmonics and interharmonics measurements and and equipment connected thereto, 2.1. 2009.

[45] IEC, “Electromagnetic compatibility (EMC) — Part 4-15: Testing and measurement techniques — Flickermeter — Functional and design specifications,” vol. 1, p. 28, 1997.

[46] U. Minnaar *et al.*, *Power Quality in Electrical Power Systems - A Holistic Approach*, 8th ed. Crown Publication, 2013.

[47] IEC, “Electromagnetic compatibility (EMC) — Part 3-6: Limits — Assessment of emission limits for the connection of distorting installations to MV, HV and EHV power systems,” vol. 3, 2008.

[48] NERSA, “RPP Power Quality Guideline.”

[49] CIGRE, “Review of Disturbance Emission Assessment Techniques,” no. June, 2011.

[50] E. De Jaeger, “Disturbance Emission Level Assessment Techniques (CIGRE / CIRED Joint Working Group C4-109),” *20th Int. Conf. Electr. Distrib.*, pp. 1–4, 2009.

[51] B. Peterson, J. Rens, G. Botha, and J. Desmet, “A Discriminative Approach to Harmonic Emission Assessment,” in *2015 IEEE International Workshop on Applied Measurements for Power Systems (AMPS)*, 2015, pp. 7–12.

[52] J. Rens and P. Swart, “On Techniques for the Localization of Multiple Distortion Sources in Three-phase Networks: Time-Domain Verification,” *Eur. Trans. Electr. Power*, vol. 11, pp. 317–322, 2001.

[53] F. Li and Z. Yang, “Analysis and management research on the impact of Shanghai-Nanjing intercity railway traction Load on Power grid,” in *CICED 2010 Proceedings*, 2010, pp. 1–6.

[54] T. H. Chen and H. Y. Kuo, “Network modelling of traction substation transformers for studying unbalance effects,” *IEE Proc. - Gener. Transm. Distrib.*, vol. 142, no. 2, pp. 103–108, 1995.

[55] S. Chen, R. Li, and P. Hsi, “Traction system unbalance problem - analysis methodologies,” *IEEE Trans. Power Deliv.*, vol. 19, no. 4, pp. 1877–1883, 2004.

[56] T. H. Chen, W. C. Yang, and Y. F. Hsu, “A systematic approach to evaluate the overall impact of the electric traction demands of a high-speed railroad on a power system,” *IEEE Trans. Veh. Technol.*, vol. 47, no. 4, pp. 1378–1384, 1998.

[57] C. Y. Lee, “Effects of unbalanced voltage on the operation performance of a three-phase induction motor,” *IEEE Trans. Energy Convers.*, vol. 14, no. 2, pp. 202–208, 1999.

[58] F. J. Foley, “The impact of electrification on railway signalling systems,” in *2009 4th IET professional Development Course on Railway Electrification Infrastructure and*

Systems, 2009, pp. 141–148.

[59] S. M. Mousavi Gazafrudi, A. Tabakhpour Langerudy, E. F. Fuchs, and K. Al-Haddad, "Power quality issues in railway electrification: A comprehensive perspective," *IEEE Trans. Ind. Electron.*, vol. 62, no. 5, pp. 3081–3090, 2015.

[60] V. M. Mtech and I. Member, "Unbalance and Voltage fluctuation study on AC Traction System," pp. 315–320, 2014.

[61] N. Gunavardhini, M. Chandrasekaran, C. Sharmeela, and K. Manohar, "A case study on Power Quality issues in the Indian Railway traction sub-station," in *2013 7th International Conference on Intelligent Systems and Control (ISCO)*, 2013, pp. 7–12.

[62] C.A. Brebbia, J. M. Mera, N. Tomii, and P. Tzieropoulos, *Computers in Railways XV: Railway Engineering Design and Operation*. Wit Pr/Computational Mechanics, 2016.

[63] B. K. Chen and B. S. Guo, "Three phase models of specially connected transformers," *IEEE Trans. Power Deliv.*, vol. 11, no. 1, pp. 323–330, 1996.

[64] Y. Zhongming, E. Lo, K. H. Yuen, and M. H. Pong, "Probabilistic characterization of current harmonics of electrical traction power supply system by analytic method," in *Industrial Electronics Society, 1999. IECON '99 Proceedings. The 25th Annual Conference of the IEEE*, 1999, pp. 360–366.

[65] M. Brenna, F. Foiadelli, and D. Zaninelli, "Electromagnetic Model of High Speed Railway Lines for Power Quality Studies," *IEEE Trans. Power Syst.*, vol. 25, no. 3, pp. 1301–1308, 2010.

[66] Z. He, H. Hu, Y. Zhang, and S. Gao, "Harmonic Resonance Assessment to Traction Power-Supply System Considering Train Model in China High-Speed Railway," *IEEE Trans. Power Deliv.*, vol. 29, no. 4, pp. 1735–1743, 2014.

[67] L. Battistelli, M. Pagano, and D. Proto, "2 x 25-kV 50 Hz High-Speed Traction Power System: Short-Circuit Modeling," *IEEE Trans. Power Deliv.*, vol. 26, no. 3, pp. 1459–1466, 2011.

[68] M. Brenna, F. Foiadelli, D. Zaninelli, and S. Member, "New Stability Analysis for Tuning PI Controller of Power Converters in Railway Application," *IEEE Trans. Ind. Electron.*, vol. 58, no. 2, pp. 533–543, 2011.

[69] B. Busco, P. Marino, M. Porzio, R. Schiavo, and F. Vasca, "Digital control and simulation for power electronic apparatus in dual voltage railway locomotive," *IEEE Trans. Power Electron.*, vol. 18, no. 5, pp. 1146–1157, 2003.

[70] J. Wang, M. Zhang, S. Li, T. Zhou, and H. Du, "Passive filter design with considering characteristic harmonics and harmonic resonance of electrified railway," in *2017 8th*

International Conference on Mechanical and Intelligent Manufacturing Technologies (ICMIMT), 2017, pp. 174–178.

[71] M. Brenna, A. Capasso, M. C. Falvo, F. Foiadelli, R. Lamedica, and D. Zaninelli, “Investigation of resonance phenomena in high speed railway supply systems : Theoretical and experimental analysis,” *Electr. Power Syst. Res.*, vol. 81, no. 10, pp. 1915–1923, 2011.

[72] J. Holtz and H. Klein, “The propagation of harmonic currents generated by inverter-fed locomotives in the distributed overhead supply system,” *IEEE Trans. Power Electron.*, vol. 4, no. 2, pp. 168–174, 1989.

[73] H. Hu, Z. He, X. Li, K. Wang, and S. Gao, “Power-Quality Impact Assessment for High-Speed Railway Associated With High-Speed Trains Using Train Timetable — Part I : Methodology and Modeling,” *IEEE Trans. Power Deliv.*, vol. 31, no. 2, pp. 693–703, 2016.

[74] B. Badrzadeh, M. Gupta, N. Singh, ɣ A. P., ɣ L. M., and M. Høgdahl, “Power System Harmonic Analysis in Wind Power Plants- Part I : Study Methodology and Techniques,” in *2012 IEEE Industry Applications Society Annual Meeting*, 2012, pp. 1–11.

[75] J. Arrillaga and N. R. Watson, *Power System Harmonics*, 2nd ed. John Wiley and Sons, Ltd, 2003.

[76] A. Reznik, M. G. Simoes, A. Al-Durra, and S. M. Muyeen, “LCL Filter Design and Performance Analysis for Grid-Interconnected Systems,” *IEEE Trans. Ind. Appl.*, vol. 50, no. 2, pp. 1225–1232, 2014.

[77] H. Hu, Y. Shao, L. Tang, J. Ma, Z. He, and S. Gao, “Overview of Harmonic and Resonance in Railway Electrification Systems,” *IEEE Trans. Ind. Appl.*, vol. 54, no. 2, pp. 5227–5245, 2018.

[78] N. Mesbahi, L. Monji, and L. Sainz, “Study of Resonance in 1x25 kV AC Traction Systems with External Balancing Equipment,” *IEEE PES Trans. power Deliv.*, pp. 1–9, 2015.

[79] L. Guo, Q. Li, and Y. Xu, “Study on Harmonic Resonance of Traction Line in Electrified High-speed Traction System,” in *2009 International Conference on Sustainable Power Generation and Supply*, 2009, pp. 1–4.

[80] H. Hu *et al.*, “Harmonic Resonance Evaluation for Hub Traction Substation Consisting of Multiple High-Speed Railways,” *IEEE Trans. Power Deliv.*, vol. 32, no. 2, pp. 910–920, 2017.

[81] NRS, *NRS 048-2 : 2007 Electricity Supply — Quality of Supply Part 2: Voltage characteristics compatibility levels , limits and assessment methods*, 3rd ed. ESLC,

2007.

[82] A. Bagheri, *Extracting Information from Voltage Dip Monitoring*. .

[83] D. M. Tagare, *Reactive Power Management*. New Delhi: Tata McGraw-Hill, 2004.

[84] S. Whaite, B. Grainger, and A. Kwasinski, “Power Quality in DC Power Distribution Systems and Microgrids,” *Energies*, vol. 8, no. 5, pp. 4378–4399, 2015.

[85] M. K. Mits, A. Pradesh, and M. Krishna, “Types of Power Quality Disturbances on AC Electric Traction Drives : A Survey Types of Power Quality Disturbances on AC Electric Traction Drives : A Survey,” no. June 2013, 2014.

[86] G. Olguin, *Voltage Dip (Sag) Estimation in Power Systems based on Stochastic Assessment and Optimal Monitoring*. 2005.

[87] G. Lin, X. Yonghai, X. Xiangnin, L. Yingying, and J. Peisi, “Analysis of adverse effects on the public power grid brought by traction power-supply system,” in *2008 IEEE Canada Electric Power Conference*, 2008, pp. 1–7.

[88] Y. Oura, N. Hiroki, and Y. Mochinaga, “Railway electric power feeding systems,” *Japan Railw. Transp. Rev.*, vol. 16, no. 10, pp. 48–58, 1998.

[89] C. Wu, A. Luo, J. Shen, F. J. Ma, and S. Peng, “A negative sequence compensation method based on a two-phase three-wire converter for a high-speed railway traction power supply system,” *Japan Railw. Transp.*, vol. 27, no. 2, pp. 706–717, 2012.

[90] C. P. Huang, C. J. Wu, Y. S. Chuang, S. K. Peng, J. L. Yen, and M. H. Han, “Loading characteristics analysis of specially connected transformers using various power factor definitions,” *IEEE Trans. Power Deliv.*, vol. 21, no. 3, pp. 1406–1413, 2006.

[91] T. H. Chen, “Comparison of Scott and Leblanc transformers for supplying unbalanced electric railway demands,” *Electr. Power Syst. Res.*, vol. 28, no. 3, pp. 235–240, 1994.

[92] M. Salehifar, M. Ranjbar, A. Amirahmadi, and A. Shoulaie, “A combined system of passive filter and TCR for power quality improvement in a 25-kV electrified railway system,” in *2009 International Conference for Technical Postgraduates (TECHPOS)*, 2009, pp. 1–5.

[93] Z. Sun, X. Jiang, D. Zhu, and G. Zhang, “A Novel Active Power Quality Compensator Topology for Electrified Railway,” *IEEE Trans. Power Electron.*, vol. 19, no. 4, pp. 1036–1042, 2004.

[94] M. Z. El-Sadek, “Static var compensation for phase balancing and power factor improvement of single phase train loads,” *Electr. Mach. Power Syst.*, vol. 26, no. 4, pp. 347–361, 1998.

[95] S. Lee, C. Wu, and W. Chang, “A compact control algorithm for reactive power

compensation and load balancing with static Var compensator," *Elsevier Sci.*, vol. 58, no. 2, pp. 63–70, 2001.

[96] J. H. Chen, W. J. Lee, and M. S. Chen, "Using a static var compensator to balance a distribution system," *IEEE Trans. Ind. Appl.*, vol. 35, no. 2, pp. 2321–2326, 1999.

[97] G. Zhu, J. Chen, and X. Liu, "Compensation for the negative-sequence currents of electric railway based on SVC," in *2008 3rd IEEE Conference on Industrial Electronics and Applications, ICIEA 2008*, 2008, pp. 1958–1963.

[98] F. Ma, A. Luo, X. Xu, H. Xiao, C. Wu, and W. Wang, "A Simplified Power Conditioner Based on Half-Bridge Converter for High-Speed Railway System," *IEEE Trans. Ind. Electron.*, vol. 60, no. 2, pp. 728–738, 2013.

[99] L. Sainz, L. Monjo, S. Riera, and J. Pedra, "Study of the Steinmetz circuit influence on AC traction system resonance," *IEEE Trans. Power Deliv.*, vol. 27, no. 4, pp. 2295–2303, 2012.

[100] A. Kazemi, A. M. Koochi, and R. Rezaeipour, "A dynamically SVC based compact control algorithm for load balancing in distribution systems," *Int. J. Energy*, vol. 1, no. 3, 2007.

[101] L. S. Czarnecki and S. M. Hsu, "Thyristor controlled susceptances for balancing compensators operated under nonsinusoidal conditions," *IEE Proc. - Electr. Power Appl.*, vol. 141, no. 4, pp. 177–185, 1994.

[102] Y. Wei, Q. Jiang, and X. Zhang, "A novel control strategy for optimization of power capacity based on railway power static conditioner," in *2008 Twenty-Third Annual IEEE Applied Power Electronics Conference and Exposition*, 2008, pp. 1669–1674.

[103] M. Chen, Q. Li, and G. Wei, "Optimized Design and Performance Evaluation of New Cophase Traction Power Supply System," in *2009 Asia-Pacific Power and Energy Engineering Conference*, 2009, pp. 1–6.

[104] Z. Shu, S. Xie, and Q. Li, "Single-Phase Back-To-Back Converter for Active Power Balancing , Reactive Power Compensation , and Harmonic Filtering in Traction Power System," *IEEE Trans. Power Electron.*, vol. 26, no. 2, pp. 334–343, 2011.

[105] K. Lao, N. Dai, W. Liu, and M. Wong, "Hybrid Power Quality Compensator With Minimum DC Operation Voltage Design for High-Speed Traction Power Systems," *IEEE Trans. Power Electron.*, vol. 28, no. 4, pp. 2024–2036, 2013.

[106] N. Y. Dai, K. W. Lao, M. C. Wong, and C. K. Wong, "Hybrid power quality conditioner for co-phase power supply system in electrified railway," *IET Power Electron.*, vol. 5, no. December 2011, pp. 1084–1094, 2012.

[107] N. Dai, K. Lao, and M. Wong, “A hybrid railway power conditioner for traction power supply system,” in *2013 Twenty-Eighth Annual IEEE Applied Power Electronics Conference and Exposition (APEC)*, 2013, pp. 1326–1331.

[108] X. He *et al.*, “Advanced Cophase Traction Power Supply System Based on Three-Phase to Single-Phase Converter,” *IEEE Trans. Power Electron.*, vol. 29, no. 10, pp. 5323–5333, 2014.

[109] DIgSILENT GmbH, “Eskom Distribution chooses DIgSILENT’s PowerFactory,” *DIgSILENT News*, 2003. [Online]. Available: http://www.digsilent.de/index.php/company-news-detail/items/eskom-distribution-chooses-digsilents-powerfactory.html. [Accessed: 12-Jun-2017].

[110] “Power Systems Analysis Software,” *OpenElectrical Wiki*, 2017. [Online]. Available: https://wiki.openelectrical.org/index.php?title=Power_Systems_Analysis_Software#DIgSILENT_.28PowerFactory.29. [Accessed: 12-Jun-2017].

[111] DIgSILENT GmbH, “DIgSILENT PowerFactory 2016 Brochure,” 2016.

[112] A. Latif, M. Shahzad, P. Palensky, and W. Gawlik, “An alternate PowerFactory Matlab coupling approach,” *Proc. - 2015 Int. Symp. Smart Electr. Distrib. Syst. Technol. EDST 2015*, pp. 486–491, 2015.

[113] F. M. Gonzalez-Longatt and J. Luis Rueda, *PowerFactory Applications for Power System Analysis*. Springer, 2014.

[114] L. Lategan, “System Analysis for Improved Energy Recovery on Prasa ’ s Electrical Traction Network by,” no. December, 2016.

[115] DIgSILENT GmbH, “DIgSILENT PowerFactory 15 User Manual,” p. 1513, 2015.

[116] O. Lennerhag, “Modelling of VSC-HVDC for Slow Dynamic Studies,” 2013.

[117] N. Mazibuko, “INTERCONNECTION OF SOLAR POWER TO THE GRID THROUGH THE POWER PLANT AUXILIARY SYSTEM,” Kwazulu-Natal, 2015.

[118] DIgSILENT GmbH, “DIgSILENT PowerFactory Technical Reference Documentation PWM Converter,” 2015.

[119] F. M. Gonzalez-longatt, L. Rueda, and H. Verdejo, “Modelling of Transmission Systems Under Unsymmetrical Conditions and Contingency Analysis Using DIgSILENT PowerFactory.”

[120] L. Grman, M. Hraško, J. Kuchta, and J. Buday, “Single phase PWM rectifier in traction application,” *J. Electr. Eng.*, vol. 62, no. 4, pp. 206–212, 2011.

[121] J. Bauer, “Single-Phase Pulse Width Modulated Rectifier,” *Acta Polytech.*, vol. 48, no. 3, pp. 84–87, 2008.

[122] D. M. Brod and D. W. Novotny, “Current Control of VSI-PWM Inverters.pdf,” *Ieee Trans. Ind. Appl.*, vol. IA-21, no. 3, pp. 562–570, 1985.

[123] L. Malesani and P. Tenti, “A Novel Hysteresis Control Method for Current-Controlled Voltage-Source PWM Inverters with Constant Modulation Frequency,” *IEEE Trans. Ind. Appl.*, vol. IA-21, no. 3, pp. 562–570, 1985.

[124] B. H. Kwon, T. W. Kim, and J. H. Youm, “A novel SVM-based hysteresis current controller,” *IEEE Trans. Power Electron.*, vol. 13, no. 2, pp. 297–307, 1998.

[125] M. P. Kaimierkowski and W. Sulkowski, “Novel space vector based current controllers for PWM-inverters,” *IEEE Trans. Power Electron.*, vol. 6, no. I, pp. 158–166, 1991.

[126] T.-Y. Chang and C.-T. Pan, “A practical vector control algorithm for µ-based induction motor drives using a new space vector current controller,” *IEEE Trans. Ind. Electron.*, vol. 41, no. 1, pp. 97–103, 1994.

[127] L. Malesani, P. Mattavelli, and P. Tomasin, “Improved constant-frequency hysteresis current control of VSI inverters with simple feedforward bandwidth prediction,” *IEEE Trans. Ind. Appl.*, vol. 33, no. 5, pp. 1194–1202, 1997.

[128] B. K. Bose, “An Adaptive Hysteresis-Band Current Control Technique of a Voltage-Fed PWM Inverter for Machine Drive System,” *IEEE Trans. Ind. Electron.*, vol. 37, no. 5, pp. 402–408, 1990.

[129] S. Buso, S. Fasolo, L. Malesani, and P. Mattavelli, “A dead-beat adaptive hysteresis current control,” in *Conference Record of the 1999 IEEE Industry Applications Conference. Thirty-Forth IAS Annual Meeting (Cat. No.99CH36370)*, 1999, pp. 72–78.

[130] Q. Yao and D. G. Holmes, “A simple, novel method for variable-hysteresis-band current control of a three phase inverter with constant switching frequency,” *Conf. Rec. 1993 IEEE Ind. Appl. Conf. Twenty-Eighth IAS Annu. Meet.*, pp. 1122–1129, 1993.

[131] A. N. Jog and N. G. Apte, “An adaptive hysteresis band current controlled shunt active power filter,” in *2007 Compatibility in Power Electronics*, 2007, pp. 1–5.

[132] S. Poulsen and M. A. E. Andersen, “Hysteresis controller with constant switching frequency,” *IEEE Trans. Consum. Electron.*, vol. 51, no. 2, pp. 688–693, 2005.

[133] N. Adhav, P. Student, and S. Agarwal, “Comparison and Implementation of Different PWM Schemes of Inverter in Wind Turbine,” *Int. J. Innov. Technol. Explor. Eng.*, vol. 2, no. 2, pp. 85–92, 2013.

[134] T. Nguyen-Van, R. Abe, and K. Tanaka, “A Digital Hysteresis Current Control for Half-Bridge Inverters with Constrained Switching Frequency,” *Energies*, vol. 10, 2017.

[135] G. Pinares, “On the analysis of the dc dynamics of multi-terminal VSC-HVDC systems

using small signal modeling."

[136] V. Converters, L. Zhang, L. Harnefors, S. Member, H. Nee, and S. Member, "Power-Synchronization Control of Grid-Connected," vol. 25, no. 2, pp. 809–820, 2010.

[137] B. Bahrani, S. Kenzelmann, and A. Rufer, "Multivariable-PI-Based dq Current Control of Voltage Source Converters With Superior Axis," *Ieee Trans. Ind. Electron.*, vol. 58, no. 7, pp. 3016–3026, 2011.

[138] A. Župan, A. T. Teklić, and B. F. Grčić, "Modeling of 25 kV Electric Railway System for Power Quality Studies," in *Eurocon 2013*, 2013, no. July, pp. 844–849.

Appendix

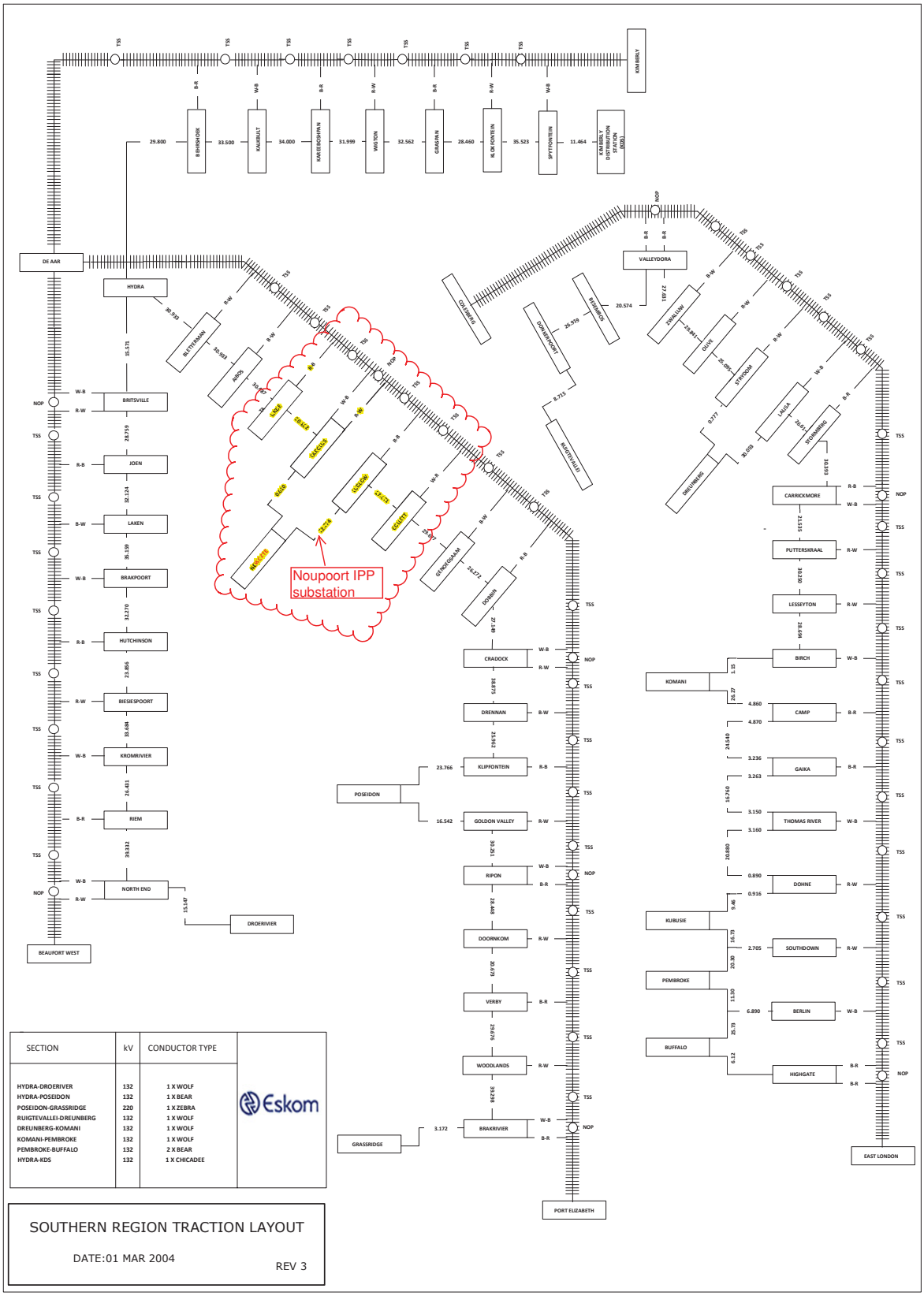

Figure 171: Detailed traction layout diagram

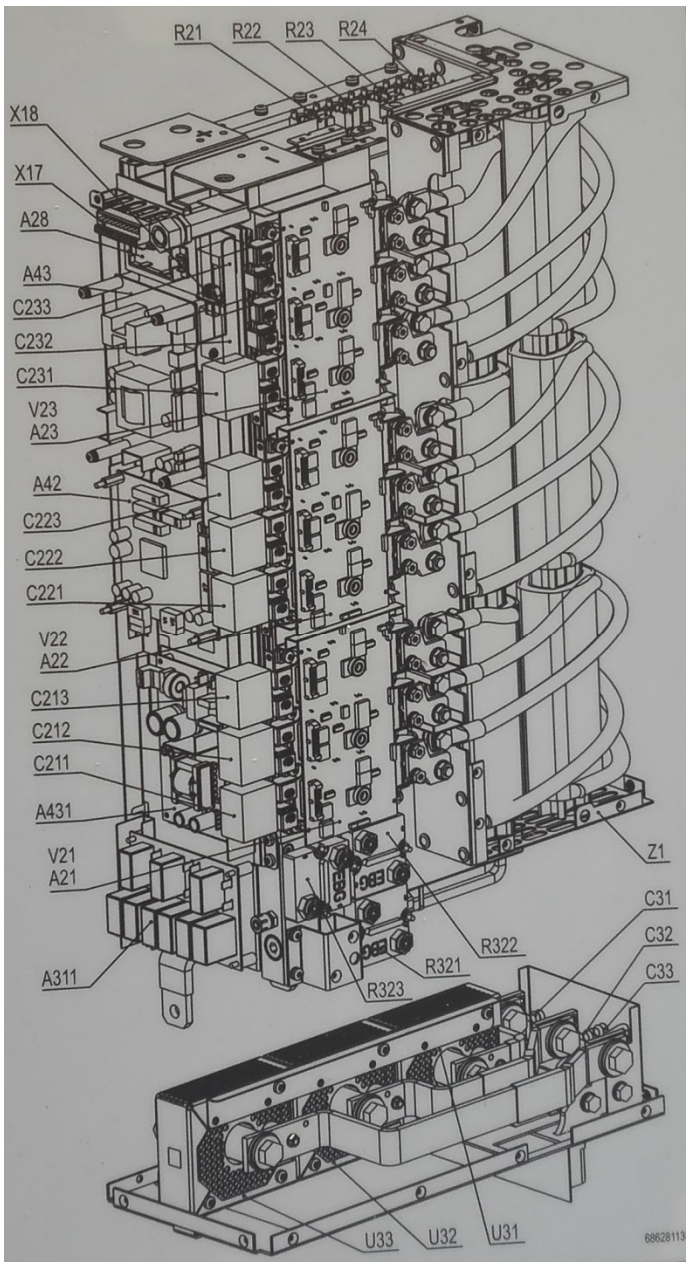

Figure 172: ABB inverter module drawing

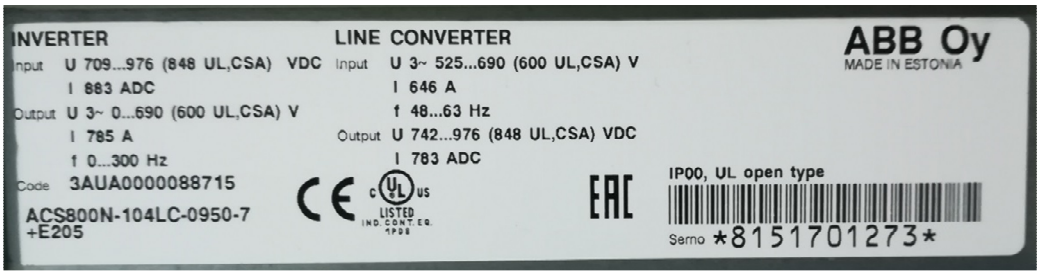

Figure 173: Nameplate of the ABB inverter module

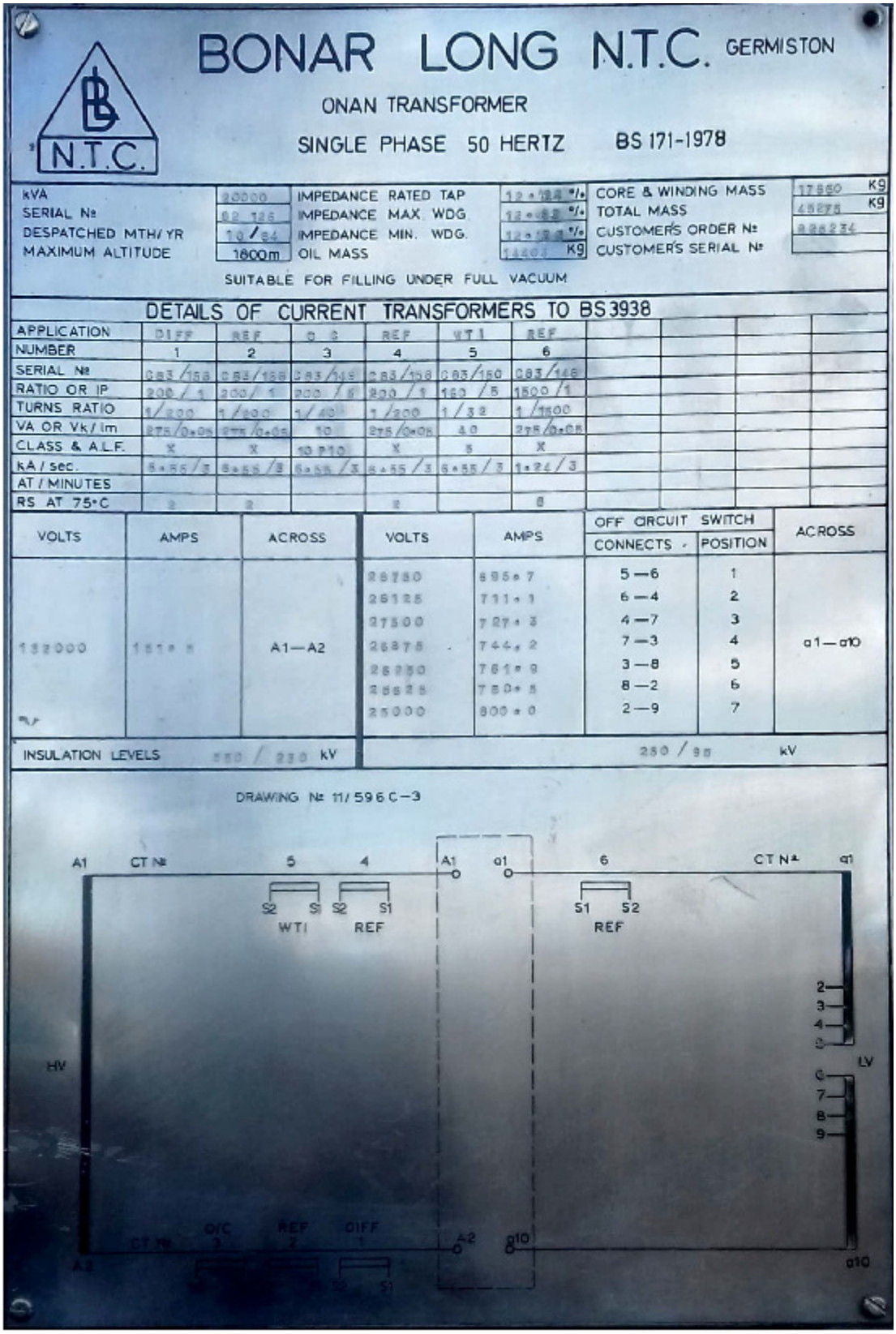

BONAR LONG N.T.C. GERMISTON

ONAN TRANSFORMER

SINGLE PHASE 50 HERTZ BS 171-1978

kVA	20000	IMPEDANCE RATED TAP	12.[illegible] %	CORE & WINDING MASS	17850 KG
SERIAL №	82 126	IMPEDANCE MAX. WDG.	12.[illegible] %	TOTAL MASS	45275 KG
DESPATCHED MTH/YR	10/84	IMPEDANCE MIN. WDG.	12.[illegible] %	CUSTOMER'S ORDER №	886234
MAXIMUM ALTITUDE	1800m	OIL MASS	14403 KG	CUSTOMER'S SERIAL №	

SUITABLE FOR FILLING UNDER FULL VACUUM

DETAILS OF CURRENT TRANSFORMERS TO BS 3938

APPLICATION	DIFF	REF	O/C	REF	WTI	REF				
NUMBER	1	2	3	4	5	6				
SERIAL №	C83/158	C83/158	C83/158	C83/158	C83/158	C83/158				
RATIO OR IP	200/1	200/1	200/1	200/1	150/5	1500/1				
TURNS RATIO	1/200	1/200	1/40	1/200	1/32	1/1500				
VA OR Vk/Im	275/0.05	275/0.05	10	275/0.05	40	275/0.05				
CLASS & A.L.F.	X	X	10 P10	X	5	X				
kA/sec.	6.55/3	6.55/3	6.55/3	6.55/3	6.55/3	1.24/3				
AT/MINUTES										
RS AT 75°C	2	2		2		8				

VOLTS	AMPS	ACROSS	VOLTS	AMPS	OFF CIRCUIT SWITCH CONNECTS	OFF CIRCUIT SWITCH POSITION	ACROSS
			28780	695.7	5—6	1	
			26125	711.1	6—4	2	
			27500	727.3	4—7	3	
132000	1514.5	A1—A2	26875	744.2	7—3	4	a1—a10
			26250	761.9	3—8	5	
			25625	780.5	8—2	6	
			25000	800.0	2—9	7	
INSULATION LEVELS	550 / 230 kV				250 / 95 kV		

DRAWING № 11/596C-3

Figure 174: Nameplate of traction transformer